Development of new advanced therapies to mitigate ischemia-reperfusion-induced injury during acute myocardial infarction

Doctoral Thesis

Author: Sandra Tejedor Gascón

Supervisors: Dra. Pilar Sepúlveda Sanchis
Dra. Imelda Ontoria Oviedo

Tutor: Dr. Ramón Serrano Salom

Valencia, March 2021

Development of new advanced therapies to mitigate ischemia-reperfusion-induced injury during acute myocardial infarction

Doctoral thesis

Author: Sandra Tejedor Gascón

Supervisors: Dra. Pilar Sepúlveda Sanchis

Dra. Imelda Ontoria Oviedo

Tutor: Dr. Ramón Serrano Salom

Valencia, March 2021

Agradecimientos

Me gustaría dejar aquí reflejados mis agradecimientos a las personas que, de una forma u otra, han formado parte de este proceso de aprendizaje tanto a nivel personal como profesional, y me han acompañado durante esta etapa de mi vida.

En primer lugar, me gustaría agradecer a Pilar Sepúlveda, por darme la oportunidad de llevar a cabo mi tesis doctoral en su grupo de investigación. Gracias por confiar en mí durante estos años, proporcionarme los recursos que han sido necesarios para llevar a cabo los experimentos que hemos propuesto y, sobre todo, por haberme dado libertad de decisión. He aprendido mucho durante esta etapa.

A todas/os mis compañeras/os de RETRACAR. A Imelda, mi codirectora de tesis, que me introdujo en el mundo de las iPSC, lo cual me ha abierto muchas puertas para el futuro. A Rubén Primero, que me acogió en mis primeros meses en el laboratorio. A Amparo, por cuidarnos tanto y por haber compartido conmigo muchas largas tardes con los cerditos. A María, Marta, Rafa, Marc, Nacho, Elena, Marina, Rosa, Marilú, Marta Segunda y Silvia, me llevo buenos momentos con todas y todos. A Alicia y Domingo, del Servicio de Citómica del CIPF, por ser los mejores vecinos de laboratorio. Gracias por ayudarme siempre y confiar en mí. A Mónica y Javier, no habría sido posible sin las deliciosas tostadas y sin los mejores cafés con leche de avena que he probado nunca para recargar pilas. Tampoco puedo olvidarme de Rubenchu, el tiempo que compartimos en el lab fue corto, pero lo que salió de ahí ha sido ESPECIIAAAAL, gracias por coger siempre el teléfono, ayudarme con cualquier duda y hacerme reír tanto.

A Ángel Raya y su grupo de investigación en el CMRB. Gracias por acogerme durante mi breve estancia en Barna. Sois un gran equipo y me encantó trabajar y aprender con vosotros. En especial a Rubén, me alegro mucho de haber compartido contigo una parte de esta experiencia.

To Niek, my supervisor during my internship in Astra. Thank you for giving me the opportunity to be part of your team. You have been very supportive since the first moment we met, and I have learnt a lot working with you. Thank you also to the rest of the Discovery Sciences department, and specially to the EV team: Andreia, Alena, Xiaoqin, Nia and Elisa, for being amazing lab mates.

A mi Gente Maja del máster. Fue una bonita casualidad coincidir con vosotros. Sólo por eso ya mereció la pena. También a mis compis de Biotec, juntos empezamos este camino hacia el mundo de la ciencia.

A USLAND, mis compañeras de vida. Gracias por seguir creciendo conmigo. Todas y cada una de vosotras sois magníficas. También quiero nombrar a Sarah, gracias por tantas aventuras y por apoyarme siempre.

No puede faltar aquí mi familia, por todos los buenos momentos que hemos compartido juntos. No veo el día en el que podamos reunirnos todos de nuevo. En especial infinitas gracias a mis padres y mi hermana, por su apoyo incondicional, os quiero. Como no, a Bambú, mi perri. Este bicho tiene claro lo que es importante en la vida.

A Hernán, por ser mi mejor amigo, por todo tu apoyo y por poner el mundo en perspectiva siempre que lo he necesitado. Gracias por tantas charlas y por proponerme siempre nuevos retos. Hemos compartido unos años muy intensos en los que hemos formado un gran equipo. Eres una persona extraordinaria, te quiero.

"Every day for us something new,

Open mind for a different view,

And nothing else matters"

Contents

Contents

Abbreviations

7-AAD: 7-aminoactinomicin D

AA: Arachidonic acid

AAR: Area at risk

ACC: Acetyl-CoA carboxylase

ACE: Angiotensin-converting-enzyme

AEC: Animal Ethics Committee

AF4: Asymmetric flow field-flow fractioning

AKT: RAC-alpha serine/threonine-protein kinase

Alix: ALG-2 interacting protein X

AMI: Acute myocardial infarction

AP: Activator protein

APS: Ammonium persulfate

ARNI: Angiotensin receptor-neprilysin inhibitors

ATCC: American Type Cell Culture Collection

Atg14L: Beclin-1-associated autophagy-related hey regulator

ATP: Adenosine triphosphate

AWC: Animals Welfare Committee

Bax: Apoptosis regulator BAX

BCA: Bicinchoninic acid

Bcl-2: B-Cell lymphoma 2

Bpm: Beats per minute

BrdU: Bromodeoxyuridine

BSA: Bovine serum albumin

CABG: Coronary artery by-pass grafting

CCD: Charge-coupled device

CCL2: C-C motif chemokine 2

CD: Cluster of differentiation

cDNA: complementary deoxyribonucleic acid

cFib: Cardiac fibroblasts

cm: Centimetres

CM: Cardiomyocytes

CMR: Cardiac magnetic resonance

CPC: Cardiac Progenitor Cells

CPT: Carnitine palmitoyl transferase

CRT: Cardiac resynchronization therapy

CSC: Cardiac Stem Cells

cTn: Cardiac troponin

CVD: Cardiovascular diseases

CXCL: C-X-C motif chemokine

DAMP: Danger-associated molecular patterns

DAPI: 4',6-diamino-2-phenylindole

DH5α: Douglas Hanahan 5 α

DHA: Docosahexaenoic acid

diDHA: di-docosahexaenoic acid

DMEM: Dulbecco's Modified Eagle's Medium

DMSO: Dimethyl sulfoxide

DNA: Deoxyribonucleic acid

EC: Endothelial cells

ECG: Electrocardiogram

ECM: Extracellular matrix

EDTA: Ethylenediaminetetraacetic acid

EFA: Essential fatty acids

Em: Emission

EPA: Eicosapentaenoic acid

ER: Endoplasmic reticulum

ERK: Extracellular signal-regulated kinase

ESC: Embryonic stem cells

ESCRT: Endosomal sorting complexes required from transport

$EtCO_2$: End-tidal carbon dioxide

EtOH: Ethanol

EV: Extracellular vesicles

Ex: Excitation

FA: Fatty acid

FABP: Fatty acid binding protein

$FADH_2$: Flavin adenine dinucleotide

FAT: Fatty acid translocase

FATP: Fatty acid transport protein

FBS: Fetal bovine serum

FDA: Food and Drug Administration

FFA: Free fatty acids

FGF-2: Fibroblast growth factor-2

$Fi0_2$: Fraction of inspired oxygen

G-CSF: Granulocyte colony-stimulating factor

G6P: Glucose-6-phosphate

GM-CSF: Granulocyte-macrophage colony-stimulating factor

GFP: Green fluorescence protein

GLUT: Glucose transporter

GMP: Good manufacturing practices

Gp130: Glycoprotein 130

GPIHBP1: Glycosylphosphatidylinositol-anchored high-density lipoprotein-binding protein 1

GRB2: Growth factor receptor-bound protein 2

GRP-78: Glucose-regulated protein 78

GTP: Guanosine triphosphate

GTPase: Small GTP-binding proteins

h: Hour

HBSS: Hank's balanced salt solution

HEK 293T: Human embryonic kidney cells 294 type T

HEPES: 4-(2-hydroxyethyl)-1-piperazineethanesulfonic acid

HF: Heart failure

HIF1α: Hypoxia-inducible factor 1-alpha

HMVEC-C: Human cardiac microvascular endothelial cells

HRP: Horseradish peroxidase

HSC70: Heat shock cognate 71 kDa protein

HSP90β: Heat shock protein HSP 90-beta

HSPCGs: Heparin sulphate proteoglycans

I: Ischemia

I/R: Ischemia/Reperfusion

ICAM: Intercellular adhesion molecule

IL: Interleukin

IL-1ra: Interleukin-1 receptor antagonist

IL-31RA: Oncostatin-M receptor

ILV: Intraluminal vesicles

IMS: Mitochondrial intermembrane space

IP: Intraperitoneal

IPSC: Induced pluripotent stem cells

IS: Infarct size

JAK: Janus Kinase

JNK: C-Jun-amino-terminal kinase-interacting protein

LA: Linoleic acid

LAD: Left anterior descending

Lamp2b: lysosome-associated membrane glycoprotein 2 transcript variant b

LB: Lysogeny broth

LC: Lethal concentration

LDH: Lactate dehydrogenase

LIF-R: Leukaemia inhibitory factor receptor-beta

LN: Linolenic acid

LpL: Lipoprotein lipase

LV: Left ventricle

LVAD: Left ventricle assist devices

LVEF: Left ventricle ejection fraction

MAPK: Mitogen-activated protein kinase

MCD: Malonyl-CoA decarboxylase

MFG-E8: Milk fat globule-EGF factor 8

MIF: Macrophage inhibitory factor

min: Minute

miRNA: Micro ribonucleic acid

MMP: Mitochondrial membrane potential

mPTP: Mitochondrial permeability transition pore

MPC: Mitochondrial pyruvate carrier

MR: Mineralocorticoid-receptor

MSC: Mesenchymal stromal cells

Mst1: Mammalian sterile 20-like kinase 1

MTS: 3-(4,5-dimethylthiazol-2-yl)-5-(3-carboxymethoxyphenyl)-2-(4-sulfophenyl)-2H-tetrazolium, inner salt

MUFA: Monounsaturated fatty acids

MV: Microvesicles

MVB: Multivesicular bodies

NA: Numerical aperture

NTA: Nanoparticle Tracking analysis

NADH: Nicotinamide adenine dinucleotide

NF-κB: Nuclear factor kappa-light-chain enhancer of activated B cells

NLRP3: NACHT, LRR and PYD domains-containing protein 3

nm: Nanometers

NRBF2: Nuclear receptor-binding factor 2

Nrf2: Nuclear transcription erythroid 2-related factor 2

NSF: N-ethylmaleimide-sensitive factor

Nx: Normoxya

NRVM: Neonatal rat ventricular myocytes

OG: Oregon Green

OGD: Oxygen-glucose deprivation

OGD-R: Oxygen-glucose deprivation-reoxygenation

OSM: Oncostatin-M

P/S: Penicillin/Streptomycin

p150: Phosphoinositide-3-kinase, regulatory subunit 4

p38: Mitogen-activated protein kinase 38

$PaCO_2$: partial arterial CO_2 pressure

PAGE: Polyacrylamide gel electrophoresis

PB: Phosphate buffer

PBS: Phosphate buffer saline

PCI: Percutaneous coronary intervention

PCR: polymerase chain reaction

PDH: Pyruvate dehydrogenase

PDK: Pyruvate dehydrogenase kinase

PEI: Polyethilenimine

PFA: Paraformaldehyde

PGA: Poly-L-glutamic acid

PI3K: Phosphoinositide 3-kinase/protein kinase B

PKCδ: Protein kinase C delta

PLGA: Poly(lactic-co-glycolic acid)

PM: SEV production medium

PMA: Phorbol 12-myristate 13-acetate

PMS: Phenazine methosulfate

PPAR: Peroxisome proliferator-activated receptor

PQC: Protein folding quality control

PRR: Pattern recognition receptors

PS: Phosphatidylserine

psPAX: Paired box gene

PUFA: Polyunsaturated fatty acids

PVDF: Polyvinylidene difluoride

pVSV: Vesicular stomatitis virus

R: Reperfusion

Rab: RAS related protein Rab

RAS: GTPase Ras protein

RIPA: Radioimmunoprecipitation assay buffer

RNA: Ribonucleic acid

ROS: Reactive oxygen species

RPM: Revolutions per minute

RT: Room temperature

s: Second

SV40: Simian vacuolating virus 40

SDF: Stromal-derived factor

SDS: Sodium dodecyl sulphate

SEV: Small extracellular vesicles

SFA: Saturated fatty acids

SH-2: SH2B adapter protein 1

SHP-2: Tyrosine-protein phosphatase non-receptor type 11

SMA: Smooth muscle actin

SNAP: Soluble NSF-attachment protein

SNARE: SNAP-attachment protein receptors

SR: Sarcoplasmic reticulum

STAT: Signal transducer and activator of transcription

STEMI: ST elevation myocardial infarction

TAG: Triacylglycerol

TBS: Tris saline buffer

TEM: Transmission electron microscopy

Tet-On: Tetracycline controlled transcriptional activation

TG: Triglycerides

TGF: Transforming growth factor

TMRM: Tetramethylrodamine, methyl ester

TNF: Tumor necrosis factor

tRNA: Transference RNA

TSG101: Tumor susceptibility gene 101 protein

TTC: 2,3,5-Triphenyltetrazolium

TYK2: Non-receptor tyrosine-protein kinase TYK2

uPA: Urokinase-type plasminogen activator

UPR: Unfolded protein response

V: Volts

VCAM: Vascular cell adhesion molecule

VEGF: Vascular endothelial growth factor

VLDL: Very-low-density lipoproteins

Vps34: Vacuolar sorting-associated protein 4

VSMC: Vascular smooth muscle cells

VSP4: Vesicle-fusing ATPase

WB: Western Blot

Abstracts

Abstract

Current therapeutic approaches against acute myocardial infarction (AMI) are focused on myocardial ischemic zone revascularization. The most common strategy is called primary angioplasty, in which a catheter is introduced to unblock the affected artery and restore blood flux, in a process called reperfusion. Nevertheless, an additional injury on cardiac tissue is caused after reperfusion, and the combination of primary angioplasty with the use of cardioprotective molecules has emerged as a potential strategy to reduce cardiac tissue injury.

In this context, cell-free therapies by using customized nanoparticles which can preconditionate heart ischemic area before reperfusion and reduce cardiomyocyte's apoptosis and increase its proliferation rate, promote new tubes formation and/or have an anti-fibrotic effect have gained attention. In this doctoral thesis, two new cell-free therapeutic strategies with cardioprotective potential have been proposed to reduce cardiac injury after AMI.

It is known that cardiomyocytes are deprived from nutrients and oxygen during ischemia, causing massive cell death. Fatty acids are the main source of energy of adult mammal cardiomyocytes in healthy conditions. Based on that, the first therapeutic strategy proposed consisted on the input of a free fatty acid (di-docosahexaenoic acid, diDHA) covalently bound to a polymeric backbone (poly-L-glutamic acid, PGA) in order to increase diDHA solubility and stability and modulate its effect on target cells. Results showed that PGA-diDHA$_{6.4}$ conjugate administration during ischemia protected cardiomyocytes from reperfusion-induced injury, as apoptotic number of cells and oxidative stress was reduced, and mitochondrial function was less affected when compared to untreated cells. In addition to this, PGA-diDHA$_{6.4}$ also showed therapeutic effects when locally administered in an ischemia-reperfusion *in vivo* model in rats and pigs, where a modest reduction of area at risk was observed compared to control groups.

The second cell-free strategy proposed in this work was focused on enhancing the therapeutic potential of small extracellular vesicles (SEV or exosomes) isolated form mesenchymal stromal cells (MSC) conditioned media. Previous studies have described the therapeutic potential of paracrine factors released by MSC, where both soluble factors and vesicular components are included. In particular, SEV have gained special attention. One study published by our laboratory showed that

hypoxia inducible factor-1α (HIF1-α) overexpression in MSC (HIF-MSC) augmented native cells therapeutic potential in an AMI *in vivo* model in rats by promoting angiogenesis in cardiac tissue. Moreover, it was described that this effect was partially mediated by notch ligand jagged-1 loading on SEV secreted by HIF-MSC). In this context, it was proposed MSC genetic modification in order to load proteins of interest on SEV and potentiate its native therapeutic potential. Based on previous findings, where it has been described a potential anti-fibrotic role of oncostatin-M (OSM) in AMI context, we decided to incorporate OSM on SEV surface by its fusion to CD81 tetraspanin, a protein naturally loaded on SEV surface, in order to trigger functional effects on target cells. OSM sequence modification was necessary in order to load the protein on SEV surface efficiently, and preliminary data showed that modified OSM-CD81 loaded on SEV had a functional effect on human ventricular cardiac fibroblasts. Concretely, decrease of proliferation rate after starvation and telo-Collagen1α1 location pattern modification was observed after stimulation with a pro-fibrotic cocktail (containing TGFβ-1, α-dextran and ascorbic-L-acid sulphate) *in vitro* when cells were treated with modified OSM-CD81-SEV compared to ctrl and CD81-loaded SEV treatments.

Overall, two new advanced cell-free therapies with preliminary promising results have been proposed in order to reduce myocardial injury after AMI in terms of cardiomyocytes apoptosis reduction and fibrosis mitigation.

Resumen

Las intervenciones actuales utilizadas en el ámbito clínico durante el infarto agudo de miocardio (IAM) se centran en la revascularización de la zona isquémica. Entre dichas estrategias, la angioplastia coronaria, procedimiento por el cual se utiliza un catéter para desobstruir la arteria ocluida, es el proceso más utilizado. Sin embargo, se ha descrito este proceso (conocido como reperfusión) desencadena un daño adicional en el miocardio, por lo que la combinación de dicha intervención con moléculas cardioprotectoras resulta de gran interés para tratar de reducir el tamaño del infarto.

En este contexto, el uso de terapias libres de células mediante la síntesis personalizada de nanopartículas capaces de precondicionar el área isquémica antes de la reperfusión mediante la reducción de la tasa de apoptosis de cardiomiocitos, la inducción de nueva formación de tubos o que consigan un efecto anti-fibrótico ha ganado especial interés en los últimos años. El presente trabajo propone dos nuevas moléculas con potencial cardioprotector en el contexto del IAM.

Estudios previos han descrito que durante la isquemia los cardiomiocitos no disponen de oxígeno ni nutrientes necesarios para obtener la energía necesaria y, en consecuencia, se produce una muerte masiva de los mismos. En base al metabolismo de los cardiomiocitos adultos, cuya fuente principal de energía son los ácidos grasos, la primera estrategia propuesta se ha basado en el aporte de un ácido graso (diDHA) en la zona isquémica antes de la reperfusión para tratar de reducir el estrés de los cardiomiocitos y el número de células muertas antes de la reperfusión. Además, se han sintetizado nanoconjugados basados en la unión covalente de diDHA a un unido covalentemente a un esqueleto polimérico (ácido poli-L-glutámico, PGA) con el fin de incrementar la estabilidad del diDHA y conseguir una liberación controlada de la molécula, modulando su efecto en los cardiomiocitos. Los resultados obtenidos mostraron que la formulación PGA-diDHA$_{6.4}$ fue la más optimizada, mostrando un mejor efecto en el precondicionamiento de los cardiomiocitos antes de la reperfusión en términos de reducción de apoptosis, generación de especies reactivas de oxígeno y mantenimiento de la función mitocondrial *in vitro*. Además, el nanoconjugado PGA-diDHA$_{6.4}$ también mostró un modesto efecto terapéutico cuando se administró en modelos *in vivo* de isquemia-reperfusión en ratas y cerdos, reduciendo el tamaño final de infarto respecto a los grupos control.

La segunda estrategia terapéutica propuesta se ha centrado en aumentar el potencial terapéutico de las vesículas celulares de pequeño tamaño (SEV o exosomas) procedentes de medio condicionado de células madre estromales (MSC). Numerosos estudios han descrito el papel terapéutico de factores paracrinos secretados por las MSC, donde se incluyen tanto factores solubles como vesículas extracelulares (EV) y, en especial, SEV. En este contexto, estudios previos en nuestro laboratorio demostraron que la sobrexpresión del factor inducible por hipoxia-1α (HIF1-α) en MSC aumentaba el efecto terapéutico de las células nativas en un modelo de IAM en ratas, aumentando la angiogénesis en el corazón. Además, se describió que este efecto venía parcialmente mediado por la incorporación del ligando de la vía de notch, jagged-1, a las EV secretadas por dichas células. Así, se pensó en la modificación genética de las MSC con el objetivo de enriquecer las SEV en proteínas de interés que pudiesen potenciar el efecto terapéutico de las SEV nativas. En base a estudios previos, donde se ha visto que la oncostatina-M (OSM) podría jugar un papel anti-fibrótico en el contexto del IAM, se decidió incorporar dicha proteína en la superficie de las SEV derivadas de MSC mediante su fusión con proteínas presentes de forma natural en la superficie de las SEV, con el objetivo de desencadenar una respuesta en las células diana. La modificación de la secuencia de la OSM y su fusión con la tetraspanina CD81 permitieron cargar de manera

efectiva la OSM en la superficie de las SEV, y los resultados preliminares en fibroblastos ventriculares cardíacos mostraron un efecto funcional beneficioso con respecto a los SEV control y los enriquecidos en CD81, reduciendo la tasa de proliferación de las células en condiciones de ayuno, y modificando la expresión y la liberación de la proteína telo-Col1α1 en las células después de ser estimuladas con TGFβ-1, α-dextrano y ácido ascórbico-L-sulfato, simulando una activación de los fibroblastos *in vitro*.

En resumen, dos nuevas estrategias terapéuticas avanzadas libres de células han sido propuestas en el presente trabajo, donde se han mostrado resultados preliminares prometedores para reducir el daño en el miocardio tras el IAM en términos de reducción de apoptosis de cardiomiocitos y de activación de fibroblastos cardiacos.

Resum

Les intervencions actuals utilitzades en l'àmbit clínic durant l'infart agut de miocardi (IAM) se centren en la revascularització de la zona isquèmica. Entre aquestes estratègies, l'angioplàstia coronària, procediment pel qual s'utilitza un catèter per a desobstruir l'artèria oclosa, és el procés més utilitzat. No obstant això, s'ha descrit que aquest procés (conegut com a reperfusió) desencadena un mal addicional en el miocardi. En conseqüència, la combinació d'aquesta intervenció amb molècules cardioprotectores resulta de gran interés per a tractar de reduir la grandària de l'infart.

En aquest context, l'ús de teràpies lliures de cèl·lules mitjançant la síntesi personalitzada de nanopartícules capaces de precondicionar l'àrea isquèmica abans de la reperfusió mitjançant la reducció de la taxa d'apoptosi de cardiomiocitos, la inducció de nova formació de vasos sanguinis o que aconseguisquen un efecte anti-fibròtic ha guanyat especial interés en els últims anys. El present treball proposa dues noves molècules amb potencial cardioprotector en el context del IAM.

Estudis previs han descrit que durant la isquèmia els cardiomiocitos no disposen d'oxigen ni nutrients necessaris per a obtindre l'energia necessària i, en conseqüència, es produeix una mort massiva d'aquests. Sobre la base del metabolisme dels cardiomiocitos adults, que tenen com a principal font d'energia els àcids grassos lliures, s'ha proposat l'aportació d'un àcid gras (diDHA) a la zona isquèmica del miocardio abans de la reperfusió per a tractar de reduir l'estrés dels

cardiomiocitos i el nombre de cèl·lules mortes abans de la reperfusió. A més, s'han sintetitzat nanoconjugats basats en la unió covalent de diDHA a un esquelet polimèric (àcid poli-L-glutàmic, PGA) amb la finalitat d'incrementar l'estabilitat del diDHA i aconseguir un alliberament controlat de la molècula, modulant el seu efecte en els cardiomiocitos. Els resultats obtinguts van mostrar que la formulació PGA-diDHA$_{6.4}$ va ser la més efectiva, mostrant un millor efecte en el precondicionament dels cardiomiocitos abans de la reperfusió en termes de reducció d'apoptosi, generació d'espècies reactives d'oxigen i manteniment de la funció mitocondrial *in vitro*. A més, el nanoconjugat PGA-diDHA$_{6.4}$ també va mostrar un modest efecte terapèutic quan es va administrar en models *in vivo* d'isquèmia-reperfusió en rates i porcs, reduint la grandària final d'infart respecte als grups control.

La segona estratègia proposada s'ha centrat en potenciar l'efect terapèutic de vesícules extracelul·lars de xicoteta grandària (SEV o exosomes) que son secretades per cèl·lules mare estromales. Nombrosos estudis han descrit el paper terapèutic de factors paracrinos secretats per les MSC, on s'inclouen tant factors solubles com vesícules extracelul·lars (EV) i, especialment, les SEV. En aquest context, estudis previs en el nostre laboratori van demostrar que la sobrexpressió del factor inducible per hipòxia-1α (HIF1-α) en MSC augmentava l'efecte terapèutic de les cèl·lules natives en un model de IAM en rates, augmentant la angiogénesis en el cor. A més, es va descriure que aquest efecte venia parcialment mediat per la incorporació del lligant de la via de notch, jagged-1, a les SEV secretades per aquestes cèl·lules. Així, es va pensar en la modificació genètica de les MSC amb l'objectiu d'enriquir les SEV en proteïnes d'interés que pogueren potenciar l'efecte terapèutic de les SEV natives. Sobre la base d'estudis previs, on s'ha vist que la oncostatina-M (OSM) podria jugar un paper anti-fibròtic en el context del IAM, es va decidir incorporar aquesta proteïna en la superfície de les SEV derivades de MSC mitjançant la seua fusió amb proteïnes presents de manera natural en la superfície de les SEV, amb l'objectiu de desencadenar una resposta en les cèl·lules diana. La modificació de la seqüència de la OSM i la seua fusió amb la tetraspanina CD81 van permetre carregar de manera efectiva la OSM en la superfície de les SEV, i els resultats preliminars en fibroblastos ventriculars cardíacs van mostrar un efecte funcional respecte als SEV control i els enriquits en CD81, reduint la taxa de proliferació de les cèl·lules en condicions de dejuni, i modificant l'expressió i la secreció de la proteïna telo-Col1α1 en les cèl·lules després de ser estimulades amb TGFβ-1, α-dextran i àcid ascòrbic-L-sulfat, simulant una activació dels fibroblastos *in vitro*.

En resum, dues noves estratègies terapèutiques avançades lliures de cèl·lules han sigut proposades en el present treball, on s'han mostrat resultats preliminars prometedors per a reduir el mal en el miocardi després del IAM en termes de reducció d'apoptosi de cardiomiocitos i d'activació de fibroblastos cardíacs.

1. Introduction

1. Introduction

1.1. The heart

1.1.1. Cardiac tissue: structure and function

The cardiovascular system comprises both heart and the entire circulatory network. Particularly, the heart acts as a blood pump distributing oxygen and nutrients throughout organs, tissues and cells. At the anatomical level, it is composed of four cavities: two atria in the upper position and two ventricles in the bottom. Right and left parts of the heart are separated by a muscular wall; while atria and ventricles are communicated by cardiac valves. The right half receives oxygen-depleted blood from the entire body and sends it to the pulmonary circulation, where it is charged with oxygen. The oxygenated blood is returned to the left half of the heart and it is distributed to the systemic circulation[1]. At the histological level, heart is composed by three layers: endocardium, myocardium and epicardium (**Figure 1.1**). Endocardium is the inner part and consequently is in contact with cardiac cavities. It is composed by endothelium and connective tissue. The intermediate and thicker layer is the myocardium, which is composed by striated cardiac muscle (mainly contractile cells called cardiomyocytes [CM]), extracellular matrix (ECM, which is a complex architectural network consisting of structural and nonstructural proteins, creating strength and plasticity) and blood capillaries. The outer layer is the pericardium, which is divided in epicardium, pericardial space, parietal pericardium and fibrous pericardium, and it is primarily composed by connective tissue, including elastic fibers and adipose tissue. Pericardium forms a membrane that covers and holds the heart. Additionally, it avoids friction with other structures and ventricular distension during cardiac beating[2].

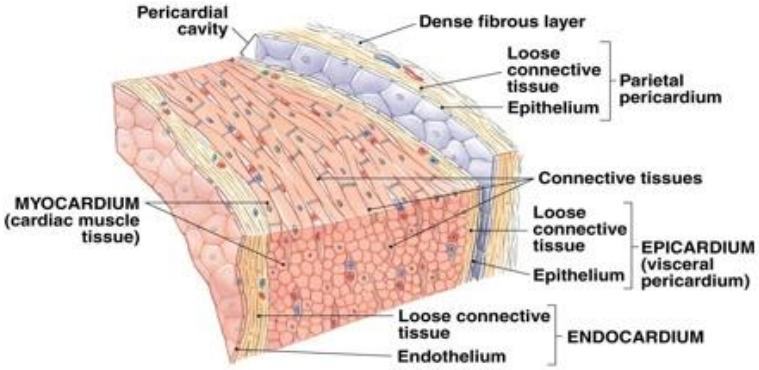

Figure 1.1. Structure of the heart wall*. Cardiac tissue is formed by three main layers: endocardium, myocardium and epicardium. Adapted from www.guwsmedical.info.*

The pumping action of the heart is based on a rhythmic sequence of ventricles systole (contraction) and diastole (relaxation) which is driven by electrical signals and mechanical actions intimately intertwined. Cardiac cycle is normally represented by electrocardiogram (ECG) and includes six phases: atrial systole (P wave), isovolumetric ventricular systole (QRS wave), ventricular ejection (S-T segment), ventricular relaxation (T wave), isovolumetric relaxation (end of T wave) and diastole (period between the end of T wave and the beginning of P wave), represented in **Figure 1.2**.

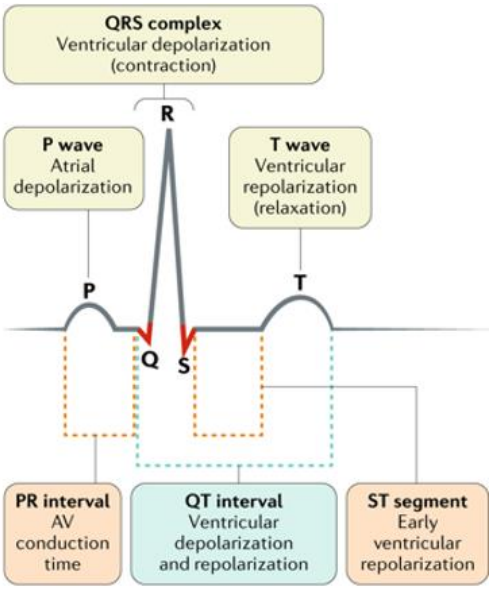

Figure 1.2. Cardiac cycle Electrical activity of the heart showed by ECG. *The different segments of an ECG trace indicate electrical events during cardiac cycle: atrial depolarization (PR interval, P wave), QT interval, divided in ventricular depolarization or contraction (QRS complex) and ventricular repolarization (ST segment, T wave). Adapted from Vogel B. et al., 2019[3].*

1.1.2. Resident cells in the myocardium

The heart is composed of several cell populations, and each of them has specific functions and regulatory roles. Given the importance of the heart as a muscular pump, cardiac striated muscle cells (CM) account for ~25-35% of the total number of cells in the myocardium[4] and occupy ~70-85% of the volume of the mammalian heart[5, 6]. The use of genetic tools and cellular markers has allowed the identification of non-myocytic populations, which include endothelial cells (EC), vascular smooth muscle cells (VSMC), pericytes, cardiac fibroblasts (cFib), neurons, immune cells and cardiac stem or progenitor cells (CSC or CPC)[4, 7-9]. However, their proportion with respect to number and volume in the heart remains controversial due to the lack of feasible markers to differentiate each individual identity[10].

The most relevant cardiac resident cells for the present project will be explained below.

1.1.2.1. Cardiomyocytes

CM are the muscle cells of cardiac tissue and they are responsible for maintaining 3D structural integrity of the heart and generating synchronous contraction force in the intact heart in order to pump blood throughout the body[11]. Striated muscle cells have a unique membrane system (sarcolemma) with transverse-axial-tubular (t-tubules) invaginations, where most Ca^{2+}-handling proteins are located[12].They are large (100-150 µm in length and 10-35 µm in width) cylindrical cells with end-to-end intercellular connections, called intercalated disks, which ensure mechanical and electromechanical coupling[13]. Additionally, CM are communicated by intercellular channels, named gap junctions and composed by connexins[14]. Ions, small molecules and small peptides can cross these junctions.

CM cytoplasm (also called sarcoplasm) is primarily composed by sarcomeres, which are the contractile units of muscle cells, and mitochondria. In deep, mitochondria correspond to approximately one third of the volume of each CM and are needed to cover energy requirements[13]. Individual sarcomeres are composed of long, fibrous proteins that slide past each other during contraction and relaxation. The most important proteins contained in sarcomeres are actin, which form thick filaments and is bound to Z-discs, tropomyosin (forming thin filaments) and troponin[15]. Together, they form myofibrils. CM function is principally regulated by local ion concentrations that establish membrane potential and stimulate myofibrils contraction, and their electrophysiological properties are highly regulated by a number of ion channels, pumps and auxiliary proteins to control intracellular Na^+, Ca^{2+} and K^+ ion concentrations[16-18].

1.1.2.2. Endothelial cells

EC form the inner layer of blood and lymphatic vessels. They have an essential role in heart development, vascular homeostasis and promoting CM survival and organization[19]. Previous scientific research has demonstrated a strong interaction between EC and CM, both by physical interaction and/or paracrine signaling[20, 21]. Coronary vasculature is highly organized in a network which maintains cardiac irrigation and ensures cardiac muscle is fed. In fact, each CM is in contact with at least one capillary, and it has been estimated that endothelial cells outnumber cardiomyocytes by ~3:1[9, 22], representing up to 60% of non-CM population in the heart[9].

1.1.2.3. Vascular smooth muscle cells and pericytes

VSMC and pericytes are mural cells with multipotent progenitor potential surrounding blood vessels, adjacent to EC[23]. VSMC cover large-diameter vessels like

arteries and veins, while pericytes cover micro-vessels such as arterioles, venules and capillaries[24, 25]. However, the distinction between VSMC and pericytes morphologies and location is not absolute, and they seem to exist in a continuum of phenotypes distributed among intermediate and small vessels[26]. They are critical for vascular stability and structure and cell-cell contact with EC maintain capillaries in a quiescent state. Angiogenesis requires the detachment of pericytes to enable EC migration, but they also stabilize and mature nascent vessels[19].

1.1.2.4. Cardiac fibroblasts

It has been estimated that resident cFib represent the 20% of the non-CM cells[9]. They are a dynamic and versatile population of cells of mesenchymal origin that present a regulatory phenotype in healthy conditions. cFib are continually assessing homeostasis in the environment and have a pivotal role in cardiac tissue support by the synthesis of the cardiac ECM components, which provides a scaffold to cells to migrate, proliferate, differentiate and preserve their normal function[27, 28]. In addition to this, they interact with CM through functional gap junctional channels, facilitating electro-mechanical transduction and, consequently, the proper maintenance of the conduction system[29, 30].

1.2. Cardiac metabolism: Role of fatty acids in the heart

Heart proper function depends on the availability of high adenosine triphosphate (ATP) molecules, and this is supported by the energy obtained in the mitochondria from fatty acids and carbohydrates[31].

Fatty acids (FA) are the main source of energy in mammal adult heart. FA are carboxylic acids structures as a long hydrocarbon chain, with a methyl terminus end, and a carboxylic acid group (-COOH)[32]. They are organized into three broad categories according to their unsaturation degree (carbon-carbon double bounds): (1) saturated, (2) monounsaturated and (3) polyunsaturated; and can be further subdivided depending the location of the first double bond relative to the methyl terminus chain. FA nomenclature is usually presented according to the position of the first unsaturation, where the final carbon in the FA chain is called omega (ω)[33].

Saturated FA (SAF), such as lauric, myristic, palmitic and stearic acid, do not present any carbon-carbon double bond. They are easily synthesized by the body and their intake is associated with an increase in the amount of low-density protein cholesterol in the bloodstreams and inflammatory processes, which is linked to cardiovascular diseases (CVD) or diabetes development, among other chronic conditions[34, 35]. Monounsaturated fatty acids (MUFA) are molecules with one

unsaturated carbon bond, such as oleic acid (ω-9) and palmitoleic acid (ω-7), and are mainly obtained from diet, although they are synthesized endogenously in minor concentrations[36]. Polyunsaturated fatty acids (PUFA) are molecules with more than one unsaturated carbon bond synthesized from linoleic acid (LA) and α-linoleic acids (α-LA) and can be subdivided in ω-6 and ω-3 PUFA, respectively. LA downstream products include arachidonic acid (AA) and docosapentaenoic acid; while α-LA derived PUFA include eicosapeontaenoic acid (EPA) and docosahexaenoic acid (DHA). LA and α-LA, together with their derivates, are classified as essential FA (EFA) because they are not synthesized by the body, but rather must be obtained from dietary intake[33]. It has been described that ratio between ω-6 and ω-3 PUFA intake determines the composition of cellular membranes and triggers tissue functional changes. In fact, ω-3 PUFAs are considered as a beneficial dietary intervention for the prevention and treatment of CVD. Their beneficial effects have been described through several mechanisms, including antiatherogenic properties[32, 37], lowering serum triglycerides[32], decreasing blood pressure[37, 38], improving endothelial function[37], reducing inflammatory responses[37], inhibiting platelet aggregation and thrombosis[32, 37] and decreasing the incidence of arrhythmias[32, 37].

EFA are usually present in dietary intake as triacylglycerol (TAG) and phosphatidylcholine, and must be processed before they can be released into blood and, eventually, cardiac muscle. Firstly, gastric lipase is responsible for 10 to 30% of FA lipolysis by mechanical emulsification and partial TAG hydrolysis, resulting in two products: diacylglycerol and free FA (FFA); while the remaining percentage of TAG digestion is performed by pancreatic lipase in duodenal lumen, releasing 2-monoacylglycerol and FFA[39, 40]. Secondly, solubilization of these products is achieved by formation of disc-shaped micelles and liquid crystalline vesicles[41]. Next, lipolytic products are translocated to enterocytes, where they are re-esterified and packaged in chylomicrons or very-low-density lipoproteins (VLDL). Finally, they are exocytosed into systemic circulation and adipose tissue[42, 43].

FA used by the heart originate mainly from adipose tissue triglycerides (TG) and circulation, both as FFA bound to albumin or released from TAG contained in chylomicrons or VLDL[43-45]. FA translocation across sarcolemma membrane of CM occurs both by passive diffusion and via a protein carrier-mediated pathway, which includes FA translocase (FAT)/CD36, the plasma membrane isoform of fatty acid binding protein (FABPpm) and fatty acid transport protein (FATP) 1/6[46-49] (**Figure 1.3**). Of important note, lipoprotein lipase (LpL) presence on the capillary endothelial cell surface is necessary for TG hydrolysis and subsequent β-oxidation by the heart[50, 51].

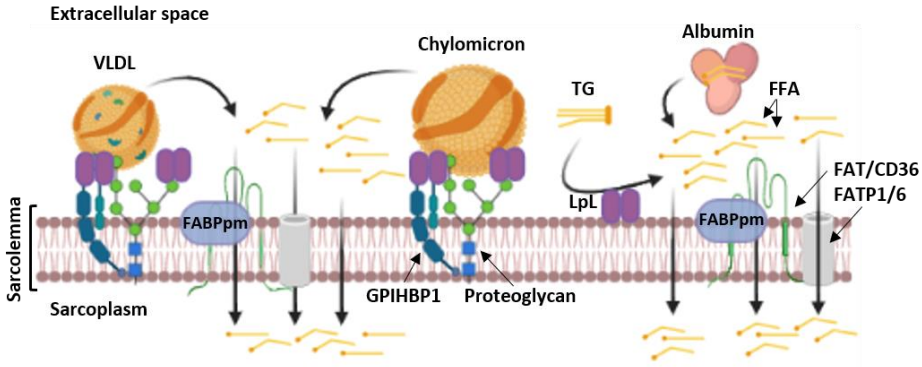

Figure 1.3. FFA uptake mechanisms by CM. *FA are transported in VLDL, chylomicrons or bound to albumin in the blood stream. Alternatively, adipose tissue can release TG as an additional source of energy. FFA released from VLDL, chylomicrons, albumin and TG are necessary for their transport across sarcolemma. Proteoglycans, GPIHBP1 and LpL are essential for this step. Next, FFAs are transported into sarcoplasm by passive diffusion across the phospholipidic membrane or by active transport, which involves FABPpm and FAT/CD36 proteins or FATP1/P transporter. VLDL: very low-density proteins; FABPpm: plasma membrane isoform of fatty acid binding protein; GPIHBP1: Glycosylphosphatidylinositol-anchored high-density lipoprotein-binding protein 1; TG: Triglyceride; LpL: lipoprotein lipase; FFA: Free fatty acid; FAT: Fatty acid translocase; FATP1/6 Fatty acid transport protein. Illustration created in BioRender.*

FA are commonly known because of their essential participation in cardiac metabolism, being the main source of energy in adult hearts, and their prominent presence in cell phospholipidic membrane. Nevertheless, additional works have shown that FA also participate in intracellular signal transduction and post-translational modifications[52].

1.2.1. Cardiac mitochondrial metabolism

Every event in every cell requires ATP to get energy and maintain their normal function. Mammalian heart is constantly contracting, and energy requirement to fuel its continuous mechanical work is immense. Consequently, myocytes need ATP to maintain normal heart, rates, pump blood and support increased work, as well as for grow, repair itself and survive. Under normoxic conditions, >95% of ATP produced in the heart is derived from oxidative phosphorylation in the mitochondria, and around 5% of ATP is generated from glycolysis and citric acid cycle [53, 54]. Attending to the substrate origin, FA oxidation accounts for 70 to 90% of cardiac ATP production; while the remaining 10 to 30% comes from the oxidation of glucose and lactate, small amounts of ketone bodies and certain amino acids[54-56]. These percentage ranges are due to results of studies which support that cardiac metabolism is flexible depending on substrate availability to confer the advantage

of adequate ATP supply for continual cardiac function under several physiological conditions[57-60]. In fact, it has been described a metabolic shift from glucose and lactate to FA in the transition of fetal to newborn hearts, when there is an increase in oxygen availability and FA dietary intake[61, 62]. Interestingly, there are evidences pointing that hypertrophic and dysfunctional hearts present the same preference for glucose as a substrate as observed in fetal hearts[63, 64]. Studies in animal models of left ventricle (LV) hypertrophy progressing to LV systolic dysfunction have shown a downregulation of FA oxidation enzymes related to downregulation of peroxisome proliferator-activated receptor (PPAR)-α pathway, which indeed regulates the expression of genes involved in FA β-oxidation and is a major regulator of energy homeostasis and responsible for glycolytic enzymes upregulation [65-67].

A schematic representation of the main cardiac metabolic processes is showed in **Figure 1.4**.

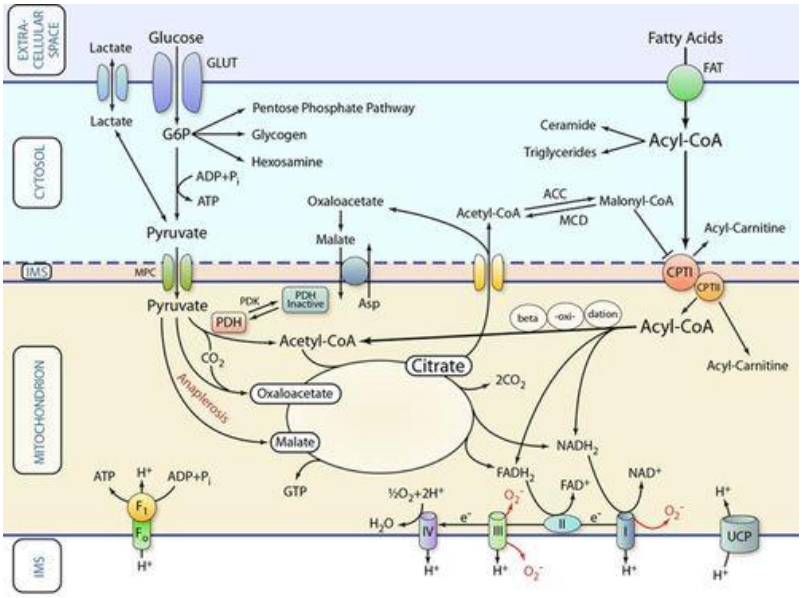

Figure 1.4. Cardiac metabolism classic pathways outline. *Substrates are transported across the extracellular membrane into the cytosol and are metabolized via specific catabolic pathways. For oxidation, the respective metabolic intermediates (pyruvate or acyl-coenzyme A [CoA]) are transported across the inner mitochondria membrane by specific transport systems. These metabolic intermediates are then β-oxidized or carboxylated (anaplerosis) and give place to reducing equivalents (reduced nicotinamide adenine dinucleotide [$NADH_2$] and reduced flavin adenine dinucleotide [$FADH_2$]) and guanosine triphosphate (GTP) through Krebs cycle. The reducing equivalents are used by the electron transport chain to generate a proton gradient, which in turn is used for ATP production. ACC: acetyl-CoA carboxylase; CPT: carnitine palmitoyl transferase; FAT:*

fatty acid translocase; G6P: glucose 6-phosphate; GLUT: glucose transporter; IMS: mitochondrial intermembrane space; MCD: malonyl-CoA decarboxylase; MPC: mitochondrial pyruvate carrier; PDH: pyruvate dehydrogenase; and PDK: pyruvate dehydrogenase kinase. Illustration from Doenst T. et al., 2015[68].

1.2.2. Signal transduction in cardiomyocytes

Previous studies have demonstrated an important role of FA, and specifically of ω-3 PUFA, as transcription regulators. FA can modulate the activity of various transcription factors in CM, such as nuclear factor kappa-light-chain enhancer of activated B cells (NF-κB), PPAR-α/β/δ/γ, retinoid X receptors and hypoxia inducible factor 1-alpha (HIF1α)[69-71]. These transcription factors are translocated to the nucleus and bind the appropriate response elements, modulating the expression of genes involved in the regulation of cell proliferation, survival, neo-angiogenesis and inflammatory processes. Some examples are proteins of B-Cell lymphoma 2 (Bcl-2) family, DNA topoisomerases and polymerases, cyclins, cyclin dependent kinase inhibitors, protein-phosphatases and kinases, cyclooxygenase-2, lipoxygenase-5, VEGF and matrix metalloproteinases. Additionally, lipid metabolism enzymes, such as FA synthase and 3-hydroxy-3-methyl-glutaryl-CoA reductase expression, are dependent on FA[72, 73].

1.2.3. Post-translational modifications

FA are involved in protein post-translational modifications in CM, such as acylation. It is widely known that the attachment of a FA to a protein increases its overall hydrophobicity, modulating the biological activity, stability, function and intracellular location. Consequently, ion channels and cellular receptors function are also sensitive to the lipid composition of cell membrane and plasma and the ratio of saturated, monounsaturated and polyunsaturated FA also has an impact in the normal functioning of CM in terms of ion channels functionality and myocytes contractility[74]. Despite a study made by Van der Vusse G.J. and Roemenhowed T.H.M. showed that only 0.3% of the total cardiac FA pool resulted to be bound to proteins[75], additional studies have shown that proteins which are crucial for normal cellular functioning, such as many ion channels[76-79], receptors[80] and kinases[81, 82] are present in the acylated form. As an example, one study published in 2007 showed that ω-3 PUFA supplementation prevented calcium overload and reduced the incidence of triggered arrhythmogenic activity in response to norepinephrine in porcine ventricular myocytes[83]. This finding would explain, at least in part, the mechanism underlying antiarrhythmic effects attributed to ω-3 PUFA, although it is still under debate if it is by acting at some lipid-anchoring sites near the channels or directly on the channel protein itself[84, 85].

1.3. Acute myocardial infarction

1.3.1. Epidemiology

CVD are the first cause of death globally. It has been estimated that 17.9 million people die each year from this group of diseases, representing 31% of deaths worldwide[86]. CVD are a group of disorders of the blood vessels and heart which includes coronary artery diseases, cerebrovascular disease, peripheral arterial disease, rheumatic heart disease, congenital heart disease and deep vein thrombosis and pulmonary embolism[86]. Up to 85% of all CVD deaths are due to heart attacks and strokes, and survival at 5 years after a heart failure (HF) event is only around 50% despite the great advances already done in the cardiovascular research field[87]. Risk factors for CVD comprise behavioral factors, including tobacco use, unhealthy diet, excessive alcohol intake and non-physical activity; and physiological factors, such as hypertension, raised blood glucose or lipids, overweight and obesity. The later factors are also related to underlying determinants as social, economic and cultural elements, such as ageing, economic income, urbanization, stress and hereditary factors[88, 89]. In consequence, a percentage of heart attacks and strokes could be prevented by controlling major risk factors through lifestyle changes and drug treatment when necessary.

Understanding heart functioning at the metabolic and anatomical level before, during and after an acute myocardial infarction (AMI) and the changes triggered throughout the process is of vital importance to hypothesize about new therapies to address this disease and improve life quality of patients after HF.

1.3.2. Pathophysiology

The orchestrated function of different cell populations in the heart, in combination with a complex network of intercellular communication systems, is vital to maintain a healthy heart, and its disruption provokes pathological conditions[90]. AMI is caused by the occlusion of a coronary vessel, which dramatically reduces blood flow and, consequently, oxygen and nutrients supply to cardiac tissue[91]. Under these circumstances, all the cells depending on the irrigation of the occluded vessel become ischemic, causing a quick cell death. CM from higher adult vertebrates have very limited potential for proliferation, and while it can be barely increased after injury, the rate is too slow (~0.5-2% per year) to replace the large number of cells lost after AMI and recover cardiac function[92, 93], leading to decreased contractibility capacity.

The main causes of vessel occlusion are atherosclerosis, which refers to the development of atheromatous plaques in the inner arterial surface, and acute coronary obstruction, which is common in patients with a previous severe atherosclerotic coronary cardiopathy [94]. Acute coronary obstruction involves the rupture of an atheroma fibrous cap, initiating thrombus formation by exposing blood components to tissue factor, triggering coagulation and platelets recruitment, and leading to plate growth until blood vessel lumen is obstructed. In some cases, thrombus can be detached and provoke the obstruction of a blood vessel with a smaller diameter[95, 96].

Prolonged ischemia induces AMI, which can be detected by ST-segment elevation (ST elevation myocardial infarction, STEMI) observing the ECG parameters and leads to necrosis of a vast number of cardiac cells, causing irreversible myocardial injury. This damage is extended in a wavefront manner, starting in the subendocardial layers in the center of the hypoperfused myocardial zone (area at risk, AAR) and progressing into subepicardial layers to the infarct border zones[97, 98]. Early reperfusion, which consists on the reopening of the occluded coronary arteria, is the main clinical objective in patients with STEMI. However, myocardial reperfusion causes additional damage in the infarcted region (process called ischemia-reperfusion[I/R]-induced injury) and it is associated with larger infarct size, transient contractile dysfunction, arrhythmias and metabolic acidosis, between others[99].

As described before, cardiac energetic requirements are highly demanding, and proliferative rate of cardiomyocytes is extremely low. Consequently, affected cardiomyocytes cannot generate enough energy to maintain their normal function during an ischemic event, and pathologic cardiac remodeling is triggered. In this process, molecular, cellular, histological, structural and functional changes occur in the heart. Three overlapping phases can be distinguished after AMI: inflammatory, proliferative and healing[100], which will be explained in more detail below and are summarized in **Figure 1.5**.

Importantly, irreversible damage in the myocardium can be produced after 20 minutes of ischemia if occlusion is not reverted. Despite the cardioprotective effects of some secreted cytokines and chemokines both in infarcted tissue and surrounding unaffected regions, local heart repair capacity is limited, and cardiomyocytes death triggers acute **inflammatory response** modulated through selectins, integrins, cell adhesion molecules and endogenous ligands (danger-associated molecular patterns, DAMP), attracting circulating immune cells via binding to pattern recognition receptors (PRR)[101, 102]. The first infiltrated cells into the damage area are neutrophils, which peaks ~24 h post-AMI. At this stage, neutrophils release proteolytic enzymes and reactive oxygen species (ROS), leading to further injury in surrounding cells[101, 103]. Additionally, they release chemotactic

factors[104] and induce accumulation of monocytes, which reaches a peak ~3 days after reperfusion[105]. These monocytes differentiate into macrophages and have phagocytic, proteolytic and pro-inflammatory functions, promoting removal of necrotic debris and tissue digestion[106]. Although it has been demonstrated that an appropriate tempered inflammatory response is necessary after AMI, the adverse effects of neutrophil infiltration can be extended after the early post-reperfusion period, as excess of neutrophil accumulation could interfere with the recruitment of additional leukocyte populations and the transition from inflammatory to proliferative phase of cardiac repair, which begins~4-7 days after reperfusion[107].

Proliferative phase is defined by resolution of inflammation and proliferation of fibroblasts to initiate the formation of collagen-rich scar. Neutrophils that had infiltrated the damaged zone early after reperfusion undergo apoptosis in this stage are phagocyted by macrophages, inducing a switch toward a pro-resolving phenotype. These macrophages exhibit attenuated inflammatory characteristics and promote tissue repair through increased expression of anti-inflammatory, pro-fibrotic and angiogenic factors, such as IL-10, transforming growth factor (TGF)-β and VEGF[108]. Anti-inflammatory T-lymphocyte populations also infiltrate the infarcted area and limit adverse ventricular remodeling by promoting wound healing, inflammation resolution and scar development via collagen matrix formation[109].

During this phase, fibroblasts try to compensate loss of CM and provide mechanical support for the newly formed structures. Inactive fibroblasts start to express contractile proteins, such as α-smooth muscle actin (α-SMA)[110], and become activated (myofibroblasts) leading to proliferative activity and synthesis of ECM proteins, including collagen, fibrin and fibronectin, all of which contribute to the early phases of scar formation[107].

In the **healing phase**, which starts around two or three weeks after AMI, the emerging scar undergoes a maturation process in which ECM becomes cross-linked and reparative cells, including myofibroblasts, come into a quiescent state, and may enter in apoptosis[111]. Significant loss of contractile function and electrical uncoupling occurs, which leads to LV geometric and functional changes, provoking left ventricle ejection fraction (LVEF) reduction due to chamber dilatation, global systolic dysfunction, and the onset of HF. At this point, volume of blood pumped by the heart is not enough to supply oxygen and nutrients demand of the body.

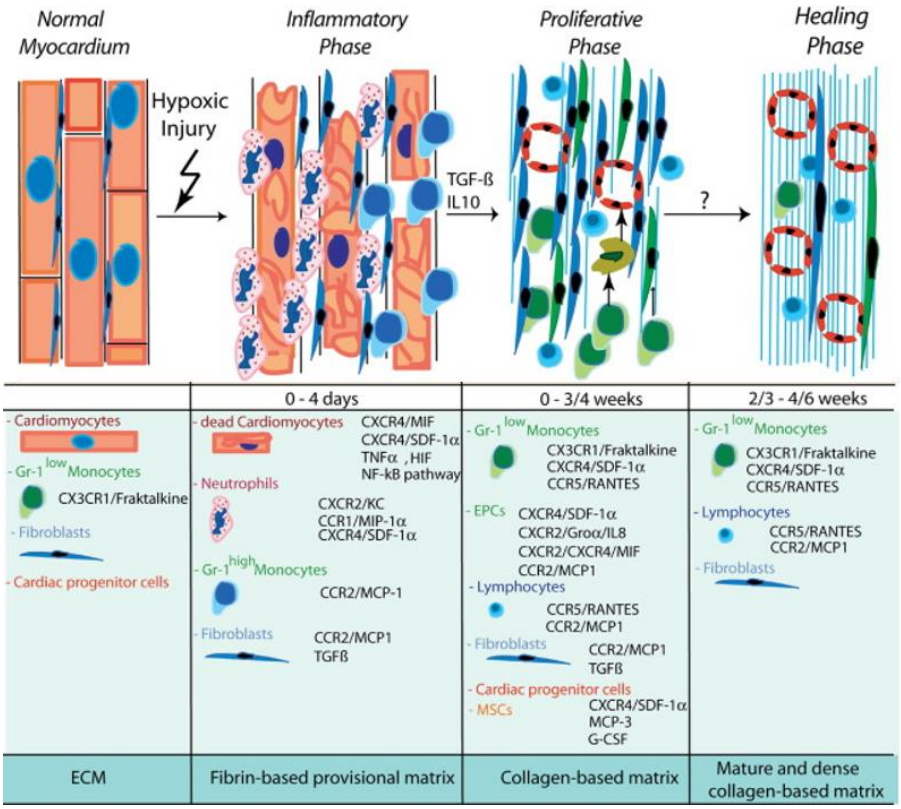

Figure 1.5. Cellular and molecular events after AMI. *Inflammatory, proliferative and healing phases are characterized by specific events, involving types of cells and molecules. ECM: extracellular matrix; HIF: Hypoxia inducible factor; IL: Interleukin; MCP: Monocyte chemotactic protein; AMI: Acute myocardial infarction; MIF: Macrophage inhibitory factor; MSC: Mesenchymal stromal cell; NF-κB: Nuclear factor kappa B; SDF: Stromal-derived factor; TGF: Transforming growth factor; TNF: tumor necrosis factor. Adapted from Liehn E.A. et al., 2011*[100].

It has been described that the main problems after AMI are the massive loss of contractile tissue, which cannot be recovered due to low regeneration rate of CM, and the subsequent massive proliferation of myofibroblasts, which eventually become in non-functional tissue. In this work, new therapeutic strategies for cardiac tissue pre-conditioning to avoid I/R-induced injury will be proposed. With this purpose, understanding the mechanisms triggering cardiomyocytes death during the I/R process is of vital interest and are discussed below.

1.3.3. Underlying molecular mechanisms of cardiomyocytes death during I/R-induced injury

Experimental studies over the last decades have identified complex signal transduction processes underlying cardiomyocytes death during and after an ischemic event. Necrosis in the infarcted myocardium is characterized by histological signs, including myofibrillar contraction bands, swollen and/or ruptures mitochondria, sarcolemma rupture, destruction of CM membranes, microvascular break up, hemorrhage and presence of infiltrating leukocytes (inflammatory response). Most of these features are aggravated by reperfusion[97, 112]. This process is thought to originate from unregulated and uncoordinated pathophysiological mechanisms as a result of an overwhelming stress. However, regulated modes of cell death, such as apoptosis, autophagy or necroptosis, also occur in infarcted myocardium[113-115].

During ischemia, a sudden cut in oxygen and nutrients supply in the infarcted zone occurs. As a response, mitochondria consume the available oxygen to generate ATP and anaerobic pathways are activated as an alternative to obtain energy and maintain functionality. Consequently, FA metabolism is dramatically reduced, and anaerobic glycolysis becomes the main source of energy, leading to hydrogen ions accumulation and lactate production, which is eventually translated into tissue acidosis. Increase of Na^+ influx trough the Na^+/H^+ exchanger, and intracellular Na^+ accumulation is supported by the inhibition of Na^+/K^+-ATPase due to lack of available ATP[116, 117]. The subsequent exchange of Na^+ and Ca^{2+} by reverse mode operation induces intracellular Ca^{2+} overload. Upon reperfusion, there is a quick pH normalization, leading to Ca^{2+} oscillatory release and reuptake into the sarcoplasmic reticulum and myofibrillar hypercontraction[117]. Ca^{2+} oscillations also induce the activity of xanthine oxidases, promoting ROS production, which exacerbate membrane damage by promoting mitochondrial permeability transition pore (mPTP) opening and mitochondrial matrix swelling[118, 119]. mPTP opening is a crucial event for apoptosis initiation, and it is partially dependent on the Bcl-family proapoptotic (e.g. Bax, Bak and Bid) and antiapoptotic (e.g. Bcl-2) proteins ratio, which interact with the mitochondrial membrane to regulate cellular fate[118]. Mitochondrial disruption leads to cytochrome c release to the cytosol, which activates programmed cell death by the caspase cascade, typically without inflammation response[120] (**Figure 1.6**). Necroptosis is considered a regulated form of necrotic cell death and shares characteristics with both necrosis and apoptosis, but it is controlled by activation of receptor-interacting protein kinases 1 and 3[121].

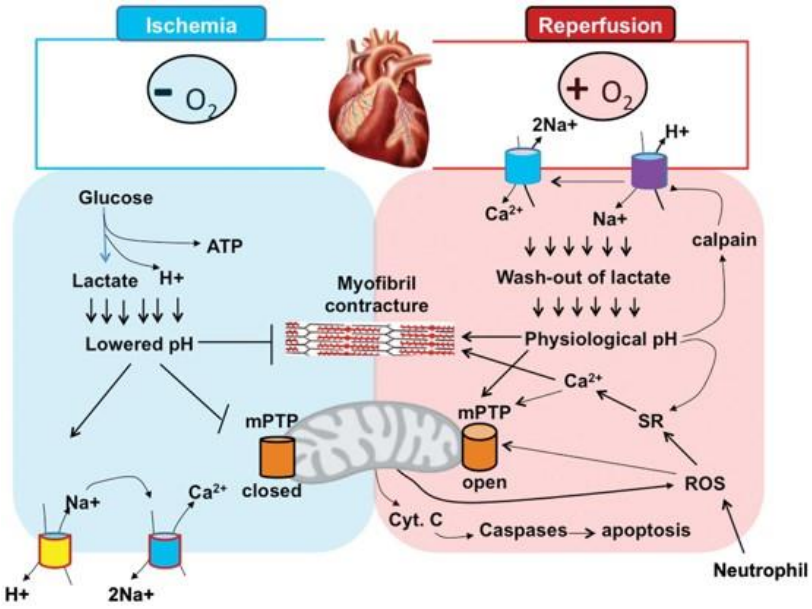

Figure 1.6. Main contributors of myocardial injury during cardiac ischemia-reperfusion-induced injury. *The absence of oxygen and FAs during ischemia involves a sudden change in CM metabolism, with Glucose as a new main source of energy. Lactate and H+ produced during anaerobic glycolysis decrease pH in the cells, which creates an imbalance in ions exchange and intracellular Ca^{2+} accumulation. Physiological pH is restored immediately after reperfusion, triggering oscillations in Ca^{2+}, ROS production, myofibril hypercontraction and mPTP opening, which is responsible for Cyt. C release and apoptosis cascade initiation. ATP: Adenosine triphosphate; mPTP: Mitochondrial permeability transition pore; SR: Sarcoplasmic reticulum; ROS: Reactive oxygen species; Cyt. C: Cytochrome C. Illustration from Li X. et al., 2016[122].*

The alternative method of programmed cardiomyocyte death during I/R process is macroautophagy, often referred to as autophagy. Several evidences suggest that proteostasis, which includes protein folding quality control (PQC) in endoplasmic reticulum (ER), is essential for maintaining the long-term wellbeing of low rate-proliferating mammalian cells, such as neurons or CM[123, 124]. I/R-induced injury induces the loss of proteostatic control, and the unfolded protein response (UPR) is activated in the ER, triggering the expression of stress response genes and subsequent translation of proteins, such as the ER chaperone glucose-regulated protein 78 kDa (GRP-78), which contributes to I/R-induced stress mitigation[125]. The UPR is initially an adaptative response. Nonetheless, it can lead to autophagy and programmed cell death activation if unresolved. In this sense, autophagy corresponds to one of the major components of the PQC system and occurs in a highly conserved constitutive mechanisms for homeostatic clearance of organelles and aggregated or misfolded proteins. It involves intracellular segregation of cargo

within double-membrane-bound autophagosomes that fuse with and are degraded within lysosomal degradative process[126, 127]. Myocardial ischemia induces autophagy via the AMP-activated protein kinase pathway induction, and it is considered a protective event. Nonetheless, reperfusion activates autophagy via Beclin-1 upregulation, which impairs autophagosome processing, causing an increased autophagosome accumulation, ROS generation, mitochondrial permeabilization and, subsequently, cell death[128-130].

I/R-induced cell programmed death by apoptosis and autophagy may be linked events, as showed in **Figure 1.7**. Under physiological conditions, Beclin-1 is bound to Vps34 complex I to induce autophagy. Concurrently, Bcl-2 binds to Bax to prevent the activation of mitochondria-mediated pro-apoptotic signaling pathway. During cardiac I/R-induced injury, mammalian sterile 20-like kinase 1 (Mst1), phosphorylates Beclin-1, enhancing its physical interaction with Bcl-2. Therefore, free Bax in the cytoplasm is translocated to mitochondria membrane and contributes to cytochrome c release, triggering apoptosis and enhancing autophagy.

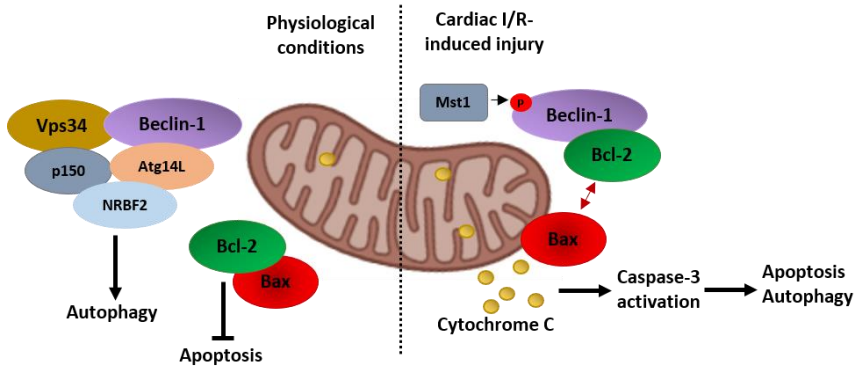

Figure 1.7. Cross-talk between apoptosis and autophagy via Beclin-1-mediated signaling pathway. *Bcl-2 is bound to Bax under physiological conditions, inhibiting the activation of apoptotic signals. At the same time, Beclin-1 forms a protein complex responsible for maintaining homeostatic levels of autophagy. Under stressing conditions, Mst1 phosphorylates Beclin-1, promoting its Bcl-2 separation from Bax and the physical interaction between Beclin-1 and Bcl-2. Once Bax is free, it is accumulated in the mitochondrial membrane, enhancing its permeabilization and the release of cytochrome C, which finally derivates in caspase-3 activation and apoptosis and autophagy induction. Vps34: Vacuolar sorting-associated protein 4; p150: Phosphoinositide-3-kinase, regulatory subunit 4; Atg14L: Beclin 1-associated autophagy-related hey regulator; NRBF2: Nuclear receptor-binding factor 2; Bcl-2: B-Cell lymphoma 2; Mst1: Mammalian sterile 20-like kinase 1. Illustration adapted from Maejima Y. et al., 2017[131] and created in BioRender.*

Despite the contribution of each process to cell death remains unknown, a role of mitochondria is vital in all of them. Recognition of the different modes of CM death during AMI opens the possibility of identifying new therapeutic targets to modulate cell loss[113].

1.3.4. Dynamics of fibroblast activation during AMI

Proliferation and activation of fibroblasts after cardiac insult is crucial for tissue repair. However, these processes also contribute to fibrosis, tissue remodeling and, eventually, HF. Cardiac fibroblasts undergo important phenotypic plasticity in response to stimulation with defined soluble mediators or mechanical stress[132]. Necrotic CM release DAMP during AMI and trigger resident non-CM cell types activation and leukocytes infiltration during inflammatory phase, which release pro-inflammatory cytokines and chemokines. Fibroblasts respond to environment signals and contribute to proinflammatory signaling, releasing soluble factors, such as TNF-α, IL-6 or IL-1β[133]. In addition to this, it has been described a pro-survival and anti-proliferative phenotype of cardiac fibroblasts at day 1 after AMI. Fibroblasts in the infarct zone become proliferative, show an increased activation and are polarized to an anti-inflammatory and pro-angiogenic phenotype during the following days after AMI. In this context, galectin-3 has been proposed as an activator of TGFβ-1/α-SMA/Collagen I pathway in cardiac fibroblasts during this phase, which leads to ECM accumulation[134]. TGFβ-1 interacts with a heterodimer on targe cell surface, formed by TGFβ receptors 1 and 2, and induces phosphorylation of SMAD2 and SMAD3 transcription factors, which form a complex with SMAD4 that is translocated to the nucleus to promote fibroblasts differentiation-specific gene expression, such as collagen type I[135, 136]. TGFβ receptors signaling also trigger fibroblasts activation through the activation of MAPK effectors, such as p38, inducing α-SMA transcription and the formation of stress fibers[135]. At day seven after AMI, fibroblasts continue producing ECM components and contribute to scar formation. Concretely, Collagen I and III are the main components of ECM, and are the predominant proteins supporting scar generation. Fibroblasts also show anti-angiogenic potential and reduced migration rates one week after AMI, which correlates with an observed shift in adhesion preference from laminin to collagen IV[137].

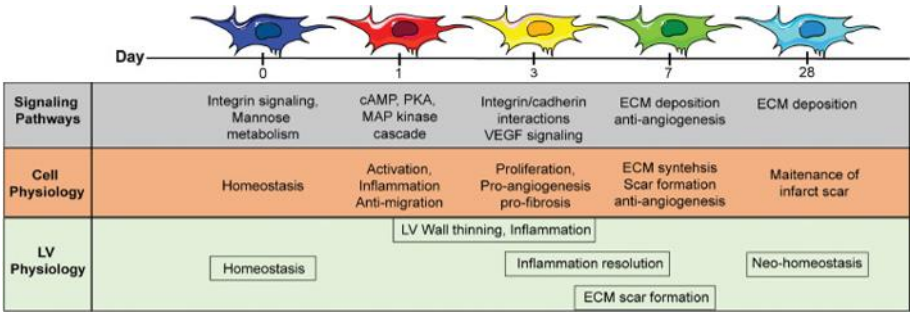

Figure 1.8. Fibroblasts' phenotype shift through the different phases of cardiac remodeling during and after AMI. *Cardiac fibroblasts are activated, and acquire pro-inflammatory and anti-migratory capabilities after myocardial insult (day 1). After three days, resolution of the previous inflammation starts, and cardiac fibroblasts change to a proliferative, pro-angiogenic and pro-fibrotic phenotype, leading to ECM-related proteins synthesis. After one week, ECM deposition is increased and scar formation starts. Neo-homeostasis state is reached around 28 days after AMI. Fibroblasts are de-activated, but they keep producing enough ECM to orchestrate the new kinetics turnover. LV: Left ventricle; ECM: Extracellular matrix. Picture adapted from Daseke II MJ and collaborators, 2020[28].*

1.4. Diagnosis and conventional treatments of AMI

Myocardial injury and infarction can be diagnosed by biomarkers detection, patient's history and clinical manifestations. The most reliable and used markers are cardiac troponin I (cTnI) and T (cTnT), which form part of the contractile machinery of CM and are expressed almost exclusively in the heart. These molecules are released from skeletal muscle cells and can be detected in peripheral blood[138]. Indicative but not specific symptoms for myocardial ischemia include chest and upper extremity pain, dyspnea, fatigue or nausea. Electrocardiographic study is the most quick and effective method to asses cardiac function and detect changes in systolic and diastolic functions or arrhythmias. As previously mentioned, ECG manifestations of AMI include ST-segment elevation and/or ST-segment depression and T wave changes[139].

Nowadays, AMI treatments comprise both acute therapeutic strategies and post-infarction approaches (**Figure 1.9**). Interventions in the acute stage of AMI are related to revascularization procedures to avoid infarct extension, such as percutaneous coronary intervention (PCI) by a nonsurgical procedure consisting on the insertion of a catheter tube (formerly known as coronary angioplasty), coronary artery by-pass grafting (CABG) or clot-busting drugs (thrombolysis)[139]. Pharmacological approaches are used in combination with the previous strategies to limit myocardial I/R-induced damage. Compounds that slow or reverse cardiac remodeling and decrease heart oxygen demands, such as angiotensin-converting-

enzyme (ACE) inhibitors, angiotensin receptor-neprilysin inhibitors (ARNI), β-blockers (e.g., metoprolol or Esmolol), and mineralocorticoid-receptor (MR) antagonists, have demonstrated a decrease in HF-associated mortality[140-142]. Other strategies include immunosuppressant drugs, anti-inflammatory compounds, metabolic modulators (e.g. nitric oxide) blood thinners (e.g. aspirin) and pain relievers[143]. Mechanical support therapies, such as LV assist devices (LVAD) and cardiac resynchronization therapy (CRT), show beneficial effects in patients with a previous HF[144, 145]. Heart transplantation remains the only effective solution. Nevertheless, it is not realistic as a standard approach since surgical procedure is highly complex and donors are limited[146].

Despite the above-mentioned treatments have allowed to improve quality life and survival of AMI patients, the development of new therapeutic strategies to avoid pathologic cardiac remodeling and regenerate the injured area is still necessary.

1.5. Advanced therapies for AMI

Over the last years, several approaches have emerged to improve patients' clinical outcome after AMI. The study of the precise molecular mechanisms which drive cardiac remodeling during AMI is key to select which potential therapeutic molecules can be used to fight the pathology. In this context, rational integration of knowledge from decades of research is crucial to find new combinations and innovative approaches to make a step forward in cardiovascular nanomedicine.

It has been estimated that up to 1 billion of CM can be lost after myocardial insult, and CM turnover is insufficient to restore the contractile function of an injured human heart[147]. Consequently, the common aim of advanced therapies is to protect damaged area after AMI, promote mechanical function recovery and enhance heart regeneration (**Figure 1.9**). The two major groups of strategies are cell-free and cell-based therapies. Cell-free approaches for ischemic heart disease are based on cardiac resident cells targeting. In this context, induction of the remaining endogenous CM proliferation[148] or addressing the pro-fibrotic response after AMI have been of special interest: while a line of research has been focused on pathogenic cardiac remodeling blocking[149], other studies are based on cardiac fibroblasts direct reprogramming to cardiomyocytes by the expression of a combination of developmental transcription factors[150, 151]. Cell therapy strategies involve cell transplantation to replace or repair damaged tissue. Cells from different origin have been used for this purpose, such as skeletal myoblasts[152], bone-marrow derived cells[153, 154], mesenchymal stromal cells (MSC), CSC[155] and functional CM derived from embryonic stem cells (ESC) or induced pluripotent stem cells (iPSC)[156-158]. Despite cell-based approaches conferred some beneficial effects in patients with AMI by improving LVEF and cardiac function, not consistent positive results in

the treatment of AMI and clinical translation problems have been noticed. Additionally, long-term follow-up studies have shown adverse effects, such as poor engraftment rates, arrhythmias derived from mature CM, immune rejection and tumorigenesis risk due to the presence of non-differentiated cells when ESC or iPSC are differentiated to CM[159].

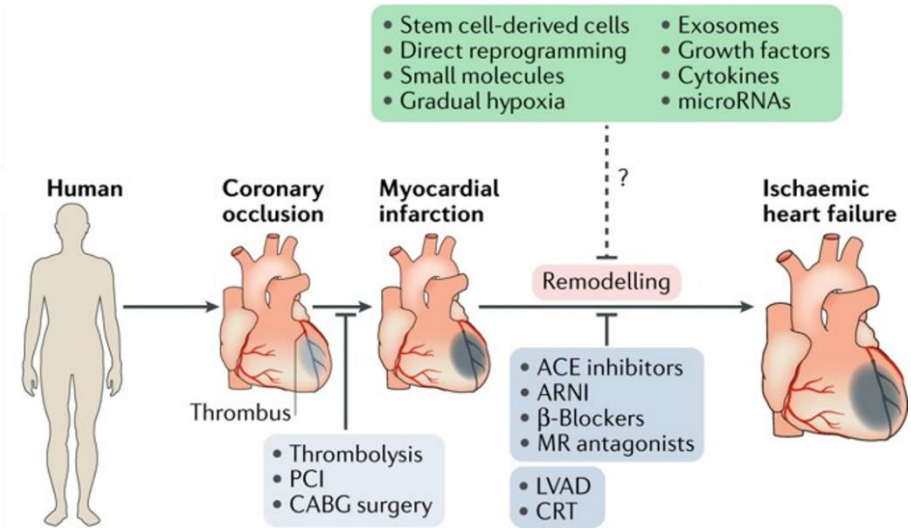

Figure 1.9. Therapeutic approaches to AMI. *In humans, the default response to I/R-induced injury is fibrosis, where necrotic tissue is replaced with a fibrotic scar, causing loss of cardiac contractility and, eventually, HF. The aim of clinical therapies is either to salvage the ischemic myocardium by early revascularization (light blue box) or to prevent pathological cardiac remodeling through pharmacological therapy or electromechanical support (dark blue box). Despite current clinical translation problems, advanced therapies (green box) have demonstrated promising outcomes against cardiac remodeling. PCI: Percutaneous coronary intervention; CABG: Coronary artery by-pass grafting; ACE: Angiotensin-converting enzyme; ARNI: Angiotensin receptor-neprilysin inhibitors; MR: Mineralocorticoid receptor; LVAD: Left ventricle assist devices; CRT: Cardiac resynchronization therapy. Illustration adapted from Hashimoto H. et al., 2018[159].*

Two novel advanced cell-free therapeutic strategies to reduce cardiac remodeling after myocardial I/R-induced injury are proposed in the present project. In the first section, the cardioprotective potential of new nanoparticles based on the conjugation of a ω-3 PUFA (di-docosahexaenoic acid, diDHA) with poly-L-glutamic acid (PGA) was explored; while the second section was focused on the specific loading of a soluble factor (Oncostatin-M, OSM) in small extracellular vesicles (SEV) derived from MSC to enhance the beneficial effects of their paracrine signaling. In the following sections, a more detailed discussion of these approaches is provided.

1.5.1. Nanotechnology and polymer-drug nanoconjugates

Nanotechnology is a multidisciplinary research field that address the design, synthesis and characterization of materials with controlled shapes and sizes at the nanometer scale[160]. One of the most active research areas is nano-biotechnology, which involves the use of nanoparticles as vehicle for therapeutic agents' delivery and have been implemented for AMI treatment to mitigate inflammation, oxidative stress and necrosis, among other pathological processes during I/R-induced injury. A summary of some strategies that have been proposed in this field is shown in **Figure 1.10**. Nonetheless, any of the mentioned approaches has been approved by the Food and Drug Administration (FDA) federal agency for clinical practice.

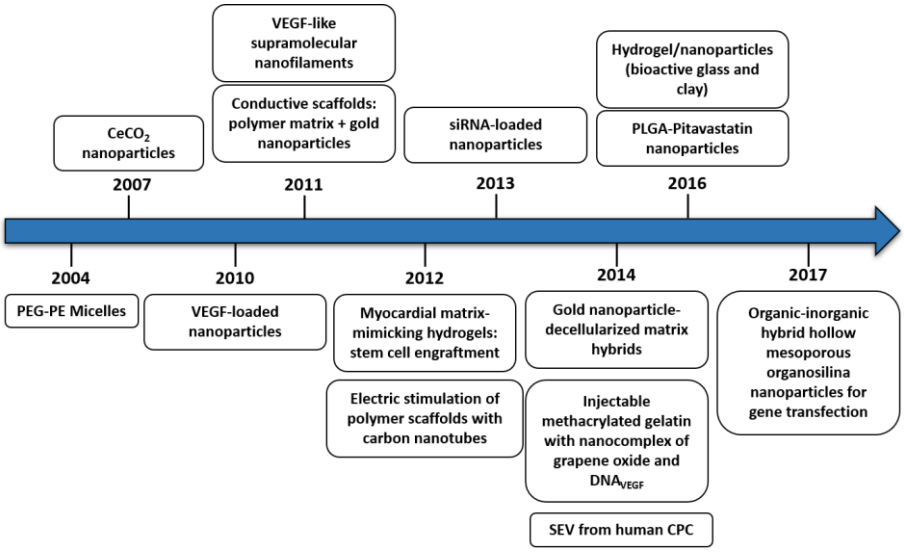

Figure 1.10. Timeline of nanotechnology for AMI treatment. *PEG-PE: Polyethyleneglycol/ phosphatidyl-ethanolamine; CeCO2: Cerium oxide; VEG: Vascular endothelial growth factor; SEV: Small extracellular vesicles; CPC: Cardiac progenitor cells; PLGA: Poly(lactic-co-glycolic acid. Illustration adapted from Bejarano, J. et al., 2018[161].*

Among the wide variety of nanoparticles, polymer-drug nanoconjugates are pharmacologically active macromolecular constructs comprising one or more therapeutic agents, such as small molecules, peptides, proteins or aptamers, covalently bound to a polymeric carrier[162]. The first polymer-drug nanoconjugate was synthetized in 1955 by Von Horst Jatzkewitz[163], but the field of "polymer therapeutics" was established by the intensive work of Ringsdorf, Kopecek and Duncan, among others, in the 1970s[164-166]. Nowadays, more than 15 polymer-drug nanoconjugates have been successfully translated into the clinical practice to treat

liver and renal acute cancer[167], lymphoblastic leukaemia[168], neovascular age-related macular degeneration[169] or anemia associated with chronic kidney disease[170], among others[162]. They present several advantages compared to free-drug administration, including improved drug solubilization, prolonged circulation in the blood stream, controlled release, reduced immunogenicity and enhanced biosafety[162].

Attending to their structure, polymer-drug nanoconjugates on the market or in clinical development can be classified in four classes: polymer-protein conjugates, polymer-small-molecule drug candidates, dendrimers and polymer nanoparticles[162]. Conformation and size of the different types of nanoconjugates are summarized in **Figure 1.11**.

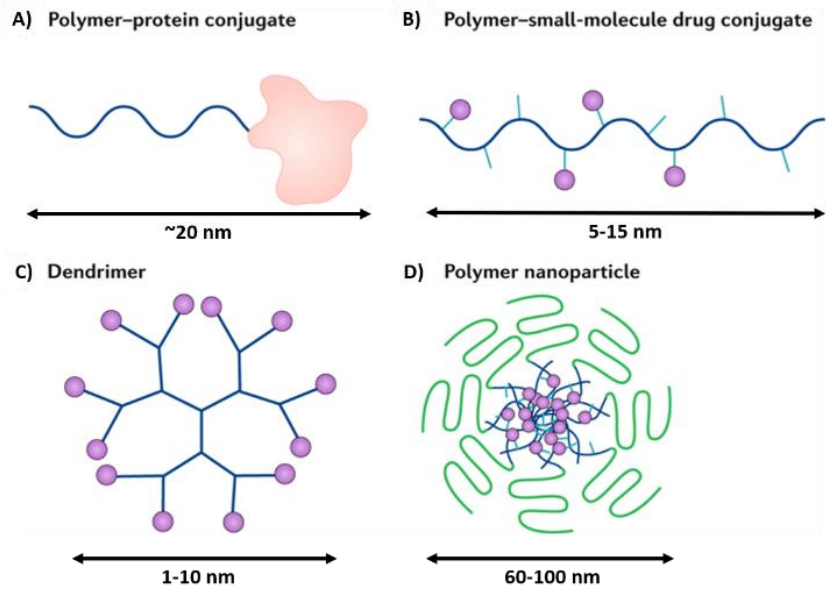

Figure 1.11. Schematic representation of polymer-drug nanoconjugates types on the market or in clinical development. (A-B) *Polymer-protein or small molecule drug conjugates 3D structure, where protein is represented in orange and small-molecule drug in purple.* ***(C)*** *Dendrimers present a highly branched structure with high functionality for drug conjugation.* ***(D)*** *Polymeric nanoparticles have a micellar shape and are characterized by a core-shell architecture, with a hydrophobic core sequestered by a hydrophilic corona. Illustration adapted from Ekladious I. et al., 2019[162].*

The first section of this thesis is focused on the use of a FA with cardioprotective potential (diDHA) conjugated to a polymeric carrier (PGA) to mitigate cardiac I/R-induced injury via passive targeting. In this context, polymer nanoparticles are the

preferred option for the delivery of hydrophobic agents, offering enhanced stability and biodistribution[162]. This type of nanoconjugates is commonly composed of three main components: a water-soluble polymeric carrier, a bio-responsive linker and a bioactive agent (drug)[164, 171]. Rational selection of each component is crucial to achieve optimized physicochemical properties of the polymer-drug nanoconjugate, such as size, surface charge and conformation.

Polymeric carrier of choice should present specific properties, including biodegradability (facilitating excretion *in vivo*), low polydispersity (providing homogeneity of the final product), prolonged half-life in the blood (enhancing adequate biodistribution) and multivalence (allowing flexible drug loading)[172]. The nano-system self-assembly behavior also depends on the polymer and drug characteristics. Of important note, several hydrophilic polymers fail to aggregate in the presence of water, but self-assembly is induced after conjugation with a hydrophobic drug. In this context, PGA has been used as a polymeric backbone for the conjugation of potential therapeutic molecules and disease treatment, including wheat germ agglutinin for bladder cancer[173], doxorubicin and paclitaxel for breast cancer and other solid tumors[174, 175], apoptotic protease activating factor 1 against I/R-induced injury in kidney[176, 177] or glatiramer acetate for autoimmune inflammatory central nervous system disorders[178]. These research works have shown that PGA is water-soluble, non-toxic, biodegradable and non- immunogenic, which makes it interesting for therapeutic use[179]. Additionally, the use of bio-responsive linkers can optimize drug release profiles in specific microenvironments and influence the % loading of the drug to the carrier and drug stability. In this context, linkers can respond to both endogenous (e.g. pH or ROS presence) or exogenous (e.g. magnetic field, temperature, light) stimulus[180].

As previously mentioned, dietary intake of ω-3 PUFA has been recommended as a strategy to reduce the risk to develop CVD, and several studies have linked PUFA uptake with a reduced cardiac injury after stress induction[181-187]. Nonetheless, such experimental models do not fit to daily clinical practice, where AMI patients are admitted at the hospital and need for emergency reperfusion. Additionally, the clinical benefit of ω-3 supplementation remains controverted, although they seem relevant as prevention of coronary events and mortality[188]. Different ω-3 formulations have also been administered as cardioprotective agents at the onset of the ischemic process by culture medium enrichment, *ex vivo* infusion, intravenous injection or intraperitoneal injection *in vitro* and *in vivo* pre-clinical models[189-195]. However, these studies do not study if beneficial effects against reperfusion-induced injury are a result of the combined action of DHA and EPA contained in the ω-3 emulsion or related more to one of them. Moreover, the amount of PUFA that reach cardiac tissue after administration and possible side effects on additional organs have not been taken into account. Previous studies

have described that carbon-carbon double bonds confers PUFA a higher susceptibility to be peroxidized and FFA can be sequestrated by albumins in the blood stream, reducing the amount of drug which reaches the target tissue. In addition to this, the resulting free radicals and hydroperoxides after lipid peroxidation, which can be oxidized into aldehydes and ketones, may contribute to oxidative stress, which stimulates NF-κB and the production of inflammatory cytokines, chemokines and adhesion factors[196, 197]. A review of the experimental approaches where PUFA against cardiac I/R-induced injury have been used is summarized in **Table 1.1**.

Table 1.1. Experimental approaches using FA to reduce cardiac I/R-induced injury.

Formulation	Administration	Experimental model	Effect	Ref.
Lipid emulsion enriched on DHA or EPA	Infusion prior to I/R	Isolated rat hearts: 30 min I + 30 min R	Not-protective effects found	189
EPA, DHA or EPA+DHA	6 weeks dietary intake before I/R	Isolated rat hearts: 17 min I + 33 min R	Recovery of cardiac pump activity related to EPA accumulation in CM membrane	181
Enriched ω-6 or ω-3 PUFA media	4 days before OGD-R in culture media	OGD-R *in vitro* NRVM	α- and β-adrenoreceptor response modulation by ω-3 PUFA	182
Individual LA, LNA, DHA, EPA or AA	90 s preincubation prior to chemical induction	LV cardiac sarcolemma from pigs: NA^+/H^+ exchanger activity	DHA and EPA antiarrhythmic properties by altering sarcolemma composition	190
Flaxseed-rich diet (source of ω-3 PUFA)	16 weeks dietary intake	Isolated hearts from hypercholesterolemic rabbits: 30 min I + 45 min R	Antiarrhythmic effect	183
DHA	Infused within the pericardial space before, during and after I	I/R *in vivo* pig model: 45 min I + 180 min R	Reduced IS and mortality	191
ω-6 PUFA, ω-3 PUFA or SFA	6 weeks dietary intake before infusion	Isolated rat hearts: 30 min I + 120 min R	ω-3 PUFA reduced arrhythmias	184
DHA	Infusion pre and pre/post I	Isolated heart rats: 20 min I + 30 min R	Reduced cardiac damage and afforded antioxidant protection	198
ω-6 PUFA, ω-3 PUFA or SFA	6 weeks dietary intake before I/R	Isolated rat hearts: 30 min I + 120 min R	ω-3 PUFA reduced oxidative damage	185
DHA:EPA (3:1)	8 weeks dietary intake prior to I/R	Isolated rat hearts: 30 min I + 120 min R	Reduced IS Increased antioxidant activity Decreased NF-κB and Nrf2 activation	186

ω-3 PUFA	4 weeks dietary intake or during prenatal period, before damage	I/R *in vivo* rat model: 20 min I + 40 min R NRVM: 30 min I + 60 min R	Increase of mRNA level of PPARγ-target genes (FATP and IL-1ra), BCL2 and Connexin-43	[187]
EPA:DHA (6:1)	Intravenous bolus before R	I/R *in vivo* rat model: 30 min I + 4 h R	Improved arterial pressure and decreased cTnI plasma levels	[193]
EPA or DHA	Infused prior to I/R	Isolated mouse hearts: 30 min I + 40 min R	DHA attenuated NLRP3 inflammasome cascade and preserved mitochondria function	[194]
ω-3 rich TG emulsion	Infusion or IP injection at the onset and 1 h after R	Isolated mouse hearts: 30 min I + 60 min R I/R *in vivo* mouse model: 30 min I + 48 h R	Reduced IS, improved cardiac function recovery and promoted cell survival (PI3K/AKT signaling pathway)	[195]

DHA: Docosahexaenoic acid; EPA: Eicosapentaenoic acid; PUFA: Polyunsaturated fatty acids; LA: Linoleic acid; LN: Linolenic acid; AA: Arachidonic acid; SFA: Saturated fatty acid; TG: Triglyceride; I: Ischemia; R: Reperfusion; IP: Intraperitoneal; NRVM: Neonatal rat ventricular myocytes; CM: Cardiomyocytes; IS: Infarct size; NF-κB: Nuclear factor kappa light-chain enhancer of activated B cells; Nrf2: Nuclear transcription erythroid 2-related factor 2; PPAR: Peroxisome proliferator-activated receptor; FATP: Fatty acid transport protein; IL-1ra: Interleukin-1 receptor antagonist; BCL-2: B-Cell lymphoma 2; cTn: Cardiac troponin; NLRP3: NACHT, LRR and PYD domains-containing protein 3; PI3K: Phosphoinositide 3-kinase/protein kinase B; AKT: RAC-alpha serine/threonine-protein kinase.

The use of polymeric carriers to facilitate the translation and clinical utility of novel agents is a particularly exciting and promising avenue for the next generation of polymer therapeutics. So far, there are no records of previously designed nanoparticles for cardiac repair that have been used in clinical practise[161, 162]. Here, passive targeting via a single dose local administration in relevant *in vitro* and *in vivo* cardiac I/R-induced injury models is proposed, where a hydrophobic drug (diDHA) has been attached via covalent binding to a polymeric chain (PGA) and a micelle structure is formed. In addition to this, an ester bond pH-responsive linker has been used to favor drug release in the injury area because of the acidic pH during cardiac ischemia and inflammatory environment expected in comparison with normal blood (pH 7.4)[99]. The solubility in water and healing properties of diDHA could be improved by polymeric conjugation, triggering its controlled and sustained release at the injury site. Of important note, the stabilization of diDHA in nanoconjugates could also avoid lipid peroxidation or albumin sequestration in the blood stream, which eventually could become in a reduced drug activity.

1.5.2. Cell therapy based on the use of MSC

MSC are a subpopulation of multipotent stromal cells first reviewed by Friedenstein A.J. et al. in 1966 as a population of non-hematopoietic stem cells in the bone marrow[199]. Nowadays, it is known that MSC can be easily isolated from additional tissues, such as dental pulp, adipose tissue or fetal tissues. The Mesenchymal and

Tissue Stem Cell Committee of the International Society for Cellular Therapy provides minimal criteria to define human MSC. These features are summarized in **Figure 1.12**. First, they should be plastic-adherent when maintained in standard culture conditions. Second, MSC must express CD105, CD90 and CD73 and lack expression of CD14 or CD11b, CD19 or CD79α, CD34, CD45 and HLA-DR surface molecules. Third, they must differentiate to chondroblasts, adipocytes and osteoblasts *in vitro*[200].

Increasing evidences over the last decades show that MSC are multipotent cells, that can replicate as undifferentiated cells and have the potential to differentiate to additional lineages of mesenchymal tissues, including hepatocytes, neurons and skeletal muscle cells[201]. Although previous *in vitro* and *in vivo* studies described that MSC may be differentiated into CM-like cells[202-206], MSC transplantation *in vivo* beneficial effects after AMI have been associated to additional factors, such as cell fusion[207] or paracrine signaling[208].

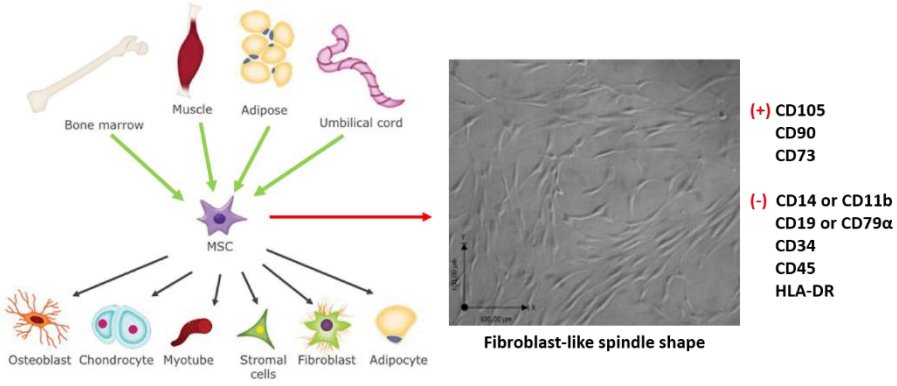

Figure 1.12. MSC main sources and characteristics. *Green arrows indicate the most common sources for MSC isolation (bone marrow, muscle, adipose tissue and umbilical cord). MSC multipotency relies on their ability to differentiate into multiple cell types (black arrows). Observed in vitro characteristics (red arrow) include plastic adherence, fibroblast-like spindle morphology and expression or lack of specific cell surface markers, represented as (+) and (-), respectively. Illustration adapted from Ibraheim H. et al., 2017[209] and Rodríguez-Pardo V. et al., 2013[210].*

1.5.2.1. Therapeutic potential of MSC: Paracrine hypothesis

The above-mentioned characteristics of MSC along with their easy manipulation and expansion *ex vivo* made cellular therapy based on the use of these cells very promising. Nonetheless, the low-rate survival of cells after transplantation *in vivo* suggests that long-term survival of MSC might not be essential for their beneficial effects[211-213]. Additionally, not only MSC but also their conditioned media have

proven to ameliorate kidney[214], lung[215, 216] and heart[217, 218] function after insult. Therefore, the protective mechanism of MSC transplantation might mainly be related to their ability to stimulate survival and recovery of damaged tissue by paracrine factors release (secretome). This phenomenon is known as the "paracrine hypothesis" of MSC therapeutic potential (**Figure 1.13**).

MSC secretome includes a protein soluble fraction (mostly growth factors, chemokines and cytokines) and a vesicular component (extracellular vesicles, EV), which transfer proteins, lipids, and genetic material between cells[219]. Vast experimental evidences support the active participation of MSC paracrine signaling in the protection of the cardiac damaged tissue after AMI modulating apoptosis, ROS generation, angiogenesis, fibrosis and inflammation[220-225] (**Figure 1.13**).

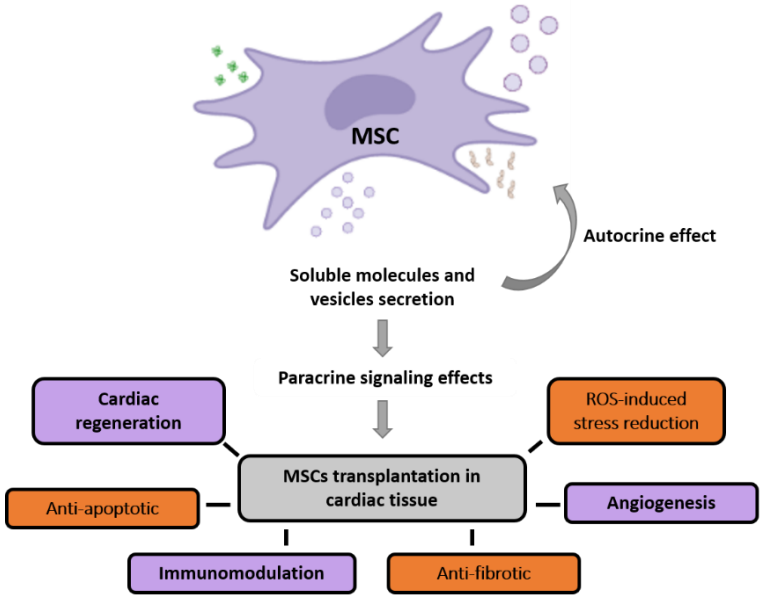

***Figure 1.13. MSC paracrine signaling effects in cardiac cell therapy**. Illustration adapted from Yánez-Mó M. et al., 2015[226] and built using Biorender.*

In spite of the healing features showed by MSC in AMI experimental *in vivo* models, clinical trials have shown inconspicuous outcomes[227]. Consequently, alternative approaches to enhance therapeutic potential of MSC have been implemented. With this purpose, MSC preconditioning and genetic modification have been tested. In a study developed by Feng Y. et al. in 2014, paracrine factors released by MSC after ischemic preconditioning led to reduced apoptosis in ischemic CM,

ameliorated fibrosis and improved cardiac function after myocardial infarction[228]. Another similar work showed that preconditioned MSC cultures activated survival Akt signaling pathway and increased their regenerative potential in a hindlimb ischemia *in vivo* model[229]. In this context, our research team generated a stable MSC line overexpressing HIF1-α (MSC-HIF), which is a protective transcription factor expressed by MSC under hypoxia but degraded in the presence of oxygen. Results showed that intramyocardial injection of MSC-HIF provided higher healing potential than native MSC in a rat *in vivo* model after AMI in terms of cardiomyocytes survival, fibrosis reduction and angiogenesis induction[230]. Later studies from our laboratory found that angiogenic potential was partly mediated by the enrichment of jagged-1 protein in MSC-HIF derived SEV in comparison with SEV isolated from native MSC conditioned culture media[231]. The use of EV derived from genetically modified MSC to enhance cardiac protection has been also explored by cellular overexpression of Akt[232, 233], C-X-C chemokine receptor type 4 (CXCR4)[234] or transcription factor GATA-4[235], among others.

Taking together, these experimental data have evidenced the important role of MSC-derived EV for cardiac repair and aroused our interest in the rational modification of EV in order to enhance their therapeutic potential.

1.5.2.2. Extracellular vesicles bioengineering

EV are natural carriers of wide-ranging origin biomolecules and play a key role in cell-to-cell communication. Their intrinsic similarity to cell membranes, deformable cytoskeleton[236], slightly negative zeta potential for long circulation[237, 238], biocompatibility[239] and small size for penetration into deep tissues[240] has increased the scientific community interest for their use as nanocarriers for clinical applications.

In order to augment the therapeutic efficacy of native EV, several technical approaches to improve EV bioactivity, stability, targeting and presentation to the target cells have been developed. In this context, a wide range of biomolecules, such as mRNA, miRNA, proteins or hydrophobic and hydrophilic small molecules have been loaded in EV using two major strategies: active or passive encapsulation. On the one hand, active SEV loading techniques include physical approaches, such as sonication[241], extrusion[242], electroporation[242] and freeze-thaw cycles[243], and chemical techniques, such as lipofection[244], incubation with membrane permeabilizers[242, 245], click chemistry[246, 247] and antibody binding[248]. These methods have demonstrated to achieve a high loading efficiency, but the majority of them compromise membrane integrity and favor EV aggregation[249]. On the other hand, passive loading approaches include incubation of SEV or donor cells with free

biomolecules[245, 250, 251]. Unlike active approaches, passive loading do not compromise EV membrane integrity, but loading efficiency is low[249].

The use of EV for protein delivery is a promising method which opens the possibility of loading EV through genetic engineering of the donor cells, which are transfected with a plasmid carrying the gene of interest fused to a gene encoding a protein which is naturally present in EV membrane[252]. Consequently, donor cells synthetize the desired encoded protein, which is incorporated and secreted into EV. In this context, tetraspanins, lysosome-associated membrane glycoprotein 2 transcript variant b (lamp2b) and lactadherin c1c2 domains (protein also known as MFG-E8) have been widely used as fusion partners for distinct applications to display a protein of interest on the EV surface[239, 253].

Nanotechnology has unlocked a new dimension of possibilities regarding to potential therapeutic molecules delivery. Polymeric carriers and SEV have shown to present several advantages to succeed as promising clinical tools, such as low immunogenicity and cytotoxicity, which correlate with long-term biosafety. Polymers and EV customization to get an enrichment in a particular molecule has been only minimally explored in the field of AMI.

1.6. Cellular communication mechanisms

The rise of multicellularity was a major transition in evolution and set the stage for unprecedent increase in complexity, especially in land plants and animals. Consequently, new ways for cells to stick together, communicate and share resources were necessary, and cells went through a developmental program, where distinct subpopulations assumed specialized jobs and were organized in each organism[254].

Cell-to-cell communication is a process by which one cell behavior is influenced by signals transferred from another cell or itself. Messages from cells in complex organisms are sent by a huge variety of signal molecules, which include proteins, amino acids, nucleotides, steroids, retinoids, fatty acid derivatives, and even dissolved gases such as nitric oxide or carbon monoxide. These messages or ligands are sent to receptor cells, and trigger a biological response. The first basic idea around specific receptors that bind transmitter substances onto the cells, thereby initiating or inhibiting cellular functions, was formulated by the Cambridge physiologist John Newport Langley[255]. Nowadays, four different cellular communication mechanisms have been described based on the distance between the involved cells[256] (**Figure 1.14**):

- **Autocrine:** Signal agent is secreted to the extracellular space, but transmitter and receptor cell is the same.

- **Paracrine:** Transmitter and receptor cell are in a short distance, so ligands are directed to neighbor cells.
- **Juxtracrine:** Signals are transferred to adjacent cells through cell-cell contact.
- **Endocrine:** Cells transmit the signal over long distances. Messengers are produced by specialized cells and released into the bloodstream, which carries them to target cells in distant parts of the body.

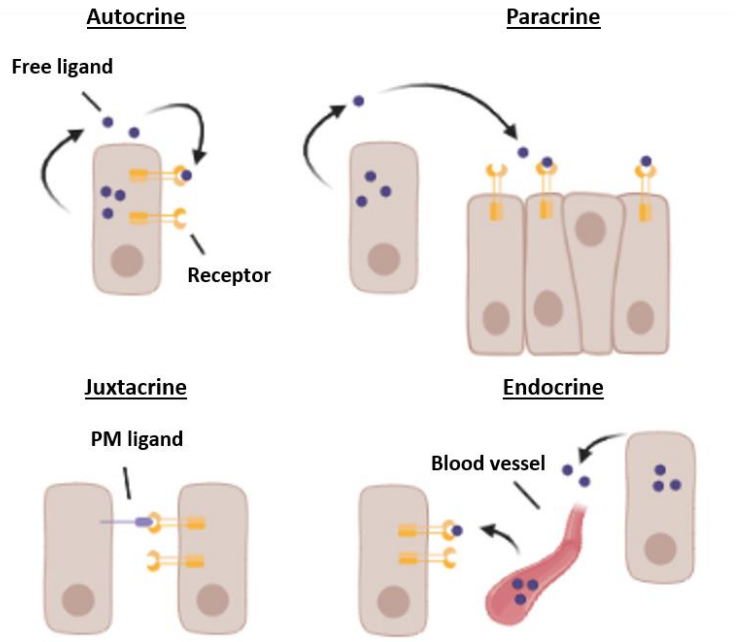

Figure 1.14. Cellular communication mechanisms. *One cell can interact with itself by autocrine signaling or with other cells in a paracrine, juxtracrine or endocrine manner. PM: Plasma membrane. Illustration created in Biorender.*

Therefore, cells in multicellular organisms receive stimulus from their environment, interpret the signals and respond accordingly by activating specific signaling pathways.

1.6.1. Extracellular vesicles

As previously mentioned, EV are secreted by cells to communicate with both neighboring and distant cells, or with the parent cell itself. These vesicles present a nanosized spherical structure with a lipidic membrane and aqueous lumen.

Additionally, they contain both in the membrane and the lumen, a wide range of biomolecules, which include proteins, lipids, multiple RNA species (mRNAs, miRNAs or long non-coding RNAs) and DNA fragments[257-262]. EV selective content mostly reflects the aims and the physiological state of the parent cells, and they have been found in a number of body fluids, such as blood plasma[263-265], urine[266], saliva[267] or breast milk[268]. Additionally, they can be secreted by plant cells[269, 270], bacteria[271, 272], fungi[273, 274], parasites[275] and archaea[22], suggesting a highly conserved evolutionary function of intercellular communication. There are four main subtypes of EV: apoptotic bodies, ectosomes or microvesicles (MV), exosomes and exomeres, which are differentiated from each other based on their biogenesis, release pathways, size, content and function[226, 276] (**Figure 1.15**).

Apoptotic bodies range from 1 to 5 µm and are formed during programmed cell death as a result of cell fragmentation. They contain cell organelles, proteins, nuclear fractions, DNA, RNA and lipids[277, 278]. MV are vesicles with sizes between 0.1 and 1 µm which are assembled and secreted by shedding or outward budding of the plasma membrane[279]. Their time of release is only a few seconds, and it can occur in a constitutive way or in response of a stimuli[280, 281]. Exosomes are extracellular membrane vesicles sized from 50 to 150 nm in diameter whose biogenesis by exocytosis of multivesicular endosomes was described for the first time in 1983 by two independent research articles, published within a week of each other[282, 283]. Nowadays, they are considered as key players in fundamental mechanisms of intercellular communication, signaling and regulation of cell fate, and also as a tool for many clinical applications. Cells can secrete exosomes with unique characteristics. Indeed, two distinct subpopulations, called small-exosomes (Exo-S, 50-80 nm) and large-exosomes (Exo-L, 90-120 nm), have been recently isolated by asymmetric flow field-flow fractioning (AF4) from conditioned media of more than 20 cell lines, showing different cargo and composition between them and confirming the heterogeneity of EV subpopulations[284]. Finally, a new subpopulation of EV, called exomeres, has been identified by Zhang H., et al. in 2018[284]. In this work, exomeres have been presented as non-membranous nanoparticles sizing less than 50 nm in diameter, and recent evidences point that they have different biophysical characteristics compared to both Exo-S and Exo-L[284, 285].

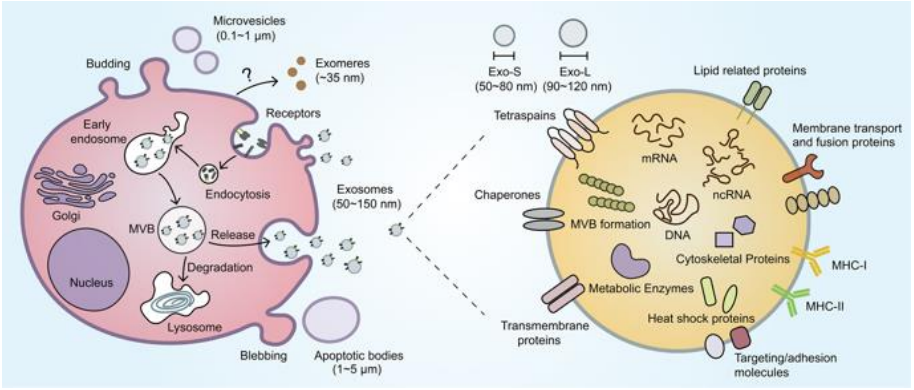

Figure 1.15. Types of EV, biogenesis and exosomes composition. *Apoptotic bodies are secreted by plasma membrane blebbing. Microvesicles are formed directly by plasma membrane evaginations. Exosomes are originated by the endocytic pathway. First, early endosomes are formed from plasma membrane invaginations and accumulate in multivesicular bodies (MVB). Finally, MVB content can be degraded by fusion with lysosomes or released to the extracellular space by fusion with plasma membrane. Two subpopulations of exosomes (Exo-S and Exo-L) can be distinguished. The content of exosomes includes several types of RNA, metabolic enzymes, heat shock and cytoskeletal proteins, while the membrane is enriched in lipids and other types of proteins with different functions, including transport, targeting, adhesion, fusion or immune system presentation (major histocompatibility complex, MHC, I and II). A new type of nanovesicle, called exomeres, have been found recently, but their biosynthesis process is still unknown. Illustration from Zhou X. et al., 2020[279].*

Despite the efforts made to fully characterize the different types of EV and clarify their functional differences, the lack of standardized isolation methods which fully separate MV from exosomes has made this task challenging[286]. Moreover, there is an overlap in their physicochemical and biochemical properties and an evidenced heterogeneity among subpopulations of exosomes[226, 287, 288]. Numerous scientific works have optimized isolation protocols involving 220 nm ultrafiltration and serial ultracentrifugation steps to obtain small-sized vesicles, using the term “exosomes” for the obtained samples. The combination of these techniques allow the isolation of an enriched-exosomes fraction containing exosomes specific markers and lacking the expression of other contaminating markers that will be specified below; but the obtained sample will also include other small vesicles with a diameter inferior to 220 nm[289]. This population will be referred to as SEV in this work. More detailed discussion of MV and exosomes biogenesis, composition, release and uptake mechanisms will be explained in the next sections.

1.6.1.1. Synthesis and release mechanisms

MV are described as vesicles released to the extracellular space directly by outward budding from the plasma membrane; while exosomes are originated from intraluminal vesicles (ILV) within MVB as part of the endocytic pathway and are released from cells when MVB are fused to the plasma membrane[290-292]. First, early endosomes are formed by plasma membrane invaginations by endocytosis. After that, ILV are formed from early-endosome vesicles membrane micro invaginations, forming MVB. These MBV can be fused to lysosomes for degradation of their content or follow the secretory itinerary and fuse with the plasma membrane to release exosomes into extracellular space (**Figure 1.16**).

ILV generation pathway can be regulated by the endosomal sorting complexes required from transport (ESCRT)-dependent or independent pathways[281] (**Figure 1.16**). ESCRT machinery consists of four ESCRT complexes (ESCRT-0, -I, -II and -III) and accessory proteins (e.g., Alix and VSP4), and it is responsible of sorting intracellular cargos that are destined or not for lysosomal degradation[293-295]. Two ESCRT-independent mechanisms of exosomes formation and release have been described: the first one depends on sphingomyelinase, an enzyme which produces ceramide[296]; while the second involves tetraspanins[297]. Next, intracellular vesicle transport between different compartments, necessary for the approximation of MVB to the plasma membrane, is mainly controlled by the Rab family of small GTPases. Finally, intracellular membrane-fusion, where MVB membrane and plasma membrane are involved, is thought to be regulated by both soluble factors (e.g. N-ethylmaleimide-sensitive factor [NSF] and soluble NSF-attachment protein [SNAP]) and membrane complexes (such as SNAP-attachment protein receptor, SNARE), although the fully mechanism is not still understood[298].

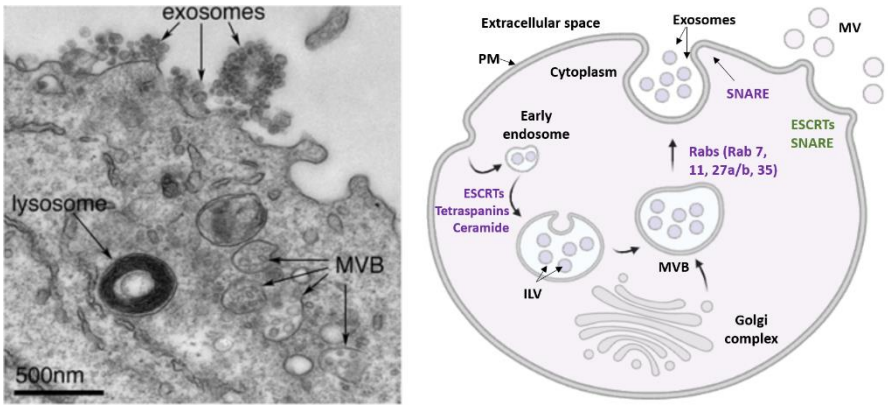

Figure 1.16. Exosomes and MV biogenesis. *Electron microscopy capture of exosomes releasing process from MVB can be observed in the left panel. Main proteins implicated in the exosomes and*

MV biogenesis and release are highlighted (in purple and green, respectively) in the right panel. PM: Plasma membrane; ILV: Intraluminal vesicles; MVB: Multivesicular body; MV: Microvesicles; ESCRT: Endosomal sorting complexes required from transport; Rab: Ras related proteins Rab; SNARE: SNP-attachment protein receptor. Illustration showed in left panel taken from Edgar J.R., 2016[299]. Image in the right panel created in Biorender.

The route of MV formation has not been completely described neither, but it is thought to require cytoskeleton components (e.g. microtubules and actin), molecular motors (kinesins and myosins) and fusion machinery molecules (SNARE and tethering factors)[300]. It is known that that an accumulation of specific molecules in certain regions of plasma membrane leads to a process of phospholipids redistribution driven by calcium-dependent enzymes, such as flippases and floppases, and at least ESCRT complexes I and III, which are responsible for plasma membrane deformation into buds and vesicles scission, respectively[301, 302].

1.6.1.2. Recognition and downstream signaling in target cells

Once exosomes and MV have been released into the extracellular space, they can interact with target cells and induce phenotypic changes on them. The preferred mechanism of SEV to induce changes in the physiological state might depend on their size and specific surface composition, as well as the recipient cell origin, although an SEV population could possibly trigger more than one SEV-cell interaction mechanism simultaneously. It has been described that SEV direct bonding to acceptor cells through ligand/receptor molecules on their respective surfaces is sometimes sufficient to activate signaling pathways and have an impact on cell function, without the need of releasing their luminal content[303, 304]. In other cases, the cargo of SEV must be transferred inside the recipient cells. Although there are still questions to answer, various mechanisms for SEV uptake, including direct membrane fusion[305] and endocytosis[306]. Indeed, a wide range of endocytic portals, such as clathrin-dependent[307, 308], caveolae-mediated[309] and lipid raft-mediated endocytosis[310], macropinocytosis[311] or phagocytosis[312, 313] have been described in specific cell types. A schematic illustration representing the mechanisms by which SEV interact with the receptor cells in shown in **Figure 1.17**.

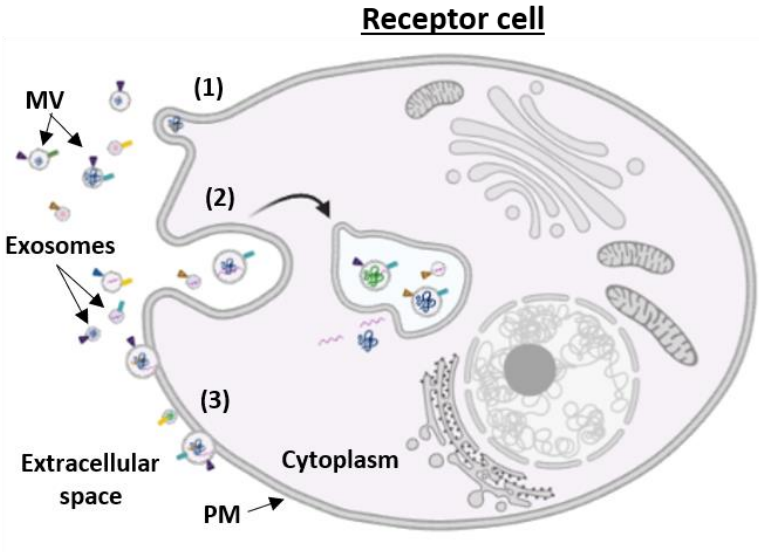

Figure 1.17. MV and exosomes interaction mechanisms with receptor cells. *MV and exosomes in the extracellular space can release their content and modify receptor cell behavior by (1) direct membrane fusion; (2) endocytosis (3) direct interaction with receptors in plasma membrane. Endocytosis can be clathrin-dependent, caveolae-mediated and lipid raft-mediated. Additionally, micropinocytosis and phagocytosis has also been demonstrated in specific types of cells. After endocytosis, vesicles can fuse with the endocytic membrane and release their content to the cell cytoplasm. MV: Microvesicle; PM: Plasma membrane. Illustration created with BioRender.*

There is a growing list in the literature of specific protein-protein interactions that mediate SEV attachment and uptake into recipient cells. Accumulated experimental evidence suggest that tetraspanins, which are membrane proteins involved in cell adhesion, motility and proliferation, are highly abundant on SEV surface and cell plasma membranes[314], and several studies have suggested their role in SEV-cell interaction[315-317]. Integrins and immunoglobulins, which participate in several functions (including cell-to-cell adhesion, cell signaling and leukocytes endothelial transmigration), have been also related to SEV uptake in additional scientific works[317, 318]. Other authors have suggested the role of proteoglycans, and specifically of heparin sulphate proteoglycans (HSPCGs), and lectins as mediators of vesicular entry in bladder cancer cells[319] and dendritic cells[320], respectively.

1.6.1.3. Cytosolic and membrane composition

Exosomes and MV present similarities on their lipid bilayer composition. Concretely, both exosomes and MV contain lipid rafts, are enriched in cholesterol

and expose phosphatidylserine (PS)[262, 291]. In addition to this, a lipidomic analysis revealed that membranes of both Exo-S and Exo-L subpopulations are enriched in ceramide, diglyceride, phosphatidylcholine, sphingomyelin and triglycerides, although total lipid level and composition among the different exosomes subpopulations showed cell-type dependent differences[279].

Exosomes biogenesis, specific cargo and release to the extracellular space responds to the cellular needs, but they present common components which are expected to be found regardless of the parent cell type because they are linked to their origin (e.g.: Alix, TSG101, HSC70 and HSP90β)[321, 322]. The presence of these proteins along with the absence of Calnexin, which is expressed in vesicles from ER and not in exosomes, are currently used to identify exosomes *in vitro*. Proteins of the tetraspanin family, such as CD9, CD63 and CD81, are also commonly found in exosomes membrane, although they have been also identified in MV[323]. In addition to this, exosomes tend to be enriched in glycoproteins; while MV are thought to contain higher levels of proteins carrying posttranslational modifications, such as phosphorylation and glycosylation[314, 324]. MV origin by outward budding of plasma membrane also influences their content, which includes cytosolic and plasma membrane-associated proteins such as cytoskeletal proteins, integrins, heat shock proteins and the previously mentioned tetraspanins. Additionally, they contain mRNAs, miRNAs and lipids[291]. A wide range of proteins with different functions, including membrane transport, fusion, adhesion or targeting have been found in exosomes; while their cargo is composed by other proteins (e.g., cytoskeletal and heat shock proteins), mRNA, noncoding RNAs (such as miRNA or tRNAs) and lipids (**Figure 1.15**)[279, 325]. The content of DNA in exosomes remains controversial, since it has not been clarified whether DNA is contained in exosomes or in other type of EV[287].

Although markers to distinguish between both exosomes and MV are still lacking[287], a wide range of specific additional molecules can be found in EV, which can also change regarding to the physiological state and the origin of the parent cell. In consequence, the biological response triggered in the target cell will be determined by the specific EV cargo[281, 326, 327].

1.6.2. Soluble factors: Oncostatin-M

Cells can also communicate with each other by secreting soluble factors, such as cytokines, growth factors and metabolites, to the extracellular space and act in a paracrine, autocrine or endocrine manner. These signals can interact with the target cell directly by crossing the hydrophobic phospholipidic membrane or binding to a receptor on the target cell surface[328].

One of the biggest families of secreted factors is cytokines, which include other groups of proteins like lymphokines, monokines, chemokines and IL. The term cytokine (from Greek -*cyto* = cell and -*kinos* = movement) was proposed by Stanley Cohen in 1974[329]. Although the definition is still under evolution, growing scientific evidence have shown that cytokines include peptides, proteins and glycoproteins that are secreted by immune cells (e.g. lymphocytes, neutrophils, monocytes or macrophages) and a few types of non-immune cells (e.g. epithelial cells, fibroblasts or EC) and function by strongly binding to specific receptors on target cells and activating a downstream signaling cascade that culminate in the expression of a set of genes necessary for specialized responses[330]. Cytokines play overlapping and pleiotropic roles controlling hematopoiesis, growth, differentiation, angiogenesis, tissue remodeling, would healing and cell or death survival as well as the effector functions in tissues and immune cells having both anti- and pro-inflammatory effects[331-333].

In this context, recent scientific evidences showing a possible beneficial role of OSM, a cytokine classified in the group of the IL 6-type cytokine family[334], counteracting fibrosis aroused our interest in the study of OSM as a possible therapeutic agent in cardiac repair[335-338]. Further details regarding to OSM synthesis, structure and function with a focus on the cardiovascular system will be provided in the next subsections.

1.6.2.1. OSM Synthesis

OSM was first reported and purified from U937 monocytic cells conditioned media after phorbol 12-myristate 13-acetate (PMA) treatment by Zarling J.M. et al., in 1986[339]. Nowadays, it is known that OSM is a protein secreted mainly from hematopoietic sources, including activated T lymphocytes, macrophages, monocytes, neutrophils, eosinophils and mast cells[339, 340]. Although the mechanisms that regulate OSM expression are not completely described, various research works have reported a role of the signal transducer and activator of transcription 5 (STAT5) on OSM induction. Particularly, it has been described that STAT5-dependent OSM expression can be induced by other cytokines, such as erythropoietin, granulocyte colony-stimulating factor (G-CSF), IL-2 and IL-3[341, 342]. Additional cytokines, such as IL-15 and granulocyte-macrophage colony-stimulating factor (GM-CSF) or PMA can also stimulate OSM production in neutrophils with a role of STAT5 not confirmed[343-345]. IL-12 has been pointed as an additional agent which plays a role in OSM production, which could be positively regulated by STAT4 and negatively regulated by STAT6 in $CD4^+$ T cells[346]. Finally, expression of OSM in monocyte-derived macrophages after thrombin or complement component C5a

stimulation can be regulated via activation of activator protein (AP)-1 transcription factor family[347, 348].

1.6.2.2. Structure and ligand-receptor interaction

At a structural level, human OSM is initially formed by 252 amino acids and divided in three parts: signal peptide, chain and propeptide. Signal peptide and propeptide are excised by proteolytic cleavage inside the cells in order to secrete mature OSM into the extracellular space, which has a four-helix bundle structure joined by loops, two disulfide bonds and two sites of glycosylation[340]. Once released, OSM can interact with two specific heterodimers present in the surface of the target cells, named Type I and Type II receptors. Type I receptor complex is formed by leukemia inhibitory factor receptor (LIF-R) and glycoprotein 130 (gp130 or IL-31RA); while Type II receptor complex consists on the Oncostatin-M receptor (IL-31RB) and IL-31RA. Scientific evidences have shown that Type I receptor can interact with different proteins of the IL-6-type cytokine family, whereas Type II heterodimer is specific for OSM[349-351].

Interaction of OSM and IL-31RA is mainly carried out by the glycine in the position 120, along with two glutamines and one asparagine (Gly120, Gln16, Gln20 and Asn124, respectively), which form a dimple located on helices A and C of OSM. LIF-R and IL-31RB binding site consists of two critical residues (Phenylalanine [Phe, F] 160 and Lysine [Lys, K] 163) in a conserved *FXXK* motif, located at the beginning of D-helix and the loop between helix A and B. Recent experimental data showed that additional residues in OSM (tyrosine [Tyr]-34, Gln-38, Gly-39 and leucine [Leu]-45 in the AB loop and proline [Pro]-153 in the D-helix) and punctual amino acid sequence changes between OSM and the rest of IL-6 cytokine family proteins which binds LIF-R and IL-31A might be key for specific IL-31RB activation by OSM[351, 352].

1.6.2.3. Downstream signaling in target cells

The binding of OSM to either Type I or Type II receptor induces the activation of Janus Kinase (JAK) family members (JAK1-2 and TYK2) through tyrosine phosphorylation, which induce the activation and nuclear translocation of STAT proteins (STAT1, 3, 5A and B). In deep, Type I complex activates STAT1 and 3, whereas Type II complex stimulates STAT1, 3 and 5[353, 354]. Alternatively, the activated receptors can also trigger mitogen-activated protein kinases (MAPK, including ERK, p38 and JNK), phosphoinositide 3-kinase/protein kinase B (PI3K)/RAC-α serine/AKT and the protein kinase C delta (PKCδ) pathways. However, the signaling pathways activated by OSM are not completely described[355, 356]. A schematic representation of OSM signaling is showed in **Figure 1.18**.

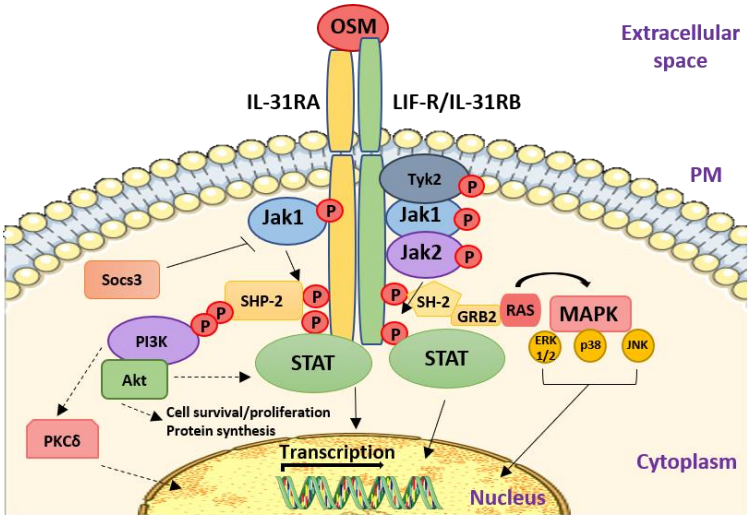

Figure 1.18. OSM signaling pathway. *OSM induces signal transduction via the IL-31-RA-LIF-R or IL-31RA-IL-31-RB receptor complexes. This engagement triggers the activation of Jak1, Jak2 and Tyk2, which phosphorylate tyrosine residues in the cytoplasmic domains of the receptors. Phosphorylated residues recruit STAT proteins and regulate their nuclear translocation. In addition, OSM triggers the activation of and RAS-MAPK, PI3K and PKCδ pathways, although the fully mechanisms of activation is not fully understood (dashed arrows). OSM: Oncostatin-M; IL-31RA: Interleukin-31 receptor subunit alpha; LIF-R: Leukemia inhibitor factor receptor subunitbeta; IL-31RB: Oncostatin-M-specific receptor subunit beta or interleukin-31 receptor subunit beta; Jak: Janus kinase; Tyk2: Non-receptor tyrosine-protein kinase TYK2; SHP-2: Tyrosine-protein phosphatase non-receptor type 11; PI3K: Phosphoinositide 3-kinase/protein kinase B; Akt: RAC-alpha serine/threonine-protein kinase; PKCδ: Protein kinase C delta; STAT: Signal transducer and activator of transcription; SH-2: SH2B adapter protein 1; GRB2: Growth factor receptor-bound protein 2; RAS: GTPase Ras protein; MAPK: Mitogen-activated protein kinase; ERK: Extracellular signal-regulated kinase; p38: Mitogen-activated protein kinase 38; JNK: C-Jun-amino-terminal kinase-interacting protein; PM: Plasma membrane. Illustration created with Medical Art. Data source: Richards C., 2013[357] and West N.R. et al., 2018[358].*

The biological activities of OSM vary in different species and depend on ligand concentration and the specific cell type, but also on its physiological state and microenvironment[359]. Notably, OSM has been related to both pro- and anti-inflammatory properties. Pleiotropic responses to OSM include production of inflammatory chemokines and cytokines, expression of leukocytes adhesion factors, expression of ECM components and remodeling factors together with alterations in cell proliferation and differentiation. Under appropriately regulation, such previous mentioned responses contribute to homeostasis and tissue repair following injury. In contrast, dysregulated OSM expression can promote sustained inflammation and organ disfunction[358, 360].

Attending to the cardiovascular system, OSM has been related to proliferation, chemotaxis and tube formation in cultures of human microvascular endothelial cells[361-363]. Furthermore, OSM could also indirectly regulate angiogenesis by modifying the expression of VEGF[364, 365], fibroblast growth factor (FGF)-2[362, 366], angiopoietin-2[97] and urokinase-type plasminogen activator (uPA)[367]. According to this, OSM promoted revascularization and tissue regeneration in a mouse model of acute muscle injury[368]. Inflammatory responses evolution can be also modulated by OSM gene activation in EC, including adhesion factors and cytokines (e.g. ICAM1, VCAM1, IL-6, CCL2, P-Selectin and E-Selectin) and chemokines (e.g. CXCL1, 2 and 5), which induce neutrophil rolling and adhesion[369, 370].

CXCL1, 2 and 5 chemokines expression in response to OSM treatment have also been described in cardiac fibroblasts and myocytes, reinforcing the hypothesis of OSM as an inflammation modulator following cardiac tissue injury[371, 372]. Importantly, recent results published by Abe H. et al. and Huguier V. et al., demonstrated a role of OSM counteracting the inductive effects of TGFβ1 on fibrosis[337, 338]. In addition to this, it has been described a role of OSM promoting CM dedifferentiation and tissue remodeling after cardiac injury[335, 373]. Nonetheless, growing evidence have pointed that these effects are consequence of punctual OSM stimulation, but sustained OSM production can also have detrimental effects in the heart, leading to HF and dilative cardiomyopathy[335, 358, 373].

2. Hypothesis and objectives

2. Hypothesis and objectives

Therapies proposed to fight against AMI have not shown major improvements on patients' outcome. Consequently, new therapeutic strategies that can prevent I/R-induced injury during and after AMI are still needed.

Here, two cell-free based strategies have been proposed in order to pre-conditionate ischemic area and reduce reperfusion-induced injury. First, we focused on the metabolic switch in cardiomyocytes during ischemia. Under those stressing conditions, where oxygen and nutrients are not enough to maintain normal cardiac function, it was thought that local administration of a fatty acid (diDHA) bound to PGA could help cardiomyocytes metabolism and avoid a massive cardiomyocytes death before reperfusion. Second, previous studies have described a pro-angiogenic potential and anti-apoptotic role on cardiomyocytes of small extracellular vesicles (SEV) secreted by mesenchymal stromal cells (MSC) in AMI context. Moreover, SEV are stable *in vivo* and they can regulate biological processes by transferring bioactive molecules to target cells. Consequently, they have emerged as a novel cell-free carrier for therapeutic purposes. In this sense, it was proposed the specific loading of a protein with anti-fibrotic potential (OSM) on MSC-SEV surface, and evaluate its ability to counteract fibroblasts activation in the context of AMI, enhancing the native therapeutic potential of native MSC-SEV. Based on these ideas, the following objectives were proposed:

- Evaluate the cardioprotective potential of nanoconjugates based on PGA covalent union to diDHA in *in vitro* and *in vivo* ischemia-reperfusion models.

- Test the feasibility of OSM loading in SEV-MSC through its fusion to membrane proteins naturally present on SEV.

- Assess the functional role of OSM loaded on MSC-SEV surface on *in vitro* models of cardiac fibroblasts proliferation and activation.

3. Methodology

3. Methodology

3.1. Cellular models

3.1.1. Prokaryote cell types

Douglas Hanahan 5 α^{TM} (DH5α) Competent Cells (ThermoFisher Scientific) have been used in this work. They are a non-pathogenic versatile bacteria strain and excellent hosts for routine cloning applications and lentiviral transformation. Additionally, they are endonuclease deficient, which improves the quality of plasmid DNA prepared form minipreps, and recombinant deficient, increasing insert stability. This bacteria strain includes an ampicillin antibiotic resistant gene for colony selection. Genotype: F^{-} *Φ80lac*ZΔM15 Δ(*lac*ZYA-*arg*F) U169 *rec*A1 *end*A1 *hsd*R17(rk^{-}, mk^{+}) *pho*A *sup*E44 *thi*-1 *gyr*A96 *rel*A1 λ^{-}.

3.1.2. Eukaryotic primary cultures and cell lines

The following cell types were used during this work: human cardiac microvascular endothelial cells (HMVEC-C), normal human ventricular cardiac fibroblasts (NHCF-V), primary cultures of ventricular myocytes (NRVM) and cardiac fibroblasts (cFib), both from neonatal rats, embryonic kidney cells 293 type T with human origin (HEK 293T), human embryonic kidney Expi293 type F (Expi293F) cells, primary cultures of native and genetically modified Mesenchymal Stromal Cells (MSC) and human induced pluripotent stem cells (iPSC). All cellular types but Expi293F^{TM} were cultured in a Forma Series II Incubator Model 3141 (Thermo Fisher Scientific) at 37 °C and 5 % of CO_2. Expi293^{TM} cells were maintained in suspension culture and constant orbital shaking. A Ruskinn INVIVO$_2$ 400 Workstation chamber (Ruskinn Technology) was used to culture cells in hypoxia (1% O_2).

3.1.2.1. Primary culture of human cardiac microvascular endothelial cells

HMVEC-C were obtained from Lonza and cultured with EGM^{TM}-2 MV (Microvascular Endothelial Cell Growth Medium-2 BulletKit^{TM}, Lonza), following manufacturer's instructions.

3.1.2.2. Primary culture of human ventricular cardiac fibroblasts

NHCF-V were obtained from Lonza or PromoCell and cultured with FGM™-3 Cardiac Fibroblasts Growth Medium-3 BulletKit™ (Lonza or PromoCell), following manufacturer´s instructions.

3.1.2.3. Primary culture of neonatal rat ventricular myocytes and cardiac fibroblasts

NRVM were obtained following the Worthington Neonatal Cardiomyocyte Isolation System (Worthington Biochemical Corporation)[374]. One- or two-days Wistar neonatal rats' hearts were removed, washed twice with cold calcium and magnesium free Hank's Balanced Salt Solution (HBSS, Gibco) and cut in small pieces (0.5-1 mm^3). Thereafter, hearts were incubated with 0.05% trypsin at 4 °C overnight. Next day, enzymatic digestion with 2% collagenase II and 10 mg/mL DNase I was performed at 37 °C for 40 min, passed by a 40 µm filter and centrifuged at 100 g for 5 min. Cell suspension was pre-plated and incubated for 30 min in high glucose Dulbecco's Modified Eagle's Medium (DMEM) supplied with 10% heat inactivated fetal bovine serum (FBS), 1% pyruvate solution, 1% L-glutamine and 1% penicillin/streptomycin (P/S) (all from Gibco) to allow the attachment of fibroblasts to the plate. Enriched cardiomyocyte cell suspension was recovered, centrifuged at 100 g during 5 min and plated in 0.02% Gelatin-1% Fibronectin coated plates at a density of 200.000 cell/cm^2. NRVM do not allow additional passages, so obtained cells were directly seeded in plates for each experiment. Cardiac fibroblasts remaining in the culture dishes were cultured high glucose DMEM supplied with 10% of heat inactivated FBS and 1% of P/S (all from Gibco) and used for experiments between passage 1 to 4.

3.1.2.4. Embryonic human kidney cells 293 type T

HEK 293T was obtained from ATCC. This cell line is competent to replicate vectors carrying the SV40 region of replication. HEK 293T gives high yields when used to produce retroviruses. HEK 293T were cultured in high glucose DMEM supplied with 10% of heat inactivated FBS and 1% of P/S, all from Gibco.

3.1.2.5. Embryonic human kidney cells Expi293 type F

Expi293F cells were obtained from Thermo Fisher Scientific. These cells were maintained in suspension and continuous orbital shaking at 150 rpm in a humidified

CO_2 cell culture incubator using Expi293 Expression Medium (Gibco). Expi93F cells have a high transfection rate and generate superior protein yields compared to standard HEK 293T cell lines in transient protein expression.

3.1.2.6. Dental pulp Mesenchymal Stromal Cells

Dental pulp MSC in passage 1/2 were obtained from the Spanish National Cell line Bank (BNLC) through Inbiobank Foundation (San Sebastián, Spain), where cells were processed according to the specific requirements on ISO90001:2000 quality system under Good Manufacturing Practices (GMP) conditions. The same biopsy of MSC was immortalized and characterized in our laboratory through telomerase reverse transcriptase lentiviral transduction (iMSC). MSC and iMSC were cultured in low glucose DMEM supplied with 10% of heat inactivated FBS and 1% P/S, all from Gibco. Genetically modified MSC contain a Tet-On inducible vector system whose expression depends on the presence of doxycycline. Consequently, lentiviral transduced MSC were seeded in the same conditions but standard FBS was replaced for heat inactivated tetracycline-free FBS (BioWest) to allow the expression of the desired gene only when doxycycline is added to cell culture medium.

3.1.2.7. Human induced pluripotent stem cells

Foreskin fibroblasts from a Caucasian male were obtained from Coriell Institute for Medical Research, and human induced pluripotent stem cell line (iPSC-Ctrl[clonF5]) was generated and characterized by Dra. Ana María Cervera Zamora and Dr. Kenneth James McCreath in Cardiovascular Research National Centre (CNIC). iPSC were cultured in mTeSR™1 culture medium (Stem Cell Technologies). iPSC need special care for maintaining cells in an undifferentiated state. Consequently, culture medium was daily changed, and colonies were picked up when necessary to remove any cell starting to differentiate. iPSC were cultured on Matrigel® (Corning® Matrigel® hESC-qualified Matrix) coated surfaces, which contains extracellular matrix components as laminin, collagen IV, entactin, and heparan sulphate proteoglycan, among other undefined components. Matrigel® was diluted following manufacturer´s instructions and coated plates were prepared and maintained at RT 3 h before cell seeding.

3.2. Cell culture

3.2.1. Cells thawing

Cells were stored in cryovials placed in liquid nitrogen tanks at -195.8 ˚C. In order to achieve a proper cell conservation, cryovials were placed in a 37 ˚C pre-warmed thermostatic water bath directly from liquid nitrogen. Once thawed, cryovial content was placed in a 15 mL tube containing 10 mL of the correspondent cell culture medium. Cells were centrifuged at 300 g for 5 min, resuspended in culture medium and seeded in the proper dish. HMVEC-C were seeded directly skipping the centrifugation step according to manufacturer´s instruction. Next day, cell culture medium was changed.

3.2.2. Cell expansion

HMVEC-C, NHCF-V, cFib, MSC and HEK 293T were expanded until reaching 80% of confluency and cellular passages were performed. Cells were washed with balanced salt solution without calcium and magnesium (Phosphate Buffer Saline, PBS) and treated with Trypsin/EDTA 0.25% (Gibco) to detach them from plate surface, centrifuged at 300 g for 5 min, resuspended in the proper cell culture medium and counted. Next, cells were seeded in the correspondent culture flask at the desired density. Expi293F™ were subcultured 3 times each week at a density of one million of cell per milliliter in Erlenmeyer culture flasks.

iPSC were also expanded until reaching 80% of confluency before cellular passage. Next, cells were washed twice with PBS and incubated with 0.5 mM EDTA (UltraPure™ 0.5 M EDTA, pH 8.0, Thermo Fisher Scientific diluted in PBS) at 37 ˚C for 3 min or until a distinction of cell-forming inside colonies could be seen. Next, EDTA was removed, cells were detached from dish surface by pipetting carefully to avoid cell individualization, transferred to a 15 mL tube containing 2 mL of fresh culture medium and centrifuged at 300 g for 5 min. Finally, cells were carefully resuspended and seeded in previously Matrigel-coated dishes at the desired density.

3.2.3. Cell cryopreservation

Cells were submitted to a similar protocol for cryopreservation. After cells detaching and centrifugation, they were resuspended in FBS, FBS TTC free or Knockout Serum (Gibco) in case of iPSC, counted and diluted to a density of 1 million

of cells per 900 µL of the appropriated FBS. After that, cell suspension was divided between the different cryotubes and 10% of dimethyl sulfoxide (DMSO) was added to favor cell cryopreservation. Cryotubes were stored on a recipient with isopropanol, which allows a gradual temperature decrease (1 °C/h) at -80 °C freezer. After 24 hours, cryotubes were transferred to a liquid nitrogen tank.

3.2.4. Cell viability counting

HMVEC-C, NHCF-V, cFib, MSC and HEK 293T viability of obtained cell suspensions after trypsin/EDTA digestion and subsequent centrifugation was analysed mixing 10 µL of cell suspension with 10 µL of 0.2% trypan blue diluted in PBS. Expi293F™ do not require enzymatic digestion, so viability was directly measured after centrifugation. Trypan blue is a reagent able to stain dead or damaged cells while healthy cells can actively expel it. In order to count the number of viable cells, a Neubauer chamber was used. This chamber has an area of $0.01 cm^2$ and is 0.01 cm depth (Volume = 0.1 mm^3 or 10^{-4} mL). Consequently, 10 µL of the obtained suspension were placed in the Neubauer chamber and viable cells (not stained) were counted. The following mathematical formula to obtain the concentration of viable cells in each sample was used: Concentration (Nº of viable cells/mL) = Nº of viable cells x 10.000 / Number of counted squares x Dilution factor.

In order to obtain single cell suspensions of iPSC and count the number of viable cells to start a differentiation protocol, 10 µm ROCK pathway inhibitor (Y-27632, Stem Cell Technologies) was added 1 h before cell disaggregation to increase cell viability and favour undifferentiated state. After that time, iPSC were washed twice with PBS and incubated with Accutase (Innovative Cell Technologies Inc.) at 37 ˚C for 7 min to obtain individualized cells. After centrifugation, the same counting protocol applied to the rest of cell types was followed.

3.2.5. Cardiomyocytes differentiation from iPSC

In vitro differentiation of iPSC to cardiomyocytes mimics the sequential stages of embryonic cardiac development. Three families of protein growth factors are thought to control mesoderm formation and cardiogenesis: bone morphogenetic proteins (BMPs), Wingless/INT proteins (WNTs) and the fibroblasts growth factors[156]. iPSC-CM differentiation protocol relies on the use of small molecules to inhibit or stimulate Wnt signalling pathway and drive cardiac progenitor cell formation.

iPSC were individualized as described in the previous section and seeded in 12 multi well plates at a density of 263.158 cells/cm^2 in mTeSR™1 culture medium containing 5 µM ROCK pathway inhibitor. Seeding day was considered Day -3 of differentiation. Culture medium was replaced with fresh mTeSR™1 culture medium on differentiation days -2 and -1. On day 0, cell culture medium was replaced for mTeSR™1 and CHIR99021, which is an inhibitor of GSK3α and GSK3β and activates Wnt signalling pathway, was prepared at 8 µm (StemCell Technologies) in differentiation culture medium 1 (DM1: 95.4 % RPMI 1640 culture medium, 1% 100X GlutaMAX, 1% mL 100X non-essential amino acids, 0.5% P/S, 0.1 % β-Mercaptoethanol and 2% 50X B27 without insulin supplement). CHIR99021 was maintained for 24 h and was replaced for fresh DM1 (day1). On day 3, IWP-4, which is a Wnt signalling pathway inhibitor, was prepared at 5 µM in DM1 and added to the cells for 48 h. After that time, fresh DM1 was added (day 5). Differentiation medium 2 (DM2: 95.4 % RPMI 1640 culture medium, 1% 100X GlutaMAX, 1% mL 100X non-essential amino acids, 0.5% P/S, 0.1 % β-Mercaptoethanol and 2% 50X B27 with insulin supplement) was prepared at day 7 of differentiation, added to the cells and replaced every 48 h. Cell cultures were monitored routinely until the cells began to beat.

Since adult cardiomyocytes proliferative rate is extremely low, cardiomyocytes derived from iPSC (iPSC-CM) obtained from each differentiation process were directly used for the desired experiments. For this purpose, cells were washed with PBS twice and incubated with Trypsin/EDTA 0.25% at 37 ˚C for 7 min. Cells were detached from dishes by pipetting, transferred to a tube containing DM2 and centrifuged at 300 g for 5 min. Next, cells were counted and seeded in Matrigel pre-coated plates in DM2 containing 20% FBS and 5 µM ROCK pathway inhibitor at the required concentration. Next day, medium was replaced for DM2 and refreshed every 48 h until day of differentiation 30.

All components in DM1 and DM2 were obtained from Gibco. CHIR99021 and IWP4 were reconstituted following manufacturer's instructions and stored in small-volume aliquots at -20 ˚C.

3.3. Molecular genetics techniques

During this work, lentiviral vectors and other vectors for protein production in mammalian cells were used to genetically modify target cells. Conventional genetic engineering techniques have been used to edit and introduce genetic material stably into eukaryotic cells.

Expi293F™ were used for transient protein expression and initial fusion protein stability screening using pEBNAZ mammalian cells expression vector backbone, and MSCs were transfected with lentiviral vectors for stable cell generation. MSC and Expi293F cells were genetically modified to express fusion proteins composed by different OSM isoforms bound to three SEV anchoring proteins: lactadherin, CD81 or TSPAN14, and control vectors to express only SEV anchoring proteins were included. Plasmids used for this project are summarized in **Table 3.1**:

Table 3.1. *List of plasmids used during the project.*

Plasmid name	Fusion protein name	OSM isoform	AP*	AP isoform**	Plasmid backbone	Source
Tet-On® 3G in and GFP in XSTP_Oncostatin	OSM-XSTP	Native OSM	Lactadherin	Lactadherin c1 TD-c2 FD	Lentiviral	SBI and Gene Universal
Tet-On® 3G in and GFP in XSTP_Oncostatin without Oncostatin	XSTP	-	Lactadherin	Lactadherin c1 TD-c2 FD	Lentiviral	SBI and Gene Universal
Tet-On® 3G in and GFP in CD81_MatureOncostatin	MatureOSM-CD81	Mature OSM	CD81	Native	Lentiviral	AZ-IIS La Fe
Tet-On® 3G in and GFP in CD81_MutantOncostatin	MutantOSM-CD81	Mutant OSM	CD81	Native	Lentiviral	AZ-IIS La Fe
Tet-On® 3G in and GFP in CD81_without Oncostatin	CD81	-	CD81	Native	Lentiviral	AZ-IIS La Fe
MatureOncostatin_Lactadherin in pEBNAZ	MatureOSM-Lactadherin	Mature OSM	Lactadherin	c1-c2 domains	pEBNAZ	AZ-IIS La Fe
MutantOncostatin_Lactadherin in pEBNAZ	MutantOSM-Lactadherin	Mutant OSM	Lactadherin	c1-c2 domains	pEBNAZ	AZ-IIS La Fe
Lactadherin in pEBNAZ	Lactadherin	-	Lactadherin	c1-c2 domains	pEBNAZ	AZ-IIS La Fe
MatureOncostatin_CD81 in pEBNAZ	MatureOSM-CD81	Mature OSM	CD81	Native	pEBNAZ	AZ-IIS La Fe
MutantOncostatin_CD81 in pEBNAZ	MutantOSM-CD81	Mutant OSM	CD81	Native	pEBNAZ	AZ-IIS La Fe

CD81 in pEBNAZ	CD81	-	CD81	Native	pEBNAZ	AZ-IIS La Fe
MatureOncostatin_TSPAN14 in pEBNAZ	MatureOSM-TSPAN14	Mature OSM	TSPAN14	Native	pEBNAZ	AZ-IIS La Fe
Mutant Oncostatin_TSPAN14 in pEBNAZ	MutantOSM-TSPAN14	Mutant OSM	TSPAN14	Native	pEBNAZ	AZ-IIS La Fe
TSPAN14 in pEBNAZ	TSPAN14	-	TSPAN14	Native	pEBNAZ	AZ-IIS La Fe

*AP: Anchoring protein; **FD: Full domain; TD: Truncated domain

Lactadherin c2 domain binds specifically to phosphatidylserine in SEV membrane, while CD81 and TSPAN14 are transmembrane proteins also present on SEV surface. In consequence, OSM is expected to specifically be loaded in SEV isolated from parental cells. On the one hand, expression of fusion proteins in lentiviral vectors was controlled by the addition of a TetOn inducible system, where addition of doxycycline to culture media is necessary to induce the expression of the vector encoded fusion protein. Green Fluorescent Protein (GFP) was also included for tracking and selection purposes and its expression was controlled by a constitutive promoter (EF1). On the other hand, pEBNAZ vectors backbone sequence consisted on a human cytomegalovirus (CMV) promoter. An example of both types of vectors are showed in **Figures 3.1** and **3.2**.

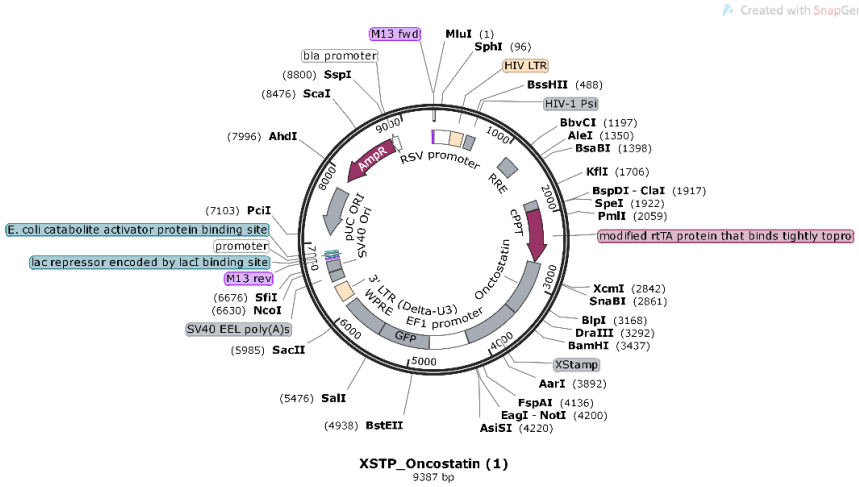

Figure 3.1. *TeT-On® 3G in and GFP in XSTP_Oncostatin lentiviral vector outline.*

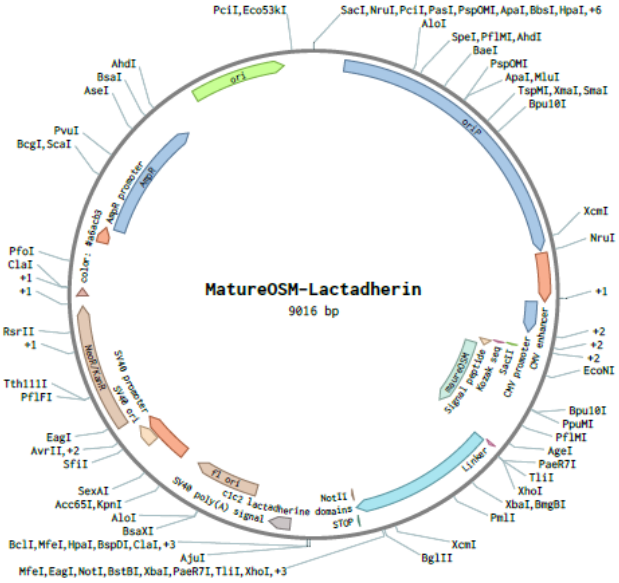

Figure 3.2. *MatureOSM-Lactadherin in pEBNAZ vector scheme.*

3.3.1. Bacterial transformation and amplification

Once plasmids were received, they were transformed and amplified in DH5α^{TM} bacteria. Firstly, 100 µL of bacteria were mixed with 200 ng of the correspondent plasmid dissolved in MiliQ H_2O and the resultant solution was incubated for 20 min on ice. Next, bacteria were transformed by heat shock technique using a water batch pre-warmed at 42 °C for 45 seconds and were put back on ice for 2 min. After that, 1mL of 42 ˚C pre-warned lysogeny broth medium (LB: 10 g NaCl, 10 g tryptone and 5 g yeast extract in 1L of water and pH adjusted to 7.4 with NaOH) was added and samples were incubated at 180 revolutions per minute (RPM) in an orbital shaker at 37 °C for 1h. Next, samples centrifuged at 400 g for 1 min and pellet was resuspended in 50-100 µL of LB. The resulting mixture was added to Petri dishes previously covered by LB-agar LB agar (5 g of bacteriological agar per 1L of LB) with ampicillin (100 µg/mL) was used for bacterial clone selection. This method allows only the growth of bacteria which have incorporated the plasmids and therefore are ampicillin resistant. Plates were placed in a bacteriological incubator at 37 °C overnight. Resulting plates with growth colonies were stored at 4 °C until their use. Reagents used in this section were purchased from Sigma Aldrich.

3.3.2. Isolation and purification of plasmid DNA from bacteria

Colonies obtained in **Section 3.3.1** were individually picked and inoculated in tubes containing 3 mL of LB with ampicillin. Samples were incubated in an orbital shaker at 180 RPM at 37 °C until the optimal optical density was obtained. Once the pre-inoculum was growth, DNA isolation was performed using the Plasmid MiniPrep kit (GE Healthcare) following manufacturer's instructions.

To obtain greater amounts of DNA, 2 mL of transformed bacteria were transferred to flasks with 200 mL of LB containing the antibiotic for selection and were incubated in an orbital shaker at 180 RPM at 37 °C overnight. Next day, plasmid DNA isolation was carried out with the Plasmid Maxi Prep Kit (Jetstar) following manufacturer's instructions. Resultant DNA was quantified by spectrophotometry (NanoDrop 1000, Thermo Fisher Scientific) and quality of samples was corroborated according to the absorbance standard ratios 260/280 (ratio above 1.8 indicates insignificant RNA contamination) and 230/260 (ratio between 2.0-2.2 indicates low contamination of sample by proteins or different molecules). DNA obtained was diluted to a stock concentration of 1 µg/mL and was stored at a -20 °C freezer.

3.3.3. Enzymatic digestion

Enzymatic digestions of two lentiviral vectors were performed to test if plasmids had the expected length and digestion pattern. With this purpose, HindIII restriction enzyme was used. Number and length of expected fragments for each plasmid are detailed in **Table 3.2**:

Table 3.2. *Expected fragments' number and length after plasmid digestion with HindIII.*

Plasmid	Expected fragment number	Expected fragment length (base pairs)
Tet-On® 3G in and GFP in XSTP_Oncostatin without Oncostatin	5	553; 583; 2252; 1819; 3424
Tet-On® 3G in and GFP in XSTP_Oncostatin	5	553; 583; 3008; 1819; 3424

Plasmid digestion was carried out by mixing 10 µL of each plasmid with 10 units of HindIII (1 µL of stock) in a final volume of 25 µL containing 2.5 µL of NEBuffer (New

England Biolabs Inc, UK) and 11.5 µL H_2O_2 for each sample. Resulting samples were incubated at 37 °C for 1h.

The digestion patterns obtained were analyzed using agarose gel electrophoresis technique. With this purpose, 1X trys-acetate EDTA (TAE) buffer was previously prepared, which is composed by 40 mM trys-acetate 1% agarose gel and 1 mM EDTA (all from Sigma Aldrich) in MiliQ H_20 and pH was adjusted to 8.3. Gel with 1% of agarose in 1X TAE was prepared and electrophoresis at 100 V was run. In order to see the bands obtained, gel was incubated with GelRed (Biotium) at 60 RPM in an orbital shaker for 40 min. Gels were revealed with Bio-Rad Gel Doc XR system.

3.3.4. Lentiviral transduction and engineered MSC lines generation

Five different lentiviral transductions were carried out in MSC using the vectors described in **Section 3.3**. Consequently, five genetically modified two of them from a primary MSC cell line (MSC-XSTP, MSC-OSM-XSTP) and three from the same cell line, but previously immortalized (iMSC-CD81, iMSC-MatureOSM-CD81 and iMSC-MutantOSM-CD81) were generated. With this purpose, HEK 293T cells were used as a packaging cell line in order to produce lentiviral particles, which would be used as a vehicle to introduce the desired genetic material in MSCs. HEK 293T cells were transfected with the plasmids psPAX2 and pVSV (Addgene), necessary to produce the entire virus and package the genetic construct in the resulting lentiviral particle. Detailed process is explained here:

- Day 1: HEK 293T seeding. HEK 293T were seeded in 55 cm^2 plates at a density of 6 x 10^6 cells per culture dish.
- Day 2: Plasmid transfection. One hour before transfection, HEK 293T cell culture medium was changed by high glucose DMEM with 1% P/S and chloroquine (Sigma Aldrich) at a final concentration of 25 µm. After that, the following solutions were prepared:
    - Solution A (µL/55 cm^2 dish): 5 µL of desired plasmid, 3 µL psPAX2 plasmid, 1.5 µL VSV2 plasmid, 62 µL 2M $CaCl_2$ and 428.5 µL 0.2 µm filtered MiliQ H_2O_2. All plasmids' stocks were prepared at 1 µg/µL.
    - Solution B (µL/55 cm^2 dish): 500 µL HBS 2X buffer (280 mM NaCl, 50 mM HEPES buffer and 1.42 mM Na_2HPO_4, all from Sigma Aldrich). HBS 2X pH was adjusted to 7.05 and 0.2 µm filtered.

Once Solution A and B are prepared, solution A is added to solution B in a drop-wise manner while Solution B is in continuous vortex shaking. After that, mixture is leaved still for 10-15 min and is added carefully to HEK 293T cells for 8 hours. After that time, cell culture medium is replaced by MSC culture medium (low glucose DMEM supplemented with 10% TTC-free FBS and 1% P/S) for 48h. During this time, packaging cell line produces the lentiviral particles with the genetic construct of interest inside.

- Day 3: MSC seeding. MSC were seeded in 55 cm^2 plates at a density of 3 x 10^5 cells per culture dish. For viral tittering, MSC were seeded in 24 well plates at a density of 100.000 cells/well.
- Day 4: Lentiviral particles collection and MSC infection. HEK 293T supernatant was collected, centrifuged at 300 g for 5 min to remove possible floating cells and 0.45 µm filtered to avoid cell debris contamination. Collected culture medium was used for both viral tittering and large-scale infection.

On the one hand, different dilutions of collected culture medium in low glucose medium with 1% P/S were prepared for viral tittering. Tested dilutions were: 1/50, 1/25, 1/10, 1/5 and 1/2.5 and 1/1. Cells with low glucose DMEM with 1% P/S were used as a control. In all cases, polybrene (Sigma Aldrich) at a final concentration of 8 µg/mL was added to improve viral particle efficiency. After 7 hours, cell culture medium was replaced by low glucose DMEM supplied with 10% TTC-free FBS and 1% P/S. 48h later, cells were analyzed by flow cytometry to evaluate the number of GFP positive cells in each sample and the optimal number of viral particles to infect 3 x 10^5 MSC was calculated based on titration curves previously performed.

On the other hand, MSC medium was changed for a mixture of low glucose DMEM with 1% P/S supplemented with 8 µg/mL polybrene (Sigma-Aldrich) and the volume of collected culture medium containing viral particles previously calculated. The final volume on each dish was 8 mL. After 7 hours, cell culture medium was replaced by low glucose DMEM supplied with 10% TTC-free FBS and 1% P/S.

3.3.5. Large scale transfection in Expi293F cells

Expi293F cells were used for protein transient expression to get a faster screening of designed fusion proteins stability. 40 kDa linear Polyethilenimine (PEI, from Polysciences Inc.) was used as plasmidic DNA encapsulator. The procedure

described below was carried out for all the pEBNAZ-based plasmids described in **Section 3.3**.

- Day 1: Expi293F™ seeding. Cells were seeded at a density of 2 million cells per mL in a final volume of 45 mL.
- Day 2: Transfection. Twenty-four hours after seeding, cell density and viability was measured. Cell viability should be higher than 95%, while cell density should range from 3.5 to 4.2 million of cells per mL to proceed. If parameters match, two different solutions are prepared:
    - Solution A: 75 µg of DNA in 2.5 mL of Expi293F™ expression media.
    - Solution B: 300 µL of PEI Max in 2.5 mL of Expi293F™ expression media.

After all reagents were prepared, Solution A was added to Solution B. Components were carefully mixed and incubated for 15 min at RT. Thereafter, DNA-PEI complexes were added to Expi293F™ cells.

- Day 3: Culture media addition and culture parameters check. Twenty-four hours after transfection, cell density and viability were measured to ensure cell growth and well-being. If viability was acceptable, 50 mL of fresh expression media were added to each Erlenmeyer culture flask.
- Day 4: Media and samples recollection. Forty-eight hours after transfection, one million of cells were used for the generation of cell lysates and protein samples and cell supernatant was collected for SEV isolation.

3.4. SEV isolation from cell culture supernatants

3.4.1. SEV production medium

FBS is routinely used for cell culture medium as a supplement to favor cell growth. However, it contains EV which would contaminate the experiments. To avoid this, culture media from which the cell-derived SEV will be purified must be depleted of the contaminating EV. Consequently, EV in FBS were eliminated by ultracentrifugation as previously described by C. Théry et al[375]. In the present work, fixed angle 50.2Ti rotor (Beckman Coulter) and ultracentrifuge CD80NX (Hitachi) were used.

Low or high glucose DMEM were supplemented with 20% of tetracycline free FBS and ultracentrifuged at 100.000 g at 4 °C for 16 h for MSC-derived SEV isolation.

After that, supernatant was filter sterilized by pouring the contents of each tube into a vacuum-connected 0.22 µm filter on top of a sterile bottle and diluted in one volume of low or high glucose DMEM medium without FBS and 1% of P/S to obtain the SEV production mediums (PM1 and 2, respectively). PM1 or PM2 was added to the desired cells for 48 h for SEV purification by ultracentrifugation or for experiments. Doxycycline was added to induce OSM expression in the correspondent experimental conditions.

3.4.2. SEV isolation

SEV isolation secreted by cells to the extracellular space was performed by serial ultracentrifugation of PM. PM1 or 2 was added to the cells of interest, recollected after 48 h of incubation, and centrifugated at 2.500 g at 4 °C for 20 min to precipitate and remove live cells. Supernatant was transferred to ultracentrifuge tubes and centrifuged at 15.000 g for 45 min to rush to the bottom cellular debris. Supernatant was collected and 0.2 µm filtered to exclude large EV. Next, supernatant was transferred to clean tubes and ultracentrifuged at 100.000 g for 2 h at 4 °C. After that, supernatant was completely removed, and each pellet was resuspended in 1 mL of cold PBS. Resulting solutions from the same biological conditions were pooled in only one tube for a final washing step. With this objective, tubes were filled with cold PBS and samples were ultracentrifuged at 100.000 g for 2 h at 4 °C. Finally, supernatant was removed as completely as possible and SEV pellet was resuspended in the desired solution.

3.5. Molecular biology techniques

3.5.1. RNA purification and quantification

RNA was isolated from eukaryotic cells in culture. Firstly, culture dishes were placed on ice and three cold PBS washed were done. After that, RNeasy Plus Mini Kit (Qiagen) was used following manufacturer's instructions. Experimental process consists on cellular lysis with RLT buffer supplemented with 1% of β-Mercaptoethanol and subsequent RNA purification with a column system which combines the selective binding properties of a silica-based membrane with the speed of microspin technology.

Concentration of obtained RNA in samples was measured with NanoDrop ND-1000 (Thermo Fisher Scientific) spectrophotometer. After the addition of 1 µL of sample

RNA concentration was obtained from the resultant absorbance spectrum. Samples' quality was checked calculating the absorbance ratios 260/280 nm (when value is 2.0 is considered that nucleic acid contamination or another molecule with similar spectra is not significant) and 230/260 nm (range of 2.0-2.2 means an insignificant protein or other molecules contamination).

3.5.2. Reverse transcription and Real Time PCR

Expression of genes of interest from total cellular RNA was measured by real time PCR (RT qPCR). This process requires reverse transcription of RNA to complementary DNA (cDNA) and the use of the obtained cDNA as a template for amplification by PCR.

3.5.3. Reverse transcription: cDNA synthesis

Reverse transcription consists on the synthesis of DNA from RNA. Therefore, RNA can act as a template to obtain a DNA chain with complementary sequence. In order to obtain cDNA from RNA samples, the high-capacity cDNA reverse transcription kit (Applied Biosystems) was used following manufacturer's instructions using the protocol detailed in **Table 3.3** in an Eppendorf Thermal Cycler. Reaction mix was prepared using 1 µg of RNA for each sample and the rest of components provided by the mentioned kit: RT buffer, RT Random Primers, dNTP Mix, MultiScribe Reverse Transcriptase and ultrapure water.

Table 3.3. *Reverse transcription protocol for cDNA synthesis.*

Step	Number of cycles	Temperature	Time
1	1	25 °C	10 min
2	2	37 °C	60 min
3	1	85 °C	5 min
4	-	4 °C	∞

3.5.4. Relative quantification of gene expression by real time quantitative PCR

Real time quantitative PCR (RT qPCR) was carried out from 100 ng of previously synthetized cDNA. Predesigned primers to amplify the sequences of target genes

were acquired from KiCkStart™ Primers Service of Sigma Aldrich or TaqMan Assay Probes™ from Thermo Fisher Scientific. In this work, expression of the genes detailed in **Table 3.4** was analysed. Expression of GUSB was measured as control or housekeeping gene for iPSC or differentiated iPSC, while GAPDH and β-ACTIN were used for the rest of cell lines for SYBR Green and TaqMan Assay probes, respectively.

Table 3.4. *Primers sequences used for gene expression quantification by RT qPCR.*

Gene	Assay ID
OCT4	NM_00173531
NKX2-5	D6021-C02/C03
TNNT2	NM_000364
GP130	Hs00384276_m1
LIFR	Hs01123581_m1
OSMR	Hs00174360_m1
GUSB	NM_000181
GAPDH	NM_017008.3
β-ACTIN	Hs01060665_g1

RT qPCR for each gene of interest was performed using the correspondent pair of primers, SYBR green master mix (1X Light Cycler 480 SYBR Green I Master, Roche) and Taq DNA polymerase NETZYME (1 U/µL, NEED) when SYBR Green Assay Probes were used. cDNA amplification was performed in the LightCycler 480 Instrument (Roche). Each PCR reaction mix contained: 3 µL of previously synthetized and diluted cDNA, 1 µL Taq DNA Polymerase NETZYME, 2.5 10X Polymerase buffer, 1 µL $MgCl_2$ 50 mM, 2.5 µL 2.5 mM dNTPs, 0.5 µL of forward primer, 0.5 µL of reverse primer and MiliQ H_2O_2 to reach a final volume of 15 µL. Once samples were ready, they were introduced into the thermal cycler following the protocol detailed in **Table 3.5**.

Table 3.5. *Protocol for DNA amplification by RT qPCR using SYBR Green Gene Expression Assays.*

Step	Temperature	Time	Number of cycles
Pre-incubation	95 °C	10 min	-
Amplification	95 °C 58 °C 72 °C	15 s 10 s 20 s	45
Melting Curve	94 °C 60 °C	5 s 15 s	1

	97 °C	Continuous	
Cooling	4 °C	10 s	-

In case of gene expression analysis with TaqMan® Gene Expression Assays, TaqMan® Fast Advanced Master Mix 2X was used, and master mix for each individual or each Taqman assay probes (20X) were prepared following manufacturers' instructions for a final volume of 10 µL/well. QuantStudio™ 7 Flex Real-Time PCR System instrument was used to run the reactions following the protocol showed in **Table 3.6**.

Table 3.6. *Protocol for DNA amplification by RT qPCR using TaqMan Gene Expression Assays.*

Step	Temperature	Time	Number of cycles
Pre-incubation	50 °C	2 min	-
Polymerase activation	95 °C	2 min	-
PCR (Denature and Anneal/Extend)	95 °C 60 °C	1 s 20 s	40
Cooling	4 °C	10 s	-

3.5.5. qPCR results analysis

Light Cycler 480 SW 1.5 (Roche) or QuantStudio™ 7 Flex Real-Time PCR System software were used to analyze results. Each sample was assayed by triplicate. Gene expression results for each sample was normalized with gene expression of housekeeping genes (β-ACTIN, GAPDH or GUSB) and were expressed as the number of times that gene expression increases or decreases compared to control sample values.

3.6. Biochemical techniques

3.6.1. Extraction of protein content

In order to obtain good quality extracts of proteins all the procedure was carried out on ice. Firstly, medium in culture was discarded and dishes were washed twice using ice-cold PBS. Next, PBS was discarded and ice-cold RIPA lysis buffer (Sigma Aldrich) was added. Lysis buffer was supplemented with a cocktail of protease inhibitors (Roche) and phosphatase inhibitors (Sigma Aldrich) to favor protein

integrity. Cells were lifted with sterile cell scrapers and transferred to Eppendorf tubes. Gentle pipetting was done to enhance extracts' lysis and disaggregation. After that, samples were incubated on ice for 20 min and centrifuged in an Eppendorf 5417R Refrigerated Centrifuge (Thermo Scientific) at 16.000 RPM for 20 min at 4 °C. Proteins contained in the resulting supernatant was collected and transferred to a new Eppendorf tube and samples were conserved in a freezer at -80 °C until use.

3.6.2. Protein quantification assay

Protein concentration was quantified by BCA technique (Pierce™ BCA Protein Assay Kit, ThermoFisher Scientific). BCA assay is based on the use of bicinchoninic acid (BCA) for colorimetric detection and quantification of the protein content in a sample. First, working solution containing 50 parts of Solution A (Composition: sodium carbonate, sodium bicarbonate, bicinchoninic acid and sodium tartrate in 0.1M sodium hydroxide) and 1 part of Solution B (Composition: Cupper sulphate) was prepared. Then, 10 µL of each previously prepared standard (protein standard curve recipe is detailed in **Table 3.7**) or 10 µL of the correspondent sample were added to a well of a 96 multi-well plate. After that, 190 µL of work solution was added to each well and plate was shacked in an orbital shaker for 30 s. Samples were covered and incubated at 37 °C for 30 min. Finally, absorbance at 562 nm was recorded in a Victor2 microplate reader using Wallac 1420 Workstation (Perkin Elmer).

Table 3.7. *Standard BSA curve for protein quantification.*

BSA Concentration (µg/mL)	BSA from stock solution at 2mg/mL (µL)	Diluent (µL)
0	0	30
25	0.375	29.62
125	1.87	28.12
250	3.75	26.25
500	7.5	22.5
750	11.25	18.75
1000	15	15
1500	22.5	7.5
2000	30	0

Protein concentration was calculated by line regression using the following formula:

$$Y = m \times X + b;\ m = \Delta Y/\Delta X = (Y_1 - Y_0)/(X_1 - X_0)$$

Where:

Y = Dependent variable (Absorbance)

m = Slope

X = Explanatory variable

3.6.3. Polyacrylamide gel electrophoresis

In the displayed experiments, 30 µg of protein from each sample have been used for Western Blot assays. Laemmly Sample Loading Buffer 4x (Bio-Rad) supplemented with β-mercaptoethanol (Sigma-Aldrich) was mixed with protein samples following manufacturer's instructions. Then, samples were transferred to a thermo-block station at 95 °C for 5 min and a short spin was performed. This step allows protein denaturalization before electrophoresis.

Sodium Dodecyl Sulphate Polyacrylamide Gel Electrophoresis (SDS-Page) allows protein separation according to their molecular weight. With this purpose, proteins are loaded with electric charge and differently migrate inside a porous matrix depending on their size due to the application of a constant electric camp. Porous matrix is achieved by linear and branched polymerization of a solution composed by 30% Acrylamide/0.8% Bisacrylamide (Bio-Rad). Consequently, the final concentration of this solution will determine gels' porous size and smaller proteins will migrate quickly than heavy proteins.

During this work, a discontinuous gradient was achieved using a gel composed by a stacking gel fraction and a running gel fraction. Stacking gel was prepared with 5% of polyacrylamide/bis-acrylamide solution to accumulate all the proteins present on the different samples in the migration front (beginning of running gel) to ensure that all the proteins start its migration at the same time. Running gel, with smaller porous size, was prepared at different percentages of polyacrylamide/bisacrylamide solution depending on the protein size of interest. Gel compositions used during this project are detailed in **Table 3.8**.

Table 3.8. *Stacking and running polyacrylamide/bisacrylamide gels recipes.*

Stock solution	5% stacking gel (mL/5mL)	7.5% running gel (mL/10mL)	10% running gel (mL/10mL)
30% Acrylamide/ 0.8% Bisacrylamide solution	0.83	2.5	3.3
1.5 M Tris-HCL, pH 8.8	-	2.5	2.5
1 M Tris-HCl, pH 6.8	0.63	-	-
10% SDS	0.05	0.1	0.1
10% APS (ammonium persulfate)	0.05	0.1	0.1
TEMED (tetramethyletilendiamine)	0.005	0.004	0.004
ddH_2O	3.4	4.8	4

Electrophoresis was carried out using a running buffer composed by 192 mM glycine, 0,1% SDS and 25 mM Tris-HCl at pH 8.3 in a MiniProtean II system (Bio-Rad) and ran at 100 V until samples reached the running gel and then at 150 V during 70-90 min. Molecular weight marker used was SM0441 (Fermentas, MD).

3.6.4. Protein transfer by Western Blot assay

Proteins were transferred to a PVDF membrane (Immobilon™–P Transfer Membrane, Millipore), which was previously activated with methanol for 2 min. Transference was performed in a buffer composed by 20% methanol, 20 mM tris and 150 mM glycine in a MiniProtean II System (Bio-Rad) with a continuous electric current of 100 V and slow shacking at room temperature for 3 h or at 4 °C overnight.

3.6.5. Membrane blocking, antibody labelling and signal detection

After proteins were transferred to PVDF membrane, they were washed with tris saline buffer (TBS: 50 mM tris-HCl and 150 mM NaCl at pH 7.6) and incubated with blocking solution (5% dairy milk in TBS) in an orbital shaker for at room temperature for 1 h. After that, antibodies were prepared in an incubation working solution composed by one part of blocking solution and one part of TBS and membranes were incubated with the correspondent antibody in continuous shake at 4 °C overnight. Antibodies employed during this work are detailed in **Table 3.9**. Next day, three TBS washes of 5 min were done and membranes were incubated with the correspondent secondary antibody conjugated to horseradish peroxidase (HRP)

in continuous shaking at room temperature for 1 h. Three TBS washes were done following the same procedure as before and membranes were prepared to proceed to the signal detection step.

Table 3.9. *List of antibodies employed for WB.*

Antibody	Dilution	Specie	Brand
anti-Bcl-2	1:500	Mouse	Santa Cruz
anti-Bax	1:500	Rabbit	Cell Signalling
anti-Beclin-1	1:500	Rabbit	Cell Signalling
anti-GRP-78	1:500	Rabbit	Cell Signalling
anti-HIF1α	1:500	Mouse	BD Biosciences
anti-hOSM	1:500	Mouse	R&D
anti-hOSM	1:500	Rabbit	Sigma-Aldrich
anti-Lactadherin	1:500	Rabbit	Sigma-Aldrich
anti-CD81	1:1000	Mouse	Abcam
anti-CD63	1:1000	Mouse	Abcam
anti-Alix	1:1000	Mouse	Abcam
anti-TSG101	1:1000	Rabbit	Abcam
anti-CD9	1:1000	Rabbit	Abcam
anti-IL-31RA	1:500	Rabbit	Abcam
anti-IL-31RB	1:500	Rabbit	Proteintech
anti-LIF-R	1:500	Mouse	R&D
anti-Calnexin	1:1000	Rabbit	Abcam
anti-β-Actin	1:2000	Mouse	Sigma-Aldrich
anti-Tubulin α-1A (Tub)	1:10000	Mouse	Sigma-Aldrich
anti-mouse IgG HRP	1:20000	Goat	Promega
anti-rabbit IgG HRP	1:10000	Goat	Santa Cruz
IRDye® 800CW Goat anti-Rabbit IgG	1:20000	Goat	LI-COR
IRDye® 800CW Goat anti-Mouse IgG	1:20000	Goat	LI-COR
IRDye® 680RD Goat anti-Rabbit IgG	1:20000	Goat	LI-COR
IRDye® 680RD Goat anti-Mouse IgG	1:20000	Goat	LI-COR

Amersham ECL Western Blotting Detection Kit (GE Healthcare) was used for chemiluminescent protein detection following manufacturer's instructions. Membranes were covered with transparent film and a Curix 60 (AGFA) film processor or an Amersham Imager 600 (Life Technologies) equip was used to measure chemiluminescence signal. Odyssey® CLx Imaging System was used for fluorescent signal detection. Results analysis were done with ImageJ software (NIH)

and relative expression of each gene of interest normalized to housekeeping gene (β-Actin or Tub) expression on each sample was calculated.

3.7. Immunocytochemistry

Immunocytochemistry is a technique which allows the use of antibodies for different molecules detection in cells or tissues.

Cells were seeded in multi-well plates, on coverslips (Menzel Gläser, Thermo Scientific) or 8 well chamber slides (Ibidi). After the correspondent treatments, cells were rinsed in PBS 3 times, fixed with 4% paraformaldehyde (PFA) or 70% ethanol (EtOH) at 4 ^{o}C for 10 min and washed again with PBS 3 times. Samples were stored in PBS supplemented with 0.05% sodium azide (Panreac) at 4 ^{o}C until used. Next, blocking solution made up of 2% Goat Serum (GS, Gibco) and 0.1 % Triton X-100 in PBS was added, and samples were incubated at 37 ^{o}C for 1 h. After that, samples were incubated with the correspondent primary antibodies diluted in antibody solution (composition: 1 part of blocking solution and 1 part of PBS) at 4 ^{o}C overnight. The following day, 3 PBS washes for 5 min each were performed, and secondary antibodies diluted in antibody solution were added. Samples were incubated at room temperature for 1 h, rinsed 3 times in PBS for 5 min each and incubated with 1µg/mL DAPI (4´-6-diamidino-2-phenylindole) in PBS at room temperature for 5 min. Additional PBS washes were performed and coverslips were placed in the microscope slides (Menzel Gläser, Afora). When chamber slides were used, silicone spacers removal was performed instead. Mounting medium (FluorSave, Millipore) was added and preparations were properly sealed with nail polish. Primary and secondary antibodies used during this work are detailed in **Table 3.10**.

Table 3.10. *List of antibodies used for immunofluorescence experiments.*

Antibody	Dilution	Specie	Brand
Anti- Tubulin α-1A (Tub)	1:500	Mouse	Sigma Aldrich
Anti-CD31	1:100	Rabbit	Sigma Aldrich
Anti-cTnT	1:1000	Mouse	Abcam
Anti-Oct4	1:200	Rabbit	Abcam
Anti-Ki67	1:1000	Rabbit	Abcam
Anti-BrdU	1:100	Rat	Abcam
Anti-teloCollagen1α1	1:500	Rabbit	Rockland
Alexa Fluor 488	1:500	Goat	Life technologies

Alexa Fluor 555	1:500	Goat	Life technologies

3.8. Imaging techniques

3.8.1. Fluorescence optical microscopy

Inverted fluorescence microscope (Model DMI4000B, Leica) equipped with a DFC350FX monochromatic CCD camera (Leica), 5 fluorescence filter cubes for the following Ex/Em wavelengths (nm: 436-20/480-40; 470-40/525-50; 500-20/535-30; 546-12/605-75; 620-60/700-75) and 3 objectives (N PLAN 10X NA 0.25; N PLAN L 40X NA 0.55; PL APO 63X 1.40), where NA refers to the numerical aperture and determines the resolution capacity of an objective, was used to observe and take pictures of live cells.

Upright fluorescence microscope (Model DM6000B, Leica) equipped with a DFC350FX monochromatic CCD camera (Leica) was used to observe immunofluorescence samples. 4 fluorescence filter cubes for the following Ex/Em wavelengths (nm: 360-40/470-40; 480-40/527-30; 546-12/600-40; 620-60/700-75) and 5 objectives (HC PL FLUOTAR 5X NA 0.15; HC PL APO 10X NA 0.40; HC PLAN APO 20X NA 0.70; HCX PL APO 40X NA 0.75; HCX PL APO 63X NA 1.40). Acquisition of the different wavelengths were made sequentially with different barrier filters (suitable for each of the fluorochromes) and were combined in a single-color overlay image.

FLIPR Penta High-Throughput Cellular Screening system (Molecular Devices) was used for high-throughput for live and fixed cells scanning.

Data were analyzed with Leica Application Suite Version 2.4.0 R1 version and ImageJ (NIH) in all cases.

3.8.2. Time-lapse microscopy

Time-lapse photography is a technique where the frequency at which film frames are captured is much more spread out than the frequency used to view a sequence. This methodology is widely used to study cell biology events like cellular movement or molecules transference between cells *in vitro*. In this work, an inverted widefield fluorescence microscope DMI6000 (Leica) with fully automated transmitted and fluorescence light axis and equipped with 4 objectives (HCX PL FLUOTAR 10X NA 0.30; HCX PL FLUOTAR L 20X NA 0.40; N PLAN L 40X NA 0.55; HCX PL APO 63X NA

1.40-0.60) and 2 filter cubes for Ex/Em wavelengths 480/535 and 560/610 nm was used for wound healing (scratch) uptake assay *in vitro*. This microscope includes an incubation chamber which allows controlled CO_2, temperature and humidity settings and makes the system suitable for live-cell imaging for long periods of time. Once samples were prepared and system was settled, coordinates in each well were fixed and images were automatically taken each 30 min for 24 or 48 h maintaining a proper atmosphere (37 ˚C and 5% CO_2). Data were analyzed using ImageJ software (NIH).

3.8.3. Confocal microscopy

Multicolor confocal TCS-SP2-AOBS microscope (Leica) was used when imaging speed, augmented resolution or additional number of colors was required. This microscope is equipped with 9 excitation laser lines which include all visible spectrum from 405nm to 633nm, 4 detectors that can work simultaneously and 5 objectives (HC PL FLUOTAR 5X NA 0.15; HC PL FLUOTAR 10X NA 0.30; N PLAN 20X NA 0.40; N PLAN 50X NA 0.75 and PL APO 100X NA 1.40). Moreover, life-cell imaging under controlled atmosphere (temperature and CO_2 adjustment) is allowed. Sequential photograms in different planes were taken to create a 3D composition which allows molecules tracking and location inside cells without fluorescence signals overlapping. Image recording was performed in collaboration with the Confocal Microscopy Service of Príncipe Felipe Research Centre, Valencia.

Two additional confocal imaging systems were used for immunofluorescence screening: CellVoyager CV8000 high-throughput screening system (Yokogawa), equipped with four cameras and 5 lasers. Image analysis was performed with Leica Application Suite Version 2.4.0 R1 version and Image J software (NIH) in all cases.

3.8.4. IN Cell

IN Cell Analyzer 1000 Workstation was used in order to capture accurate, high-speed imaging through a combination of optical technology and fast hardware. IN Cell technology allowed cellular and subcellular automated imaging in fixed and live cells thanks to an autofocus software included for high throughput image acquisition and screening applications.

IN Cell Analyzer systems are equipped with an environmental control module for live-cell assays, allowing customized temperature and gases concentration conditions. During this work, IN Cell Analyzer 1000 Workstation (GE Healthcare)

was used. This device is equipped with four different objectives (4X NA 0.20; 10X NA 0.45; 20X NA 0.45 and 40X NA 0.60), five dichroic filters for the following Ex/Em wavelengths (nm: 360/460; 480/535; 405/585; 565/620; 620/700) and a CCD camera for transmitted light imaging in bright-field, differential interference contrast (DIC) or phase-contrast. After samples preparation, a specific protocol was set up for each experiment and 10 pictures from random fields were automatically obtained from each well for representative data collection.

Data analysis was performed with the same IN Cell Analyzer 1000 Workstation software with the Cytomics Unit in Príncipe Felipe Research Institute. Segmentation process using nuclear or membrane staining allowed the division of each image in individual objects or contiguous regions, differentiating them for each other and from the image background. After that, desired parameters, as fluorescence intensity per cell, number of particles per cell, total fluorescent intensity or positive and negative cells on for each dye in every recorded field were calculated.

3.8.5. Transmission electron microscopy (TEM)

Electron microscopy is a technique based on the incision of an electron beam in a sample, obtaining an image which is dependent on the electrons able or not to cross the sample. This result involves previous steps of adsorption and contrasting of samples in TEM grids. Contrasting is achieved by joining electron-dense compounds, which deviate electrons, to the sample ultrastructure. Electrons that pass through the sample are detected by a phosphor screen, generating an image that can be viewed directly by the operator. This technology can be used to investigate the detailed structure of tissues, cells, organelles, macromolecular complexes or small extracellular vesicles isolates, among others. TEM Sections were examined with a FEI Tecnai G2 Spirit TEM (FEI Europe) and images were recorded using a Morada CCD camera (Olympus Soft Image Solutions GmbH) in collaboration with Electron Microscopy Service of Príncipe Felipe Research Institute.

3.8.5.1. Organelle's ultrastructure analysis

Samples were immobilized onto Permanox® coated chamber slides (Lab-Tek®), washed three times with 0.1 M phosphate buffer (PB) and fixed with 3% glutaraldehyde at RT for 2 h. 0.2 M PB was prepared from 0.2M NaH_2PO_4 (0.496 g/100mL) and 0.2 M Na_2HPO_4 (2.328 g/100 mL) and diluted 1:1 in MiliQ water. After that, samples were washed 3 times with 0.1 M PB, post-fixed with 2% osmium

tetroxide (EMS) in 0.1 M PB for 1 h and dehydrated in graded acetones (each step lasted 5 min and was performed twice): 30%, 50%, 70% and 90%. After that, 100% acetone was added five times for 10 min each, cleared in propylene oxide at RT for 1 h and embedded in araldite (Durkupan, Fluka UG). Thick sections were obtained using a diamond knife, placed into copper grids and stained with 2% uranyl acetate (EMS) for 10 min. Uranyl acetate is used for contrasting protocols due to its capability to precipitate in the presence of proteins, which are highly present in biological membranes. Finally, samples were washed with water, dried at RT and observed in the transmission electron microscope.

3.8.5.2. SEV morphology study

First, 10 µL of the SEV fraction isolated from PM1 resuspended in PBS was placed in a carbon grid (Formvar coated grid, SPI® Supplies) for 20 min for SEV attachment by electrostatic forces. After that, SEV were fixed in 2% PFA (Aurion) in 0.1 M PB at RT for 10 min and washed twice with PBS. A second fixation step was performed using 1% glutaraldehyde (Aurion) in 0.1 M PB at RT for 5 min and 8 washed of 2 min were performed with distilled water. At this point, samples are ready to start with the contrasting protocol. Samples were incubated with 1% uranyl acetate in 0.1 PB at RT for 5 min and with 1% methylcellulose and 1% uranyl acetate in PBS at 4 ˚C for 10 min. Methylcellulose was used to improve membrane stability. Grids were dried at RT for 30 min and observed in the electron microscope.

3.9. Cytomics

Flow cytometry is a widely used method for analyzing the expression of cell surface and intracellular molecules, characterizing and defining different cell types in a heterogeneous cell population, assessing the purity of a cell culture and analyzing cell size and volume. In addition to this, simultaneous multi-parameter analysis of single cells is allowed by fluorescent-labelled antibodies detecting proteins, ligands that bind to specific cell-associated molecules, proteins fused to a fluorescent reporter or soluble molecules conjugates to fluorescent dyes, among others. During this work, CytoFLEX S (Beckman Coulter) equipped with 4 lasers and FACSCanto II Flow Cytometer (Becton Dickinson) equipped with 3 lasers were used. Protocols were set up in collaboration with Cytomic Units in Príncipe Felipe Research Centre and IIS La Fe and data analysis was performed with CytExpert, FACSDiva and FlowJo software.

3.10. SEV quantification

3.10.1. Nanoparticle tracking analysis

Nanoparticle tracking analysis (NTA) was used to determine SEV concentration and particle size distribution. All particle tracking analyses were performed using a LM14C NanoSight instrument (Malvern Instruments Ltd) using the same settings (camera level 16, 3 videos of 90 s and 1300/512 slider shutter/gain, respectively) at the proper concentration to obtain around 50 particles/frame. Analysis of the acquired videos was performed with threshold 5 and gain 12 with NTA3.2 program.

3.10.2. SEV protein quantification

Protein concentration in SEV was quantified by BCA technique (Pierce™ BCA Protein Assay Kit, Thermo Fisher Scientific) as described in **Section 3.6.2**.

3.11. Ischemia-reperfusion *in vitro* model

Oxygen-glucose deprivation (OGD) and OGD-R are widely used as *in vitro* models for stroke, showing similarities with the *in vivo* models of heart ischemia. In order to perform OGD-R, HMVEC-C, cFib, NRVM, iPSC-CM or NHCF-V were counted and seeded at the recommended concentration on different transwell inserts, multi well plates or chamber slides. After that, culture medium was removed, cells were washed with PBS and glucose-free DMEM (Gibco) containing 1% P/S was added. Cells were placed under a deoxygenated atmosphere (1% 0_2, 5%CO_2) in a hypoxic chamber for 6 h (Ischemic cells, I). After that, reperfusion was simulated *in vitro* by adding complete culture medium and placing cells in an oxygenated atmosphere (21% O_2, 5% CO_2) for 1 h (Ischemia-reperfusion cells, I/R). Cells in normoxia (Nx) were used as control.

3.12. Chemicals and Nanoconjugates

Poly-L-glutamic acid (PGA) was obtained from Polypeptide Therapeutic Solutions S.L., di-docosahexaenoic acid (diDHA) was purchased from Nu-Chek Prep Inc. and Oregon Green 488 cadaverine (OG) was obtained from Invitrogen. PGA-diDHA conjugates with different diDHA loadings were obtained from the Therapeutic Polymers laboratory in Príncipe Felipe Research Centre. During this work, three different conjugates were used (conjugated or not with OG): PGA-diDHA$_{2.2}$, PGA-

diDHA$_{6.4}$ and PGA-diDHA$_{9.1}$. The different loadings correspond to the number of diDHA units present in one unit of PGA. PGA and free diDHA were used as controls. Esmolol (Brevibloc®), a common β-blocker used as cardioprotective drug[376], was added at 1 µg/mL as a positive control for AMI treatment. Doxycycline to induce fusion protein expression in lentiviral-infected cells was purchased from Sigma-Aldrich. Recombinant human OSM (R&D) was used as control in experiments where engineered SEV were added.

3.13. Functional *in vitro* assays

3.13.1. Cytotoxicity assays

3.13.1.1. Cell viability assessment

Cells were seeded in 96 multi well plates at a density of 100.000 cells/cm^2. One day later, compounds were diluted in fresh medium and added to each well. After 72 hours, cell viability was measured with Cell Titer 96® Aqueous Non-Radioactive Cell Proliferation Assay Kit (Promega), a colorimetric method for determining the number of viable cells in a sample. The assay is composed of solutions of a novel tetrazolium inner salt compound (MTS) and an electron coupling reagent (phenazine methosulfate, PMS). MTS is reduced by cells into a formazan product that is soluble in tissue culture medium. MTS and PMS mix were prepared (50MTS:1PMS) and 10 µL were added to each well. Samples were incubated at 37 ^{o}C for 3 h and absorbance at 490 nm was recorded with a 96-well plate reader (Perkin Elmer). The quantity of formazan product as measured by the amount of 490 nm absorbance is directly proportional to the number of living cells in culture. Results were presented as the percentage of live cells in a sample compared to control cells.

3.13.1.2. Lactate dehydrogenase release measurement

Cells were seeded in 96 multi well plates at a density of 100.000 cells/cm^2. Next day, medium was replaced with fresh culture medium containing the correspondent treatments. After 72 hours, lactate dehydrogenase (LDH) release was measured with LDH-Cytotoxicity assay Kit (Abcam). The LDH assay protocol uses an enzymatic coupling reaction: LDH oxidizes lactate to generate nicotinamide adenine dinucleotide hydrogenase (NADH), which then reacts with stable

tetrazolium salt (WST) to generate a yellow color. The intensity of the generated color correlates directly with the cell number lysed. In brief, 100 µL of cell culture medium were transferred to a new 96 multi well plate, 100 µL of LDH reaction mix were added to each well. Samples were incubated 30min at RT and absorbance at 450 nm was analyzed with a microplate reader (Perkin Elmer).

3.13.2. Internalization assays

3.13.2.1. Uptake analysis

HMVEC-C, NRVM or cFib were seeded in 18 mm coverslips or directly in 24 multi well plates at a density of 50.000 cells/cm^2 or in 8 well chamber slides at a density of 30.000 cells/cm^2. Next day, cells were submitted to Nx or I/R, compounds were added for 30 min and washed three times with PBS.

Three different approaches were followed to study compounds uptake *in vitro*:

- Confocal microscopy analysis: cells were fixed with 70% EtOH and immunocytochemistry protocol described in **Section 3.7** was followed.
- IN Cell analysis: cells were labelled with 1 µg/mL Hoechst 33342 staining solution and 50 nM Tetramethylrodamine, methyl ester (TMRM, Ex/Em: 488/570 nm), both from ThermoFisher Scientific, following manufacturer´s instructions and analyzed on the IN Cell 1000 Work Station to count the percentage of OG positive cells on each sample. TMRM was used for cytoplasm labelling to allow segmentation process during results analysis.
- Flow cytometry analysis: cells were labelled with 1 µg/mL Hoechst 33342 staining solution (ThermoFisher Scientific) to exclude apoptotic cells, enzymatically detached using trypsin, pelleted and resuspended in a cell culture medium for flow cytometry analysis. Cells were selected considering cellular size and shape, and aggregates were discarded. From the resultant population, living cells were selected as the subpopulation not stained by Hoecsht33342 (Ex/Em: 361/497). Finally, OG positive cells (Ex/Em: 488/526 nm) were gated and percentage of positive cells from live cells was obtained.

3.13.2.2. Transcytosis assay

Transwell assay was set up to evaluate the ability of compounds to traverse from HMVEC-C to NRVM under physiological or ischemic conditions. To test if ischemia

could favor nanoconjugates transference between both type of cells, NRVM under Nx or I/R were used. With this purpose, nanoconjugates were added to HMVEC-C previously seeded in 24 well plate transwell inserts (pore size: 0.4 µm, Corning) at a density of 100.000 cells/cm^2. After 30 min of exposure, cell culture medium was removed, cells were washed with PBS three times, fresh culture medium was added and transwell inserts carrying HMVEC-C were transferred to 24 multi well plates where NRVM were previously seeded in 18 mm coverslips or directly at a density of 50.000 cells/cm^2. After 24 h, OG positive cell number was measured by confocal microscopy or flow cytometry as described before. Schematic process is shown in **Figure 3.3**.

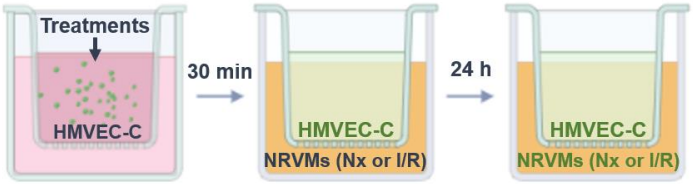

Figure 3.3. Transcytosis assay scheme protocol. *HMVEC-C were incubated with compounds for 30 min. Next, HMVEC-C were gently washed with PBS and inserts were transferred to the top of wells containing NRVM under Nx or I/R conditions. After 24h, OG positive NRVM were measures by flow cytometry or immunofluorescence.*

3.13.3. Apoptosis assays

Apoptosis is a form of programmed cell death considered a vital component of various processes as normal cell turnover, proper development and functioning of the immune system or chemical-induced cell death. Inappropriate apoptosis is a factor in many human conditions, including ischemic damage. During this project, apoptosis rate in response to different stimulus and compounds was evaluated in target cells.

3.13.3.1. Annexin V/7-AAD staining

The combination of Annexin V and 7-aminoactinomicin D (7-AAD) staining is widely used to distinguish cells in different states of apoptosis. Annexin V is a cellular protein in the annexin group which can bind to phosphatidylserine, a marker of apoptosis when it is on the outer leaflet of the plasma membrane. 7-AAD is a fluorescent chemical compound which has a high DNA binding constant and is

efficiently excluded by intact or early apoptotic cells. After completing experimental procedures, cell culture medium containing apoptotic and necrotic cells was recollected and cells were washed once with PBS. PBS used for cell washes was also recollected in the same tube. Next, cells were trypsinized, transferred to the tubes with cell culture medium and PBS previously recollected, centrifuged at 300 g for 5 min and resuspended in ice-cold PBS. After that, cells were centrifuged again at the same conditions and resuspended in 100 µL Annexin Binding Buffer (mM: 10 HEPES, 140 NaCl, 2.5 $CaCl_2$; pH adjusted to 7.4). 1 µL of CF Blue Annexin V (Ex/Em: 410/450 nm, Immunostep) and 1 µL 7-AAD (Ex/Em: 546/647 nm, Molecular Probes) were added to each sample and they were incubated in darkness at RT for 15 min. Unstained cells and single stained cells for each dye were used as controls. Samples were analyzed by flow cytometry in a CytoFLEX S instrument (Beckman Coulter) and analyzed with CytExpert Software. Double positive cells for Annexin V and 7-ADD indicated cells in late-apoptosis, while positive cells for Annexin V and negative for 7-AAD indicated an early- apoptosis state. Total apoptotic cells in each sample were indicated by the addition of the two previous values.

3.13.3.2. Caspase-3/7 activity

Caspase-3 and -7 are members of the caspase family of proteins and have been shown to be executioner proteins during apoptosis. In order to measure Caspase-3/7 activity *in vitro*, Caspase-Glo®-3/7 Assay (Promega) was used. The assay provides a luminogenic Caspase-3/7 substrate, which contains the tetrapeptide sequence DEVD, in a reagent optimized for caspase activity, luciferase activity and cell lysis. Caspase-Glo®-3/7 reagent was prepared and equilibrated to RT following manufacturer´s instructions and 50 µL were added to each sample. Culture medium mixed with Caspase-Glo®-3/7 reagent was used as blank sample. Samples were incubated in darkness at RT for 30 min and luminescence was recorded in a plate-reading luminometer (Perkin Elmer).

3.13.3.3. Bcl-2/Bax protein expression ratio

Bcl-2 is a protein responsible for apoptosis suppression by controlling the mitochondrial membrane permeability. Additionally, inhibits caspase activity and is associated with autophagy regulation. Apoptosis regulator Bax is a protein located in the cytosol under physiological conditions. However, it undergoes a conformation change that causes its translocation to the mitochondria membrane under stress conditions, promoting Caspase-3 activation and triggering

apoptosis[118]. The expression ratio of these two proteins is considered an indicative of therapeutic response of cells under different stimulus. Cells were seeded in 24 multi well plates at a density of 500.000 cs/cm^2 and protein extracts were obtained as described in **Section 3.6** for Western Blot assays. Bcl-2/Bax protein expression ratio was measured by Western Blot normalizing the obtained signals with Tub protein expression level in each sample. An increased value of Bcl-2/Bax protein expression ratio indicated a low rate of cells in apoptosis, while a decrease indicates a pro-apoptotic phenotype in sample.

3.13.4. Reactive oxygen species generation measurement

Oxidative stress results from an imbalance between the production of ROS and the ability of cells to scavenge them. CellROX® Orange Reagent (Ex/Em: 545/565 nm, Thermo Fisher Scientific) is a fluorogenic probe for measuring oxidative stress in live cells. This cell-permeant dye is non-fluorescent while in a reduced state and exhibits bright orange fluorescence upon oxidation by ROS. CellROX® Orange Reagent was resuspended and stabilized following manufacturer´s instructions. Thereafter, it was added at a concentration of 2.5 µM diluted in the correspondent culture medium to previously seeded cells in 96 multi well plates at a density of 100.000 cells/cm^2. Hoescht33342 (Ex/Em: 361/497 nm) at a final concentration of 1 µg/mL was used to stain cell nuclei. Samples were incubated in darkness at 37 ^{o}C for 30 min, rinsed in PBS 3 times and analyzed in the IN Cell Analyzer 1000 Workstation (GE Healthcare) using a 40X magnification objective. Results were represented as orange fluorescence intensity per cell in each sample.

3.13.5. Autophagy and endoplasmic reticulum stress study

3.13.5.1. Beclin-1 and GRP-78 protein expression

I/R process triggers endogenous cytoprotective mechanisms, as autophagy and unfolded protein response activation[377]. However, massive activation of these processes can undergo detrimental effects. Autophagy initiation is dependent on a protein complex which includes Beclin-1[378]; while ER response to regulate unfolded protein requires the upregulation of GRP-78[379]. Analysis of the expression of these two proteins after I/R-induced injury and ischemic preconditioning with candidate nanoconjugates was assayed. With this purpose, cells were seeded in 24 multi well plates at a density of 500.000 cs/cm^2 and protein extracts were obtained as

described in **Section 3.6**. Beclin-1 and GRP-78 protein expression levels were measured by Western Blot normalizing the obtained signals with Tub protein expression level in each sample.

3.13.5.2. Acidic organelle tracking

Lysosomes are acidic organelles which degrade molecules taken by endocytosis, phagocytosis and autophagy. In order to measure the number of acidic vesicles in live cells, Lysotracker® Red probes (Thermo Fisher Scientific) were used. This fluorescent acidotropic probes consist of a fluorophore (Ex/Em: 577/590 nm) linked to a weak basic amine which are permeant to cell membrane, selectively accumulate in cellular compartments with low internal pH and can be used to investigate the biosynthesis and pathogenesis of lysosomes. Cells were seeded in 96 multi well plates at a density of 100.000 cells/cm^2 and submitted to the correspondent experimental conditions. After that, they were stained with Lysotracker® Red probe (0.02 µg/mL) and Hoesch33342 (1 µg/mL; Ex/Em: 361/497 nm) at 37 ^{o}C for 30 min, washed with PBS and pictures were taken in the INCell Analyzer 1000 Workstation (GE Healthcare) using a 40X magnification objective. Results were represented as the number of red fluorescent particles per cell in each sample.

3.13.6. Mitochondria integrity tests

Mitochondria play a critical role in maintaining cellular function by ATP production. They are also a source of ROS and proapoptotic factors. Since mitochondrial disfunction has been described as one of the hallmarks of I/R-induced injury[118, 119], changes in mitochondrial membrane potential (MMP) and morphology in response to stressing-conditions and different treatments were assessed in this work.

3.13.6.1. Mitochondrial membrane potential measurement

A distinctive feature of the early stages of programmed cell death is the disruption of active mitochondria due to the opening of mPTP, which induces changes in the MMP and alterations in the oxidation-reduction potential. The membrane-permeant JC-1 dye (Thermo Fisher Scientific) is widely used to monitor mitochondrial health. JC-1 dye exhibits potential-dependent accumulation on mitochondria, indicated by a fluorescent emission shift from green (Ex/Em: 488/529 nm) to red (Ex/Em: 535/590 nm). In order to measure MMP, cells were

seeded in glass bottom 96 square well plates (GE Healthcare) at a density of 50.000 cells/cm^2. The use of glass bottom plates allowed to analyze live cells in a confocal microscope with high-resolution. After the appropriate experimental procedures, cells were stained with JC-1 dye (0.3 µg/mL) and incubated at 37 ^{o}C for 20 min. Next, cells were washed twice with PBS and images were captured immediately in a defined atmosphere (37 ^{o}C, 5% CO2) using a multicolor confocal TCS-SP2-AOBS microscope (Leica) and a N PLAN 50X NA 0.75 oil immersion objective. Data were calculated as the relative ratio of red to green florescence intensity by ImageJ, where mitochondrial depolarization is indicated by an increase in the green/red fluorescence ratio.

3.13.6.2. Mitochondria morphology

Defective mitochondria play an important role in the activation of death signaling pathways. In this study, mitochondrial morphology and structure changes after induced-stressed conditions and administration of different molecules was explored by TEM as described in **Section 3.8.5.1**. Mitochondria phenotype was evaluated considering the following features: tubular/regular versus irregular shape, inner and outer membrane definition and cristae grade of definition, presence or lack of swelling and dilatation.

3.13.7. Migration and proliferation assays

3.13.7.1. Migration assay

Cells were seeded in 24 well plate transfer inserts (pore size: 8 µm, BD Falcon) in basal culture medium (low/high-glucose DMEM + 0.5% FBS TTC free + 1% P/S) at a density of 10.000 cells/cm^2. After cells stabilization, lower chamber medium was replaced for basal culture medium supplemented with IL-1β (25 ng/mL). Basal medium was used as migration negative control and complete low/high glucose DMEM (10% FBS TTC free + 1% P/S) was used as migration positive control. After 8 h, non-migrated cells were removed from the upper side of the transwell inserts with cotton swabs and cells in the lower part of the transwell insert were fixed with ice-cold 70% EtOH for 10 min at 4 ^{o}C. After that, membranes were washed with PBS, stained with 1µg/mL DAPI, cut and transferred to microscope slides (Menzel Gläser, Afora). Mounting medium was added and samples were sealed with nail

polish. Pictures were taken in an upright fluorescence microscope (Model DM6000B, Leica) and number of nucleus on each sample were counted.

3.13.7.2. Bromodeoxyuridine cell proliferation assay

Bromodeoxyuridine (BrdU) is a pyrimidine-analogue synthetic nucleotide which can be used to label nascent DNA in viable cells. During the process of DNA replication, BrdU can replace thymidine and incorporate into the synthesized DNA of actively dividing cells.

Firstly, cells were seeded in 18 mm coverslips in 24 multi-well plates in low-glucose DMEM supplemented with 10% FBS TTC free, 1% P/S at a density of 50.000 cells/cm^2. Next day, BrdU reagent (10 µg/mL, Life Technologies) was diluted in cell culture medium containing the correspondent treatments and incubated for 8 h. After this time, cells were washed 3 times with PBS and fixed with ice-cold 70% EtOH at 4 ^{o}C for 10 min. Coverslips were washed 3 more times with PBS and incubated with 1N hydrochloric acid (HCl) at 37 ^{o}C for 30 min. HCl was used to unmask BrdU incorporated in newly synthetized DNA. For acid neutralization, borate buffer (nM: 100 boric acid, 75 sodium chloride, 25 sodium tetra-borate in distilled water; pH adjusted to 8.3) was added and samples were incubated at RT for 10 min. Then, the standard protocol for immunocytochemistry described in **Section 3.7** was followed.

Pictures of random fields were taken using an upright fluorescence microscope (Model DM6000B, Leica) and a total of 100 nucleus were counted in each sample. Proliferation rate was calculated as the ratio of double stained DAPI and BrdU number of cells (replicative cells) and single stained DAPI cells (non-replicative cells).

3.13.7.3. Cell counting Kit -8 (CCK-8) assay

Cells were seeded in 96 well plates at a density of 1000 cells/cm^2. Next day, treatments were added and maintained for 48 h. Thereafter, CCK-8 (Sigma) reagent was used following manufacturer's instructions and absorbance at 490 nm was read in a 96-well plate reader 3 h after reagent addition. This colorimetric method determines the number of viable cells in a sample. Samples where a higher signal is found will be expected to correlate with a higher number of cells and, consequently, with samples that had a higher proliferation rate. Results were presented as the rate of proliferative cells in a sample compared to control cells.

3.13.7.4. Scratch assay in vitro

Cells were seeded in 48 or 96 multi well plates at a density of 25000 cells/cm^2 and distributed in a proper monolayer. Two days after seeding, 10 µL tips were used to make a line across each well in order to simulate a scratch. Cells were washed with PBS and the correspondent cell culture medium and treatments for each sample were added. Scratch healing was monitored using an automatized time lapse microscope (DMI6000, Leica) or Incucyte® System (Essen BioScience). Healing area was measured with ImageJ software and expressed as the closed area percentage in each sample.

3.13.8. Fibrosis stimulation

NHCF-V were seeded in 6, 48 or 96 multi well plates at a density of 25000 cells/cm^2 and were allowed to attach for 24 h. Therefore, culture media was replaced for starvation media (high glucose DMEM, 0.5% EV-depleted FBS, 1% non-essential amino acids and 1% P/S). After 16 h, fibroblasts were stimulated with 100 µM L-ascorbic acid 2-phosphate (Sigma-Aldrich), 3.16 ng/mL ng/mL recombinant TGFβ-1 (R&D Systems) and 3.16 µg/mL dextran sulphate (Sigma-Aldrich) as previously described[380]. Compounds tested for their potential antifibrotic activity were added at the same time than stimulation media. Unstimulated cells (cells starved but not stimulated) and untreated cells (neither starved nor stimulated) were used as control conditions (ctrl). After 48 h, RNA was isolated for gene expression analysis (detailed in **Section 3.5**), cells were lysed and protein samples were isolated for protein expression analysis as described in **Section 3.6**, or cells were fixed with 4% PFA and analyzed by immunofluorescence as previously explained in **Section 3.7**.

3.14. *In vivo* studies

Animal handling was done according to the stipulated requirements by the Royal Decree 53/2013 on the protection of animals used for experimentation and other scientific purposes, and in compliance with all the ruler and recommendations of the Animal Ethics Committee (AEC) and Animals Welfare Committee (AWC) of La Fe Hospital Research Institute.

3.14.1. Ischemia/Reperfusion *in vivo* models

In this work, Wistar rats (Charles River Laboratories Inc.) and Large White swine ("El Pampo" farm) were used for ischemia-reperfusion-induced injury *in vivo* model.

3.14.1.1. Ischemia/Reperfusion in vivo rat model: occlusion by left anterior coronary artery ligation

First, preparation of the operating area was necessary to ensure asepsis during surgical procedure. All surgical instruments were cleaned with hydrogen peroxide before and after each individual surgery. For this work, adult male Wistar rats weighing 400±12 g were used. Anesthesia and analgesia were induced in order to facilitate animal handling, reduce animal suffering and minimize physiologic negative consequences derived from surgical intervention. **Table 3.11** summarizes the anesthesia and analgesia protocols used before, during and after surgical intervention.

Table 3.11. *Anesthesia and analgesia protocols for AMI induction in Wistar rats.*

Stage*	**Anesthesia**				**Analgesia**		
	Product**	Adm***	Dose (mg/kg)	0_2 content (L)	Product**	Adm***	Dose (mg/kg)
Pre-S and AI	Sevorane	INH	6 %	0.6	Fentanyl	IP	0.05
AM	Sevorane	INH	2.5 %	0.3	-	-	-
Post-S	-	-	-	-	Buprenorphine	IP	0.05

*S: Surgery; AI: Anesthesia induction; AM: Anesthesia maintenance; **Sevorane (Sevoflurane, Abbott); Fentanyl (Fentanest, Kern Pharma); Burprenorphine (Buprex, Schering-Plough); ***Adm: Administration; INH: Inhalation; IP: intraperitoneal.

Prior to experiments, animals were randomized into experimental groups, with each group composed of four rats, and body weight was recorded. A dosage of fentanyl was administered to each animal before anesthesia. Then, rats were introduced in a chamber and anesthetized with sevorane, placed in supine position and endotracheal intubation was performed with a 18G catheter (diameter: 1.3 mm; length: 5 cm) exposing the neck to white light to enhance trachea visualization. Endotracheal intubation is critical to connect animals breathe to the small animal ventilator (Model 683, Harvard Apparatus). Tidal volume of 2 mL and respiratory rate of 100 breaths per minute as well as anesthetic supply were maintained during all the procedure.

Neck and chest areas were shaved and disinfected with povidone-iodine (Betadine, Viatris Manufacturing) and ethanol 70% and animals were placed on a homeothermic blanket system in order to maintain body temperature. Once breathing is stabilized, the chest is opened at the fourth intercostal space using round end scissors to avoid additional tissues or organs damage, and a chest retractor was positioned to spread the ribs and expose heart. After that, pericardium was carefully open and left anterior descending (LAD) artery was identified and transiently ligated using a 6-0 prolene suture (Premilene, Braun) for a 30-minute ischemic period. LAD artery occlusion causes a colour change in the heart tissue which depends on this artery irrigation and confirms AMI induction. Treatments were intra-myocardial injected 15 minutes after AMI induction. Two injections of 15 µL, one on each side of occlusion, were performed with a Hamilton syringe (Teknokroma). Treatments used for each group are detailed in **Table 3.12.** Two different diDHA doses were tested: 27.1 µg diDHAeq/kg (Dose 1) and 271 µg diDHAeq/kg (Dose 2). The correspondent amount of PGA in each dose of PGA-$diDHA_{6.4}$ was used: 65.4 µg PGA/kg (Dose 1) and 672.5 µg PGA/kg (Dose 2). After 30 minutes, suture was removed to induce blood flux restoration (reperfusion), chest retractor was removed and ribs were drawn together using a 3-0 prolene suture (Monosyn, Braun). Animals were carefully recovered from anaesthesia; wound was healed with povidone-iodine and one dose of buprenorphine was administrated to reduce pain after surgical procedure. PBS (30 µL) was injected in control rats (I/R+PBS). For the positive control group, Esmolol at 0.5 mg/kg was injected. SHAM-operated rats were submitted to the same surgical procedure, except LAD artery was not ligated. Animals were sacrificed 24 h after reperfusion.

Table 3.12. *Groups, treatments and doses injected in I/R rat in vivo model.*

	Group	diDHA (µg)	PGA (µg)	Compound (µL)	PBS (µL)
Dose 1	I/R+PGA	0	124		
	I/R+PGA-$diDHA_{2.2}$	10	117	9.3	20.7
	I/R+PGA-$diDHA_{6.4}$	10	124	2.5	27.5
	I/R+diDHA	10	-	2	28
Dose 2	I/R+PGA	0	229		
	I/R+PGA-$diDHA_{6.4}$	100	229	22.8	7.2
	I/R+diDHA	100	-	20	10

3.14.1.2. Ischemia/Reperfusion in vivo swine model: mid-left anterior descending artery occlusion with coronary balloon catheter

Before surgical procedure, surgical area was prepared and surgical material was washed and sterilized with sterile PBS and chlorhexidine (Sandoz, Germany) to ensure antiseptic conditions. The study population was composed by Large White female domestic pigs weighing 39.1±4.4 kg. Animals were randomized into 4 groups: I/R (n=12), I/R+PGA (n=4), I/R+PGA-diDHA$_{6.4}$ (n=8), and I/R+Esmolol (n=8). Doses of the different treatments were extrapolated from the in vivo rat model: 27.1 µg diDHA eq/kg of PGA-diDHA$_{6.4}$ and 0.5 mg/kg Esmolol. PGA dose: 72.9 µg/kg. All molecules were dissolved in a final PBS volume of 4 mL for coronary infusion. PBS alone was infused in the I/R group.

The anti-platelet aggregation drug Clopidogrel (125 mg, Chiesi Inc.) was administrated 24 h before the surgical procedure to prevent platelet aggregation during surgery. To perform the experiment, animals were pre-anesthetized with intramuscular ketamine (Ketolar, 15ml, 50 mg/ml, Pfizer) prior to tracheal intubation. To induce anesthesia, 200 mg of the sedative Propofol (Sandoz) were administrated intravenously. In order to ensure animals wellbeing during surgical process, additional medication in physiological saline was administrated at 150 ml/h using a medicine dropper. Each 500 mL of PBS contained the following compounds: 150 mg amiodarone (Trangorex, antiarrhythmic agent, Sanofi); 10 mg Metasedin (analgesic, Esteve); 15 mg Midazolam (sedative, Hameln Pharma Ltd.). Additionally, 1 g of Amoxicillin (antibiotic, Sundent Pharmaceutical Co., Ltd.) was intravenously injected to prevent infections. Animals were maintained in a surgical plane of anesthesia with inhaled Sevoflurane (2% to 3%) through a volume-controlled ventilator (tidal volume 10 to 15 ml/kg and ventilation rate 8 to 15 breaths/min). Tidal volume, respiration rate, and aspirated oxygen percentage (FiO_2) were adjusted to maintain normocapnia: end-tidal carbon dioxide ($EtCO_2$) and arterial carbon dioxide ($PaCO_2$) 35 to 45 mm Hg, as measured by a capnometer (NPB-75, Nellcor-Puritan-Bennett, Boulder) placed on the intubation tube. Electrocardiography (ECG), $EtCO_2$, rectal and esophageal temperatures, and blood pressures (aortic and central venous) were monitored and recorded throughout the procedure using a multichannel data acquisition system (AD Instruments, Colorado Springs). One bolus of 1% heparin (5000 UI/5 ml, Sagent Pharmaceuticals) was administrated at the onset of instrumentation.

Occlusion ischemia was induced using a coronary balloon catheter (LVD Biotech Medical Devices) advanced to a mid-left anterior descending artery location

typically proximal to the first diagonal branch and inflated to 3 to 6 atmospheres for 90 min. Vessel occlusion and ischemia were confirmed with gadolinium contrast medium injection by cardiac magnetic resonance (CMR) and STEMI check on ECG as illustrated in **Figure 3.4 A and B**. A second bolus of 0.5% heparin (2500 UI/2.5 ml) was injected one hour after the first administration. PBS, PGA, PGA-diDHA$_{6.4}$ or Esmolol were infused 10 min before balloon deflation (reperfusion). One week after the surgical procedure, pigs were anesthetized to perform cardiac magnetic resonance and euthanized as will be explained in **Section 3.16**. Blood samples were collected at baseline, after reperfusion, and seven days after AMI to measure cardiac troponin I (cTnI) serum levels by ELISA assay following manufacturers' instructions (Life Diagnostics Inc., West Chester, PA, USA).

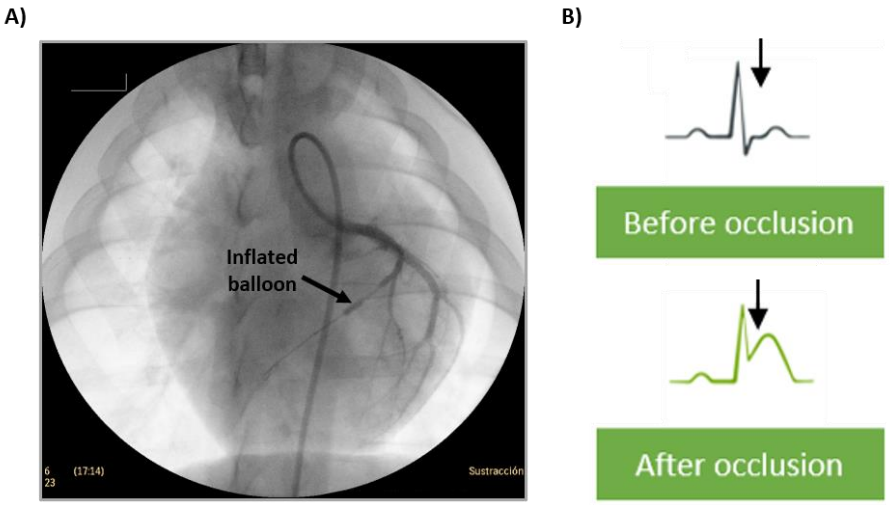

Figure 3.4. Vessel occlusion confirmation. (A) *Example of gadolinium contrast medium images taken during surgical procedure. Coronary balloon catheter was inflated to induce myocardial ischemia.* ***(B)*** *Physiological (before occlusion) and elevated (after occlusion) ST segment. Electric waves show the pattern recorded during ECG monitoring. Panel B Adapted from Vogel B et al, 2019.*

3.14.2. Cardiac magnetic resonance

One week after AMI induction in pigs, CMR examinations were conducted with RM Philips 3-Tesla Achieva Tx (Philips). The imaging protocol included a standard segmented cine steady-state free precession sequence to provide high quality anatomic references and assessment of left ventricular mass, wall thickness, and

LVEF; a T2-wheighted short-tau inversion recovery (T2wSTIR) sequence to assess the extent of edema and intramyocardial hemorrhage; a T2- gradient-spin-echo mapping sequence to provide precise myocardial relaxation time properties; and a T1-weighted inversion recovery turbo field echo sequence acquired 10 min after the administration of gadolinium contrast (late gadolinium enhancement) to assess the area at risk (AAR) and microvascular occlusion. CMR images were analyzed using dedicated software (MR Extended Work Space 2.6; QMassMR 7.6; Medis) by two observers experienced in CMR analysis and blinded to group allocation.

3.15. Histological Techniques

Histology refers to the study of the cellular organization of biological tissues and organs. In this section, the whole process developed between animals' euthanasia and the final sample production for analysis. Different techniques of euthanasia were used depending on the requirements of subsequent staining procedures.

3.15.1. Tissue collection and staining

Fixed or fresh tissue are required for histology procedures depending on the later experimental protocols. On the one hand, samples fixation allows the interruption of degradation processes after cell death, ensuring a cellular and tissue ultrastructure's good conservation. On the other hand, fresh tissue collection allows the study of metabolic processes or enzymatic activities.

3.15.1.1. Fresh tissue collection

An overdose of 50 mg/kg sodium thiopental (Braun) and 0.05 mg/kg fentanyl was administered IP to sacrifice rats. Animal decease was confirmed using toe pinch-response method and checking eyeball color. In order to euthanize pigs, an overdose of thiopental and potassium chloride was injected and asystole was confirmed in the ECG panel. Then, hearts were removed surgically by thoracotomy, rinsed twice with physiological saline buffer immediately and processed for further analysis.

3.15.1.2. 2,3,5-Triphenyltetrazolium chloride staining

Biological material has not enough contrast to appreciate its structure, integrity and composition. However, tissues can incorporate and fix several dyes or coloring

compounds, and this incorporation will be different depending on the physiological conditions. Staining techniques allowed measurement of heart healthy and damaged area and observe differences between experimental conditions.

2,3,5-Triphenyltetrazolium staining chloride (TTC) staining is a common metabolic dye used for infarct size calculation in brain or heart fresh, unpreserved tissues. TTC is a redox indicator which can differentiate between metabolically active and inactive tissues. Specifically, this dye allows to distinguish viable tissue (stained in red) from non-viable tissue (infarcted zone, in white).

Collected hearts from rats or pigs were cut carefully in 2 mm or 1.5 cm slices using a rodent guillotine or a surgical knife, respectively. Thereafter, resultant slices were immersed in 1% TTC staining solution (1% TTC in isotonic PB, pH 7.4) at 37 ˚C for 20 min in absence of light. After that time, heart slices were imaged, and regions of infarcted tissue were traced using ImageJ software (NIH). Area at risk was calculated measuring the damaged area on each slice and expressed as the volume of infarcted tissue related to the total heart volume.

3.16. Statistics

All results are expressed as average ± standard error of the mean (SEM). Data were analyzed using Graphpad Prism 5 and 8 software (La Jolla). Shapiro-Wilk test was applied to check data normal distribution. T-test for paired samples was applied to compare results between two experimental groups, while Mann-Whitney U-test was used to compare non-parametric samples. ANOVA analysis followed by Dunnett's or Tukey's post hoc tests was employed when it was required to compare data from more than two independent experimental groups. Statistically significant differences between experimental groups were considered when p value was inferior to 0.05 ($p<0.05$) in all cases.

4. Results

4. Results

Two new strategies for cardiac damage prevention during AMI have been proposed in this work. One of them is directed to the treatment of ischemia/reperfusion injury and is based on the ischemic area pre-conditioning before blood flux restoration (reperfusion) using one type of nanoparticles (NP), with therapeutic potential. The other is focused on the use of Oncostatin-M-enriched small extracellular vesicles (SEV) form genetically modified mesenchymal stem cells (MSC) to mitigate cardiac fibrosis after ischemic insult or cardiac overload.

Results are organized in two sections:

Section A: PGA-diDHA-based nanoconjugates role in cardiomyocytes pre-conditioning during ischemia-reperfusion induced injury.

Section B: OncostatinM-enriched SEV isolated from genetically modified MSC as potential anti-fibrotic agent.

Section A: PGA-diDHA-based nanoconjugates role in cardiomyocytes pre-conditioning during ischemia-reperfusion induced injury.

4.1. Human coronary microvascular endothelial cells, Neonatal Rat Cardiomyocytes and Neonatal Rat Cardiac fibroblasts characterization

NRVM and cFib isolation protocol from cardiac tissue obtained from 1-3 days-old rats is based on the enhanced ability of fibroblasts to adhere to plastic surfaces over cardiomyocytes, as previously mentioned in Section 3.1.2.3[374]. However, primary cultures obtained after cardiac tissue disaggregation can be contaminated by other types of cells, including those with endothelial origin. To test the purity of obtained cell cultures, a morphological inspection along with characterization by immunofluorescence assay was performed in three cell isolation processes. HMVEC-C line was used as positive control of endothelial cells. Additionally, since the administration of nanoconjugates into cardiac tissue *in vivo* should be intracoronary, it was also tested if nanoconjugates could be internalized by this cell line. Bright field images of HMVEC-C, NRVM and cFib are showed in **Figure 4.1 A**. CD31 expression, a marker of endothelial cells, was detected in coronary microvascular endothelial cells, but not in NRVM or cFib cultures after immunostaining. Additionally, cardiac troponin T (TnTc) was detected in NRVM, confirming the nature of each type of cell. Finally, Vimentin was detected in cFib, which is mainly indicative of a cell with vascular smooth muscle cell or fibroblast origin. Beat rate was also measured in NRVM counting the number of beats per minute (bpm) after three different NRVM isolation processes (**Figure 4.1 B**).

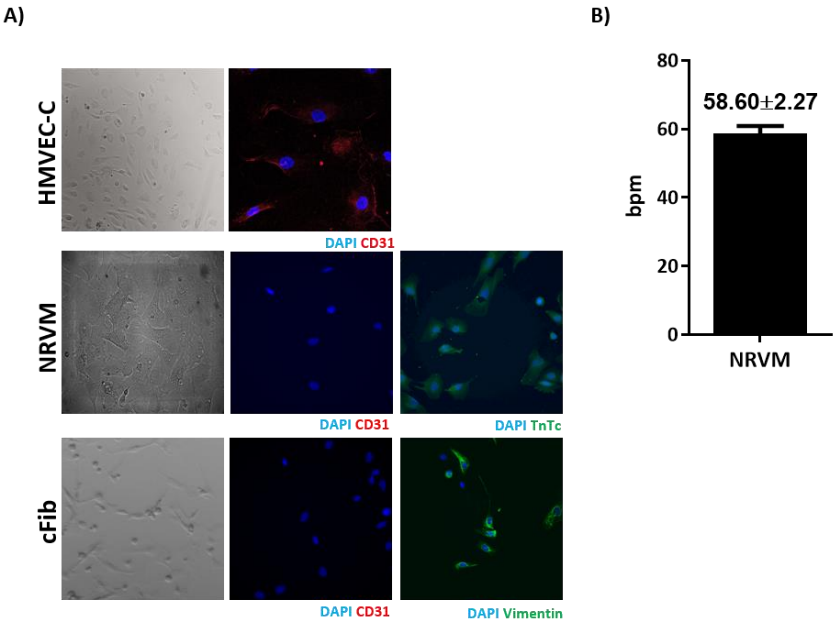

Figure 4.1. HMVEC-C, NRVM and cFib characterization. (A) *Bright field images and specific markers for endothelial, fibroblasts and myocyte cell linages staining by immunofluorescence. CD31 staining is showed in red for the three cell types, while TnTc and Vimentin are shown in green in NRVM and cFib, respectively. Nuclei are shown in blue (DAPI). Scale bar=100µm.* ***(B)*** *Number of beats per minute (bpm) of NRVM after isolation. Data represent mean ± SEM of three different cell batches.*

Cell morphology screening and protein markers expression studies consistently showed that isolated NRVM and cFib populations were highly pure and consequently suitable for use in further experiments.

4.2. Half maximal inhibitory concentration in HMVEC-C, NRVM and cFib depends on nanoconjugates diDHA loading and encapsulation

Cytotoxicity studies are key to test if candidate therapeutic molecules are compatible with relevant cell models. Cytotoxicity of PGA-diDHA-based nanoconjugates as well as PGA and free diDHA was assessed in target cells. With this purpose, different amounts of diDHAeq (µg) for each PGA-diDHA nanoconjugate and free diDHA (µg diDHAeq: 2, 5, 10, 20, 25 and 50), and the correspondent dose of PGA for each nanoconjugate concentration tested was

administered in HMVEC-C, NRVM and cFib for 72 h by MTS assay and LDH activity measurement. **Figure 4.2 A** shows cell viability values obtained by MTS assay. Free diDHA had the highest cytotoxic effect in all cell types, showing cell viability values below 50% when more than 10 µg diDHAeq were administered (LC_{50} in HMVEC-C, NRVM and cFib: 14.30, 16.10 and 11.08 µg diDHAeq). Non-significant decreases in cell viability were obtained when PGA and PGA-diDHA nanoconjugates were added at different concentrations in NRVM and cFib. HMVEC-C were more sensitive to treatments than cardiomyocytes and cardiac fibroblasts. Nevertheless, cell viability was not inferior to 50% at the higher dose tested when PGA or PGA-diDHA nanoconjugates were administered in any cell type, and LC_{50} could not be calculated.

LDH activity was measured in cell culture media 72h after nanoconjugates or free diDHA treatment (**Figure 4.2 B**). Concretely, LDH activity in both HMVEC-C and cFib was very similar after exposure to nanoconjugates and free diDHA, and only an increase of LDH activity was only detected in NRVM when treated with 25 µg of diDHAeq of all PGA-diDHA-based nanoconjugates tested and free diDHA. However, no major differences were observed on the rest of experimental conditions.

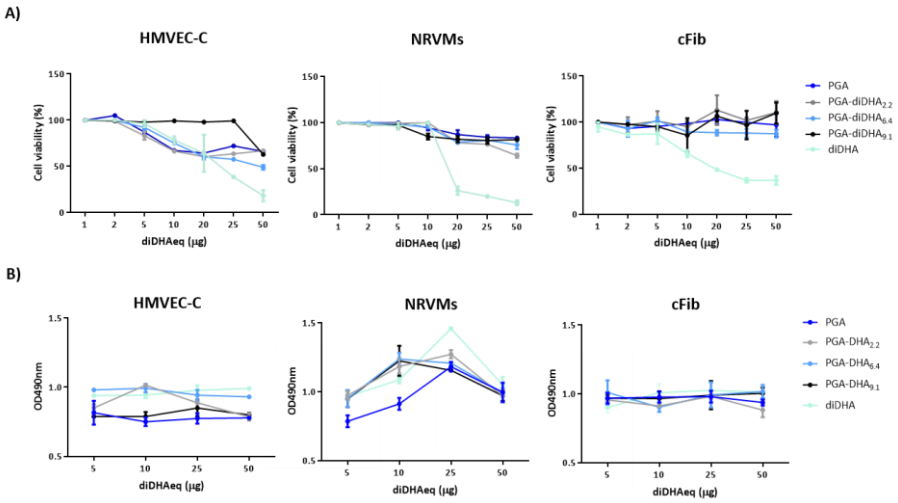

Figure 4.2. PGA, PGA-diDHA-based nanoconjugates and free diDHA cytotoxic effect in HMVEC-C, NRVM and cFib viability. *Cells were treated with increased diDHA doses (µg diDHAeq: 1, 2, 5, 10, 25, 50) for 72 and* ***(A)*** *cell viability by MTS assay and* ***(B)*** *LDH activity were measured. Read out was performed by spectrophotometry (absorbance at 490 nm) in both cases. Data presented were*

obtained from to three independent experiments, and results were normalized to values obtained from untreated cells and are represented as mean ± SEM.

These data suggest that diDHA encapsulation can be useful to increase administration dose while not affecting cell viability, and use of PGA-diDHA-based nanoconjugates could less cytotoxic than free diDHA.

4.3. PGA-diDHA-based nanoconjugates uptake evaluation in HMVEC-C, NRVM and cFib

The ability of nanoconjugates uptake by CM, HMVEC-C and cFib was evaluated after adding three different nanoconjugates concentrations. Nanoconjugates labelled with Oregon Green 488 dye (OG), were used for tracking purposes in these experiments. In order to find a balance between cell viability and biological effect and based on previous results showed in **Figure 4.2 A**, three diDHA dose (5, 10 and 20 µg diDHAeq) were chosen and PGA-OG was added at the correspondent dose. Based on previous studies, nanoconjugates uptake was measured as percentage of OG positive cells after 30 min of exposure[381]. Results are shown in **Figure 4.3 A-C**. PGA-OG, PGA-OG-diDHA$_{2.2}$, PGA-OG-diDHA$_{6.4}$ and PGA-OG-diDHA$_{9.1}$ at the selected doses were significantly uptaken by HMVEC-C, NRVM and cFib in comparison to untreated cells (ctrl), except for the lower dose of PGA-diDHA$_{6.4}$ (5 µg diDHAeq) in HMVEC-C and NRVM.

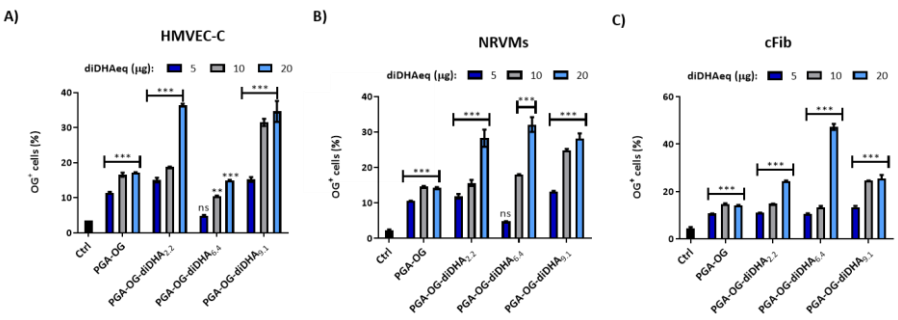

Figure 4.3. PGA and PGA-diDHA OG-labeled nanoconjugates uptake by HMVEC-C, NRVM and cFib is dose-dependent. *Compounds were added at three different concentrations (5, 10 and 20 µg diDHAeq) for 30 min and percentage of OG positive cells were measured in* ***(A)*** *HMVEC-C* ***(B)*** *NRVM and* ***(C)*** *cFib by flow cytometry (ex./em.: 488/535 nm). Data were analyzed by ANOVA and Tukey's*

*post-hoc test and are shown as mean ± SEM from three independent experiments (ns: non-statistically significant differences; **p<0.01; **p<0.001).*

These data demonstrated that the candidate nanoconjugates, as well as PGA-OG, can be internalized by coronary microvascular endothelial cells, ventricular myocytes and cardiac fibroblasts *in vitro*, making possible to asses a functional effect on target cells.

4.4. Oxygen and glucose deprivation and reperfusion protocol *in vitro*

To mimic I/R-induced injury conditions *in vitro*, an oxygen and glucose deprivation and reperfusion protocol was set up in NRVM as detailed in **Section 3.11**. Experimental outline is showed in **Figure 4.4 A**. Cell culture medium was replaced for non-glucose DMEM and cells were placed in a hypoxia chamber adjusted to 1% 0_2 and 37 ˚C for 6 h (ischemia, I). Treatments were added after 5 h 30 min of I. Next, culture medium was replaced for complete high-Glucose DMEM and plates were placed in an incubator with 21% 0_2 at 37 ˚C for 1 h (I/R). Cells in normoxia (Nx, 21% 0_2 at 37 ˚C) were used as control. Hypoxia induction was corroborated by an increase in HIF1-α protein expression measured by Western Blot in NRVM in basal conditions (Nx), after I and after I/R. As shown in **Figure 4.4 B** and **C,** statistically significant increase of HIF1-α was observed in ischemic conditions compared to Nx condition ($p<0.001$), and no-statistically significant differences were observed when Nx and I/R protein samples were compared. This protocol served as a starting point to measure functional parameters of interest in cardiac cells.

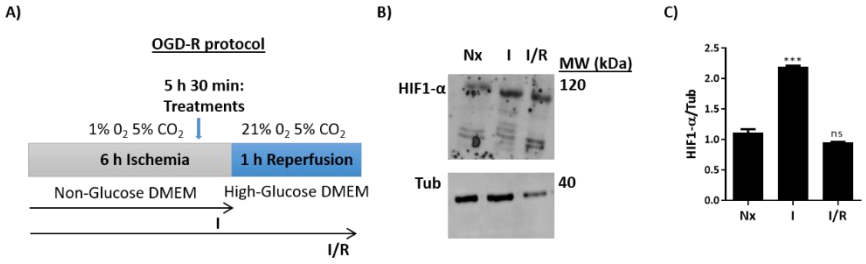

***Figure 4.4. OGD-R in vitro model set up to mimic I/R-induced injury**. **(A)** I/R protocol scheme. Cell culture media was replaced by Non-Glucose DMEM and cells were transferred to a hypoxic chamber for 6h. Compounds were added after 5h 30 min. Next, culture media was replaced by High-Glucose DMEM and placed in a standard incubator. Finally, functional parameters of interest were analyzed. **(B)** Ischemia induction confirmation by HIF1-α expression in NRVM under Nx, I and I/R conditions by Western Blot. α-Tubulin expression was measured as housekeeping gene. Protein expression levels were measured by densitometry using ImageJ software **(C)** HIF1-α signal quantification normalized to α-Tubulin expression signal. Data are represented as mean ± SEM. ANOVA and Tukey's post-hoc test were applied for statistical analysis using Nx as reference condition (ns: non-statistically significant differences; ***p<0.001).*

4.4.1. PGA-diDHA-based nanoconjugates reduce Caspase 3/7 activity after I/R-induced injury

After verifying that PGA and PGA-diDHA-based nanoconjugates were not cytotoxic and could be internalized by target cells, the optimal dose of PGA, PGA-diDHA nanoconjugates and free diDHA was set up based on those previous experiments and the ability of nanoconjugates to reduce cell apoptosis in NRVM when added shortly before reperfusion.

Three concentrations of each nanoconjugate were tested (5, 10 and 20 µg diDHAeq) in order to decide which was the most effective for I/R *in vitro* experiments, and PGA and free diDHA were added at the equivalent concentration. A significantly lower proportion of apoptotic NVRMs cultured under Nx ($p<0.001$) and I ($p<0.01$) compared to I/R condition, demonstrating that we could mimic I/R-induced injury *in vitro* under the optimized experimental conditions (**Figure 4.5**). Non-significant differences were observed when PGA was administrated in any tested dose compared to I/R condition, pointing that encapsulating polymer alone does not have a functional effect against apoptosis in our experimental model. Pre-conditioning of ischemic cardiomyocytes with the three doses of PGA-diDHA$_{2.2}$, PGA-diDHA$_{6.4}$ and PGA-diDHA$_{9.1}$ resulted in a significant decrease of apoptotic cells after reperfusion. However, free diDHA treatment only was proven to significantly

reduce Caspase 3/7 activity when added at 10 µg diDHAeq, suggesting an increase in the functional effect of encapsulated diDHA against reperfusion-induced apoptosis compared with free diDHA.

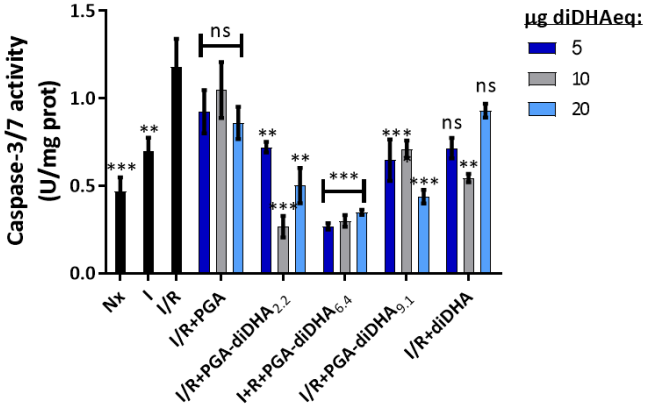

Figure 4.5. Caspase-3/7 activity screening after I/R and NRVM preconditioning. *Caspase3/7 activity was measured in NRMVs in Nx, I, I/R and I/R after adding PGA, PGA-diDHA$_{2.2}$, PGA-diDHA$_{6.4}$ and PGA-diDHA$_{9.1}$ and free PGA at 5, 10 and 20 µg of diDHA eq by luminescence. Cell lysates were obtained and data were normalized to the total protein content on each sample. Results are presented as mean ± SEM from three independent experiments. Values obtained from I/R condition was used as reference and data were analyzed with ANOVA and Tukey's post-hoc test (ns: non-statistically significant differences; **p<0.01; ***p<0.001;).*

In summary, results obtained from uptake experiments (**Figure 4.3**) showed that percentage of OG positive cells was increased when higher concentrations of NP were added to HMMVEC-C, NRVM and cFib. A statistically-significant decrease in Caspase3/7 activity was obtained when NP were added at a concentration of 20 µg diDHAeq. Contrarily, this effect was not observed when free diDHA was used. Furthermore, cell viability assay revealed that use of 20 µg diDHAeq of free diDHA had important cytotoxic effect on target cells. Alternatively, the use of the NP at a concentration of 5 and 10 µg diDHAeq did not have major cytotoxic effects in any of the cell models included and an acceptable percentage of OG positive cells after NP treatment was obtained (**Figure 4.2**). Finally, an enhanced decrease of Caspase3/7 activity was found when 10 µg diDHAeq of NP were added to preconditionate NRVM before reperfusion compared to values obtained when 5 µg diDHAeq were used in case of PGA-diDHA$_{2.2}$ and free diDHA (**Figure 4.5**). After

interpretation of the obtained data, we selected 10 µg diDHA eq as working concentration for further experiments.

4.4.2. PGA-diDHA nanoconjugates uptake depends on the physiological conditions of HMVEC-C and NRVM

Conjugates uptake by HMVEC-Cs and NRVM was assessed in normoxia and stressing conditions in order to test if there were differences in NP uptake after I/R. HMVEC-C and NRVM were cultured under physiological (Nx) and I/R conditions and NP uptake was measured after 30 min of exposure. As shown in **Figure 4.6 A** and **B** (HMVEC-C and NRVM, respectively), a higher percentage of OG positive cells was obtained when nanoconjugates were added to HMVEC-C and NRVM in Nx and I/R compared to control conditions (untreated cells in Nx or I/R), except from PGA and PGA-diDHA$_{6.4}$, where non-statistic significant differences were observed. Interestingly, it was found a significant increase in intracellular accumulation of PGA-OG-diDHA$_{2.2}$, PGA-OG-diDHA$_{6.4}$ and PGA-OG-diDHA$_{9.1}$ ($p<0.001$), but not PGA-OG, in both cell types under I/R when compared to the addition of the same dose of the compounds under Nx condition. Representative histograms of these data are displayed in **Figure 4.6 C**.

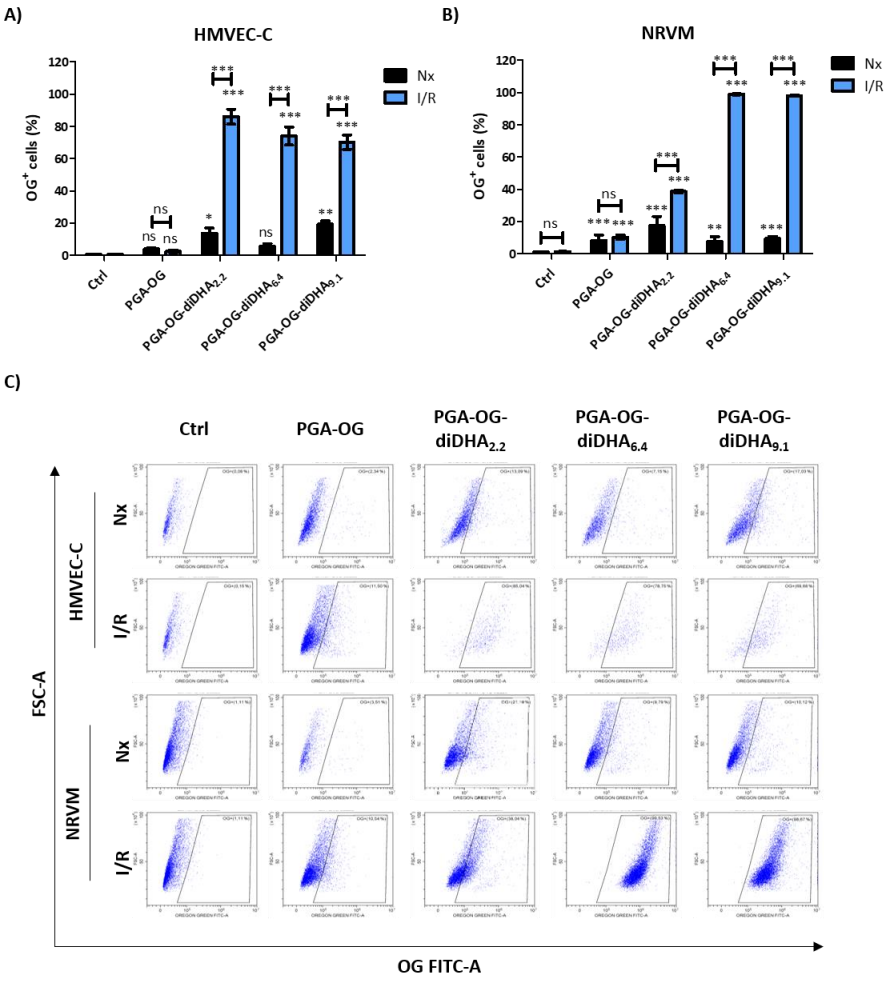

Figure 4.6. PGA-diDHA-based nanoconjugates uptake is increased in HMVEC-C and NRVM under ischemic conditions. *OG positive* ***(A)*** *HMVEC-C and* ***(B)*** *NRMV after Nx and I/R-induced injury.* ***(C)*** *Representative histograms showing OG positive cells. Data are represented as mean ± SEM of three independent experiments and analyzed by ANOVA and Tukey's post-hoc test (ns: non-statistic significant differences; *p<0.05; **p<0.01; ***p<0.001).*

Overall, these data suggest an enhanced PGA-diDHA-based nanoconjugates uptake by HMVEC-C and NRVM under I/R, favoring the internalization of our drug candidates in order to trigger a potential therapeutic effect in target cells.

4.4.3. NRVM uptake PGA-diDHA-based nanoconjugates from HMVEC-C more efficiently under I/R conditions

Given that the preferred route of administration in the clinical setting of nanoconjugates is intracoronary, a transcytosis assay from HMVEC-C to NRVM was designed in order to assess if microvascular endothelial cells would be able to transfer nanoconjugates to cardiomyocytes under Nx and I/R conditions as described in **Section 3.13.2.2**. HMVEC-C were seeded and treated with PGA-OG or PGA-OG-diDHA nanoconjugates in transwell inserts for 30 min. After that, cells were washed and culture media was refreshed. Next, inserts were transferred to a plate where NRVM under Nx or I/R conditions had been previously seeded to evaluate the ability of nanoconjugates to transverse endothelial cells and reach cardiomyocytes. Data were measured as percentage of OG positive NRVM. As shown in **Figure 4.7 A**, an increased transfer of nanoconjugates was observed when PGA, PGA-diDHA$_{2.2}$ and PGA-diDHA$_{9.1}$ were added to HMVEC-C and placed above NRVM in Nx compared to ctrl data, but not when PGA-diDHA$_{6.4}$ was used. This effect was more striking when NRVM were under I/R, where a statistically significant increase on NP uptake was observed in all cases. Importantly, a higher number of NRVM carrying OG fluorescent signal was observed under I/R conditions for PGA-OG, PGA-OG-diDHA$_{2.2}$, and PGA-OG-diDHA$_{6.4}$ ($p<0.05$ in all cases) but not PGA-OG-diDHA$_{9.1}$, compared to Nx, suggesting a selective uptake from HMVEC-C of nanoconjugates upon differential drug loading. This difference could be attributed to the different 3D conformation adopted by each conjugate in solution, since higher diDHA loading generate more compact and smaller nanosystems (data provided by Therapeutic Polymers laboratory in Principe Felipe Research Institute), probably hindering diDHA-cell membrane interactions. The increase in nanoconjugate uptake by stressed NRVM from HMVEC-C could be explained by cell communication via paracrine signaling by myocytes and endothelial cells, which is always active and variable depending on the environment and cellular physiological state[21]. Representative histograms of these results are shown in **Figure 4.7 B**.

To confirm the internalization of PGA-OG-diDHA nanoconjugates by NRVM, cells derived from the transcytosis assay were fixed and analyzed by confocal microscopy. Intracellular location of nanoconjugates in NRVM after transcytosis assay can be observed in **Figure 4.7 C**. **Figure 4.7 D** shows OG fluorescence intensity signal per cell quantification in NRVM under Nx and I/R conditions after transcytosis assay. Additionally, a significant increase in uptake of all administered compounds

under both Nx and I/R conditions compared to control was observed. Finally, a significantly higher level of compounds uptake under I/R when compared to Nx condition was also noticed.

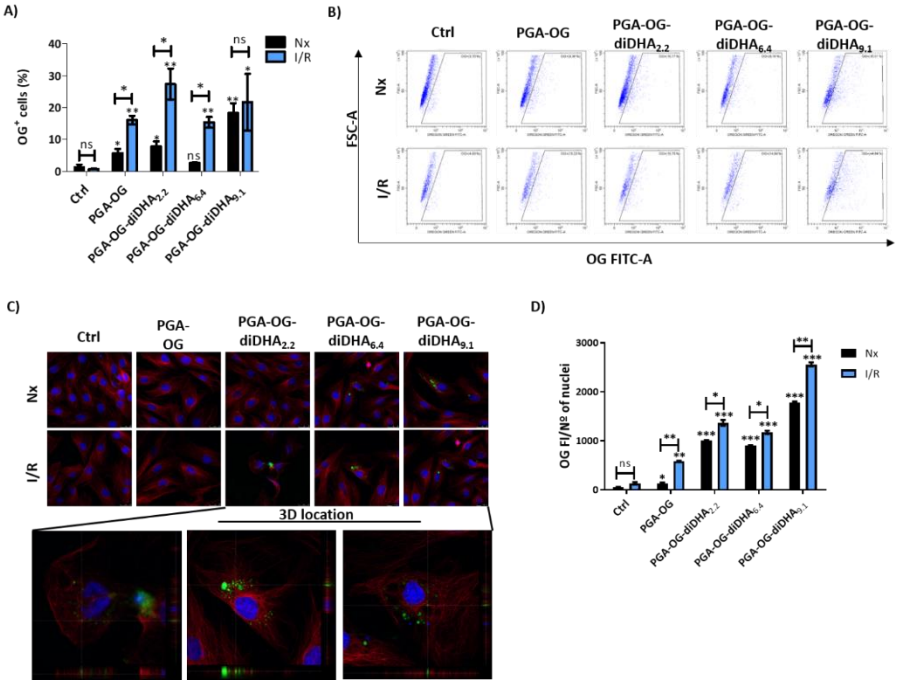

Figure 4.7. Nanoconjugates are able to traverse HVMEC-C and reach NRVM under I/R more efficiently than in physiologic conditions. (A) *OG positive NRVM percentage measured after 24 h by flow cytometry and* ***(B)*** *representative histograms from data obtained.* ***(C)*** *Representative pictures and nanoconjugates 3D location (Z stacks) in NRVM after transcytosis assay and* ***(D)*** *OG fluorescent intensity (FI) signal obtained per number of cells under all experimental conditions. Pictures were taken using 40X objective. Scale bar=50µm. Data are represented as mean ± SEM of three independent experiments and analyzed by ANOVA and Tukey's post-hoc test (ns: non-statistic significant differences; *p<0.05; **p<0.01; ***p<0.001).*

Altogether, these data provide evidence for the enhanced uptake of PGA-OG-diDHA$_{2.2}$ and PGA-OG-diDHA$_{6.4}$ from HMVEC-C by NRVM under stress-inducing conditions. When PGA-diDHA$_{9.1}$ was added to HMVEC-C, counteracting results using both experimental approaches were obtained, and flow cytometry data were unstable between experiments probably because of NP physicochemical characteristics mentioned above. Consequently, no clear conclusions about

differences between NRVM uptake in Nx or I/R could be settled for this particular nanoconjugate.

4.4.4. PGA-diDHA$_{6.4}$ limits I/R-induced injury by reducing apoptosis in NRVM

To corroborate the possible enhanced performance of some PGA-diDHA nanoconjugates as effective players to reduce I/R-induced injury of NRVM *in vitro*, additional apoptosis assays were performed. Therefore, apoptosis was measured through Annexin V/7-AAD staining by flow cytometry and the Bcl-2/Bax protein expression ratio by Western Blot. Esmolol, a cardioprotective drug commonly used for clinical practice, was included as positive control in these experiments.

Figure 4.8 A demonstrates a significantly lower proportion of total apoptotic cells when cultured under Nx (5.59±0.46 %, $p<0.01$) and I (7.00±1.44 %, $p<0.05$) conditions and compared to I/R condition (13.40±1.87 %), as expected after the obtained results in the previous experiments where Caspase 3/7 activity was measured after following the same OGD-R protocol. Detailed analysis revealed that 9.54±1.40 % of cells under I/R conditions were in late-apoptosis (Annexin V^+/7-AAD^+, in black) and 3.86±0.60 % were in early-apoptosis (Annexin V^+/7-AAD^-, in blue) compared to 3.57±0.34 % and 2.01±0.15 % in NRVM under Nx conditions, respectively.

Encouragingly, a significant decrease in the proportion of apoptotic cells following treatment with PGA-diDHA$_{6.4}$ (8.95±0.61 %, $p<0.05$) under I/R conditions was observed. Additionally, a significant reduction of cells in late apoptosis (4.61±0.40 %, $p<0.05$) when NRVM were preconditioned with PGA-diDHA$_{6.4}$ before reperfusion compared with I/R condition (9.54±1.40 %) was obtained. Of particular note, PGA-diDHA$_{6.4}$ pretreatment also leaded to a highly significant decrease in total and late-apoptotic NRVM after I/R-induced injury when compared to pretreatment with free diDHA (**Figure 4.8 A**). However, a significant decrease in NRVM apoptosis following treatment with PGA (17.41±1.87 %), PGA-diDHA$_{2.2}$ (11.22±1.61 %), PGA-diDHA$_{9.1}$(10.57±1.31 %), diDHA (16.91±0.36 %), or Esmolol (20.75±0.46 %) compared to I/R conditions was not detected. Although no significant differences in total apoptotic number of cells was obtained when NRVM were treated with PGA-diDHA$_{2.2}$, percentage of early apoptotic cells was significantly increased compared with retrievable cells found after I/R, indicating a possible beneficial

effect of this nanoconjugate avoiding massive cardiomyocytes death after reperfusion. Representative histograms for these data are shown in **Figure 4.8 B**.

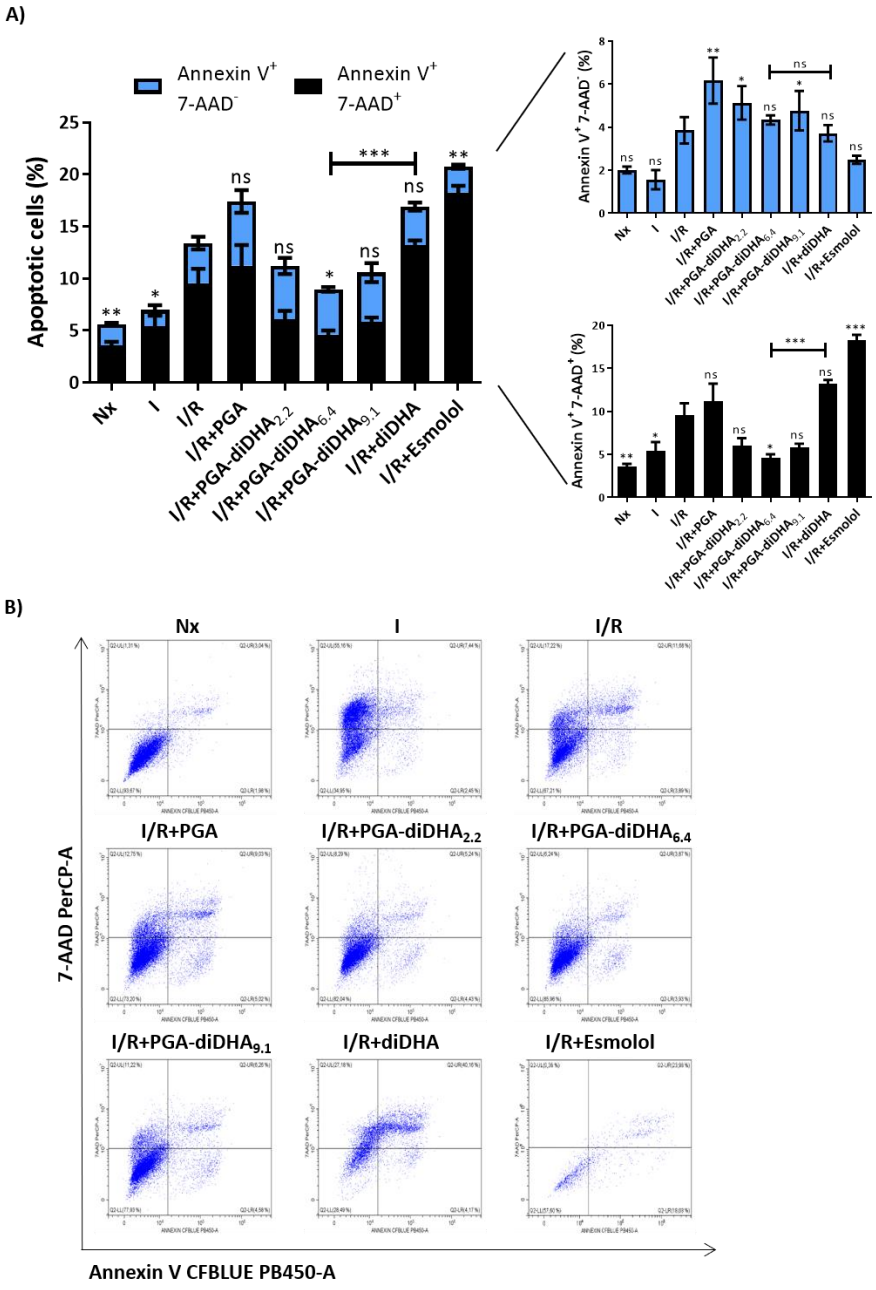

Figure 4.8. PGA-diDHA$_{6-4}$ protects NRVM against I/R induced injury by reducing late apoptosis. (A) *Total apoptotic cells measured by flow cytometry is shown in left panel, while early apoptotic cells*

(Annexin V CFBLUE PB450-A positive and 7-AAD PerCP-A negative events) and late-apoptotic cells (Annexin V CFBLUE PB450-A and 7-AAD PerCP-A double positive events) are shown in blue and black, respectively. ***(B)*** *Representative histograms of each experimental condition. Results were obtained from three independent experiments and showed as mean ± SEM and analyzed with ANOVA and Tukey's post-hoc test using values from I/R as reference condition (ns: non-significant statistic differences; *p<0.05; p<0.01; ***p<0.001).*

Proper balance of anti- and pro-apoptotic proteins of the Bcl-2 family also plays a significant role in regulating cell survival following I/R insult. While Bcl-2 inhibits apoptosis triggering, Bax expression provides a pro-apoptotic signal. **Figure 4.9** (representative Western blot and graph) demonstrates a significant increase in the Bcl-2/Bax expression ratio (suggesting an increase in anti-apoptotic signaling) in NRVM under Nx and those treated with PGA-diDHA$_{6.4}$ and Esmolol before reperfusion when compared to Bcl-2/Bax ratio in NRVM after I/R procedure. Again, we observed a trend on higher expression of anti-apoptotic signaling when PGA-diDHA$_{6.4}$ was added compared to NRVM preconditioned with free diDHA before reperfusion.

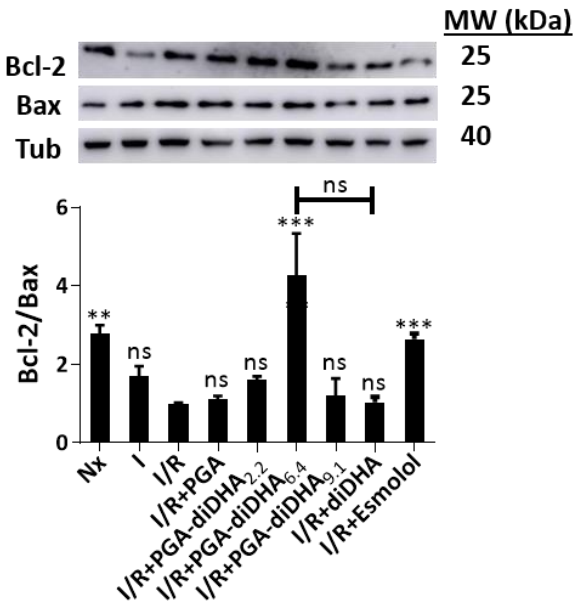

Figure 4.9. PGA-diDHA$_{6.4}$ preconditioning before reperfusion resulted in activation of anti-apoptotic signaling pathways in NRVM. *Anti-apoptotic (Bcl-2) and pro-apoptotic (Bax) protein levels were measured by Western Blot assay and quantified by densitometry using ImageJ software. Data*

*in graph are expressed as protein expression ratio (Bcl-2/Bax) normalized to Tubulin α-1A (Tub) signal for each condition. Results were obtained from three independent experiments, and are shown as mean ± SEM and were analyzed with ANOVA and Tukey's post-hoc test using values from I/R as reference condition (ns: non-significant statistic differences; **p<0.01; ***p<0.001).*

Overall, these data suggest that pre-conditioning of primary cardiomyocytes with PGA-diDHA$_{6.4}$ before reperfusion inhibits the activation of pro-apoptotic signaling pathways, leading to increased cell survival after I/R insult above the rest of nanoconjugates and compounds tested. Furthermore, comparison of free diDHA and PGA-diDHA$_{6.4}$ data highlight how an optimized PGA-conjugation approach can significantly increase the therapeutic potential of diDHA in the context of I/R-induced injury to cardiomyocytes.

4.4.5. PGA-diDHA nanoconjugates treatment attenuates autophagy activity in NRVM after I/R-induced injury

Once it was established that I/R conditions prompted apoptosis of NRVM *in vitro* and that that PGA-diDHA nanoconjugates afforded protection against apoptosis signaling pathways activation, their therapeutic potential was further explored. Myocardial I/R-injury associates with an increased abundance of structurally and functionally defective proteins; in response, the activation of the autophagic machinery leads to the sequestration of these defective proteins into a double-membranes structure known as the autophagosome, which then fuses with acidic vesicles known as lysosomes for degradation and recycling [382]. The activation of autophagy requires Beclin-1, and physical interaction between Bcl-2 and Beclin-1 has been described. Following a cell insult (such as I/R), Bcl-2 releases Beclin-1 to activate the autophagic pathway, which can cause severely detrimental effects [131, 383].

Analysis of this pathway, as shown in **Figure 4.10 A**, revealed significantly lower levels of Beclin-1 expression under Nx conditions when compared to I/R conditions in NRVM, suggesting higher autophagic activity in NRVM under I/R conditions. Pretreatment of NRVM under I/R conditions with all three PGA-diDHA nanoconjugates and Esmolol, but not PGA or and free diDHA, led to a significant reduction in Beclin-1 expression when compared to I/R condition, suggesting the attenuation of autophagy machinery activity. In this case, PGA-diDHA$_{6.4}$ failed to

provide for a significant reduction in Beclin-1 expression levels when compared to free diDHA under I/R. Overall, these data suggest that PGA-diDHA nanoconjugates may provide some marginal advantage with regards to the inhibition of massive autophagy activity.

In addition, number of lysosomes using Lysotracker® Deep Red staining in NRVM (**Figure 4.10 B** and **C**) was measured. Reduction in the number of acidic vesicles per cell under Nx conditions when compared to cells after I/R process was observed, suggesting higher lysosomal activity under I/R conditions. Significant reduction in the number of acidic vesicles per cell following PGA-diDHA$_{2.2}$, PGA-diDHA$_{6.4}$, and diDHA pre-treatment of NRVM when compared to I/R conditions was observed. However, no statistically significant differences between NRVM pre-conditioned with PGA-diDHA$_{6.4}$ or free diDHA were obtained.

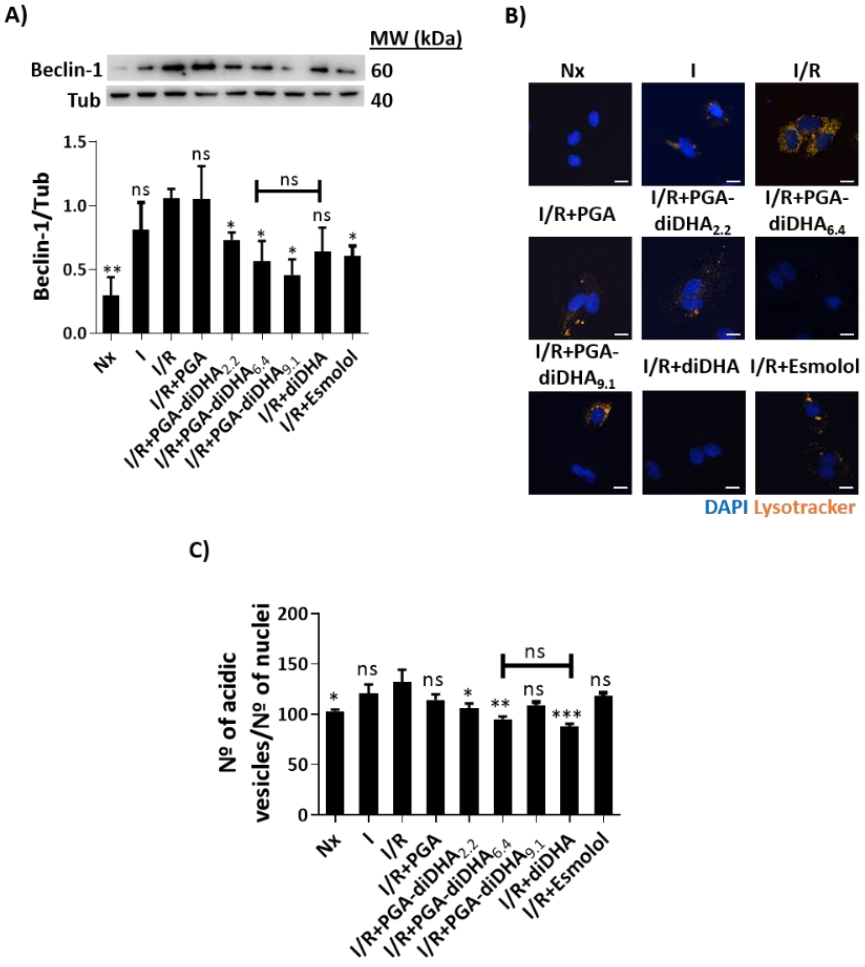

Figure 4.10. PGA-diDHA-based nanoconjugates protect NRVM against I/R-induced injury by reducing massive autophagy machinery activation and acidic vesicles accumulation. (A) *Beclin-1 protein expression under experimental conditions. Tubulin α-1A (Tub) protein expression was used to normalize Beclin-1 signal obtained from each sample. Results were quantified by densitometry using ImageJ software.* ***(B)*** *Representative pictures showing acidic vesicles screening in NRVM after LysoTracker Deep Red ® staining. Images captures at 400X magnification and captures by IN CELL analyzer 1000. Scale bar = 10 µm.* ***(C)*** *Number of acidic vesicles per number of nuclei ratio. Results were obtained from three independent experiments comparing the distinct groups with cells under I/R. Asterisks indicate statistically significant differences after ANOVA analysis followed by Tukey's post hoc test, and mean ± SEM is shown (ns: non-statistical significance; *p<0.05; *p<0.01; *p<0.001).*

These data suggested that the activation of the cellular degradation machinery after I/R insult, leading to the formation of a greater number of acidic vesicles and increased apoptosis. Pre-conditioning with PGA-diDHA nanoconjugates can reduce cell damage, with PGA-diDHA$_{6.4}$ providing the best results with regards to the amelioration of I/R-induced injury in terms of reduced apoptosis and mitigated autophagy.

4.4.6. PGA-diDHA-based nanoconjugates reduce reactive oxygen species generation and restore the I/R-induced loss of mitochondrial membrane potential in NRVM

As part of the characterization of cardioprotective processes activated by NP their role in preservation of mitochondria integrity when used for preconditioning in I/R assays was analyzed. It has been already described that additional protein quality control pathways driven by the endoplasmic reticulum (ER) become activated in response to I/R-induced stress. The ER stress response involves the upregulated expression of specific chaperones (e.g., GRP-78, GRP-94, or XBP1) that sense increased levels of unfolded proteins[379]. Reduced levels of GRP-78 expression were encountered in NRVM under Nx conditions when compared to I/R conditions ($p<0.01$), thereby suggesting higher levels of ER stress during I/R (**Figure 4.11**). However, no statistically significant differences were observed when data from I and I/R conditions were compared. Encouragingly, NRVM treated with PGA-diDHA$_{6.4}$ and free diDHA slightly inhibited the increase in I/R-induced GRP-78 expression by a similar degree ($p<0.05$), suggesting that both compounds can reduce ER-stress under these experimental conditions, but not significant differences were observed between both treatments. No significant differences were observed in NRVM under I/R following treatment with PGA, PGA-diDHA$_{2.2}$, PGA-diDHA$_{9.1}$, or Esmolol (**Figure 4.11**) when compared to I/R condition.

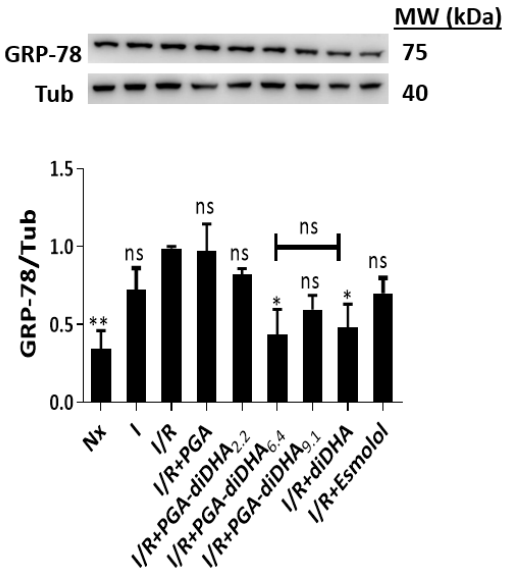

Figure 4.11. PGA-diDHA$_{6.4}$ and diDHA preconditioning before reperfusion resulted in a reduction of GRP-78 protein expression in NRVM. *GRP-78 protein expression was measured by Western Blot assay and quantified by densitometry in ImageJ software. Data were normalized by Tubulin α-1A (Tub) protein expression for each condition. Results were obtained from three independent experiments, and were analyzed with ANOVA and Tukey's post-hoc test using values from I/R as reference condition and represented as mean ± SEM (ns: non-significant statistic differences; **p<0.01; ***p<0.001).*

Given the known physical and functional links between the ER and mitochondria, studies have now provided evidence that GRP-78 regulates mitochondrial energy balance[379]. Moreover, the generation of ROS and mitochondrial function are connected to the autophagic machinery and ER stress, and this connection may represent a crucial component regulating cardioprotection under adverse conditions[384]. Additionally, most apoptotic stimuli (including oxidative stress, hypoxia, and nutrient deprivation) converge at the mitochondria, with mPTP (mitochondrial permeability transition pore) dysfunction leading to the formation of the "apoptosome" complex, which results in Caspase-3 activation[385].

In light of this potentially important role of mitochondrial function, alterations to mitochondrial membrane potential (MMP) in NRVM under I or I/R conditions using the JC-1 potential-sensitive fluorescent dye (**Figure 4.12 A** and **B**) were tested. Control NRVM (Nx) showed a granular cytosolic pattern of red fluorescence (corresponding to JC-1 aggregates), indicating the presence of mitochondria with

polarized mitochondrial membranes and a proper membrane potential. However, NRVM exhibited a loss of MMP and mitochondrial depolarization following I and I/R as indicated by increased JC-1 monomer (green fluorescence) accumulation. Significantly, pre-conditioning NRVM with PGA, PGA-diDHA$_{2.2}$, PGA-diDHA$_{6.4}$, PGA-diDHA$_{9.1}$, and Esmolol prevented the loss of MMP ($p<0.001$). On the contrary, diDHA failed to prevent the loss of MMP. Furthermore, PGA-diDHA$_{6.4}$ treatment provided the highest significant decrease in MMP in NRVM when compared to diDHA treatment before reperfusion ($p<0.001$). An additional analysis of mitochondria morphology by TEM showed differences between mitochondria structures in different conditions (**Figure 4.12 C**). Inner and outer membrane interspace as well as mitochondrial matrix seemed dilated, as showed by loss of contrast and packaging, after I and I/R-induced injury compared to control cell mitochondria (Nx). Similar effects than the ones reported for I and I/R conditions were observed after PGA and diDHA treatment, but not when NRVM were pre-conditioned with PGA-diDHA-based nanoconjugates or Esmolol. These observations support that mitochondria damage caused by I/R-induced stress could be reduced by the tested nanoconjugates.

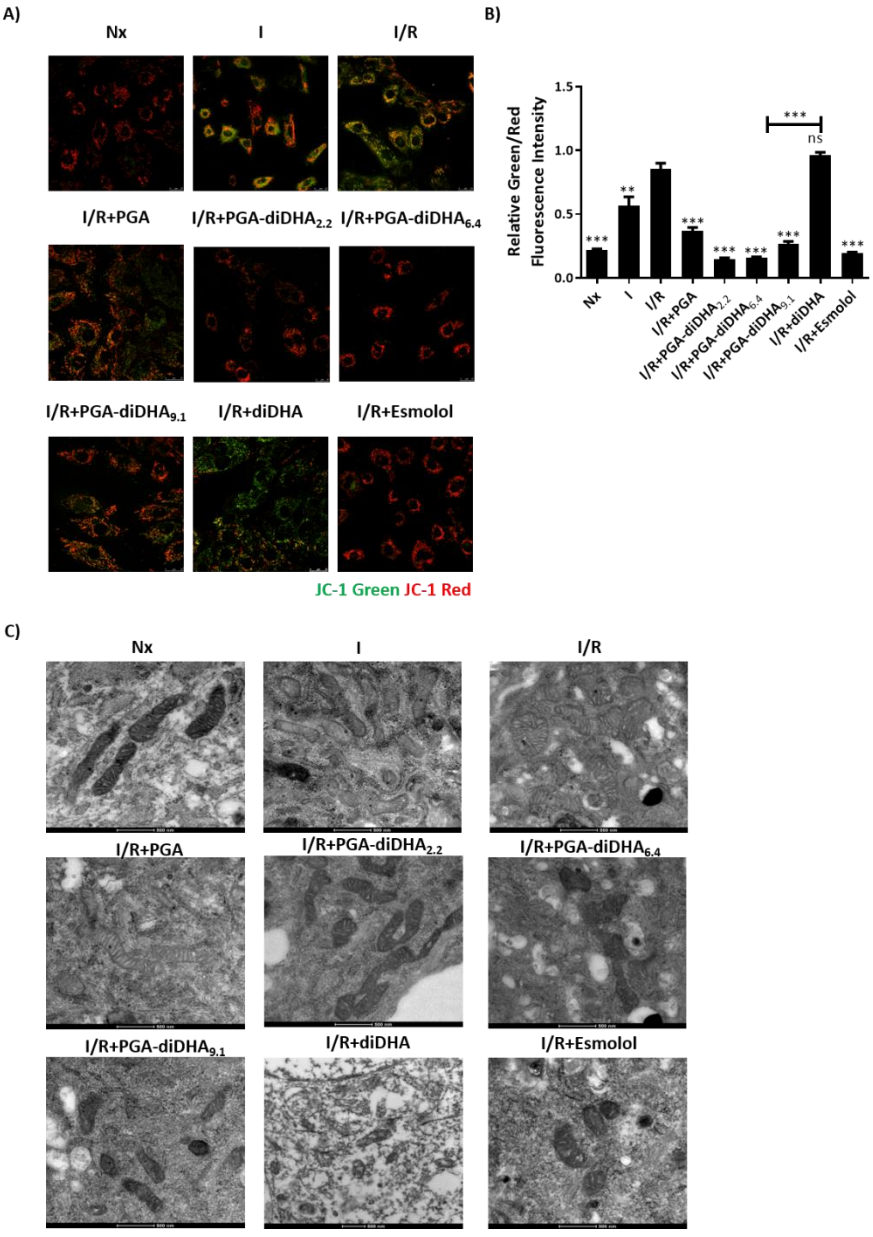

Figure 4.12. PGA-diDHA- based nanoconjugates maintain mitochondrial membrane potential (MMP) and mitochondria ultrastructure after reperfusion. (A) *Representative images for MMP destabilization measurement in the different experimental groups. Red fluorescence indicates normal MMP. Green fluorescence indicates monomer formation of JC-1 dye, and, subsequently, MMP depolarization. Images captures with confocal microscopy at 40X magnification, scale bar=25 µm.* ***(B)*** *Green to red fluorescence ratio quantification for MMP measurement by JC-1 dye staining assay.* ***(C)*** *Electron microscopy images focused on mitochondria ultrastructure under experimental conditions. Scale bar=500 nm. Three independent experiments were performed. Asterisks indicate*

*statistically significant differences after ANOVA analysis followed by Tukey's post hoc test comparing to I/R data, and are shown as mean ± SEM (ns: non-significative; **p<0.01; ***<p<0.001).*

Finally, ROS content was measured using the CellROX® orange fluorescent probe (**Figures 4.13 A and B**). Significantly reduced levels of ROS generation in NRVM in Nx and I compared to I/R condition were observed. Moreover, PGA and PGA-diDHA$_{2.2}$ pretreatment showed marginal effects on NRVM reduced ROS generation following I/R ($p<0.05$), while preconditioning with PGA-diDHA$_{6.4}$ and PGA-diDHA$_{9.1}$ led to a highly significant decrease in ROS generation in NRVM following exposure to I/R conditions ($p<0.001$). Esmolol pretreatment failed to significantly modulate ROS levels in NRVM following exposure to I/R conditions. Interestingly, pretreatment with free diDHA seemed to increase ROS production in NRVM following exposure to I/R conditions, therefore providing a highly significant difference when compared to PGA-diDHA$_{6.4}$ pretreatment ($p<0.001$).

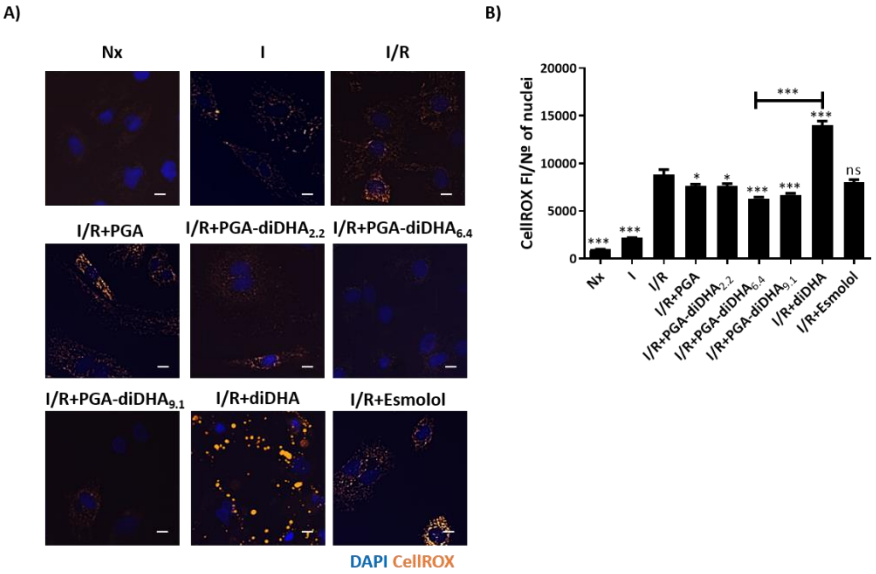

Figure 4.13. PGA-diDHA-based nanoconjugates reduced reactive oxygen species (ROS) generation after reperfusion. (A) *Representative pictures for ROS signal under Nx, I, I/R and I/R after NRVM pre-conditioning measures as Cell ROX® orange fluorescence intensity using 40X magnification lens, scale bar = 10 µm.* ***(B)*** *CellROX® orange fluorescence intensity signal per number of nuclei quantification for each experimental condition. Three independent experiments were performed. Asterisks indicate*

*statistically significant differences after ANOVA analysis followed by Tukey's post hoc test comparing to I/R data, and are shown as mean ± SEM (ns: non-significative; *p<0.05; ***<p<0.001).*

4.5. PGA-diDHA-based nanoconjugates do not promote cFib migration *in vitro*

In response to tissue mass loss and limited regeneration rate in adult mammal hearts, cardiac fibroblasts are activated, resulting in enhanced migration and proliferation in the damaged area, which provokes that previous functional cardiac tissue is replaced for non-contractile tissue. For this reason, the main goals of cardiac therapies are to avoid massive cardiomyocytes loss or replace fibrotic scar for functional tissue to improve cardiac function. In this sense, a scratch assay was performed to evaluate the effect that PGA-diDHA-based nanoconjugates could have on cardiac fibroblasts wound healing capabilities. Representative pictures and obtained results are obtained in **Figure 4.14 A** and **B**, respectively. Data showed a completely wound healing (95.46±2.35 %) in untreated cFib, while the addition of PGA (49±9.53 %, $p<0.01$), PGA-diDHA$_{2.2}$ (34±7.36 %, $p<0.001$), PGA-diDHA$_{6.4}$ (39±6.72 %, $p<0.001$) and PGA-diDHA$_{9.1}$ (27±6.47 %, $p<0.001$) diminished the closed area percentage compared to control cells, and a total wound healing was not observed in any of the conditions after 48 h. Importantly, exposure to diDHA resulted in high number of cFib death after 12 h of treatment, correlating with previous cytotoxicity *in vitro* results (**Figure 4.2**), so no further measures were possible.

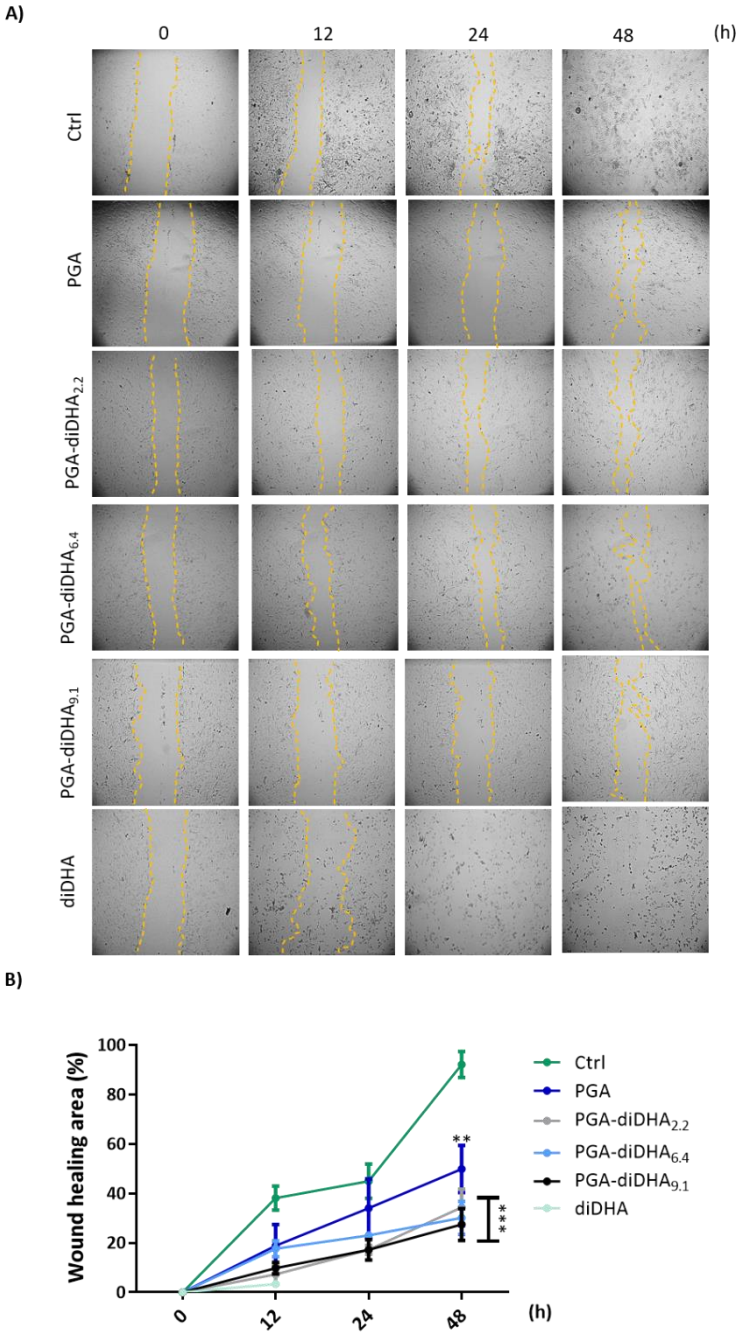

Figure 4.14. PGA-diDHA-based nanoconjugates do not enhance primary cardiac fibroblasts proliferation and migration capabilities. (A) *Representative pictures of scratch assay at 0, 12, 24 and 48 h after treatments. Yellow dashed lines indicate cell progression during selected time points.*

(B) *Wound healing area quantification over time. Area covered by cells after PGA, PGA-diDHA nanoconjugates and diDHA treatments was measured for 48 h. Control cells treated with PBS were used as control (ctrl). Three independent experiments were performed. Asterisks indicate statistically significant differences after ANOVA analysis followed by Tukey's post hoc test comparing to ctrl data, and are shown as mean ± SEM (**p<0.01; ***<p<0.001).*

Obtained results provided preliminary data indicating a possible functional effect of PGA-diDHA-based nanoconjugates in an ischemic context in terms of fibroblasts migration and proliferation modulation. Nevertheless, further studies, such as proliferation tests or gene expression analysis, would be necessary for validation.

Collectively, all PGA-diDHA nanoconjugates displayed some levels of cardioprotective activity, although their efficacy appeared to depend on diDHA loading. When considering the *in vitro* data as a whole, PGA-diDHA$_{6.4}$ was chosen as the leading candidate for subsequent *in vitro* studies in cardiomyocytes from human origin and *in vivo* studies given the enhanced outcomes compared to PGA-diDHA$_{2.2}$ and PGA-diDHA$_{9.1}$. Additionally, pre-conditioning with PGA-diDHA$_{6.4}$ provided enhanced results with regards to the attenuation of I/R-induced injury when compared to free diDHA.

4.6. PGA-diDHA$_{6.4}$ exerts a cardioprotective effect in human iPSC-derived CM

Several potential cardioprotective compounds fail when they are tested in human *in vitro* and *in vivo* studies. Because of this, the availability of *in vitro* cellular models with human origin for disease modeling and drug testing is highly important. In this context, human induced pluripotent stem cells (iPSC) are of special interest since they can be easily obtained from patients and healthy donors' peripheral blood mononuclear cells and can be differentiated into multiple cell types *in vitro*, as cardiomyocytes. In order to see if PGA-diDHA$_{6.4}$ maintained the cardioprotective potential against I/R-induced injury when tested in cardiomyocytes with human origin, a human iPSC line from a healthy donor was used. Human iPSC were differentiated to cardiomyocytes (iPSC-CM) and differentiation efficiency was confirmed by three different gene and protein expression analysis. First, increased expression TNNT2 and NKX2-5 together with OCT4 lower gene expression was obtained by RT qPCR 15 days after the induction of cell differentiation as showed in **Figure 4.15 A**. TNNT2 and NKX2-5 are expressed by cardiomyocytes, whereas OCT4 is expressed in undifferentiated or stem cells. Next, immunofluorescence

analysis for cTnT and Oct4 protein expression in cardiomyocytes after 30 days of differentiation revealed a huge enrichment of cTnT expression while a low expression of Oct4 (**Figure 4.15 B**). Furthermore, ~87% double positive cells for cTnT and MyHCα protein expression, which would represent CM population, were obtained as measured by flow cytometry (**Figure 4.15 C, Q2)**. Finally, beating rate was measured obtaining an average of 77±4 bpm (**Figure 4.15 D**).

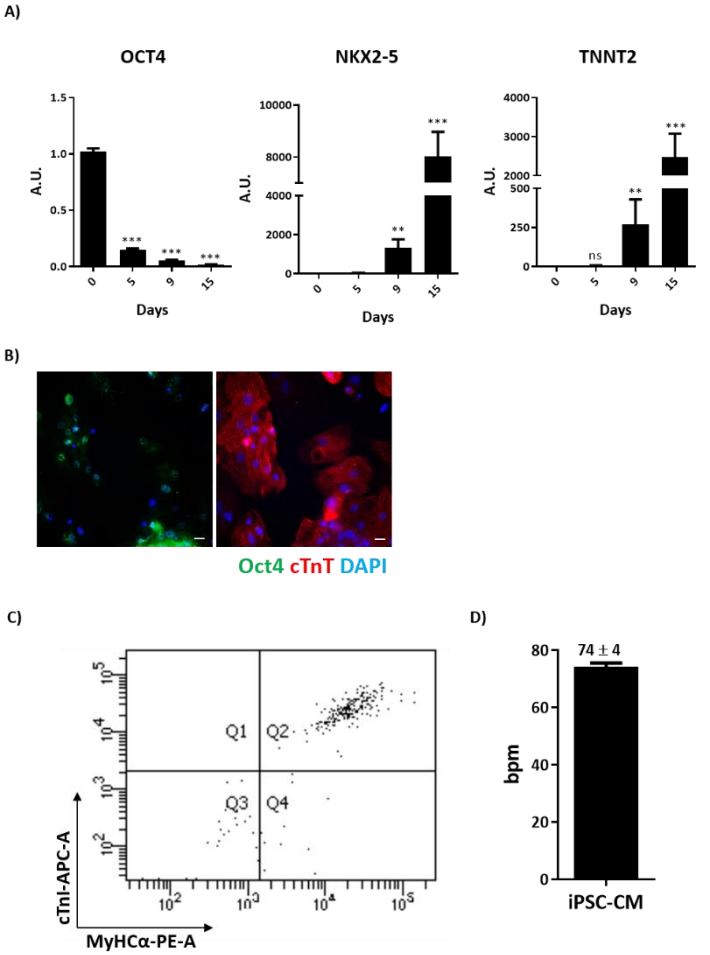

Figure 4.15. iPSC-CM quality control and characterization. (A) *OCT4, NKX2-5 and TNNT2 gene expression quantification in samples collected at day 0, 5, 9 and 15 during iPSC differentiation to CM. Fold change in gene expression compared to values obtained at day 0 are represented (arbitrary units, A.U.).* ***(B)*** *Representative pictures of Oct4 and cTnT staining in iPSC-CM at day 30 of differentiation. Scale bar = 100μm.* ***(C)*** *Representative histogram showing cTnI-APC-A and MyHCα-PE-A expression in iPSC-CM at day 30 of differentiation (Q1: cTnI-APC-A$^+$, MyHCα-PE-A$^-$; Q2: cTnI-*

*APC-A+, MyHCα-PE-A^{+}; Q3: cTnI^{-}APC-A^{-}, MyHCα-PE-A^{-}; cTnI-APC-A^{-}, MyHCα-PE-A^{+}. **(D)** Number of beats per minute (bpm) of iPSC-CM counted at day 30 of differentiation. Results obtained from three iPSC to CM differentiation processes. Asterisks indicate statistically significant differences after ANOVA analysis followed by Tukey's post hoc test comparing to data obtained at day 0 of differentiation, and are shown as mean ± SEM (ns: non-significative; **p<0.01; ***<p<0.001).*

After optimization of cardiomyocytes differentiation from iPSC, the effect of PGA-diDHA$_{6.4}$ on iPSC-CM compared to PGA and free diDHA was assayed to test if the previous results obtained in NRVM were reproducible in CM from human origin. As showed in **Figure 4.16 A** and **Table 4.1**, cytotoxicity assay and calculated LC_{50} values revealed an increased cell death rate when iPSC-CM were treated with lower amounts of PGA compared to results in NRVM. The addition of both PGA-diDHA$_{6.4}$ and free diDHA to iPSC-CM in a higher concentration than 20 µg diDHAeq also resulted in decreased percentage of viable cells, although this effect was less pronounced in iPSC-CM treated with PGA- diDHA$_{6.4}$, supporting the hypothesis that encapsulation of diDHA may be important to get a therapeutic effect in cardiomyocytes.

Next, two experiments previously performed in NRVM were repeated in an I/R-induced injury *in vitro* model of iPSC-CM. It was decided to measure apoptosis by Caspase 3/7 activity and ROS production after PGA, PGA-diDHA$_{6.4}$ or free diDHA pre-conditioning before reperfusion. As represented in **Figure 4.16 B** and **C**, iPSC-CM in Nx showed lower Caspase 3/7 activity and decreased ROS presence compared to cells after I/R protocol ($p<0.001$), confirming that I/R protocol could be applied to this cell model. Importantly, treatment of iPSC-CM with PGA-diDHA$_{6.4}$ before reperfusion resulted in a decrease of Caspase3/7 signal compared to untreated cells (I/R) and cells treated with PGA and free diDHA ($p<0.05$ in all cases). In addition to this, iPSC-CM preconditioning with both PGA-diDHA and free diDHA resulted in a decrease of ROS generation after reperfusion compared to I/R and I/R+PGA conditions ($p<0.001$).

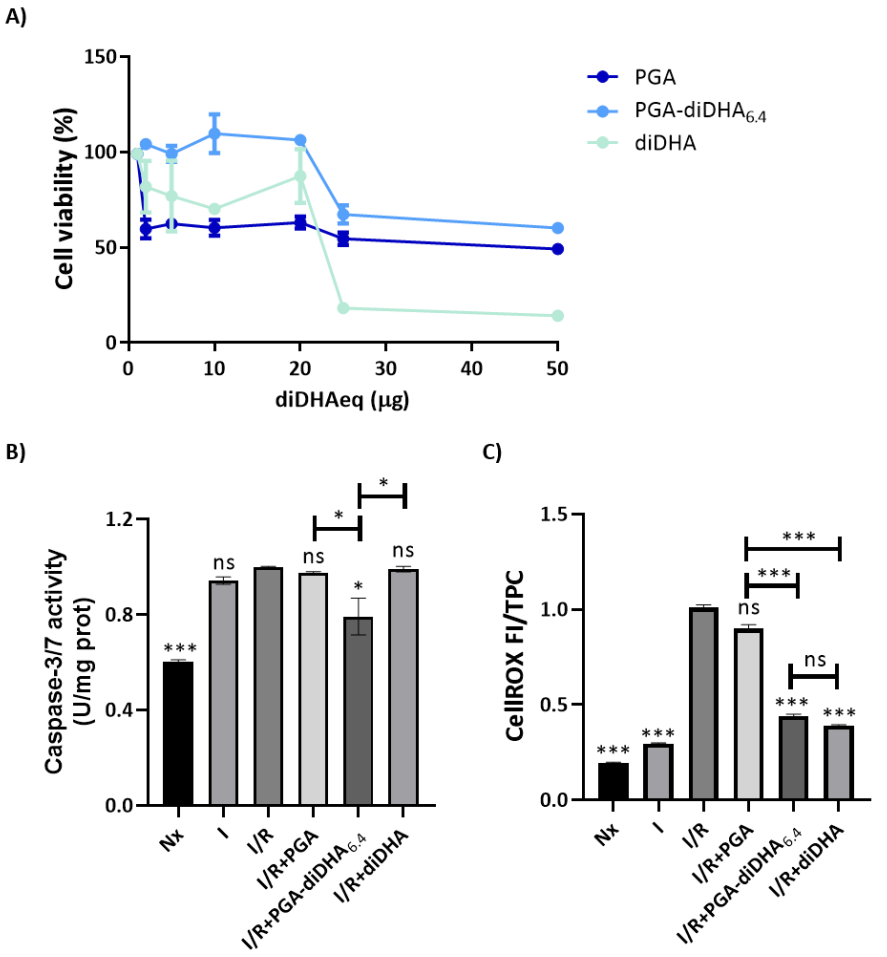

***Figure 4.16. PGA-diDHA$_{6.4}$ preconditioning* reduced iPSC-CM apoptosis and ROS generation after I/R *in vitro*.** **(A)** *PGA, PGA-diDHA$_{6.4}$ and diDHA cytotoxic effect was determined by MTS assay and measured by spectrophotometry (absorbance at 490 nm) in iPSC-CM after 72 h of exposure to increasing diDHA doses (µg diDHAeq: 1.56, 3.12, 6, 12.5, 25, 50). Results are shown as cell viability percentage in comparison to non-treated cells and represented as mean ± SEM from three independent experiments.* **(B)** *Caspase3/7 activity measured in iPSC-CM in Nx, I, I/R and I/R after adding PGA, PGA-diDHA$_{6.4}$ and free PGA at 10 µg of diDHA eq by luminescence. Cell lysates were obtained and data were normalized to the total protein content (TPC) of each sample.* **(C)** ROS generation measured as *CellROX® orange fluorescence intensity (FI) signal per TPC of each sample. Results are presented as mean ± SEM from two independent experiments, each one by triplicate. Values obtained from I/R condition was used as reference and data were analyzed with ANOVA and Tukey's post-hoc test (ns: non-statistically significant differences; *p<0.05; ***p<0.001;).*

Table 4.1. LC_{50} values for PGA, PGA-diDHA$_{6.4}$ and free diDHA in NRVM.

	LC_{50} (µg diDHA eq)
PGA	1.06
PGA-diDHA$_{6.4}$	24.05
diDHA	23.70

In summary, data presented in this section suggested that iPSC-CM pre-conditioning during ischemia with both PGA-diDHA$_{6.4}$ and free diDHA prevented a massive ROS generation upon reperfusion compared to untreated cells or PGA-treated cells. Moreover, a decrease on cell apoptosis was observed when ischemic iPSC-CM were treated with PGA-diDHA$_{6.4}$ nanoconjugate, and not with free diDHA at the same dose, as measured by Caspase3/7 activity, indicating that results showed on NRVM were reproduced in cardiomyocytes from human origin.

4.7. PGA-diDHA$_{6.4}$ ameliorated myocardial injury in a small animal model if I/R-induced injury

To ascertain whether PGA-diDHA$_{6.4}$ could protect cardiac tissue from I/R-induced injury, an *in vivo* rat model was set up. Rats were randomly distributed into the following groups: Sham (not infarcted), PBS (vehicle control), PGA, PGA-diDHA$_{6.4}$, free diDHA or Esmolol (dose: 0.5 mg/kg). PGA-diDHA$_{6.4}$ and free diDHA were administered at two different doses (dose 1: 27.1 µg diDHA eq/kg; dose 2: 271 µg diDHA eq/kg), and the amount PGA present on dose 1 or 2 of PGA-diDHA$_{6.4}$ was injected in each case. AMI was induced by left descendant anterior descending coronary aorta occlusion for 30 min and treatment modalities were intramyocardially administered 15 min before reperfusion. Hearts were collected 24 h after the surgical process and stained with TTC staining as explained in **Sections 3.14.1** and **3.15.1** in order to measure the total amount of metabolically inactive tissue after AMI, which represents area at risk (AAR).

Figure 4.17 A and **B** depict representative pictures of heart slices stained with TTC and AAR calculations, respectively. An AAR of 29.96±4.62 % following I/R induction and PBS administration was obtained, and no significant decrease in infarct size was observed following either dose of PGA alone (22.40±4.28 % and 18.69±3.23 %, respectively). However, treatment with dose 1 (11.99±3.75 %) and 2 (12.02±2.00

%) of PGA-diDHA$_{6.4}$ prompted a significant decrease in the AAR following AMI and I/R injury ($p<0.01$ in both groups compared to I/R group). No significant alterations following treatment with free diDHA at dose 1 (30.43±4.466 %), but were apparently found when dose 2 (9.566±6.77 %, $p<0.05$) was administered. A remarkable high viscosity and low solubility of free diDHA was observed when free diDHA was administered at dose 2, making manipulation and administration extremely difficult and producing an increased level of variation between animals in the same experimental group. Consequently, results were not considered as representative. Of important note, AAR was not statistically significant reduced when animals were treated with Esmolol (17.37±2.93 %). Finally, a significant AAR decrease in rats treated with dose 1 of PGA-diDHA$_{6.4}$ was observed when data were compared to the group treated with the same dose of free diDHA ($p<0.05$), but not when dose 2 was injected (**Figure 4.17 B**).

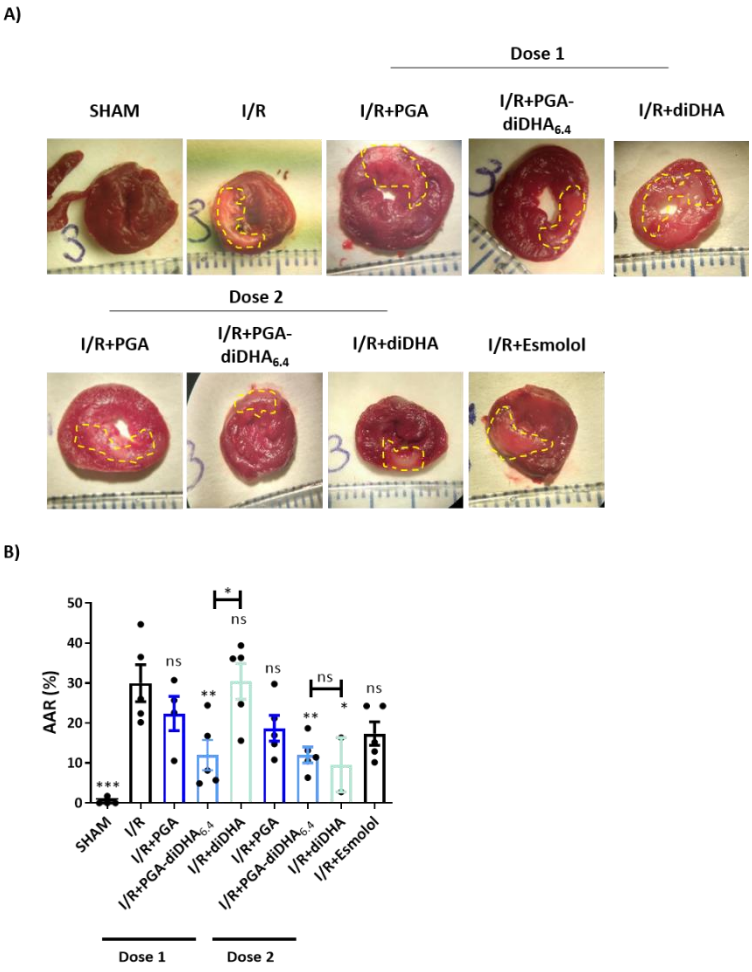

Figure 4.17. PGA-diDHA$_{6.4}$ pre-conditioning decreases myocardial area at risk in I/R rat in vivo model. (A) *Representative images of TTC staining in rat heart slices. PGA, PGA-diDHA$_{6.4}$ and free diDHA were administrated at two different doses (dose 1: 27.1 µg diDHA eq/kg; dose 2: 271 µg diDHA eq/kg) and Esmolol was injected at 0.5 mg/kg. PBS was injected in control group (I/R). SHAM animals were submitted to the same experimental procedure but no artery occlusion was performed.* ***(B)*** *Graphic representation of myocardial area at risk (AAR, %) for each experimental group, measured as percentage of tissue volume damaged related to total heart volume for each animal. Samples were collected 24h after surgical procedure. All values are compared to I/R condition and represented as mean ± SEM. Asterisks indicate statistically significant differences after ANOVA analysis followed by Tukey's post hoc tests (ns: non-significant; *p<0.05; **p<0.01; ***p<0.001).*

Overall, these data suggest that conjugation of diDHA to PGA at an optimized ratio has significant beneficial effects in a small animal model of I/R-induced injury when

compared to free diDHA treatment, allowing for greater efficiency when eadministered at a lower dose.

4.8. Ischemic zone pre-conditioning with PGA-diDHA6.4 before reperfusion reduces area at risk after AMI in a large animal of I/R-induced injury

To corroborate our findings in a more preclinically relevant setting, PGA-diDHA$_{6.4}$ cardioprotective potential was evaluated in a swine model of I/R-induced injury. AMI was induced and occlusion was maintained for 90 min, and PBS (I/R group, n=12), PGA (I/R+PGA, n=4), PGA-diDHA$_{6.4}$ (I/R+PGA-diDHA$_{6.4}$, n=8), or Esmolol (I/R+Esmolol, n=8) were infused intracoronary shortly before reperfusion. To ensure that AMI was induced, cardiac troponin I (cTnI) was measured in peripheral blood samples collected before AMI, after AMI and one week after surgical intervention (**Figure 4.18**). As expected, a transitory but significant increase in the release of cTnI for all experimental groups after AMI was observed when compared to basal cTnI levels in serum ($p<0.05$).

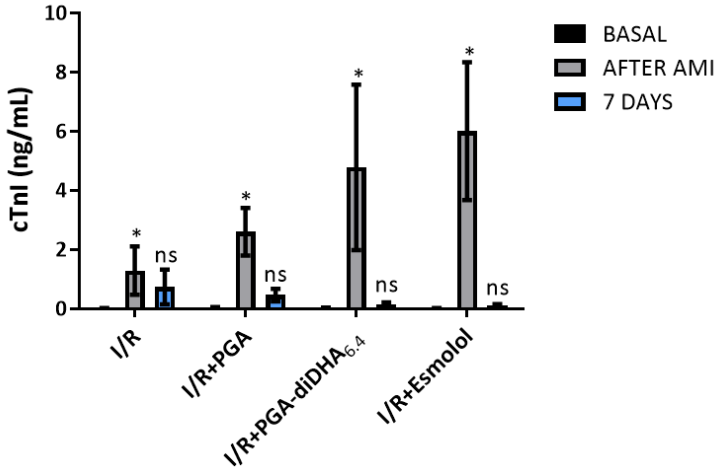

Figure 4.18. Cardiac Troponin I (cTnI) detection in blood serum samples before, after and 7 days post-AMI induction. *cTnI release (ng/mL) was measured in order to confirm AMI induction in swine in vivo model by ELISA test. Asterisks indicate statistically significant differences after ANOVA analysis followed by Tukey's post hoc test comparing to data obtained before AMI induction (basal samples), and are shown as mean ± SEM (ns: non-significative; *p<0.05).*

One week after AMI induction, CMR was performed to determine the AAR in the myocardium as an indicator of the damaged myocardial area that has yet to progress into necrosis after AMI. The representative images and measurements depicted in **Figure 4.19 A** and **B**, respectively, demonstrate that PGA-diDHA$_{6.4}$ infusion before reperfusion significantly reduced the AAR compared to I/R group (18.77±1.87 % and 38.68±5.272 %, respectively, $p<0.01$). However, treatment with PGA (61.65±36.75 %) or Esmolol (37.63±6.28 %) failed to prompt any significant alterations when compared to the I/R untreated group.

Additionally, we observed a significant reduction in AAR (as measured by TTC staining one week after surgical intervention) in pigs receiving a PGA-diDHA$_{6.4}$ infusion before reperfusion compared to control condition (15.82±1.26 % and 19.80±0.93%, respectively, $p<0.05$), but not following PGA (15.51±4.91 %) or Esmolol (17.37±3.24 %) pretreatment (**Figures 4.19 C** and **D**). Importantly, the infusion of PGA alone caused significant malignant arrhythmias and ventricular extra-systole during the intervention, resulting in the death of three animals during PGA administration or shortly after surgical procedure. While no deaths of animals associated with PBS or PGA-diDHA$_{6.4}$ treatments were observed, mild ventricular extra-systole during the intervention derived from AMI induction were found in most cases; however, no malignant arrhythmias after reperfusion occurred in those cases.

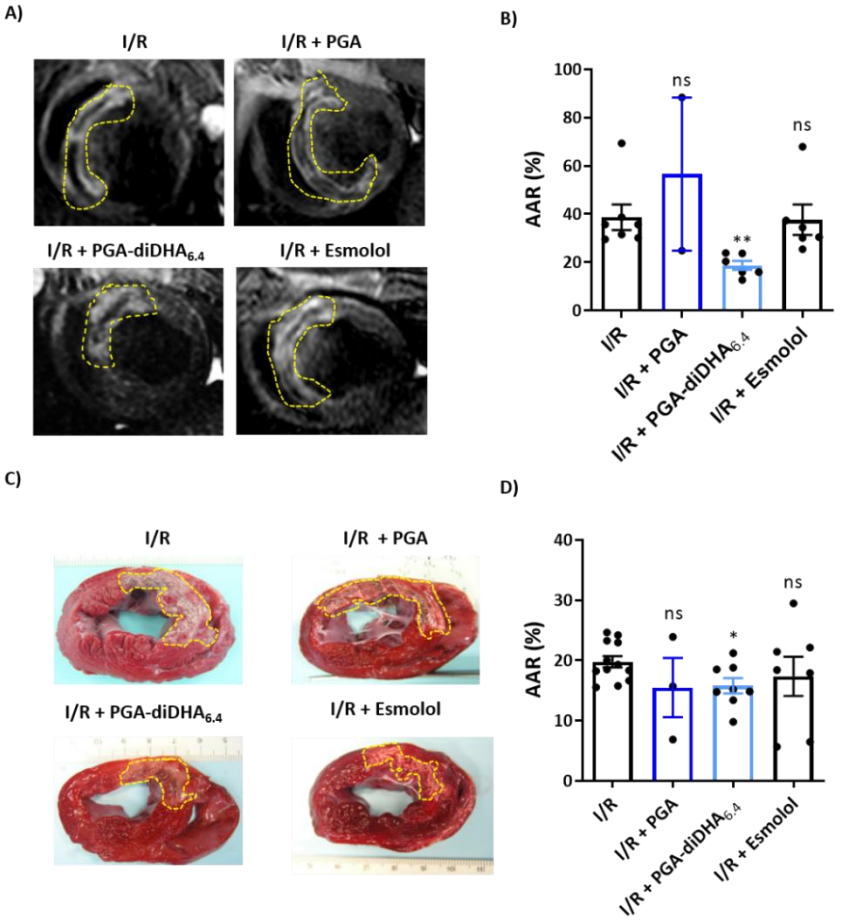

Figure 4.19. PGA-diDHA$_{6.4}$ pre-conditioning decreases myocardial area at risk in I/R swine in vivo model. (A) *Representative images from swine heart tissue that underwent 90 min ischemia followed by reperfusion and administration of PBS (I/R), PGA (65.4 µg/kg), PGA-diDHA$_{6.4}$ (27.1 µg diDHA eq/kg) or Esmolol (0.5 mg/kg); where serial CMR T2W-STIR examinations were made seven days after surgical intervention.* ***(B)*** *Myocardial area at risk (AAR) quantification (%) in left ventricle* ***(C)*** *Representative images of TTC staining in swine heart slices and* ***(D)*** *quantification of AAR (%) by morphometry analysis, measured as percentage of myocardial damaged area with respect to total heart area for each individual. Animals included in each experimental group: I/R, n=12; I/R + PGA, n=4; I/R + PGA-diDHA6.4, n=8 and I/R + Esmolol n=8. All values are compared to I/R condition and represented as mean ± SEM. Asterisks indicate statistically significant differences after ANOVA analyses followed by Tukey's post hoc tests (ns: non-significant; *p<0.05; **p<0.01).*

Altogether, data presented in Section A suggest that the intracoronary infusion of rationally-designed and optimized PGA-diDHA conjugate in a large animal I/R model prevented and diminished associated cardiac injury when compared to free diDHA and Esmolol, showed by a modest reduction on AAR.

Section B: Oncostatin-M-enriched SEV isolated from genetically modified MSC as potential anti-fibrotic agent.

4.9. OSM receptors LIFR, GP130 and OSMR gene expression is changed upon cardiac ventricular fibroblasts stimulation

Two recent studies have demonstrated a role of OSM counteracting TGFβ-1 pro-fibrotic effect and therefore attenuating fibrosis in cardiac injury models[336, 338]. Based on this idea, the specific loading of OSM in SEV derived from MSC conditioned media has been proposed in order to potentiate the beneficial effects of MSC-SEV as a new therapeutic strategy tool to reduce cardiac ventricular fibroblasts activation and uncontrolled proliferation during myocardial insult.

First, the expression OSM receptors (LIFR, GP130 and OSMR) was evaluated in target cells (normal human cardiac ventricular fibroblasts, NHCF-V) at different time points after starvation and *in vitro* stimulation through the use of a pro-fibrotic cocktail composed by L-ascorbic acid 2-phosphate, dextran sulphate and recombinant TGFβ-1 as described in **Section 3.13.8** by qPCR. As shown in **Figure 4.20**, upregulation of LIFR after starvation and after 0.5, 1, 4, 24 and 48 h of stimulation was observed ($p<0.001$), while no significant upregulation of this gene was found 2 h after stimulation when data were compared to trl condition. GP130 gene expression was significantly upregulated 0.5 and 4 h after stimulation compared to ctrl condition ($p<0.001$). Non-statistically significant differences on gene expression were observed on additional time points included. Analysis of OSMR gene expression in NHCF-V revealed a significant increase on gene expression that was only significant after 48 h of stimulation ($p<0.01$).

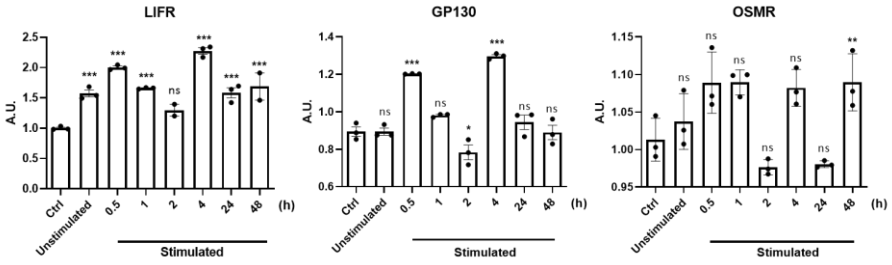

Figure 4.20. OSM receptors expression in NHCF-V at different timepoints after in vitro stimulation with L-ascorbic acid 2-phosphate, dextran sulphate and TGFβ-1. *GP130, OSMR and LIFR gene expression was measured on target cells after starvation (unstimulated) or starvation and*

*stimulation (stimulated) at different time points in vitro by qPCR. Neither stimulated nor starved cells (ctrl) were used as a reference data for fold change calculation (arbitrary units, A.U.). Three independent experiments were performed. ANOVA followed by Tukey's post-hoc test were used to compare means between groups. Asterisks indicate statistically significant differences between groups, using ctrl condition as reference (ns: non-significant; *p<0.05; **p<0.01; ***p<0.001). Results are shown as mean ± SEM.*

After that, protein levels of OSM receptors were also measured under the same experimental conditions. Representative Western Blot and densitometry quantifications are showed in **Figure 4.21 A-D**. LIFR gene is translated to LIF-R, and this protein levels were increased after starvation and after starvation and 0.5 h of stimulation compared to ctrl condition ($p<0.001$ and $p<0.01$, respectively), and were maintained during the first two hours after fibroblasts stimulation ($p<0.01$). However, LIF-R was not detected in protein samples taken from unstimulated cells or after 1, 2, 4, 24 and 48 h of NHCF-V stimulation (**Figure 4.21 A** and **B**). GP130 gene expression leads to IL-31RA receptor. Protein levels of this receptor were similar between ctrl and unstimulated cells, but were significantly increased from 0.5 to 4 h after NHCF-V stimulation, pointing to a quick production of this protein under these experimental conditions ($p<0.001$ after 0.5 and 4 h of stimulation; $p<0.01$ after 1 and 2h of stimulation). Contrarily, a reduction on IL-31RA protein levels was found in samples taken 24 and 48 h after stimulation compared to values obtained in basal conditions ($p<0.001$ in both cases). Data are represented in **Figure 4.21 A** and **C**. Lastly, IL-31RB protein levels, whose translation is the result of OSMR gene expression, were measured under the same experimental conditions. As shown in **Figure 4.21 A** and **D**, increased IL-31RB signal was observed in ctrl and unstimulated cells compared to stimulated NHCF-V at different time points ($p<0.001$ in all cases but after 1 h of stimulation where $p<0.01$).

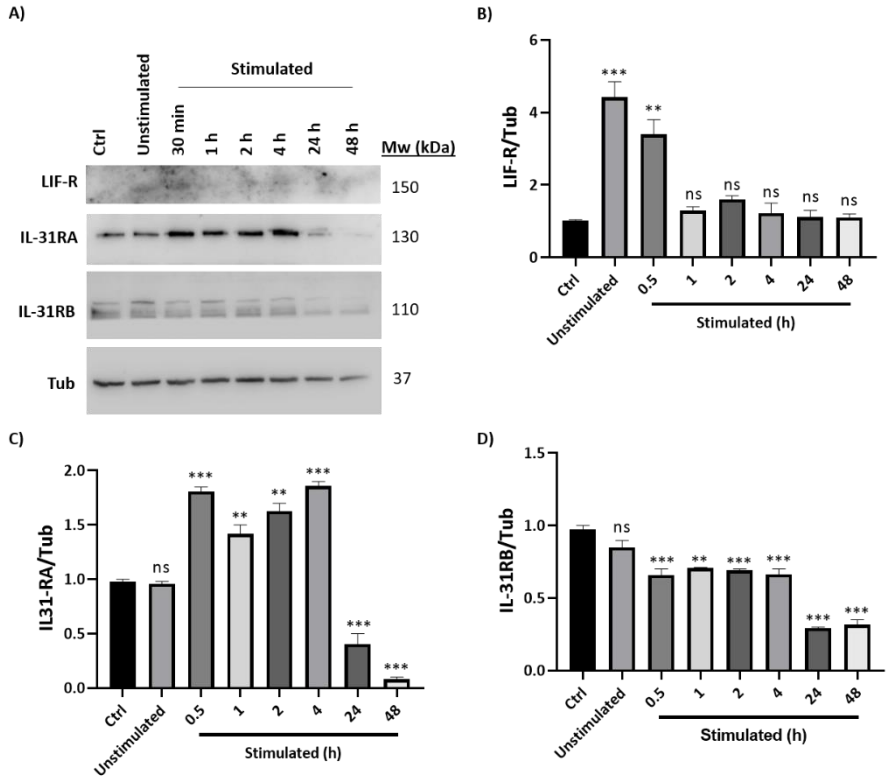

Figure 4.21. OSM receptors LIF-R and IL-31RA protein levels are increased after NHCF-V stimulation. *(A) Representative Western Blot for LIF-R, IL-31RA and IL-31RB and Tubulin α-1A (Tub) protein expression measured in basal conditions (ctrl), after starvation (unstimulated) and after starvation and different times of NHCF-V stimulation (0.5, 1, 2, 4, 24 and 48 h).* ***(B)*** *LIF-R protein expression quantification.* ***(C)*** *IL-31RA protein expression quantification* ***(D)*** *IL-31RB protein expression quantification. Protein expression levels were measured by densitometry in ImageJ software using Tub as loading control for each condition. Results were obtained from two independent experiments, and were analyzed with ANOVA and Tukey's post-hoc test using values from ctrl cells as reference condition and represented as mean ± SEM (ns: non-significant statistic differences; **p<0.01; ***p<0.001).*

These results indicated that two out of three receptors involved in OSM signaling pathways activation were upregulated in starving ventricular cardiac fibroblasts and at early time points after *in vitro* stimulation. Consequently, loading of OSM in SEV isolated from MSC cell culture supernatant could lead to functional effects on NHCF-V response modulation upon activation through its canonical pathway.

4.10. OSM reduced human cardiac ventricular fibroblasts proliferation and activation upon fibrosis stimulation *in vitro*

Once it was demonstrated that the expression of OSM receptors were upregulated in stimulated NHCF-V, it was decided to analyze the effect of recombinant human OSM (rhOSM) on NHCF-V proliferation through Ki-67 expression analysis. Additionally, mature triple helix form of collagen type I (telo-Collagen1α1), which is the main component of the ECM secreted into the extracellular space, was analyzed.

First, a study of the effect of rhOSM on cell viability was performed by treating NHCF-V with increasing doses of this molecule. As shown in **Figure 4.22**, rhOSM did impact on NHCF-V viability negatively after 48 h of treatment at any of the tested doses compared to untreated cells, so functional effects of rhOSM on NHCF-V proliferation and fibrotic properties *in vitro* were assessed.

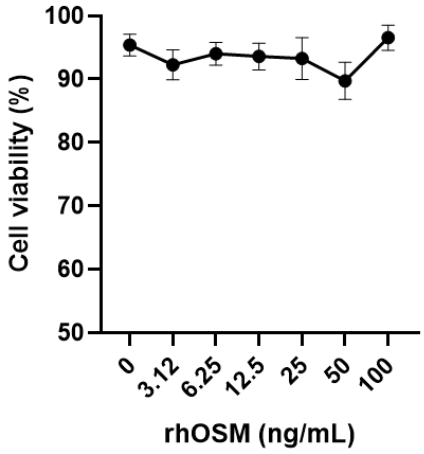

Figure 4.22. Effect of rhOSM in NHCF-V viability. *rhOSM cytotoxic effect when added at increasing doses (ng/mL: 3.12, 6.25, 12.5, 25, 50 and 100) was determined by MTS assay and measured by spectrophotometry (absorbance at 490 nm) in NHCF-V. Results are shown as cell viability percentage and normalized to non-treated cells values. Data are represented as mean ± SEM and were obtained from three independent experiments.*

Thereafter, proliferation of NHCF-V after 24 h of starvation and in the presence of rhOSM was measured through Ki-67 expression, whose presence in the nuclei indicates cells in division. As shown in **Figure 4.23 A**, a reduction in the percentage

of proliferative cells was observed after rhOSM treatment at 5 ng/mL (48±2.91%; p<0.01), 10 ng/mL (26.25±4.07; p<0.001), 20 ng/mL (25.15±3.70; p<0.001) and 50 ng/mL (38.51±3.33; p<0.01) compared to control condition (71.32±1.64). Representative pictures are included **Figure 4.23 B**.

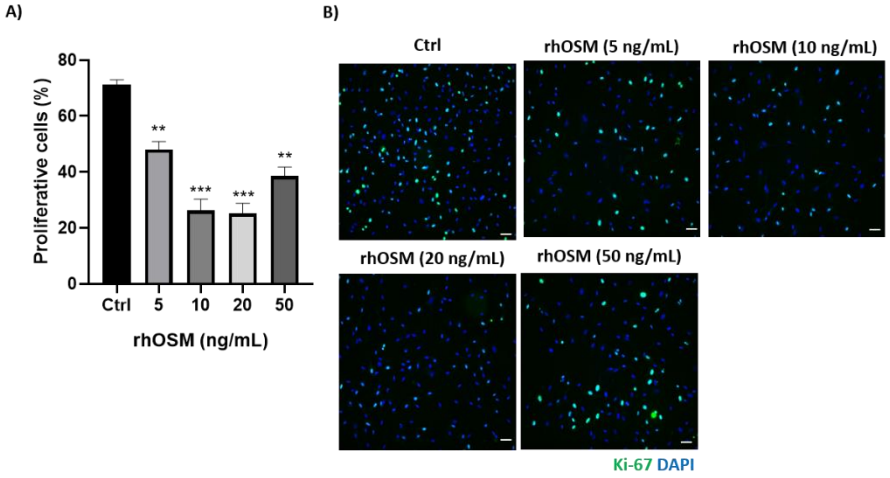

Figure 4.23. rhOSM treatment reduces NHCF-V proliferation in vitro under starving conditions. (A) *Cells in proliferation after rhOSM treatment (ng/mL: 5, 10, 20 and 50). Percentage proliferative cells (Ki-67 positive nuclei) cells was calculated as number of Ki-67 positive nuclei per number of nuclei (stained with DAPI) in each screened field.* ***(B)*** *Representative pictures of NHCF-V after rhOSM treatment and both Ki-67 and DAPI staining. Pictures were taken using 20X objective in ImageXpress FLIPR Penta High-Throughput Cellular Screening System (Molecular Devices). Scale bar=100µm. Cells under starvation and treated with PBS were used as reference (ctrl). Three independent experiments were performed. Asterisks indicate statistically significant differences after one-way ANOVA analysis and are shown as mean ± SEM (**p<0.01; ***<p<0.001).*

Finally, it was evaluated if rhOSM could interfere with fibroblasts activation after *in vitro* stimulation in terms of fibrosis related protein expression telo-Col1α1. Results are shown in **Figure 4.24.** Telo-Col1α1 protein was only detected on a small population of basal NHCF-V (ctrl), and its presence seemed to be increased after starvation. Of important note, telo-Col1α1 signal was mostly detected in the extracellular space upon fibroblasts stimulation, suggesting protein secretion for ECM formation under this condition, as expected during fibrotic process. Different patterns of telo-Col1α1 fluorescent signal were observed in NHCF-V when rhOSM was added together with stimulating factors. While rhOSM added at 5, 10 and 20 ng/mL seemed to decrease telo-Col1α1 deposit in the extracellular space, addition

of 50 ng/mL resulted in a location change, with higher extracellular presence of this protein compared to non-treated fibroblasts (stimulated).

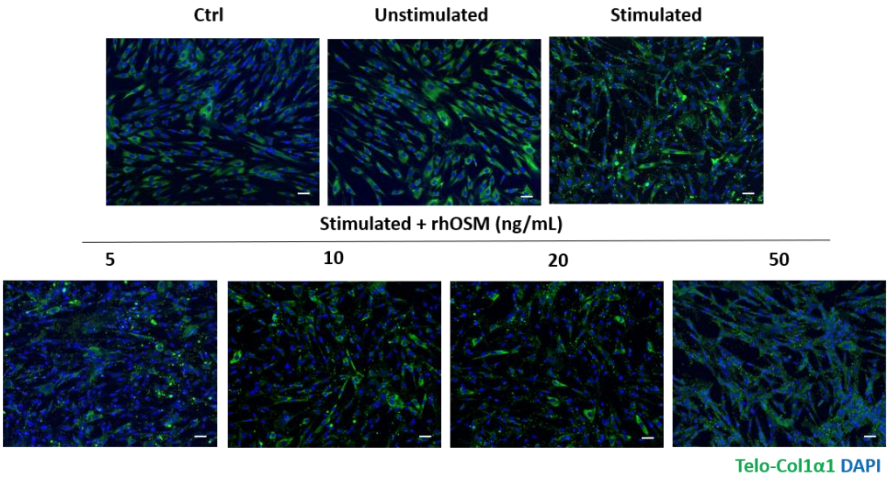

Figure 4.24. The presence of rhOSM modifies NHCF-V telo-Col1α1 expression and distribution upon stimulation. *Representative pictures of NHCF-V in basal conditions (ctrl), after 24 h of starvation (unstimulated) and after 48h of stimulation with or without the addition of rhOSM (ng/mL: 5, 10, 20 and 50). Pictures were taken using 20X objective in CellVoyager CV8000 screening system (Yokogawa). Scale bar=100µm.*

These data suggested a dose-dependent functional effect of rhOSM in NHCF-V under stressing conditions, leading to a decrease in cell proliferation and partially counteracting ECM deposition process *in vitro* in terms of telo-Col1α1 pattern expression and distribution.

4.11. rhOSM interferes with proliferation and migration capabilities of MSC from dental pulp origin

Our main goal with this project was to maintain MSC-SEV characteristics and achieve an improvement of their native therapeutic potential through the incorporation of OSM on SEV-surface. After the effects seen in NHCF-V in response to rhOSM, where a reduction of cell proliferation was found, it was questioned if we would have the same effects in MSC after OSM overexpression and that could interfere with MSC culture and expansion after cell engineering. Consequently,

rhOSM was added to MSC at different doses and cell viability, proliferation and migration were measured. Results are shown in **Figure 4.25**.

As represented in **Figure 4.25 A**, MSC viability was not significantly affected when rhOSM was added at increasing concentrations (ng/mL: 3.12, 6.25, 12.5, 25, 50 and 100) compared to control condition. After corroborating that rhOSM did not have cytotoxic effects in MSC, it was decided to continue using rhOSM at a working dose of 10 ng/mL for further experiments. The choice of 10 ng/mL of rhOSM instead of 20 ng/mL was based on the results showed in **Figures 4.23** and **4.24**, were doubling rhOSM dose did not lead to a major decrease of cell proliferation or telo-Col1α1 secretion compared to cells treated with 10 ng/mL of rhOSM. However, the use of rhOSM in a higher concentration (50 ng/mL) caused the opposite unwanted effect.

After that, proliferation rate in primary MSC was assessed after exposure to rhOSM for 48 h. Data of **Figure 4.25 B** showed significant reduction of proliferative cells ($p<0.01$) when MSC were exposed to rhOSM (3.5±1.323 %) compared to non-treated MSC (28.31±3.394 %). One important feature of MSC is their homing ability to ischemic environments. Consequently, they can migrate into injured sites and secrete cytokines, growth factors and chemokines to favour tissue regeneration [386-388]. In order to assess if treatment with rhOSM could reduce migrative capabilities of MSC, a transwell assay using IL-1β as migration inductor was designed (Detailed in **Section 3.13.7.1**). Results are summarized in **Figure 4.25 C**, where it can be appreciated a significant reduction ($p<0.05$) in the number of migrated cells when they were treated with rhOSM (47±5.657) compared to untreated cells (MSC, 92±11.31).

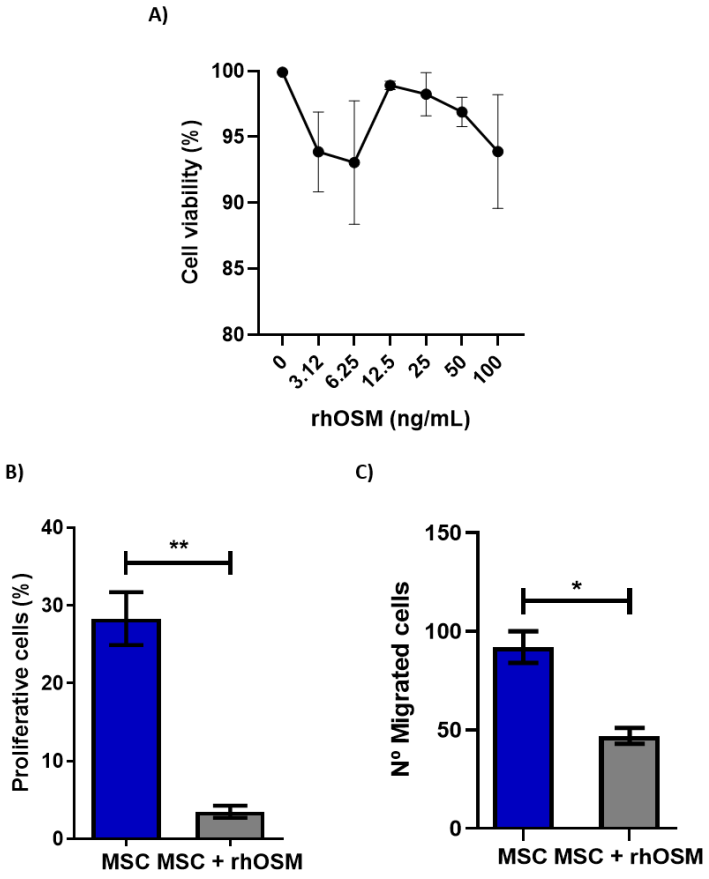

Figure 4.25. rhOSM did not show cytotoxicity effects, but reduced proliferation and migration capabilities in dental pulp derived MSC. (A) *Dose-response curve of MSC after 48 h of rhOSM exposure (ng/mL: 3.12, 6.25, 12.5, 25, 50 and 100) measured by MTS assay (absorbance read at 490 nm).* ***(B)*** *Percentage of proliferative cells untreated (MSC) or treated with rhOSM (MSC+rhOSM, dose: 10 ng/mL) after BrdU assay.* ***(C)*** *Number of migrated cells in basal conditions (MSC) and after rhOSM treatment (MSC+rhOSM, dose: 10 ng/mL) measured by transwell assay. Two independent experiments were included. ANOVA was used to compare means between more than two experimental groups, while unpaired t-test was used to compared means between two groups of data. Asterisks represent statistically significant differences (*p<0.05; **p<0.001). Mean±SEM for each data set is represented.*

Altogether, these data suggested that reduction of MSC proliferation and migration was influenced by the presence of rhOSM at non-toxic doses. Based on these results, it was decided to design the corresponding plasmids for OSM overexpression in primary MSC from dental pulp origin including an inducible

promotor (TetOn). This strategy would allow cell expansion and the induction of OSM overexpression, which would probably have a negative impact on cell proliferation, when doxycycline was added to cell culture media.

4.12. OSM native sequence fusion to lactadherin for specific anchoring in MSC derived SEV fails to load the protein of interest

Based on the previous results, which supported the rhOSM anti-proliferative effect on NHCF-V under stress conditions and reduced telo-Col1α1 deposition in human cardiac fibroblasts upon starvation and *in vitro* stimulation, lentiviral plasmids were designed for the specific loading of OSM into MSC derived SEV through its fusion to lactadherin, a protein which is naturally bound in a non-covalent manner to phosphatidylserine present in SEV membrane. As previously commented, an inducible promotor was included in the plasmids to control fusion protein expression. Additionally, a second promotor (EF1) was included for GFP constitutive expression, as explained in **Section 3.3**.

4.12.1. Engineered MSC lines characterization

Primary MSC from dental pulp origin were genetically modified by transduction of two lentiviral plasmids, one of them carrying only part of lactadherin sequence (XSTP) and a second one carrying OSM full sequence fused to the same lactadherin sequence (OSM-XSTP). First, lentiviral particles generated were titrated for highly efficient MSC infection, and GFP positive percentage of cells was measured by flow cytometry (**Figure 4.26 A-C**). Percentage of GFP positive cells obtained was above 90% and was maintained over cell passages in both cell lines (**Figure 4.26 D**). Consequently, no further selection was performed. New cell lines generated were named MSC-XSTP and MSC-OSM-XSTP, respectively.

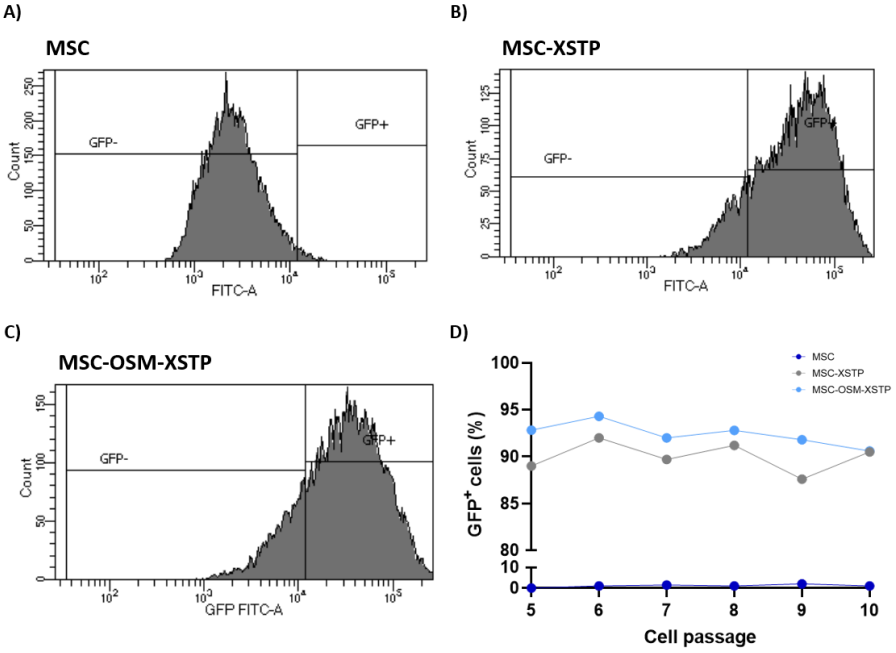

Figure 4.26. Engineered MSC screening through GFP fluorescent intensity. *Histograms derived from flow cytometry analysis showing GFP negative and postive cells populations for samples corresponding to* ***(A)*** *native MSCS,* ***(B)*** *MSC-XSTP and* ***(C)*** *MSC-OSM-XSTP.* ***(D)*** *Percentage of cells positive for GFP expression at different cell passages.*

According to the Mesenchymal and Tissue Stem Cell Committee of the International Society for Cellular Therapy, cells are required to have specific characteristics, as a profile of expression or absence of certain markers and a fibroblasts-like spindle shape to be considered as MSC (as detailed in **Section 1.1.5**). Furthermore, analysis of protein expression and morphology in MSC-XSTP and MSC-OSM-XSTP generated in comparison to native MSC was performed to ensure that those properties were maintained. As it can be appreciated in **Figure 4.27 A**, presence of CD90 and CD105 was maintained in both MSC-XSTP and MSC-OSM-XSTP, and CD34, CD45 and CD14 absence was also hold after cell engineering, showing similar levels of all proteins assayed in the three cell lines. Attending to cell morphology, it was also confirmed that fibroblasts-like spindle shape was preserved on engineered cell lines compared to native MSC (**Figure 4.27 B**).

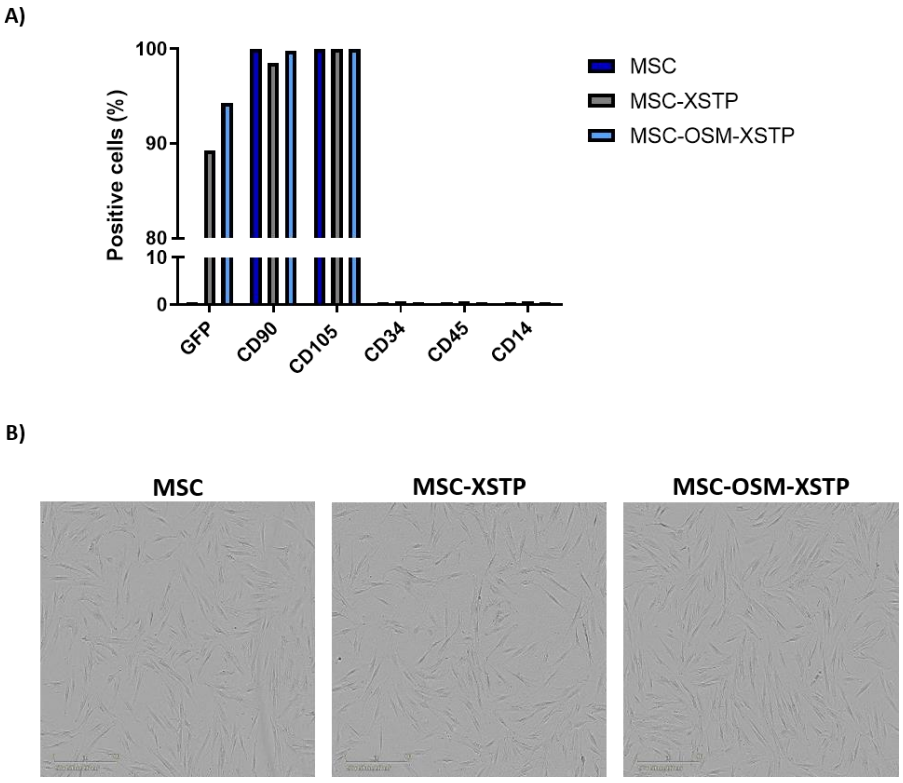

Figure 4.27. MSC characteristic markers profile and morphology are maintained after cell engineering. (A) *Expression of CD90, CD105, CD34, CD45 and CD14 was measured by flow cytometry in MSC, MSC-XSTP and MSC-OSM-XSTP. GFP positive cells were gated for tracking purposes and fluorescent channels compensation. Only one experiment was performed, so no mean and bar erros or statistic analysis are available.* ***(B)*** *Representative bright field images of MSC, MSC-XSTP and MSC-OSM-XSTP showing cell morphology. Scale bar=400µm.*

Results obtained in the present section were useful to set up working conditions with the new cell lines generated in order to set up doxycycline dose necessary for constructs expression induction, stablish a doxycycline working concentration and characterize SEV isolated from engineered-MSC conditioned culture media.

4.12.2. Doxycycline addition to engineered MSC affects cell viability and proliferation rate

Due to the fact that doxycycline addition to cell culture media was necessary to induce lactadherin and OSM fused to lactadherin expression on genetically

modified MSC and it was previously seen that OSM presence could affect MSC division negatively, dose-response curves to measure cell viability and proliferation of MSC, MSC-XSTP and MSC-OSM-XSTP after 48h of exposure to doxycycline were performed. Results are shown in **Figure 4.28**.

Cytotoxicity assays (by MTS) suggested different responses of each cell line to doxycycline (**Figure 4.28 A**). Treatment with both 100 µg/mL and 50 µg/mL of doxycycline resulted in a significant reduction of cell viability in MSC ($p<0.01$), MSC-XSTP ($p<0.01$) and MSC-OSM-XSTP ($p<0.001$) compared to the same cells when they were not exposed to doxycycline. Importantly, doxycycline also reduced MSC-XSTP and MSC-OSM-XSTP viability ($p<0.05$ and $p<0.01$, respectively) when added at 25 µg/mL, while non-significant differences were observed in native MSC treated with the same concentration of doxycycline compared to untreated cells. Cell viability was unaffected when MSC, MSC-XSTP or MSC-OSM-XSTP were treated with doxycycline at 1.56, 3.12, 6.26 or 12.5 µg/mL compared to values obtained for untreated cells. When comparing the effect on cell viability of the same doxycycline dose in genetically modified MSC and native MSC, it was observed a higher susceptibility of MSC-OSM-XSTP to doxycycline when it was added at 1.56, 3.12, 6.26, 12.5, 25 and 100 µg/mL compared to both MSC and MSC-XSTP ($p<0.01$ or $p<0.05$). Although there is a trend of reduced cell viability, non-statistically significant differences between MSC and MSC-OSM-XSTP were observed when doxycycline was added at 50 µg/mL. Contrarily, differential susceptibility to the same doxycycline dose between MSC-XSTP and MSC-OSM-XSTP was observed ($p<0.05$), probably because increased data variability in MSC. Finally, non-statistically significant differences in cell viability were observed when doxycycline was added at each concentration when MSC and MSC-XSTP data were compared.

As it can be appreciated in **Figure 4.28 B**, cell proliferation analysis (by CCK-8 assay) also showed distinct behaviours of native and engineered MSC lines in the presence of doxycycline. On the one hand, native MSC proliferation rate was significantly reduced when doxycycline was added at 25, 50 µg/mL ($p<0.05$ in both cases) or 100 µg/mL ($p<0.01$), but no significant change was observed when lower concentrations were used. This decrease in cell proliferation could be associated to augmented cytotoxic effect showed in **Figure 4.28 A** when doxycycline was added at higher doses than 12.5 µg/mL. On the other hand, a significant drop on cell proliferation rate was observed in both engineered cell lines when doxycycline was added at 6.25 µg/mL ($p<0.01$), 12.5, 25, 50 and 100 µg/mL ($p<0.001$). The decreased proliferation rate observed when doxycycline was added at 25, 50 and 100 µg/mL could be also related to cell viability changes showed in **Figure 4.28 A.** Additionally, doxycycline

did not result in cell viability reduction used at 6.25 and 12.5 µg/mL but in a change in cell proliferation in both MSC-XSTP and MSC-OSM-XSTP ($p<0.01$ and $p<0.001$, respectively).

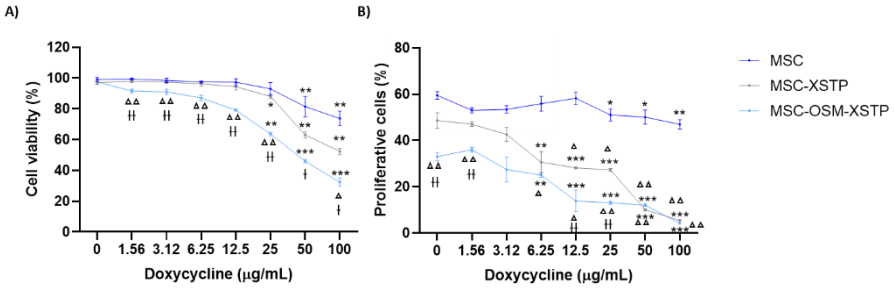

Figure 4.28. Dose-response curve of MSC, MSC-XSTP and MSC-OSM-XSTP after doxycycline treatment. (A) *Percentage of viable and* ***(B)*** *proliferative cells after 48 h of exposure to increasing doses of doxycycline (µg/mL: 1.56, 3.12, 6.25, 12.5, 25, 50 and 100). MTS assay was used for cell viability assays, while CCK-8 assay was used to measure cell proliferation. Absorbance was measured at 490 nm in a multi-well plate reader. Three independent experiments were included. ANOVA and Dunnett's post-hoc test were used to compare means between groups, using values obtained for MSC at each dose as reference to compare the effect of doxycycline tested doses in the same cell line or to compare the same dose of doxycycline in different cell lines. Asterisks represent statistically significant differences between groups belonging to the same cell line treated with increasing doxycycline concentrations, using untreated cells (0 µg/mL doxycycline) as reference values (*p<0.05; **p<0.01; ***p<0.001), while triangles and crosses show statistically significant differences between cell lines when treated with the same dose of doxycycline to compare native MSC to MSC-XSTP or MSC-OSM-XSTP and MSC-XSTP to MSC-OSM-XSTP experimental groups, respectively ($^{\Delta/\dagger}p<0.05$; $^{\Delta\Delta/\dagger\dagger}p<0.01$). Data are represented as mean±SEM.*

Although it was expected to find a decrease in proliferation MSC-OSM-XSTP line after doxycycline treatment because doxycycline presence should trigger OSM overexpression, the decrease of cell proliferation in MSC-XSTP after doxycycline exposure (doses: 12.5, 25, 50 and 100 µg/mL; $p<0.05$ or 0.01) was surprising. Results showed that proliferation of engineered MSC could be altered just by the fact of being genetically modified with lentiviral vectors, but basal proliferation of untreated MSC-XSTP cells did not change significantly compared to native MSC. However, when data resulting from the addition of the same dose of doxycycline in MSC, MSC-XSTP and MSC-OSM-XSTP were contrasted, it was evidenced that basal proliferation rate was significantly lower in MSC-OSM-XSTP compared to native MSC and MSC-XSTP ($p<0.01$), and the same results were obtained when 1.56 µg/mL of doxycycline were added to MSC-OSM-XSTP. Decrease in MSC-OSM-XSTP

proliferation rate was also statistically significant when doxycycline was added at 12.5 and 25 µg/mL compared to MSC-XSTP treated with the same doxycycline doses ($p<0.01$). Consequently, it was thought that differences on basal proliferation rate between MSC-XSTP and MSC-OSM-XSTP could be explained by the fact that TetOn inducible promotor was not completely working or residual amounts of doxycycline could be present on cell culture, but it could not be discerned if the antiproliferative effects were a consequence of OSM overexpression.

4.12.3. SEV isolated from engineered MSC conditioned media maintain characteristic EV markers content, expected morphology and same size distribution

SEV were isolated from MSC, MSC-XSTP and MSC-OSM-XSTP conditioned culture media by serial ultracentrifugation steps and ultrafiltration as detailed in **Section 3.4**, and obtained SEV fractions were analysed by Western Blot, TEM and NTA.

Since exosomes are vesicles formed within MVB and the endolysosomal pathway, and are released to the extracellular space after MVB fusion with plasma membrane, they are supposed to present proteins related to their biogenesis, such as Alix or TSG101, as well as specific tetraspanins, such as CD63 or CD9. Due to the fact that the protocol used during the present project for SEV fractions isolation counts with an intermediate ultrafiltration step, where the majority of particles with a size higher than 200 nm are discarded, it was expected to find those markers expressed on obtained vesicles from conditioned culture media. Protein expression pattern of the previously mentioned markers (Alix, CD63, CD9 and TSG101) together with β-Actin and Calnexin in both SEV and protein samples obtained from lysates of MSC, MSC-XSTP and MSC-OSM-XSTP are shown in **Figure 4.29 A**. Presence of Alix, CD63, CD9 and TSG101 was detected on the three SEV fractions. However, although Alix, CD63 and TSG101 were found on protein samples, CD9 was not detected. Of important note, Alix and TSG101 signal was more intense in SEV samples isolated from MSC-OSM-XSTP conditioned culture media than in cell lysates. Homogeneous bands corresponding to β-Actin protein expression found in cell lysates samples confirmed similar protein amounts loaded on acrylamide gel. Lastly, absence of calnexin in SEV preparations together with its presence in samples from cell lysates was used for quality control, since the expression of this protein is indicative of ER-membrane related content.

Thereafter, the morphology of SEV isolates was analysed using TEM. Representative pictures and augmented sections of MSC, MSC-XSTP and MSC-OSM-

XSTP SEV samples are displayed in **Figure 4.29 B**. Analysis of SEV samples from native and engineered MSC lines showed a predominant presence of particles with the typical shape expected for exosomes preparations, described as nearly spherical shape with concave cavity structure[389], whose size was inferior to 200 nm. Size distribution by NTA showed that the particles mean size was 142±36.8, 127±28.3 and 135±38 nm for MSC, MSC-SXTP and MSC-OSM-XSTP SEV, confirming that samples had the range of sizes previously described for a SEV preparations enriched on exosomes (**Figure 4.29 C**).

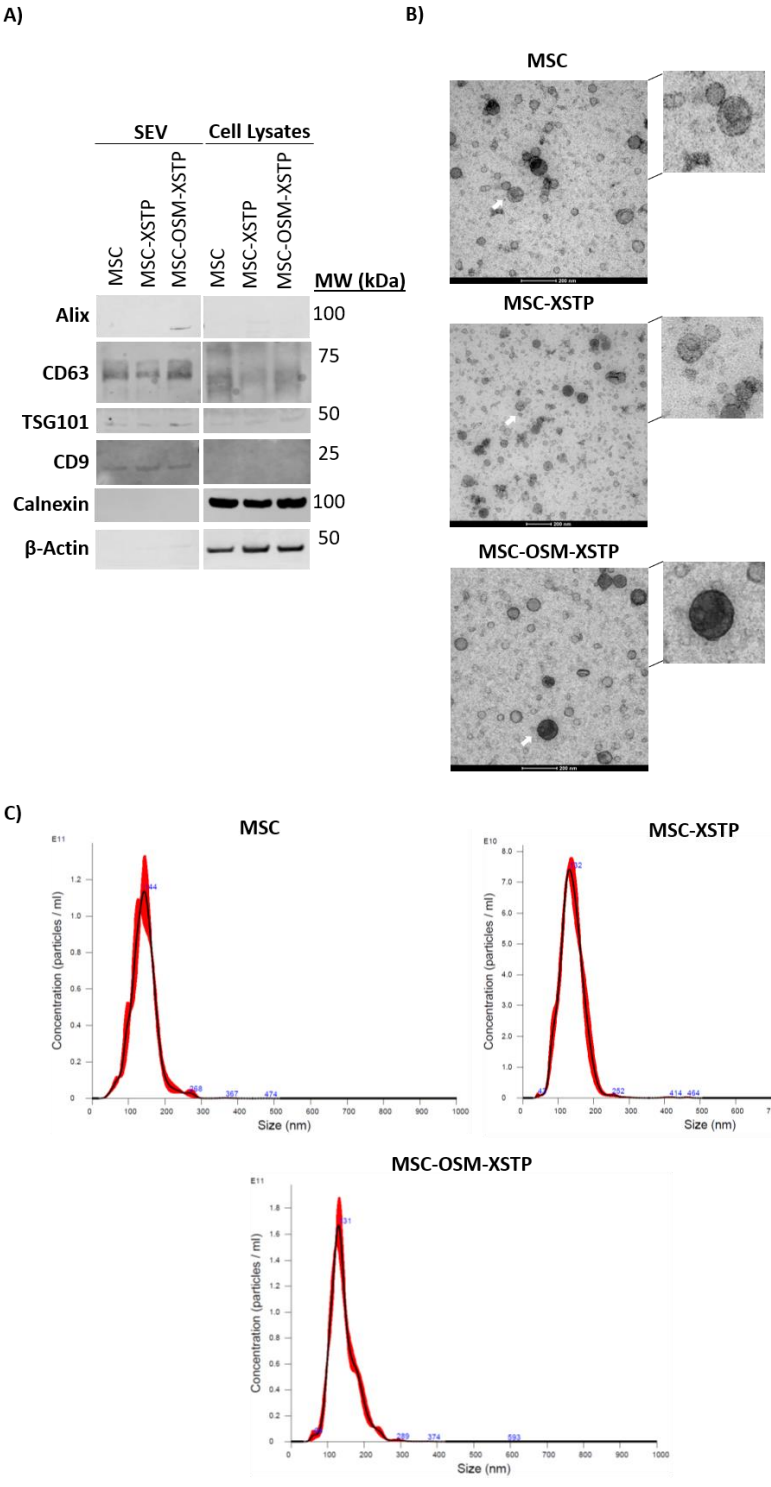
A)
SEV
Cell Lysates
MSC
MSC-XSTP
MSC-OSM-XSTP
MSC
MSC-XSTP
MSC-OSM-XSTP
MW (kDa)
Alix
CD63
TSG101
CD9
Calnexin
β-Actin
100
75
50
25
100
50
B)
MSC
MSC-XSTP
MSC-OSM-XSTP
C)
MSC
MSC-XSTP
MSC-OSM-XSTP
Concentration (particles / ml)
Size (nm)

Figure 4.29. SEV isolated from MSC-XSTP and MSC-OSM-XSTP conditioned culture media maintain SEV characteristic markers expression, size distribution and morphology compared to SEV obtained from native MSC conditioned media. (A) *Expression of Alix, CD63, TSG101, CD9, Calnexin, and β-Actin in SEV isolated from MSC, MSC-XSTP and MSC-OSM-XSTP conditioned culture media and protein samples from each cell line (Cell Lysates) measured by Western Blot assay. (**B**) Representative pictures of SEV samples from native MSC and engineered MSC obtained by transmission electronic microscopy. White arrows indicate augmented field in each picture, showed in the right part on the picture. Scale bar=200 nm. **(C)** Nanoparticle tracking analysis showing size distribution of SEV obtained from MSC, MSC-XSTP and MSC-OSM-XSTP conditioned media. Concentration of SEV obtained, represented as particles per mL is shown in Y axis, while nanoparticles size (nm) is shown in X axis.*

4.12.4. OSM is not detected in SEV isolated from engineered MSC conditioned culture media after constructs expression induction with doxycycline

After SEV samples were characterized, it was necessary to confirm the enrichment on lactadherin in SEV and cell lysates obtained from MSC-XSTP and the presence of OSM fused to lactadherin in SEV and cell lysates samples of MSC-OSM-XSTP after gene expression induction with doxycycline.

First, a quick screening was performed to assess which concentration of doxycycline was necessary for lactadherin overexpression induction in MSC-OSM-XSTP cell lysates, where doxycycline was added at non-cytotoxic concentrations (µg/mL: 1, 5 and 10) based on the results shown in **Figure 4.28 A**. Lactadherin protein expression obtained was compared to native MSC and MSC-XSTP cell lysates samples. **Figure 4.30** represents protein expression levels obtained and densitometric quantification. Minor changes in lactadherin protein levels were observed between protein samples from MSC-OSM-XSTP treated or untreated with doxycycline, native MSC and MSC-XSTP. Nevertheless, significant changes in lactadherin expression could have be masked on this experimental design, since total protein cellular content was measured instead of lactadherin protein content in SEV isolates.

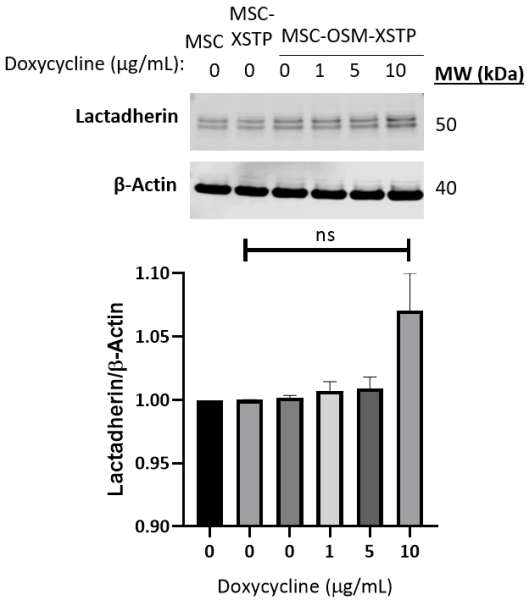

Figure 4.30. Lactadherin protein expression levels are maintained after doxycycline treatment in MSC-OSM-XSTP protein samples. *Lactadherin protein levels were measured in native MSC, MSC-XSTP and MSC-OSM-XSTP by Western Blot assay and quantified by densitometry in ImageJ software. Doxycycline was added to MSC-OSM-XSTP at 1, 5 and 10 µg/mL for 48 h prior to samples collection. β-Actin protein expression level in all samples was measured as house-keeping gene for data normalization. Two independent experiments were included, and data are showed as mean±SEM. ANOVA and Tukey's post-hoc test were used for statistical analysis to compare data from each experimental condition, using native MSC group data as reference values (ns: non-significant).*

Based on this hypothesis, it was decided to run an additional experiment to compare OSM and lactadherin expression in SEV and cell lysates samples from native and engineered MSC after doxycycline induction, using a concentration of 10 µg/mL. Results are shown in **Figure 4.31**. Although slightly increased levels of lactadherin were observed in cell lysates from MSC-XSTP and MSC-OSM-XSTP compared to native MSC samples and in SEV derived from MSC-OSM-XSTP culture conditioned media, no differences between lactadherin protein levels in MSC and MSC-XSTP were noticed. When OSM presence was assayed, no signal was obtained from any of the SEV samples included. Regarding to cell lysates samples, OSM signal did not appear in native MSC, but it appeared in MSC-XSTP and MSC-OSM-XSTP at a molecular weight around 25 kDa, which is the molecular weight expected for OSM on its free conformation, but not the molecular weight expected for the OSM fused to lactadherin (around 75 kDa). In addition to this, a band of OSM was seen in MSC-

XSTP and not in MSC, which could suggest that the fact of MSC genetic modification could induce the expression of a different pattern of cytokines.

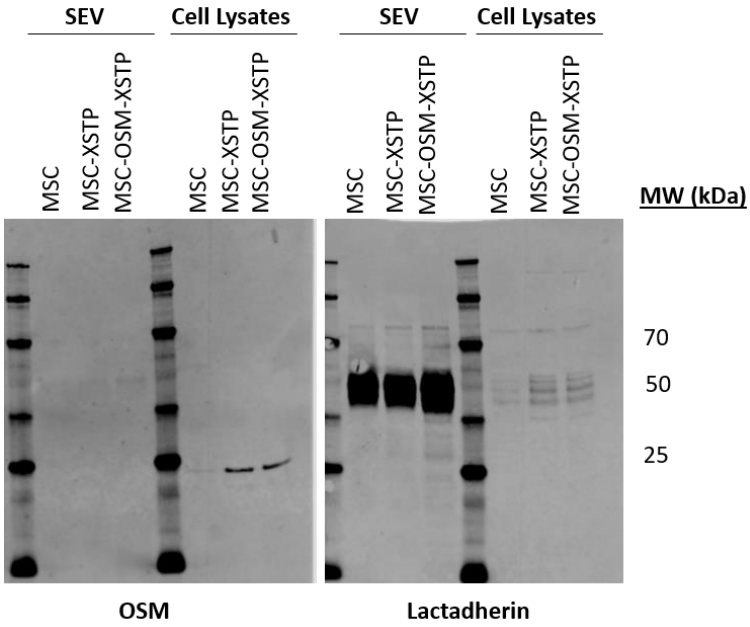

Figure 4.31. OSM and lactadherin protein expression analysis in SEV samples isolated from native and engineered MSC conditioned culture media and protein samples from cell lysates.
Representative Wstern Blot results showing an OSM-labelled membrane is shown on the left side of the figure, while lactadherin-labelled membrane is shown in the right side.

Altogether, data obtained showed that the desired fusion protein was not being loaded in SEV, and modifications should be done to achieve the initial goal proposed.

4.13. OSM sequence modification is necessary in order to anchor it to SEV surface proteins

4.13.1. OSM is loaded in Expi293F derived SEV after cell transduction with modified sequences of the protein

After the failing strategy using OSM-XTP lentiviral vector to achieve the effective load of OSM in SEV, different approaches to ensure the anchoring of OSM to the SEV membrane, where constructs with different fusion proteins and also variations in the OSM sequence were designed. Expi293F cell line was used in order to validate different constructs of OSM because of their enhanced growing and EV secretion rate compared to MSC.

Firstly, OSM sequence was studied in order to modify the sequence included in the study. A schematic view of the protein domains is represented in **Figure 4.32**. OSM is initially produced intracellularly as a protein with three domains: signal peptide (SP), chain and propeptide (PP). The excision of both SP and PP is required to secrete the mature form of the cytokine to the extracellular space and accomplish its function. In consequence, MSC machinery could have been cutting the main chain from the PP intracellularly after overexpression of the fusion protein, which could explain the fact that OSM was seen at the expected molecular weight of its free form (around 25 kDa) and not on the expected molecular weight of the OSM fused to lactadherin (around 70 kDa), as showed in **Figure 4.31.**

Thus, it was decided to include two variants of OSM in the plasmids' designs. First, the full sequence of OSM was included in the construct, but introducing a point mutation in the cleavage site between the main chain and PP domains (mutantOSM) in order to avoid enzymatic digestion. Second, since it was unknown if PP presence was necessary to maintain OSM functionality, it was also included another variant of the protein, where only the signal peptide plus the main chain from OSM (matureOSM) was included. A schematic representation of OSM variants is presented in **Figure 4.32**.

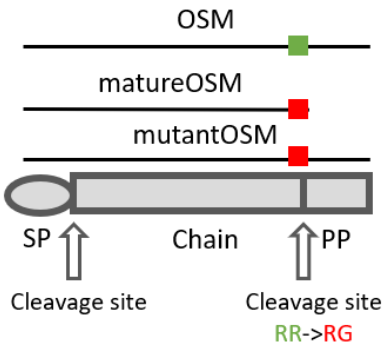

Figure 4.32. OSM secondary structure. *OSM is composed by three domains: signal peptide (SP), main chain (Chain) and propeptide (PP). Two cleavage sites, one between SP and Chain and another*

between Chain and PP are present in order to control OSM secretion to extracellular space. OSM=OSM native sequence, matureOSM=SP and Chain domains and mutantOSM=OSM full sequence with a punctual mutation in cleavage site between Chain and PP, changing the restriction site formed by two arginine amino acids (RR, showed in green) for an arginine and a glycine (RG, showed in red). Green/Red squares represent if native or mutated sequence is included.

Additionally, two more SEV anchoring proteins naturally present on SEV membrane were included in the following experiments: CD81 and TSPAN14. Of important note, the domains of lactadherin included in the study were also changed. Lactadherin is a protein formed by four domains: SP, EGF-like, F5/8 type C1 and F5/8 type C2. F5/8 type C2 domain is responsible for the anchoring of the protein to phosphatidylserine rich membranes, as it is characteristic of SEV. Thus, SBI vectors include half of the F5/8 type C1 domain and the complete sequence of F5/8 type C2 domain. However, it was decided to include the full sequence of both domains (type C1 and F5/8 type C2, c1c2) for the next tests in order to avoid major modifications on the protein structure.

Therefore, new fusion proteins were designed to include two conformations of OSM (matureOSM and mutant OSM) and three anchoring proteins (lactadherin c1c2 domains, CD81 and TSPAN14) in order to find the best constructs for future experiments. The present screening was performed in Expi293F cells due to their enhanced ability to proliferate and higher EV secretion rate compared to MSC. SEV derived from cell supernatant and cell lysates samples were obtained 48 h after transfection and both anchoring proteins and OSM presence was tested by WB assay. Results are presented in **Figure 4.33**.

CD81 protein signal was not detected in samples from neither transfected nor control Expi293F cell lysates, but bands for native CD81, expected around 25 kDa, can be seen in Ctrl, matureOSM-CD81, mutantOSM-CD81 and CD81 SEV samples isolated from control and transfected Expi293F cells supernatant (**Figure 4.33 A**). In addition to this, a clear additional band around 40 kDa was observed in mutantOSM-CD81, which would correlate with the expected molecular weight of OSM fused to CD81. Although a clear CD81 signal was not detected at 40 kDa in SEV samples from cells transfected with vectors for matureOSM-CD81 overexpression, OSM detection in the same samples showed an enrichment of matureOSM-CD81 presence in both SEV and cell lysates from cells transfected with this plasmid compared to cells transfected for CD81 overexpression and ctrl samples (**Figure 4.33 D**).

As shown in **Figure 4.33 B**, lactadherin c1c2 domains were detected in SEV samples from both Expi293F transfected and control cells, although a higher signal was obtained in SEV from cells transfected with the plasmid for c1c2 domains overexpression compared to control SEV (ctrl). A band corresponding to 70 kDa, where fusion protein signal for matureOSM-c1c2 and mutantOSM-c1c2 was expected, was observed in SEV isolated from cell culture supernatant of transfected Expi293F cells with plasmids for matureOSM-c1c2 and mutantOSM-c1c2 overexpression, suggesting that modified OSM was attached to SEV surface. The same expression pattern was observed in cell lysates, where any signal of lactadherin was detected in ctrl cells. Conversely, one band around 50 kDa, which would correspond to lactadherin free form, was observed in cells transfected with a vector to overexpress c1c2 domains of lactadherin. Finally, one band around 70 kDa was detected in both cells transfected with plasmids for matureOSM-c1c2 and mutantOSM-c1c2 overexpression. **Figure 4.33 D** shows the signal obtained for OSM protein in SEV and cell lysates from the same experimental conditions, confirming the presence of OSM in the expected molecular weight for the fusion protein.

Lastly, **Figure 4.33 C** shows that fusion proteins matureOSM-TSPAN14 and mutantOSM-TSPAN14 were also detected in both SEV and cell lysates samples from transfected Expi293F cells compared with SEV and cell lysates samples obtained from both non-transfected cells (ctrl) and cells transfected for TSPAN14 overexpression at the expected molecular weight (around 50 kDa). This finding was also confirmed in OSM-labelled membranes (**Figure 4.33 D**).

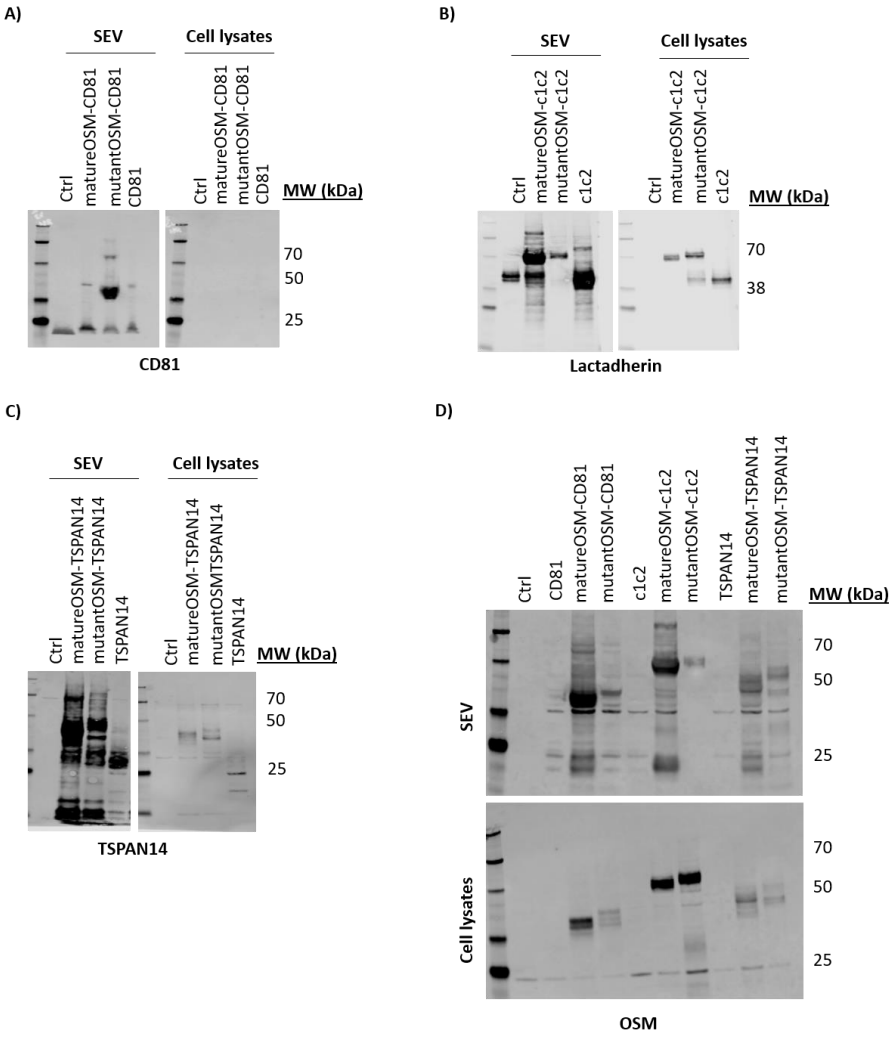

Figure 4.33. MutantOSM and matureOSM are detected fused to CD81, lactadherine c1c2 domains (c1c2) and TSPAN14 anchoring proteins in SEV and cell lysates protein samples from Expi293F cells. *Expi293F were transfected with lentiviral vectors carrying nine different inserts: matureOSM-CD81, mutantOSM-CD81, CD81, matureOSM-c1c2, mutantOSM-c1c2, c1c2, matureOSM-TSPAN14, mutantOSM-TSPAN14 and TSPAN. SEV were isolated from cell supernatant of each type of cells 48 h after transfection and doxycyclyne gene expression induction (10 µg/mL), and protein samples from cell lysates were also obtained. SEV and protein samples from non-transfected Expi293F cells were used as control (Ctrl). Fusion of one protein with another is represented with a dash (-). Representative Western Blot membranes for each experimental condition is shown.*

Overall, these data indicated that it was possible to load OSM in SEV surface when modifications on OSM native sequence were introduced. Additionally, the three

anchoring proteins included in the designed fusion proteins succeeded on the modified OSM loading in SEV membrane.

4.13.2. Mutant and Mature OSM showed functional activity in human cardiac ventricular fibroblasts

In order to decide which anchoring protein was the best choice to continue with our study and generate new MSC lines, it was also important to test if OSM was functional after sequence modification and protein fusion, and if anchoring proteins could interfere with its functional properties. Consequently, proliferation and fibrosis stimulation using the same experimental conditions than in the previous sections were repeated using SEV derived from control and transfected Expi293F cells in order to assess if OSM loaded in SEV membrane could counteract fibroblasts proliferation and/or activation *in vitro*.

4.13.2.1. Alternative OSM conformations loaded in SEV membrane points to functional antiproliferative effects in NHCF-V after stimulation

First, proliferation rate was measured after 24 h of starvation in NHCF-V. SEV isolated from cell culture media of native and transfected Expi293F cells were added at the beginning of the experiment at three different concentrations: 15, 30 and 45 µg of SEV protein/mL. As represented in **Figure 4.34 A and B**, non-statistically significant differences were observed in cell proliferation when NHCF-V were treated with any dose of ctrl SEV (which were isolated from native Expi293F supernatant) compared to untreated cells (ctrl).

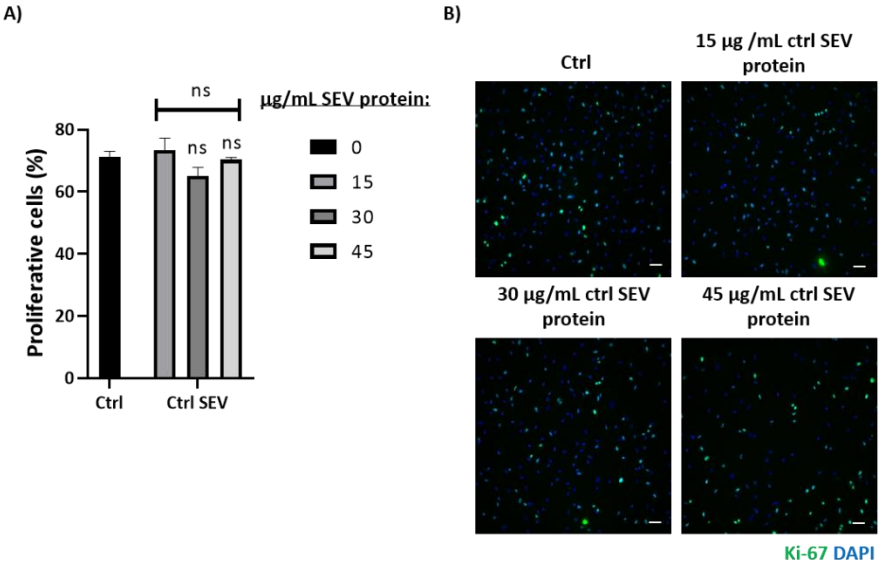

Figure 4.34. Effect of SEV isolated from native Expi293F cell culture supernatant on NHCF-V proliferation under starving conditions. (A) *Cells in proliferation after ctrl SEV exposure (µg/mL of SEV protein: 15, 30 and 45) obtained from native Expi293F supernatant. Percentage proliferative cells (Ki-67 positive nuclei) cells was calculated as number of Ki-67 positive nuclei per number of nuclei (stained with DAPI) in each screened field.* ***(B)*** *Representative pictures of NHCF-V after ctrl SEV treatment and both Ki-67 and DAPI staining. Pictures were taken using 20X objective in ImageXpress FLIPR Penta High-Throughput Cellular Screening System (Molecular Devices). Scale bar=100µm. Starved were used as reference (ctrl). Three independent experiments were performed. Asterisks indicate statistically significant differences after ANOVA and Tukey's post-hoc analysis and are shown as mean ± SEM (ns: non-statistically significative).*

After treatment with SEV isolated from Expi293F transfected with plasmids for CD81, matureOSM-CD81 and mutantOSM-CD81 overexpression, no differences in cell proliferation were observed when NHCF-V were treated with CD81 enriched SEV at any of the tested concentrations compared to ctrl condition. Contrarily, a statistically-significant decrease in cell proliferation rate was observed when NHCF-V were treated with 45 µg/mL matureOSM-CD81-SEV ($p<0.01$) and mutantOSM-CD81-SEV ($p<0.05$) SEV protein compared to NHCF-V exposed to the same concentration of CD81-SEV and ctrl condition (**Figure 3.35 A** and **B**), indicating a potential influence of the presence of OSM loaded on SEV membrane on the fibroblasts proliferation rate decrease.

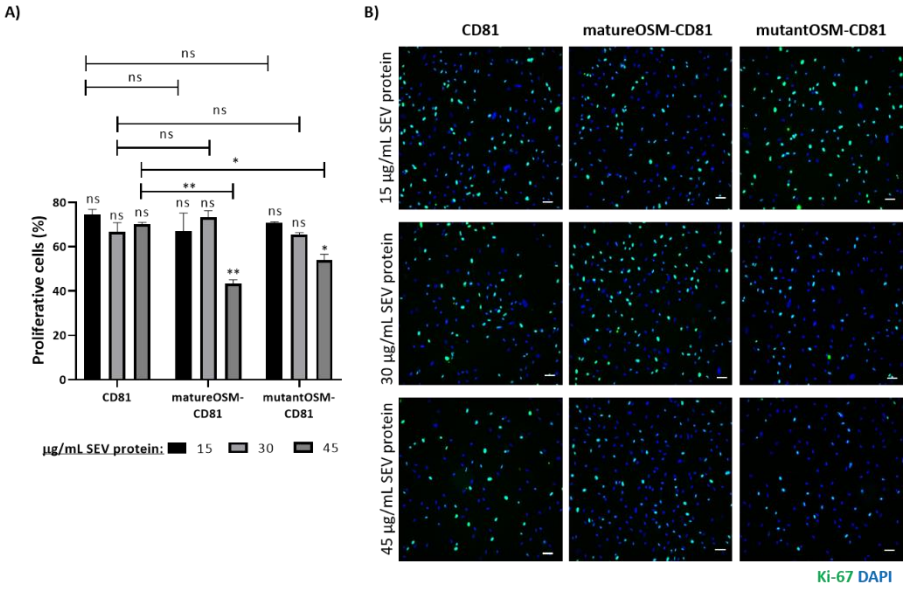

Figure 4.35. Effect of SEV isolated from Expi293F cell culture supernatant transfected with plasmids for CD81, matureOSM-CD81 and mutant-OSM-CD81 overexpression on NHCF-V proliferation under starving conditions. (A) *Cells in proliferation after ctrl SEV exposure (µg/mL of SEV protein: 15, 30 and 45) obtained from transfected Expi293F cell culture media. Percentage proliferative cells (Ki-67 positive nuclei) cells was calculated as number of Ki-67 positive nuclei per number of nuclei (stained with DAPI) in each screened field.* ***(B)*** *Representative pictures of NHCF-V after SEV treatment and both Ki-67 and DAPI staining. Pictures were taken using 20X objective in ImageXpress FLIPR Penta High-Throughput Cellular Screening System (Molecular Devices). Scale bar=100µm. Statistic comparisons between mean values obtained from different SEV doses and ctrl values as well as between values coming from the same dose of each SEV type were performed. Asterisks indicate statistically significant differences after ANOVA and Tukey's post-hoc analysis and are shown as mean ± SEM (ns: non-statistically significative; *p<0.05; **p<0.01).*

After the addition of SEV overexpressing c1c2 lactadherin domains, matureOSM-c1c2 or mutantOSM-c1c2 fusion proteins, only statistically significant differences were observed when NHCF-V were treated with 45 µg/mL of matureOSM-c1c2-SEV protein compared to data obtained for untreated cells (ctrl), showed in **Figure 4.34 A** and **B**. However, no differences were found when NHCF-V were treated with 45 µg/mL of matureOSM-c1c2-SEV compared to NHCF-V treated with 45 µg/mL of c1c2-SEV nor in. The additional conditions tested did not show a significant effect on cell proliferation decrease. Quantifications and representative pictures for these data are presented in **Figure 4.36 A** and **B**, respectively.

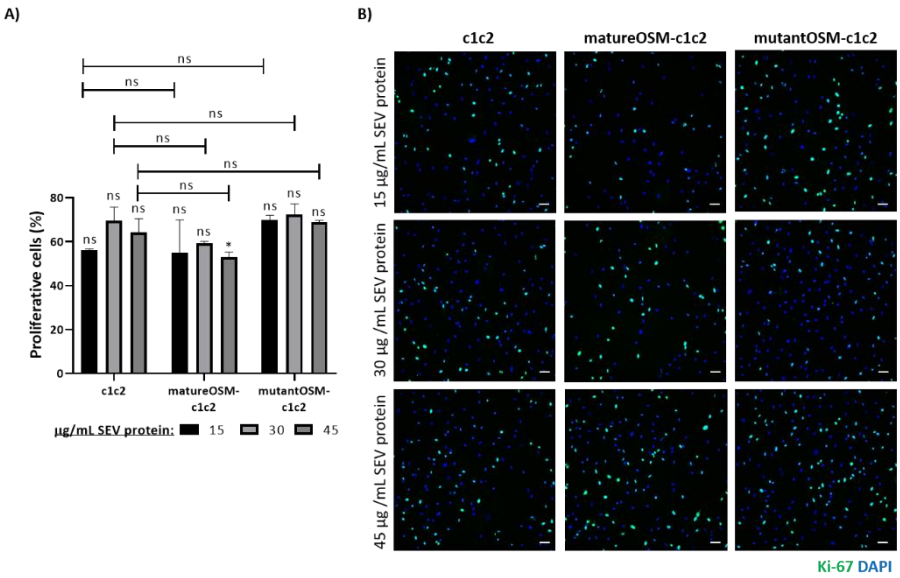

Figure 4.36. Effect of SEV isolated from Expi293F cell culture supernatant transfected with plasmids for c1c2 lactadherin domains, matureOSM-c1c2 and mutant-OSM-c1c2 overexpression on NHCF-V proliferation under starving conditions. (A) *Cells in proliferation after ctrl SEV exposure (µg/mL of SEV protein: 15, 30 and 45) obtained from transfected Expi293F cell culture media. Percentage proliferative cells (Ki-67 positive nuclei) cells was calculated as number of Ki-67 positive nuclei per number of nuclei (stained with DAPI) in each screened field.* ***(B)*** *Representative pictures of NHCF-V after SEV treatment and both Ki-67 and DAPI staining. Pictures were taken using 20X objective in ImageXpress FLIPR Penta High-Throughput Cellular Screening System (Molecular Devices). Scale bar=100µm. Statistic comparisons between mean values obtained from different SEV doses and ctrl values as well as between values coming from the same dose of each SEV type were performed. Asterisks indicate statistically significant differences after ANOVA and Tukey's post-hoc analysis and are shown as mean ± SEM (ns: non-statistically significative; *p<0.05; **p<0.01).*

Finally, the effect of SEV loaded with TSPAN14, matureOSM-TSPAN14 and mutantOSM-TSPAN14 on NHCF-V proliferation rate was evaluated. Data and representative pictures are showed in **Figure 4.37 A** and **B**, respectively. Non-statistically significant differences were obtained when primary fibroblasts were treated neither with TSPAN14-SEV at any of the tested concentrations nor with matureOSM-TSPAN14-SEV and mutantOSM-TSPAN14-SEV added at a concentration of 15 or 30 µg/mL SEV protein, when compared to untreated cells (ctrl, data showed in **Figure 4.34**). Nevertheless, a decrease in NHCF-V cell proliferation rate was observed with matureOSM-TSPAN14-SEV and mutantOSM-TSPAN14-SEV at a concentration of 45 µg/mL SEV protein compared to untreated cells ($p<0.05$). Importantly, a reduction in cell proliferation was also observed when NHCF-V were treated with 45 µg/mL SEV protein of matureOSM-TSPAN14-SEV

compared to the same dose of TSPAN14-SEV, indicating a possible influence of matureOSM loaded in SEV surface on the decrease of fibroblasts proliferation rate.

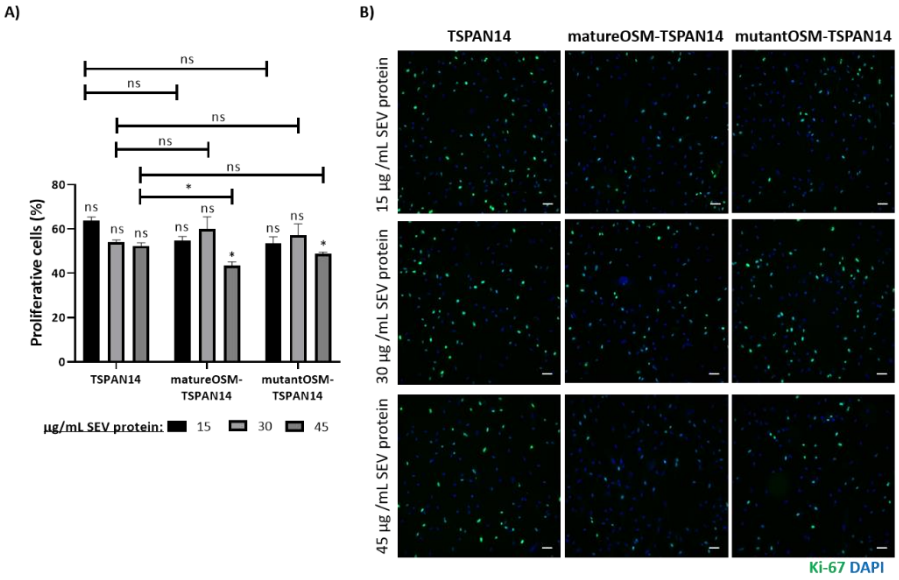

Figure 4.37. Effect of SEV isolated from Expi293F cell culture supernatant transfected with plasmids for TSPAN14, matureOSM-TSPAN14 and mutant-OSM-TSPAN14 overexpression on NHCF-V proliferation under starving conditions. (A) *Cells in proliferation after Ctrl SEV exposure (µg/mL of SEV protein: 15, 30 and 45) obtained from transfected Expi293F cell culture media. Percentage proliferative cells (Ki-67 positive nuclei) was calculated as number of Ki-67 positive nuclei per number of nuclei (stained with DAPI) in each screened field.* ***(B)*** *Representative pictures of NHCF-V after SEV treatment and both Ki-67 and DAPI staining. Pictures were taken using 20X objective in ImageXpress FLIPR Penta High-Throughput Cellular Screening System (Molecular Devices). Scale bar=100µm. Statistic comparisons between mean values obtained from different SEV doses and ctrl values as well as between values coming from the same dose of each SEV type were performed. Asterisks indicate statistically significant differences after ANOVA and Tukey's post-hoc analysis and are shown as mean ± SEM (ns: non-statistically significative; *p<0.05).*

Altogether, these data brought evidences on the functional role of OSM loaded in SEV surface as a potential tool to reduce cardiac fibroblasts proliferation under stressing conditions.

4.13.2.2. Ventricular cardiac fibroblasts activation is partially counteracted when treated with alternative OSM conformations loaded in SEV membrane

Fibrosis activation induction experiment was performed again in order to evaluate if OSM loading on SEV surface from Expi293F cells could affect telo-Col1α1 protein presence and distribution, and if this effect was dependent on the anchoring protein in each case.

First, a similar pattern of telo-Col1α1 protein labelling was observed in basal and starving NHCF-V (ctrl and unstimulated, respectively), where telo-Col1α1 presence was mostly intracellular and was only found in a small population of NHCF-V. NHCF-V stimulation was confirmed in terms of enhanced telo-Col1α1 secretion and droplets deposition in the extracellular space compared to control and unstimulated conditions. When three different concentrations of ctrl SEV (µg of SEV protein: 15, 30 and 45) isolated from non-transfected Expi293F cells supernatant were added, a similar telo-Col1α1 labelling pattern, compared to stimulated NHCF-V, was observed. These data are presented in **Figure 4.38**.

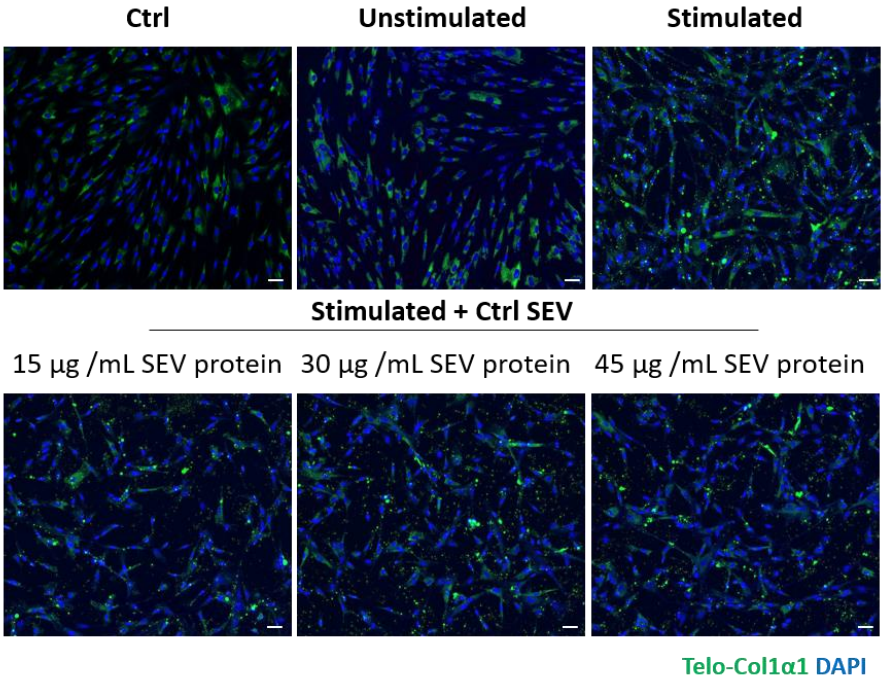

Figure 4.38. SEV isolated from non-transfected Expi293F cell culture media supernatant does not modify NHCF-V telo-Col1α1 and α-SMA expression upon stimulation. *Representative pictures of*

NHCF-V in basal conditions (ctrl), after 48h starvation (Unstimulated) and after 48h of stimulation with or without the addition of ctrl SEV (µg /mL SEV protein: 15, 30 and 45), where Telo-Col1α1 is shown in green and nuclei staining (DAPI) in blue. Pictures were taken using 20X objective in CellVoyager CV8000 screening system (Yokogawa). Scale bar=100µm.

In addition, the effect of matureOSM-CD81-SEV and mutantOSM-CD81-SEV on telo-Col1α1 location was compared to CD81-SEV 48 h added at the same time than stimulation factors after 48h of treatment. Results are shown in **Figure 4.39**. Similar pattern of telo-Col1α1 fluorescent signal was observed when CD81-SEV addition at 15, 30 and 45 µg/mL of SEV protein compared to stimulated cells and NHCF-V stimulated and treated with ctrl SEV (**Figure 4.38**). Nevertheless, reduced telo-Col1α1 extracellular deposition was noticed when matureOSM-CD81-SEV and mutantOSM-CD81-SEV at the three tested SEV protein concentrations (15, 30 and 45 µg/mL).

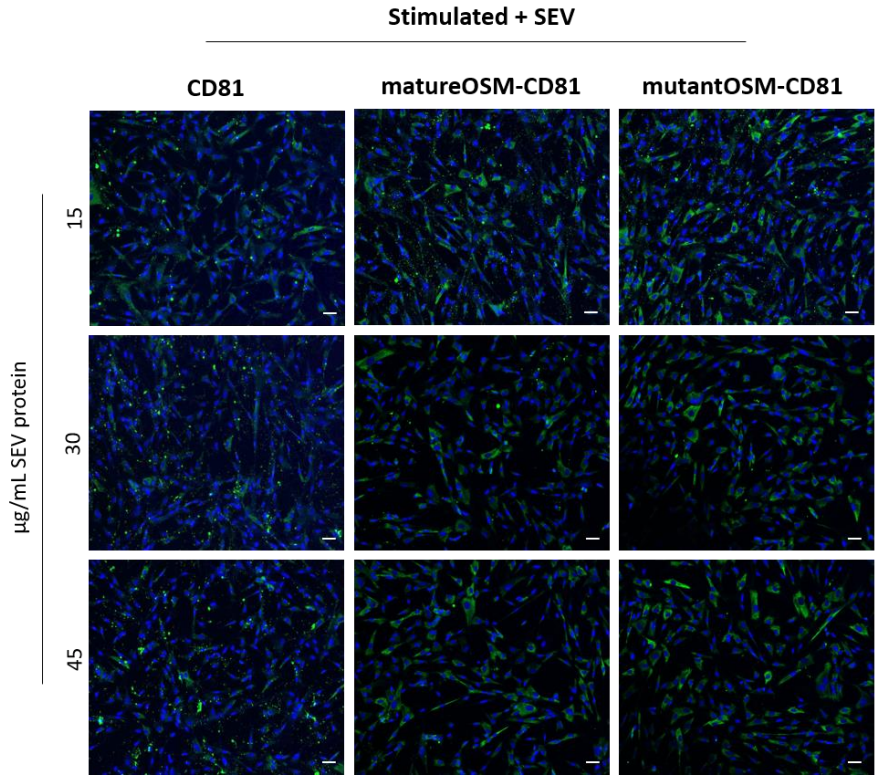

Figure 4.39. SEV isolated from transfected Expi293F cell culture media supernatant for CD81, matureOSM-CD81 and mutantOSM-CD81 fusion proteins overexpression modify NHCF-V telo-

Col1α1 expression upon stimulation. *Representative pictures of NHCF-V after 48h of stimulation and the addition of SEV loaded with CD81, matureOSM-CD81 and mutantOSM-CD81 fusion proteins at three different concentrations (µg/mL SEV protein: 15, 30 and 45). Pictures were taken using 20X objective in CellVoyager CV8000 screening system (Yokogawa). Scale bar=100µm.*

Similar results were observed when NHCF-V were treated with 15, 30 and 45 µg/mL of SEV protein from c1c2-SEV, matureOSM-c1c2-SEV and mutantOSM-c1c2-SEV. As represented in **Figure 4.40**, NHCF-V treated with c1c2-SEV presented a similar pattern on telo-Col1α1 location than stimulated cells and stimulated cells treated with ctrl SEV, where protein deposits on the extracellular space were also found. However, treatment with matureOSM-c1c2-SEV and mutantOSM-c1c2 SEV partially avoided telo-Col1α1 secretion at different levels comparing pictures obtained from NHCF-V stimulated and treated with the same dose of c1c2-SEV and matureOSM-c1c2-SEV or mutantOSM-c1c2-SEV.

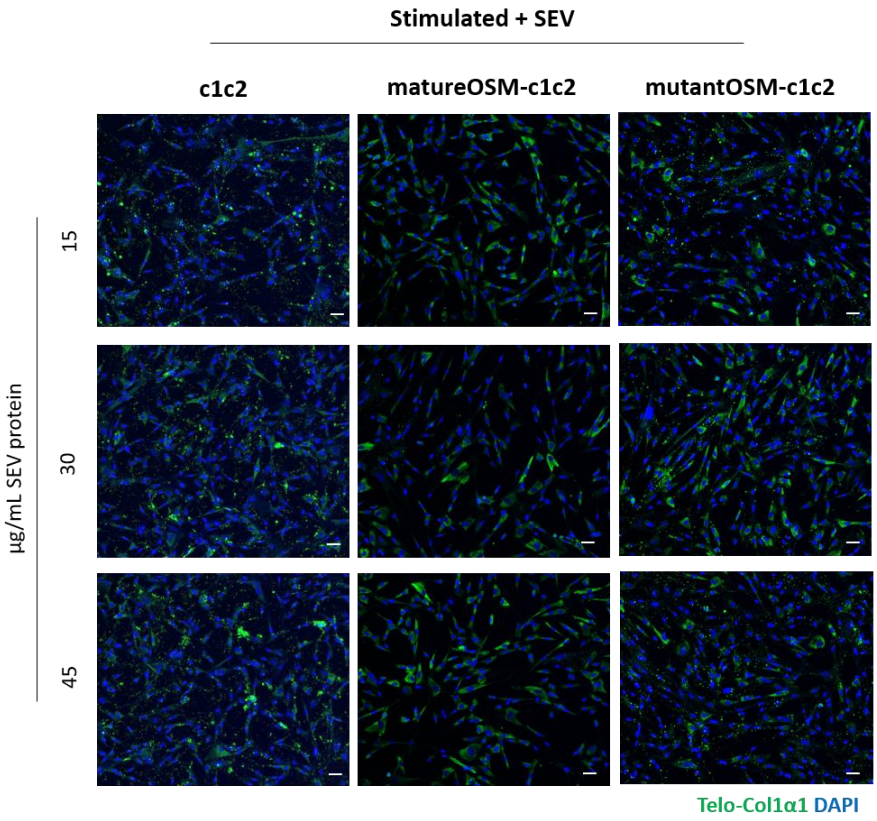

Figure 4.40. SEV isolated from transfected Expi293F cell culture media supernatant for c1c2 lactadherin domains, matureOSM-c1c2 and mutantOSM-c1c2 fusion proteins overexpression modify NHCF-V telo-Col1α1 expression upon stimulation. *Representative pictures of NHCF-V after 48h of stimulation and the addition of SEV loaded with c1c2 domains, matureOSM-c1c2 and mutantOSM-c1c2 fusion proteins at three different concentrations (µg/mL SEV protein: 15, 30 and 45). Pictures were taken using 20X objective in CellVoyager CV8000 screening system (Yokogawa). Scale bar=100µm.*

Lastly, effect of TSPAN-SEV, matureOSM-TSPAN14-SEV and mutantOSM-TSPAN14-SEV on stimulated NHCF-V was evaluated. Results are shown in **Figure 4.41**. Telo-Col1α1 location pattern was similar in NHCF-V treated with TSPAN14-SEV and mutantOSM-TSPAN14-SEV, and was comparable to the signal obtained on stimulated fibroblasts and stimulated fibroblasts treated with ctrl SEV, CD81-SEV and c1c2-SEV (**Figures 4.38, 4.39** and **4.40**). However, a reduction of telo-Col1α1 deposits was found when matureOSM-TSPAN14-SEV were added at the three different concentrations (15, 30 and 45 µg/mL SEV protein) to cardiac fibroblasts.

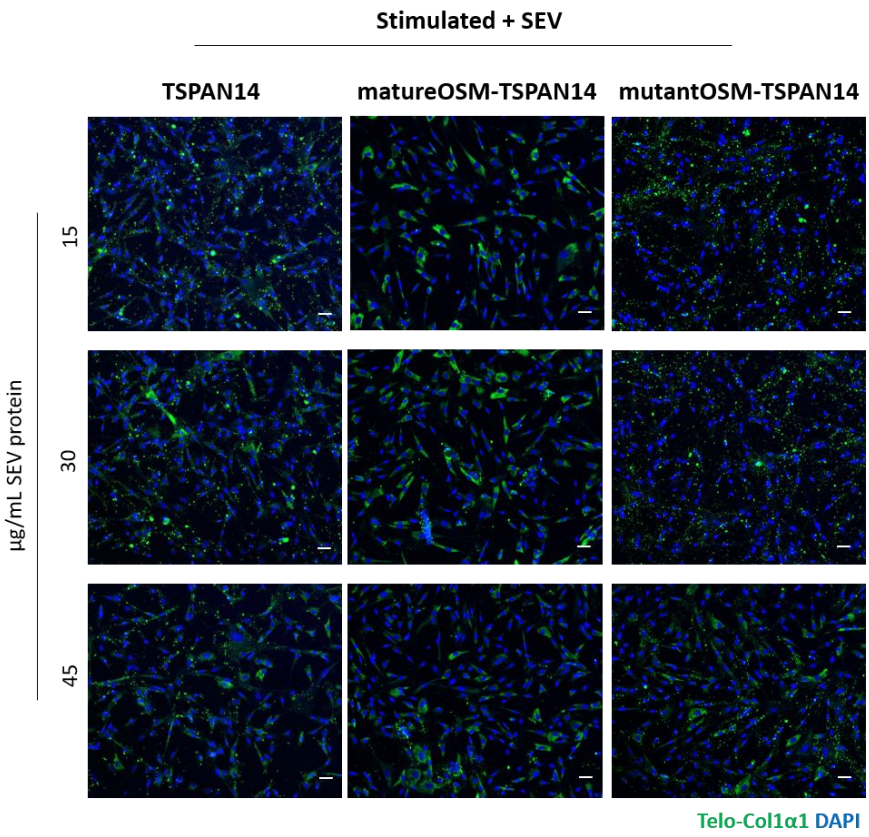

Figure 4.41. SEV isolated from transfected Expi293F cell culture media supernatant for TSPAN14, matureOSM-TSPAN14 and mutantOSM-TSPAN14 fusion proteins overexpression modify NHCF-V telo-Col1α1 and α-SMA expression upon stimulation. *Representative pictures of NHCF-V after 48h of stimulation and the addition of SEV loaded with TSPAN14, matureOSM-TSPAN14 and mutantOSM-TSPAN14 fusion proteins at three different concentrations (µg/mL SEV protein: 15, 30 and 45). Pictures were taken using 20X objective in CellVoyager CV8000 screening system (Yokogawa). Scale bar=100µm.*

In summary, an interesting shift on telo-Col1α1 fluorescent signal location from extracellular to intracellular space was found when SEV loaded with OSM were added together with stimulating factors to NHCF-V in the majority of conditions tested. Of important note, the mentioned qualitative change on telo-Col1α1 location was not observed where ctrl SEV, CD81-SEV, c1c2-SEV and TSPAN14-SEV were used, and a similar pattern of dotted extracellular labelling than in stimulated NHCF-V was observed.

4.14. Mutant and Mature OSM variants loaded in SEV isolated from Engineered Immortalized MSC suggest an enhanced therapeutic potential effect against fibrosis

Based on the results obtained in both proliferation and fibroblast activation studies, it was decided to continue with CD81 as anchor protein for OSM loading on SEV surface. Furthermore, an immortalized MSC line from dental pulp origin generated in our research team (iMSC) was used to overcome difficulties regarding to proliferative senescence reached after 10 cell passages. These cells were genetically modified in order to express telomerase reverse transcriptase. Previous data from our laboratory have validated that iMSC have a sustained doubling population rate after more than 20 cell passages, maintain MSC-characteristic markers profile and retain similar SEV features compared to native MSC. TetOn promoter was maintained in order to generate iMSC lines that could overexpress fusion proteins of interest in an inducible manner which would be dependent on the presence of doxycycline in cell culture media.

4.14.1. Immortalized MSC genetic modification for CD81, matureOSM-CD81 and mutantOSM-CD81 fusion proteins specific loading in SEV surface

Immortalized MSC from dental pulp origin were genetically modified through the insertion of three lentiviral plasmids: one of them carrying CD81 DNA sequence, a second one carrying matureOSM sequence followed by CD81 sequence (matureOSM-CD81), and a third one containing mutantOSM sequence and CD81 sequence (mutantOSM-CD81). iMSC without further genetic modifications were used as reference. First, lentiviral particles generated were titrated for highly efficient iMSC infection, and GFP positive percentage of cells was measured by flow cytometry (**Figure 4.42**). Percentage of GFP positive cells obtained was above 85% and was maintained over cell passages in the three cell lines generated (**Figure 4.43 A**). Consequently, no further selection was performed. New cell lines generated were named iMSC-CD81, iMSC-matureOSM-CD81 and iMSC-mutantOSM-CD81.

In order to ensure that MSC characteristics were maintained after genetic engineering, the expression profile of markers stablished by Mesenchymal and Tissue Stem Cell Committee of the International Society for Cellular Therapy was analyzed. As represented in **Figure 4.43 B**, more than 90% of cells were positive for CD90, CD105 and CD73 and percentage of positive cells for CD14, CD34 and CD45

was under 5% in all cell lines, and fibroblasts-like spindle shape was also conserved (**Figure 4.43 C**).

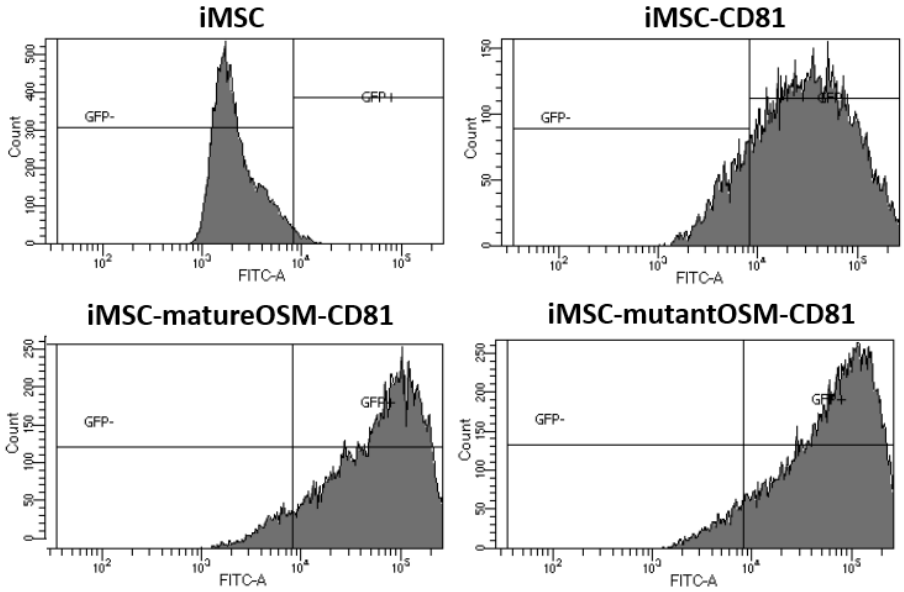

Figure 4.42. Engineered iMSC screening through GFP fluorescent intensity. *Histograms obtained from flow cytometry analysis showing GFP negative and postive cells populations for samples corresponding to iMSCS, iMSC-CD81, iMSC-matureOSM-CD81 and iMSC-mutantOSM-CD81.*

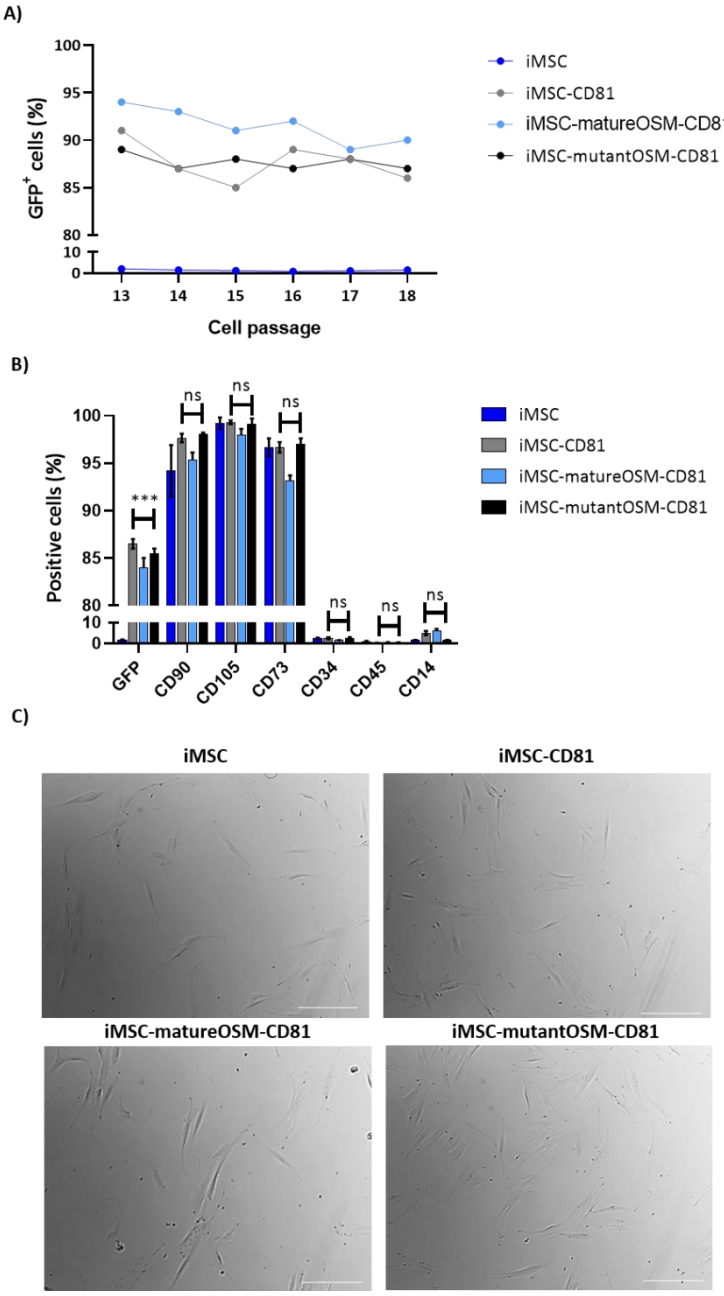

Figure 4.43. Engineered iMSC maintain GFP expression over cell passages, characteristic markers of MSC and expected spindle morphology. (A) *Percentage of cells positive for GFP expression at different cell passages in iMSC, iMSC-CD81, iMSC-matureOSM-CD81 and iMSC-mutantOSM-CD81 measures by flow cytometry.* ***(B)*** *Expression of CD90, CD105, CD73, CD34, CD45 and CD14 was measured by flow cytometry in iMSC, iMSC-CD81 and iMSC-matureOSM-CD81 and iMSC-mutantOSM-CD81. GFP positive cells were gated for tracking purposes and fluorescent channels*

*compensation. Results are presented as mean±SEM. Cell membrane markers on each cell type were measured after two different transfection batches. **(C)** Representative images of iMSC, iMSC-CD81 and iMSC-matureOSM-CD81 and iMSC-mutantOSM-CD81 showing cell morphology. Scale bar=400µm. ANOVA and Tukey's post-hc test were used in order to compare mean between groups. Data are presented as mean±SEM.*

Altogether, these data pointed that iMSC generated maintained the expected characteristics expected for a MSC, and were therefore suitable for further experiments.

4.14.2. matureOSM-CD81 and mutantOSM-CD81 fusion proteins are detected on SEV

First, cell viability after 48 h of exposure to increasing doses of doxycycline was measured in iMSC and engineered iMSC for CD81, matureOSM-CD81 and mutantOSM-CD81 expression. As represented in **Figure 4.44**, doxycycline presence did not significantly interfere with iMSC, iMSC-CD81, iMSC-matureOSM-CD81 and iMSC-mutantOSM-CD81 cell viability at any of the concentrations included in the study (µg/mL: 1.56, 3.12, 6.25, 12.5, 25, 50 and 100), since percentage of viable cells was maintained between 90 and 100 % in all the experimental conditions.

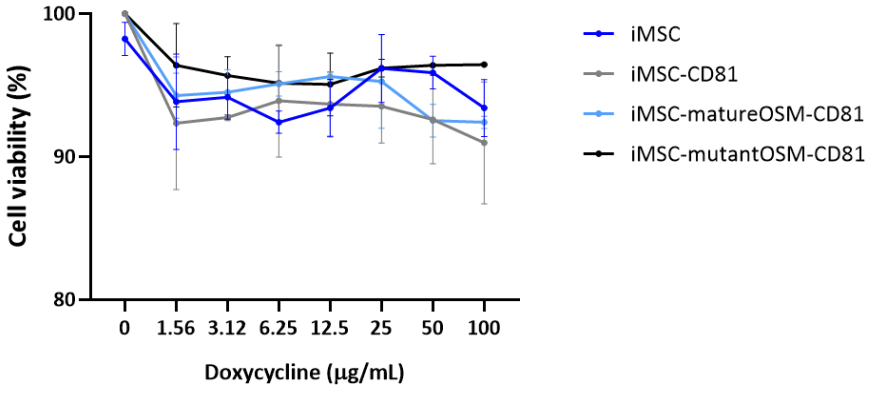

Figure 4.44. Doxycycline does not have cytotoxic effects on iMSC and genetically modified iMSC. *Percentage of cell viability after 48 h of exposure to increasing doses of doxycycline (µg/mL: 1.56, 3.12, 6.25, 12.5, 25, 50 and 100) was measured in iMSC, iMSC-CD81, iMSC-matureOSM-CD81 and iMSC-mutantOSM-CD81 by MTS assay and measured by spectrophotometry (absorbance at 490 nm), using data from each type of untreated cells (0 µg/mL of doxycycline) as reference values. Data were*

obtained from three independent experiments, each one performed by triplicate, and are presented as mean±SEM.

Second, a screening of OSM and CD81 proteins presence was performed in both cell lysates protein samples and SEV from iMSC, iMSC-CD81, iMSC-matureOSM-CD81 and iMSC-mutantOSM-CD81 by Western Blot assay. Results are shown in **Figure 4.45**, where an enrichment on OSM at the expected molecular weight when it is fused to CD81 (around 40 kDa) is observed in iMSC-matureOSM-CD81 and iMSC-mutantOSM-CD81 cell lysates samples compared to iMSC and iMSC-CD81 samples. Importantly, OSM was only detected in matureOSM-CD81-SEV and mutantOSM-CD81-SEV samples, and not in Ctrl-SEV and CD81-SEV. CD81 was observed in cell lysates and SEV samples at the expected molecular weight for the protein native form (around 25 kDa). However, fusion protein was mostly detected in matureOSM-CD81-SEV and mutantOSM-CD81-SEV samples compared to CD81-SEV and ctrl-SEV, and it was not observed in cell lysates samples. As expected, tub was detected in cell lysates, but not in SEV samples.

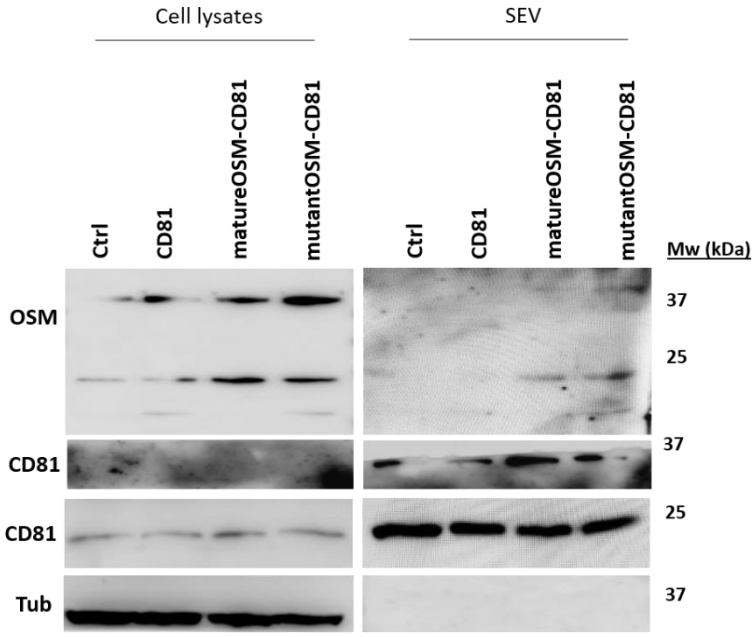

Figure 4.45. MatureOSM and mutantOSM variants fused to CD81 are detected in SEV protein samples. *Content of OSM, CD81 and tub proteins in cell lysates and SEV derived from iMSC (ctrl), iMSC-CD81, iMSC-matureOSM-CD81 and iMSC-mutantOSM-CD81. Representative Western Blot membrane is shown.*

The presented data confirmed that OSM sequence modification was crucial in order to load the protein on SEV surface. Nevertheless further experiments were necessary in order to assess if OSM present on SEV was able to trigger functional effects on target cells, and if this modification on native SEV could enhance their therapeutic potential.

4.14.3. OSM loaded on SEV affects NHCF-V proliferation under starving conditions and telo-Col1α1 protein location after stimulation

After results obtained in the previous section, where it was seen that matureOSM-CD81 and mutantOSM-CD81 SEV were enriched in OSM, proliferation and fibroblasts activation experiments were repeated. Based on the results obtained in **Figures 4.23, 4.24, 4.34 -4.41**, a concentration of 45 µg/mL of SEV protein and 10 ng/mL rhOSM were used for these experiments.

First, Ki-67 immunostaining was performed in NHCF-V after starvation in order to measure the percentage of cells in proliferation. Results are presented in **Figure 4.46 A** and **B**. Untreated cells and cells treated with ctrl and CD81-SEV showed similar proliferation rates (27.49±3.06 %, 31.80±2.61 % and 32.18±0.28 %, respectively), and no significant differences were observed between them. Treatment with matureOSM-CD81-SEV resulted in a slight decrease on NHCF-V proliferation rate (23.95±3.37 %), although no statistically significant differences were obtained when data were compared to untreated condition. Encouragingly, treatment with mutantOSM-CD81-SEV and rhOSM significantly reduced NHCF-V proliferation rate (17.35±0.78 and 19.57±2.97 %, respectively) compared to untreated cells ($p<0.05$ in both cases). When data from ctrl-SEV and CD81-SEV treatments were compared to results obtained for cells treated with matureOSM-CD81-SEV and mutantOSM-CD81-SEV, non-statistically differences were observed between ctrl-SEV, CD81-SEV and matureOSM-CD81-SEV. However, a significant decrease on cell proliferation rate was obtained when NHCF-V were treated with mutantOSM-CD81-SEV ($p<0.01$) compared to results obtained after ctrl-SEV and CD81-SEV treatments.

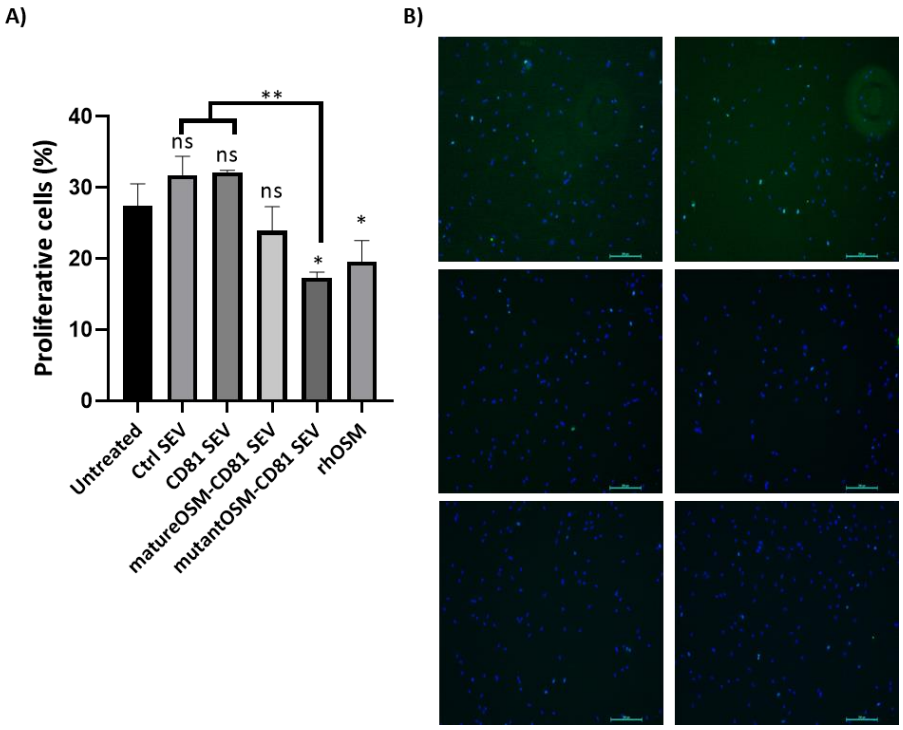

Figure 4.46. Treatment with mutantOSM-CD81 SEV reduced NHCF-V proliferation rate in vitro. *NHCF-V were submitted to starving conditions and treated with 45 µg/mL SEV protein of ctrl-SEV, CD81-SEV, matureOSM-CD81-SEV and mutantOSM-CD81-SEV or 10 ng/mL rhOSM. Starved but untreated cells were used as control. Ki-67 staining is shown in green, while DAPI staining is shown in blue. Pictures were taken using 10X objective in a Leica fluorescence microscope. Scale bar=200µm. Data were obtained from two independent experiments. ANOVA statistical analysis to analyze group means difference was used. Results are presented as mean±SEM.*

These preliminary data pointed that OSM-enriched SEV could interfere with NHCF-V proliferation, although further independent experiments should be performed to confirm these results.

Second, telo-Col1α1 protein expression and distribution was assessed in NHCF-V after 48 h of stimulation, with or without SEV and rhOSM treatments. Results are displayed in **Figure 4.47**. As it can be appreciated, telo-Col1α1 was not detected on the most majority of ctrl cells (non-starved and non-stimulated) and unstimulated cells (starved but not stimulated), although a stronger presence of this protein was observed in unstimulated cells compared to basal condition (ctrl). Nonetheless, a pronounced dotted net of telo-Col1α1 was found when NHCF-V were stimulated with L-ascorbic acid 2-phosphate, dextran sulphate and recombinant TGFβ-1,

indicating ECM matrix synthesis by cardiac fibroblasts in response to stimulation with the pro-fibrotic cocktail. Similar patterns of telo-Col1α1 labelling were found when ctrl-SEV and CD81-SEV were added to NHCF-V. On the contrary, treatment of NHCF-V with matureOSM-CD81-SEV and mutantOSM-CD81-SEV leaded to a significant reduction on telo-Col1α1 expression and secretion to the extracellular space compared to stimulated cells and stimulated cells treated with ctrl-SEV and CD81-SEV. Additionally, treatment with rhOSM also resulted in similar effects on telo-Col1α1 expression pattern as the addition of matureOSM-CD81-SEV and mutantOSM-CD81 SEV.

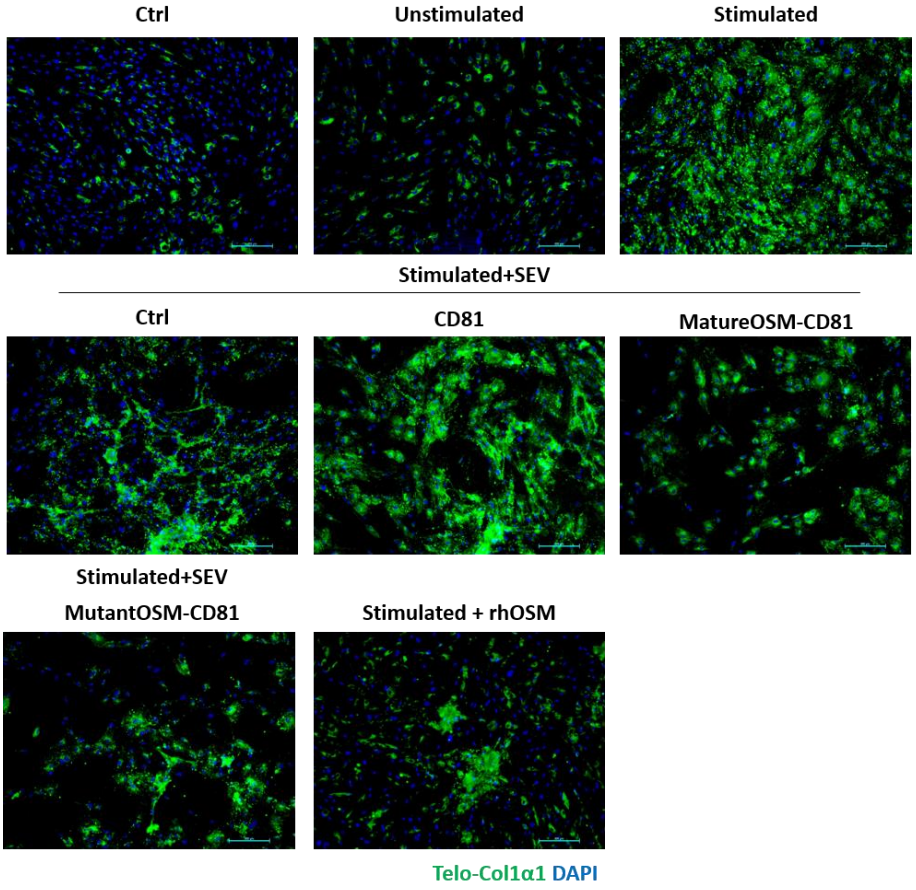

Figure 4.47. MatureOSM-CD81-SEV and MutantOSM-CD81-SEV treatment reduced telo-Col1α1 extracellular deposition upon NHCF-V stimulation. *Representative pictures of NHCF-V after 48 h of stimulation and the addition of 45 µg/mL SEV protein from ctrl SEV and SEV loaded with CD81, matureOSM-CD81 and mutantOSM-CD81 fusion or 10 ng/mL rhOSM. Non-starved and non-stimulated cells (ctrl) and starved but unstimulated cells (unstimulated) were used as control*

conditions. Telo-Col1α1 staining is shown in green, while DAPI staining is shown in blue. Pictures were taken using 10X objective using Leica fluorescence microscopy. Scale bar=200µm. Data were obtained from two independent experiments.

These data provided evidences about a functional effect of OSM-enriched SEV over ctrl-SEV and CD81-SEV, reducing telo-Col1α1 expression and avoiding its deposition on the extracellular space in an *in vitro* model of fibroblasts activation.

5. Discussion

5. Discussion

Coronary angioplasty represents an effective intervention following AMI. Nevertheless, the sudden blood flux restoration triggered by the reperfusion of the occluded vessel is related to increased cardiomyocytes apoptosis and ROS generation, mitochondrial dysfunction, intracellular calcium overload and autophagic imbalance[113, 390]. In addition to this, pathological cardiac remodeling after AMI, where necrotic myocardial tissue is replaced by a non-functional scar, leads to a significant loss of contractile function and electrical coupling[107, 110]. Although several therapeutic approaches have been attempted to attenuate I/R-induced injury, their limited clinical outcome makes still necessary the development of more effective strategies.

During the last years, cell-free therapies involving the customized design of nanoparticles as vehicles for potential therapeutic agents' delivery have gained attention as an alternative to mitigate inflammation, oxidative stress and tissue apoptosis during I/R[161].

In this work, two different strategies in order to ameliorate clinical outcome after AMI have been proposed. First, nanoconjugates based on the covalent union of a FFA (diDHA) to a polymeric carrier (PGA) have been synthetized in order to increase its stability and potentiate its potential cardioprotective propertied. Second, the genetic modification of MSC in order to load a protein of interest (OSM) on MSC-SEV surface, with the hypothesis that OSM-enriched SEV could improve therapeutic potential of native SEV in the context of cardiac remodeling after AMI.

Section A: PGA-diDHA-based nanoconjugates role in cardiomyocytes preconditioning during ischemia-reperfusion induced injury.

During the present dissertation, it has been displayed the effect of ischemia and reperfusion processes on cardiomyocytes, which include changes in metabolism leading to quick changes in intracellular pH and mitochondrial dysfunction. Under these conditions, cardiomyocytes make a switch on their metabolism, and obtain ATP from glycolytic pathway instead of Krebs' cycle. Since FA are mammal adult cardiomyocytes main source of energy and a poor availability of them is found during ischemia, the additional administration of FA before reperfusion in order to avoid massive cardiomyocytes death and improve clinical outcome after reperfusion has been proposed.

Previous studies have considered the use of different PUFA combinations in order to reduce cardiac damage after AMI[181, 189, 191]. However, the most majority of those studies have been focused on the dietary or injected PUFA administration before cardiac event induction[183, 184]. Given that the preferred route of nanoconjugates administration in the clinical setting is intracoronary, and that the objective of this work was to evaluate the effect of our nanoconjugates on ischemic area preconditioning, our experimental approach consisted on the local nanoparticles' administration before reperfusion, both in *in vitro* and *in vivo* models. Only one previous publication has used this preconditioning experimental approach using PUFA as potential bioactive agent, where a combination of EPA and DHA (6:1) was administrated via an intravenous bolus before reperfusion in an I/R in vivo rat model[193]. However, it was impossible to distinguish if beneficial effects observed were derived from EPA, DHA or a combination of both PUFA, and the amount of them that reached cardiac tissue could not be determined.

Additional studies have exposed that FFA are highly unstable and are sequestrated by albumins in the blood, and PUFA have a high susceptibility to be peroxidized, resulting in free radicals' generation and, eventually, to aldehydes and ketones, stimulating inflammation[196, 197]. Consequently, we proposed the stabilization of a PUFA, such as diDHA, through its binding to a synthetic polypeptide carrier (PGA). A rational design of conjugates with different physico-chemical properties by including varying amounts of diDHA molecules attached to PGA backbone was performed by Polymer Therapeutics laboratory in Príncipe Felipe Research Institute, which gave place to three candidates: PGA-diDHA$_{2.2}$, PGA-diDHA$_{6.4}$ and PGA-diDHA$_{9.1}$.

Uptake experiments showed a higher nanoparticles internalization by HMVEC-C and NRVM under I/R conditions compared to Nx and the use of PGA alone (**Figure 4.6**), suggesting that diDHA presence could favor nanoconjugates internalization under I/R conditions and could trigger functional effects on target cells. In addition to this, transcytosis assay showed that HMVEC-C were able to transfer nanoconjugates to NRVM, and this effect was enhanced when NRVM were under stressing conditions compared to normoxia in case of PGA, PGA-diDHA$_{2.2}$, PGA-diDHA$_{6.4}$ treatments. This increase in nanoconjugates uptake by NRVM under stressing conditions could be explained by cell communication mechanisms between HMVEC-C and NRVM, since it has been previously demonstrated that paracrine factors secreted by CM can modulate cellular responses in EC. As an example, it has been seen that CM can secrete cardiokines (such as VEGF, FGF or angiopoietin 1) that are able to induce tube formation by EC[21, 391]. However, we failed to see an increased number of cardiomyocytes labelled with OG when PGA-diDHA$_{9.1}$ was administered to HMVEC-C. We hypothesize that this difference could be a consequence of a different 3D conformation of the nanoconjugate, since higher diDHA loading leaded to smaller and more compact particles (data provided by Therapeutic Polymers laboratory), probably hindering diDHA interaction with cell membrane.

In order to evaluate nanoconjugates' ability as NRVM preconditioning molecules before reperfusion and avoid further cell damage *in vitro*, several cellular parameters associated with I/R, including cell apoptosis, oxidative stress and mitochondrial function, were measured. Esmolol, a β-blocker commonly used in clinical practice for cardiac tissue protection against AMI, was included as positive control for these experiments. Apoptosis studies revealed diverse effects depending on the cellular parameter measured. Overall, data showed a decrease on apoptosis in NRVM preconditioned with three increasing doses of PGA-diDHA-based nanoconjugates. On the contrary, treatment with free diDHA only resulted in a significant reduction of Caspase3/7 activity when used at 10 µg of diDHAeq (**Figure 4.5**). Only samples from NRVM preconditioned with PGA-diDHA$_{6.4}$ showed a consistent cell protection attending to the measurement of total apoptotic cells and Bcl-2/Bax protein expression ratio, although minor protective effects were also observed when cells were treated with PGA-diDHA$_{2.2}$ and PGA-diDHA$_{9.1}$, but not when NRVM were preconditioned with free diDHA, supporting the idea that diDHA encapsulation would be necessary in order to protect NRVM from I/R-induced injury (**Figures 4.8** and **4.9**). After seeing these data, we wanted to elucidate the adjacent causes of the observed cell apoptosis, and how PGA-diDHA-based nanoconjugates were contributing to cell damage attenuation. I/R-induced injury is

commonly associated with an increased amount of functionally and structurally defective proteins. As a consequence, protein folding system, which includes chaperones like GRP-78, is collapsed, and autophagy machinery is activated, leading to non-functional proteins sequestration in double-membraned structures (autophagosomes), which are fused with acidic vesicles (lysosomes) for proteins degradation and recycling[392]. Autophagy activation requires Beclin-1 functional effect, and previous studies have described a physical interaction between Bcl-2 and Beclin-1, which avoids Beclin-1 mediated autophagy. However, Bcl-2 releases Beclin-1 following a myocardial insult, which can trigger severely detrimental effects[131]. Data showed in **Figure 4.10** and **4.11** suggested a contribution of nanoconjugates avoiding massive autophagy activation after reperfusion in terms of Beclin-1 protein levels and the number of acidic vesicles present in NRVM. In addition to this, GRP-78 reduced levels after PGA-diDHA$_{6.4}$ and free diDHA treatment pointed to a reduction in ER-related stress compared to non-treated cells (I/R).

Most apoptotic stimuli (such as oxidative stress, hypoxia or nutrient depravation) converge at the mitochondria, leading to mPTP dysfunction and "apoptosome" complex formation, which results in Caspase-3 activation[385]. Results obtained in this work supported the idea that PGA-diDHA-based nanoconjugates could maintain mitochondrial membrane potential, preserving mitochondria ultrastructure and function, and avoiding an excessive ROS generation (**Figures 4.12** and **4.13**). Although these are preliminary data, it is important to remark that any of the nanoconjugates promoted fibroblasts wound healing under stressing conditions compared to control cFib, and long-term exposure to free diDHA, and not to nanoconjugates, confirmed diDHA toxicity on primary neonatal rat cardiac fibroblasts (**Figure 4.14**).

Overall, all PGA-diDHA conjugates displayed cardioprotective abilities *in vitro*, and these effects seemed to be dependent on the levels of diDHA loading. When considering the *in vitro* data as a whole, PGA-diDHA$_{6.4}$ provided the best results regarding to apoptosis reduction, ROS generation, autophagy machinery activation and mitochondrial function. Importantly, PGA-diDHA$_{6.4}$ treatment resulted in a reduction on late-apoptotic cells and avoided loss of MMP compared to treatment with free diDHA in NRVM, suggesting an improvement on functionality when diDHA is conjugated to PGA. When the study of the effect of these two candidates was extrapolated to a I/R *in vitro* model in human cardiac myocytes derived from iPSC, data showed a similar pattern than the obtained on NRVM, confirming the anti-apoptotic effect of PGA-diDHA$_{6.4}$ compared to free diDHA after I/R. However, both

PGA-diDHA$_{6\text{-}4}$ and free diDHA reduced ROS generation *in vitro* (**Figure 4.16**), which was contradicting with the results obtained in **Figure 4.13**. We believe that fluorescent signal obtained from NRVM treated with free diDHA could be derived from an unspecific union of CellROX probe to diDHA oil drops remaining in cell membranes, since labelling pattern is very different from the observed for the rest of experimental conditions.

One important limitation of our study was the election of Esmolol as positive control in our experimental models. Previous studies have demonstrated an anti-apoptotic of Esmolol potential in I/R *in vivo* models[393, 394]. However, we failed to reproduce this effect in our *in vitro* model of I/R using NRVM when total number of early and late apoptotic cells were measured, and did not reduce ROS generation under stressing conditions (**Figure 4.8** and **4.13**). However, NRVM treatment with Esmolol 30 min before reperfusion resulted in marginal improvement of Bcl-2/Bax protein levels ratio, lower levels of Beclin-1 and prevented cells from mitochondrial membrane depolarization (**Figures 4.9, 4.10** and **4.12**). Furthermore, Esmolol did not ameliorate AAR neither in *in vivo* I/R models of rat nor pig when it was locally administered few minutes before reperfusion (**Figures 4.17** and **4.18**). García-Ruiz JM at al showed that intravenous administration of metoprolol, another β-blocker commonly used in clinical practice, was more effective reducing infarct size and preserving LVEF using swine I/R *in vivo* model and STEMI patients after longer infusion intervals (25 min) compared to shorter infusion intervals (5 min)[395]. Although Esmolol was administered intracoronary in a large animal I/R *in vivo* models, it could be possible that the mechanism of action of this type of drug requires a longer time of administration, and potential protective effects cannot be detected when drug was administered right before ligation removing or balloon disinflation.

Cardiac tissue preconditioning with PGA-diDHA$_{6.4}$ in a I/R *in vivo* rat model resulted in a similar reduction on AAR when both dose of the nanoconjugate were administered, and dose 1 (27.1 µg diDHA eq/kg) resulted in a significant drop on AAR when diDHA was added conjugated compared to the same dose of free diDHA. Notably, although dose 2 (271 µg diDHA eq/kg) of free diDHA resulted in an apparent reduction of AAR, free diDHA physical properties lead to a high viscous preparation with low solubility, difficulty manipulation and administration. As a consequence, actual amount of free diDHA injected could not be determined and a high variability between animals from the same experimental group was obtained, making data unreliable (**Figure 4.17**). Of important note, when the same µg of diDHA eq were contained in PGA-diDHA$_{6.4}$, solubility was not a problem, and

nanoconjugate was perfectly dissolved in PBS and easy to handle for administration. In order to evaluate the potential cardioprotective effect of PGA-di$DHA_{6.4}$ nanoconjugate in a more clinically relevant scenario, a swine I/R *in vivo* model using an angioplasty catheter that allowed local infusion of drugs before occluded artery opening was set up. Our results suggested that candidate nanoconjugate may represent an interesting option to induce cardioprotection during reopening of the artery by coronary angioplasty through percutaneous intervention (PCI), since AAR 7 days after surgical intervention was reduced when nanoconjugate was infused compared to data obtained from I/R and I/R+PGA experimental groups (**Figure 4.19**). Nevertheless, relatively minor benefits observed and the low number of animals included in each experimental group suggest the need for additional experiments to fully define the extent of the therapeutic effect.

Section B: Oncostatin-M-enriched SEV isolated from genetically modified MSC as potential anti-fibrotic agent.

Cardiac fibrosis causes detrimental effects in electrical coupling and heart function, leading to HF. Several studies have proposed anti-fibrotic therapies in the context of AMI in both animal and human trials, such as the use of connective tissue growth factors antagonist, galectin-3 inhibitors, anti-miRNAs, renin-angiotensin-aldosterone system inhibitors, TGFβ or endothelin inhibitors, matricellular protein antagonists, relaxin, loop diuretics and anti-inflammatory drugs[396]. Nevertheless, patients with HF on medical therapy including previously mentioned candidates resulted in poor outcomes concerning to fibrosis reduction, including detrimental side effects probably derived from systemic drug administration. Consequently, additional work is needed to specifically direct bioactive compounds to target cells and improve cardiac function after AMI.

MSC have been widely proposed as a therapeutic option to ameliorate clinical outcome after AMI [205, 229, 397]. Moreover, recent studies have pointed that therapeutic properties of MSC could be mediated by paracrine factors, and specifically by SEV or exosomes secreted by these cells. SEV are stable *in vivo* and are able to modulate biological responses in target cells by transferring lipids, proteins or nucleic acids. Moreover, they can act as mediators of antigen presentation[398, 399]. Consequently, SEV-based therapies have emerged as novel cell-free carrier for therapeutic purposes. In this context, previous works have already observed modest anti-fibrotic effects of EV derived from ESC, umbilical cord MSC, adipose tissue-derived MSC and cardiosphere-derived cells in preclinical stroke *in vivo* models[400-403]. Data published in our laboratory showed that human dental pulp mesenchymal stromal cells reduced infarcted area and promoted angiogenesis in a myocardial infarction *in vivo* model in rats[397]. Accordingly, additional studies have also shown evidence on the effect of dental pulp MSC-SEV reproducing parent cells therapeutic potential[404, 405]. Based on this, we have proposed the possibility to potentiate MSC-SEV therapeutic potential by adding a protein of interest on SEV membrane, which could add anti-fibrotic potential to native SEV.

Previous studies have pointed to a potential anti-fibrotic role of OSM by counteracting TGFβ1 function and fibroblasts activation[337, 338]. These scientific evidences led us to propose OSM as therapeutic cargo on SEV, and to evaluate if

we could successfully load a functional protein into MSC-SEV surface that could improve native-SEV therapeutic potential in AMI context.

In order to initiate a response in receptor cells by a canonical pathway, OSM interacts with either receptor type I or II on target cells membrane, which are heterodimer formed either by LIF-R and IL-31RA or LIF-R and IL-31RB. Here, expression of OSM receptors evaluation in human cardiac ventricular fibroblasts showed an enrichment of LIF-R and IL31-RA receptors after starvation and *in vitro* activation through the addition of a pro-fibrotic cocktail composed by ascorbic-L-acid sulphate, α-dextran and TGFβ-1. Although IL-31RB was downregulated after starvation and fibroblasts activation, its presence was also detected (**Figure 4.21**). Despite additional experimental work needs to be done in order to confirm if receptors are located on cardiac fibroblasts plasma membrane, these results indicated that OSM incorporated into SEV surface could act in target cells by direct binding with its receptors through the canonical signaling pathway, and trigger cellular responses. Treatment of ventricular cardiac fibroblasts with rhOSM after starvation or after starvation and stimulation showed that this cytokine had a functional antiproliferative effect on starving fibroblasts and a role interfering with telo-Col1α1 secretion to the extracellular space after NHCF-V stimulation in a dose-dependent manner (**Figure 4.23** and **4.24**). These results supported our hypothesis, where it was proposed that OSM loaded in SEV could trigger a physiological response in starved and activated cardiac fibroblasts *in vitro.*

Given the pleiotropic effects described for OSM depending on cellular target and physiologic conditions, we wanted to study the response of MSC to OSM presence before genetic modification. Results showed a reduction on MSC proliferation and migration rate after rhOSM (**Figure 4.25**). Thus, an inducible promotor (TetOn) was included in order to control OSM expression. Taking all this information into account, our strategy consisted on native OSM anchoring to MSC-SEV surface through its fusion to lactadherin, a protein that is found associated to phosphatidylserine in SEV membrane. However, we failed to detect OSM fused to lactadherin in MSC-OSM-XSTP cell lysates and SEV protein samples (expected molecular weight ~70 kDa, **Figures 4.30** and **4.31**).

The study of OSM structure and biogenesis revealed the possibility that OSM propeptide (PP) domain could be enzymatically cut by MSC before OSM secretion, thereby breaking fusion protein and avoiding OSM anchoring to SEV. New OSM variants, including a mutation that could prevent PP enzymatic excision together with two additional anchoring proteins that would allow covalent union of OSM-fusion proteins to SEV surface were included in the study. Fusion proteins screening

on cell lysates and SEV samples from native and transfected Expi293F cells showed that cleavage site point mutation was necessary in order to avoid OSM excision from SEV, and the three anchoring proteins tested (CD81, c1c2 domains of lactadherin and TSPAN14) were able to load mutantOSM or matureOSM in SEV surface (**Figure 4.33**).

Although SEV from Expi293F origin will probably have different composition and functionality than MSC-SEV, we decided to repeat proliferation and stimulation experiments in order to see a possible functional effect of our engineered SEV loaded with both matureOSM and mutantOSM fused to CD81, c1c2 domains of lactadherin or TSPAN14, which would help to choose one anchoring protein for new engineered iMSC lines generation. Altogether, data pointed to CD81 as the most effective anchoring protein, since a lower percentage of proliferative cells was observed and telo-Col1α1 extracellular deposition was reduced when 45 µg/mL SEV protein of matureOSM-CD81-SEV and mutantOSM-CD81 were added to starved or stimulated NHCF-V compared to the treatment with the same protein concentration of CD81-SEV (**Figures 4.34-4.41**). Furthermore, CD81 is linked to SEV membranes covalently, possibly providing a more stable fusion protein than lactadherin, whose association with SEV membranes' is driven by affinity to phosphatidylserine.

The initial goal of the present project was to potentiate native MSC-SEV beneficial therapeutic features against pathological cardiac remodeling. However, primary MSC have limited proliferative potential, and undergo a limited number of population doublings before becoming senescent[406]. In order to overcome this limitation, it was decided to generate an immortalized MSC line from dental pulp origin (iMSC) in our laboratory. Starting with iMSC as our native cell type, and after we had decided that constructs based on matureOSM and mutantOSM fusion to CD81 were the most suitable to be introduced in MSC, new iMSC cell lines were generated and characterized (**Figures 4.42** and **4.43**).

Encouragingly, a lower percentage of proliferative ventricular cardiac fibroblasts was observed after cell starvation and treatment with mutantOSM-CD81-SEV and rhOSM. Although a reduction on the mean of proliferative cells was observed after matureOSM-CD81-SEV treatment, we failed to obtain statistically significant differences when data were compared to untreated cells. These data were according to the results obtained for telo-Col1α1 expression after fibroblasts stimulation, where treatment with matureOSM-CD81-SEV, mutantOSM-CD81 SEV and rhOSM reduced telo-Col1α1 extracellular deposition compared to stimulated cells and stimulated cells treated with ctrl-SEV and CD81-SEV. These data suggested

that OSM-enriched SEV could be modulating fibroblasts activation *in vitro*. Importantly, OSM content on SEV generated should be also measured in the future in order to be able to compare data obtained from rhOSM-treated NHCF-V and data obtained with OSM-enriched SEV, since it is unknown the amount of OSM that it has been added with the SEV samples in the performed experiments at this point. The specific knowledge of the OSM amount loaded on each SEV isolate would also help in order to decide which would be the most efficient OSM conformation for further experiments. Consequently, further experimental validation would be necessary in order to elucidate if one construct is better than the other in terms of loading efficiency and functionality.

In spite of the encouraging results obtained when NHCF-V under stressing conditions were treated with matureOSM-CD81-SEV and mutantOSM-CD81-SEV, only preliminary results are showed in this work. Further studies will be needed in order to evaluate the effect of engineered SEV on NHCF-V activation on OSM-target genes expression (e.g.: CKCL12, CXCL1, CXCL2 and CXCL5) and additional ECM proteins related to fibrotic process levels and location patterns, such as α-SMA, Collagen III or fibronectin[132]. In addition to the study of matureOSM-CD81-SEV and mutantOSM-CD81-SEV impact on cardiac fibroblasts, it would be also important to include additional experiments using other relevant cellular models, such as HMVEC-C and macrophages. Empoweringly, Wijelath ES at al. and Vasse M. and collaborators demonstrated a stronger role of OSM favouring HMVEC-C proliferation, chemotaxis and tube formation compared to classical angiogenic factors, such as VEGF and FGF-2[361, 362]. Additional studies have shown that infiltrating neutrophils and macrophages can trigger a positive feedback loop in which secreted OSM could play a role in myocardial healing [338, 407].

Furthermore, we also consider that OSM-enriched SEV functional effect validation in a transverse aortic constriction or I/R-induced injury *in vivo* models would be necessary in order to elucidate if OSM loaded in SEV from iMSC could modulate cardiac pathological remodelling after cardiac insult and, if so, evaluate if differences on fibroblasts activation, tube formation, cardiomyocytes apoptosis and immune response modulation between ctrl SEV, matureOSM-CD81-SEV and mutantOSM-CD81-SEV are found.

In this section, we have been able to efficiently load OSM on SEV surface through its fusion with different anchoring proteins, and test its functional effect using a single dose of OSM-loaded SEV. Previous studies have shown that OSM could have detrimental effects after sustained exposure in other tissues. As an example, a

study carried out by Hasegawa M and collaborators showed that OSM is overexpressed in peripheral blood mononuclear cells from patients with systemic sclerosis, an inflammatory disease in which pulmonary fibrosis is a dangerous side effect[408]. Additionally, other study pointed that OSM expression could protect rats from hepatic fibrosis, but sustained delivery of the cytokine intravenously led to liver fibrosis[409]. This increasing scientific evidence point to the fact that punctual and local administration of OSM into injured tissue could trigger beneficial effects counteracting fibrosis, but it could have the opposite effect if it is continuous delivered. Consequently, engineered SEV locally administration during acute ischemic cardiac insult is proposed in this work. Using this approach, we expect to enhance SEV native therapeutic potential in AMI context and to avoid further side effects. Nevertheless, SEV tracking experiments in order to see OSM delivery in *in vivo* models should be also performed in order to know which cells uptake OSM present into SEV, and if those SEV are retained in the cardiac tissue or if they can reach other organs even when administered locally.

Importantly, our data suggested a functional role of OSM loaded into SEV surface after native sequence modification compared with ctrl SEV. Furthermore, OSM loading into SEV surface would be able to trigger functional effects on target cells and potentiate innate SEV therapeutic properties. In this case, we have focused on the use of OSM-enriched SEV in CVD diseases. However, if future experimental data confirm preliminary results obtained in this work, where OSM loaded in SEV could be triggering an anti-fibrotic potential, the designed MSC-SEV in this work could be used in additional disease models, such as lung or renal fibrosis. We believe that this research project opens a high number of possibilities to test additional potential proteins of interest with a possible cardioprotective effect, and make a step forward to biological nanoparticles customizing in order to improve their therapeutic potential in numerous research fields.

6. Conclusions

6. Conclusions

Regarding to the results obtained in ***Section A:*** *PGA-diDHA-based nanoconjugates' role in cardiomyocytes pre-conditioning during ischemia-reperfusion induced injury*, we conclude that:

- Polymeric conjugation of diDHA to PGA increases diDHA stability and alows further internalization in eukaryotic cells.

- The use of an optimized conjugate, PGA-diDHA$_{6.4}$, displayed enhanced cardioprotective activity in an I/R *in vitro* model in terms of reduced apoptosis, ROS generation and mitochondrial function maintenance in NRVM.

- Locally administration of PGA-diDHA$_{6.4}$ nanoconjugate before reperfusion reduced myocardial area at risk in rat and swine I/R *in vivo* models.

Regarding to the results obtained in ***Section B****: Oncostatin-M-enriched SEV isolated from genetically modified MSC as potential anti-fibrotic agent*, we conclude that:

- OSM sequence modification is necessary in order to load the protein on SEV surface. Otherwise, the use of CD81, lactadherin or TSPAN14 as anchoring protein did not influence significantly the loading of OSM on SEV surface.

- The addition of OSM-enriched SEV isolated from engineered iMSC supernatant to NHCF-V cultured under starving conditions resulted in a reduced cell proliferation rate.

- The addition of OSM-enriched SEV isolated from iMSC supernatant to human ventricular cardiac fibroblasts after stimulation with TGFβ-1, L-ascorbic acid 2-phosphate and dextran sulphate modifies telo-Col1α1 protein secretion and location pattern, pointing towards a functional effect of OSM-SEV in reducing human ventricular cardiac fibroblasts activation *in vitro*.

7. Bibliography

7. Bibliography

1. Antoni H. Function of the Heart. In: R. F. Schmidt and G. Thews, eds. *Human Physiology* Berlin, Heidelberg: Springer Berlin Heidelberg; 1989: 439-479.
2. Best CH, Taylor NB and West JB. *Best and Taylor's physiological basis of medical practice*: Williams & Wilkins; 1991.
3. Vogel B, Claessen BE, Arnold SV, Chan D, Cohen DJ, Giannitsis E, Gibson CM, Goto S, Katus HA, Kerneis M, Kimura T, Kunadian V, Pinto DS, Shiomi H, Spertus JA, Steg PG and Mehran R. ST-segment elevation myocardial infarction. *Nature Reviews Disease Primers*. 2019;5:39.
4. Bergmann O, Zdunek S, Felker A, Salehpour M, Alkass K, Bernard S, Sjostrom SL, Szewczykowska M, Jackowska T, Dos Remedios C, Malm T, Andra M, Jashari R, Nyengaard JR, Possnert G, Jovinge S, Druid H and Frisen J. Dynamics of Cell Generation and Turnover in the Human Heart. *Cell*. 2015;161:1566-75.
5. Tang Y, Nyengaard JR, Andersen JB, Baandrup U and Gundersen HJ. The application of stereological methods for estimating structural parameters in the human heart. *Anatomical record (Hoboken, NJ : 2007)*. 2009;292:1630-47.
6. Anversa P, Olivetti G, Melissari M and Loud AV. Stereological measurement of cellular and subcellular hypertrophy and hyperplasia in the papillary muscle of adult rat. *Journal of Molecular and Cellular Cardiology*. 1980;12:781-795.
7. Xin M, Olson EN and Bassel-Duby R. Mending broken hearts: cardiac development as a basis for adult heart regeneration and repair. *Nature reviews Molecular cell biology*. 2013;14:529-41.
8. Perbellini F, Watson SA, Scigliano M, Alayoubi S, Tkach S, Bardi I, Quaife N, Kane C, Dufton NP, Simon A, Sikkel MB, Faggian G, Randi AM, Gorelik J, Harding SE and Terracciano CM. Investigation of cardiac fibroblasts using myocardial slices. *Cardiovascular research*. 2018;114:77-89.
9. Pinto AR, Ilinykh A, Ivey MJ, Kuwabara JT, D'Antoni ML, Debuque R, Chandran A, Wang L, Arora K, Rosenthal NA and Tallquist MD. Revisiting Cardiac Cellular Composition. *Circulation research*. 2016;118:400-9.
10. Psarras S, Beis D, Nikouli S, Tsikitis M and Capetanaki Y. Three in a Box: Understanding Cardiomyocyte, Fibroblast, and Innate Immune Cell Interactions to Orchestrate Cardiac Repair Processes. 2019;6.
11. Woodcock EA and Matkovich SJ. Cardiomyocytes structure, function and associated pathologies. *The International Journal of Biochemistry & Cell Biology*. 2005;37:1746-1751.
12. Brette F and Orchard C. T-Tubule Function in Mammalian Cardiac Myocytes. 2003;92:1182-1192.
13. Dorn GW, 2nd. Mitochondrial dynamics in heart disease. *Biochimica et biophysica acta*. 2013;1833:233-41.

14. Hatcher CJ and Basson CT. Disrupted intercalated discs. Is kindlin-2 required? *Circulation research*. 2008;102:392-4.
15. Ohtsuki I and Morimoto S. Troponin. In: W. J. Lennarz and M. D. Lane, eds. *Encyclopedia of Biological Chemistry (Second Edition)* Waltham: Academic Press; 2013: 445-449.
16. MacLennan DH and Kranias EG. Phospholamban: a crucial regulator of cardiac contractility. *Nature reviews Molecular cell biology*. 2003;4:566-77.
17. Lytton J. Na+/Ca2+ exchangers: three mammalian gene families control Ca2+ transport. *The Biochemical journal*. 2007;406:365-82.
18. Fuller W, Tulloch LB, Shattock MJ, Calaghan SC, Howie J and Wypijewski KJ. Regulation of the cardiac sodium pump. *Cellular and molecular life sciences : CMLS*. 2013;70:1357-80.
19. Gray GA, Toor IS, Castellan R, Crisan M and Meloni M. Resident cells of the myocardium: more than spectators in cardiac injury, repair and regeneration. *Current opinion in physiology*. 2018;1:46-51.
20. Doroudgar S and Glembotski CCJTimm. The cardiokine story unfolds: ischemic stress-induced protein secretion in the heart. 2011;17:207-214.
21. Talman V and Kivelä R. Cardiomyocyte—Endothelial Cell Interactions in Cardiac Remodeling and Regeneration. 2018;5.
22. Hsieh PC, Davis ME, Lisowski LK and Lee RT. Endothelial-cardiomyocyte interactions in cardiac development and repair. *Annual review of physiology*. 2006;68:51-66.
23. Chen WC, Baily JE, Corselli M, Díaz ME, Sun B, Xiang G, Gray GA, Huard J and Péault BJSc. Human myocardial pericytes: multipotent mesodermal precursors exhibiting cardiac specificity. 2015;33:557-573.
24. Sims DEJT and Cell. The pericyte—a review. 1986;18:153-174.
25. Allt G and Lawrenson JJCto. Pericytes: cell biology and pathology. 2001;169:1-11.
26. Armulik A, Abramsson A and Betsholtz C. Endothelial/Pericyte Interactions. 2005;97:512-523.
27. Furtado MB, Nim HT, Boyd SE and Rosenthal NAJD. View from the heart: cardiac fibroblasts in development, scarring and regeneration. 2016;143:387-397.
28. Daseke MJ, Tenkorang MAA, Chalise U, Konfrst SR and Lindsey ML. Cardiac fibroblast activation during myocardial infarction wound healing: Fibroblast polarization after MI. *Matrix Biology*. 2020;91-92:109-116.
29. Kohl P, Kamkin A, Kiseleva I, Noble DJEPT and Integration. Mechanosensitive fibroblasts in the sino-atrial node region of rat heart: interaction with cardiomyocytes and possible role. 1994;79:943-956.
30. Ongstad E, Kohl PJJom and cardiology c. Fibroblast–myocyte coupling in the heart: potential relevance for therapeutic interventions. 2016;91:238-246.

31. Stanley WC. Changes in cardiac metabolism: a critical step from stable angina to ischaemic cardiomyopathy. *European Heart Journal Supplements*. 2001;3:O2-O7.
32. Salem Jr NJB. Introduction to polyunsaturated fatty acids. 1999;3:1-8.
33. Ander BP, Dupasquier CM, Prociuk MA and Pierce GN. Polyunsaturated fatty acids and their effects on cardiovascular disease. *Exp Clin Cardiol*. 2003;8:164-172.
34. Frontiers in Neuroscience. In: J. P. Montmayeur and J. le Coutre, eds. *Fat Detection: Taste, Texture, and Post Ingestive Effects* Boca Raton (FL): CRC Press/Taylor & Francis Copyright © 2010, Taylor & Francis Group, LLC.; 2010.

35. Siri-Tarino PW, Sun Q, Hu FB and Krauss RM. Saturated Fatty Acids and Risk of Coronary Heart Disease: Modulation by Replacement Nutrients. *Current Atherosclerosis Reports*. 2010;12:384-390.
36. Schwingshackl L and Hoffmann G. Monounsaturated fatty acids and risk of cardiovascular disease: synopsis of the evidence available from systematic reviews and meta-analyses. *Nutrients*. 2012;4:1989-2007.
37. Kris-Etherton PM, Harris WS and Appel LJ. Omega-3 fatty acids and cardiovascular disease: new recommendations from the American Heart Association. *Arteriosclerosis, thrombosis, and vascular biology*. 2003;23:151-2.
38. von Schacky C. The role of omega-3 fatty acids in cardiovascular disease. *Curr Atheroscler Rep*. 2003;5:139-45.
39. Borgström B. Digestion and absorption of lipids. *International review of physiology*. 1977;12:305-23.
40. Liao TH, Hamosh P and Hamosh M. Fat digestion by lingual lipase: mechanism of lipolysis in the stomach and upper small intestine. *Pediatric research*. 1984;18:402-9.
41. Patton JS and Carey MC. Watching fat digestion. *Science (New York, NY)*. 1979;204:145-8.
42. Werner A, Kuipers F and Verkade HJ. Fat absorption and lipid metabolism in cholestasis *Madame Curie Bioscience Database [Internet]*: Landes Bioscience; 2013.
43. van der Vusse GJ, van Bilsen M and Glatz JFC. Cardiac fatty acid uptake and transport in health and disease. *Cardiovascular research*. 2000;45:279-293.
44. Riemersma RA. FACTORS REGULATING NORMAL AND ISCHAEMIC MYOCARDIAL SUBSTRATE METABOLISM. In: A. G. B. Kovách, E. Monos and G. Rubányi, eds. *Cardiovascular Physiology: Heart, Peripheral Circulation and Methodology*: Pergamon; 1981: 109-119.
45. Bharadwaj KG, Hiyama Y, Hu Y, Huggins LA, Ramakrishnan R, Abumrad NA, Shulman GI, Blaner WS and Goldberg IJ. Chylomicron- and VLDL-derived lipids enter the heart through different pathways: in vivo evidence for receptor- and non-

receptor-mediated fatty acid uptake. *The Journal of biological chemistry*. 2010;285:37976-86.
46. van der Vusse GJ, van Bilsen M and Glatz JFJCr. Cardiac fatty acid uptake and transport in health and disease. 2000;45:279-293.
47. Schwenk RW, Luiken JJ, Bonen A and Glatz JFJCr. Regulation of sarcolemmal glucose and fatty acid transporters in cardiac disease. 2008;79:249-258.
48. Goldberg IJ, Eckel RH and Abumrad NAJJolr. Regulation of fatty acid uptake into tissues: lipoprotein lipase-and CD36-mediated pathways. 2009;50:S86-S90.
49. Su X, Abumrad NAJTiE and Metabolism. Cellular fatty acid uptake: a pathway under construction. 2009;20:72-77.
50. Pulinilkunnil T and Rodrigues BJCr. Cardiac lipoprotein lipase: metabolic basis for diabetic heart disease. 2006;69:329-340.
51. Lee J and Goldberg IJJChr. Lipoprotein lipase-derived fatty acids: physiology and dysfunction. 2007;9:462-466.
52. van der Vusse GJ and Roemen THM. Protein acylation in normoxic and ischemic/reperfused cardiac tissue. *Prostaglandins, Leukotrienes and Essential Fatty Acids*. 1999;60:299-305.
53. Ingwall JS. *ATP and the Heart*: Springer Science & Business Media; 2002.
54. Opie LH. *Heart physiology: from cell to circulation*: Lippincott Williams & Wilkins; 2004.
55. Wisneski JA, Gertz EW, Neese RA, Gruenke LD and Craig JCJJotACoC. Dual carbon-labeled isotope experiments using D-[6-14C] glucose and L-[1, 2, 3-13C3] lactate: a new approach for investigating human myocardial metabolism during ischemia. 1985;5:1138-1146.
56. Gertz E, Wisneski J, Stanley W and Neese RJTJoci. Myocardial substrate utilization during exercise in humans. Dual carbon-labeled carbohydrate isotope experiments. 1988;82:2017-2025.
57. Kaijser L and Berglund BJAps. Myocardial lactate extraction and release at rest and during heavy exercise in healthy men. 1992;144:39-45.
58. Jeffrey F, Diczku V, Sherry A and Malloy CJBric. Substrate selection in the isolated working rat heart: effects of reperfusion, afterload, and concentration. 1995;90:388-396.
59. Schonekess BO. Competition between lactate and fatty acids as sources of ATP in the isolated working rat heart. *J Mol Cell Cardiol*. 1997;29:2725-33.
60. Wentz AE, d'Avignon DA, Weber ML, Cotter DG, Doherty JM, Kerns R, Nagarajan R, Reddy N, Sambandam N and Crawford PAJJoBC. Adaptation of myocardial substrate metabolism to a ketogenic nutrient environment. 2010;285:24447-24456.
61. Breuer E, Barta E, Zlatos L and Pappová E. Developmental changes of myocardial metabolism. II. Myocardial metabolism of fatty acids in the early postnatal period in dogs. *Biologia neonatorum Neo-natal studies*. 1968;12:54-64.

62. Warshaw JB. Cellular energy metabolism during fetal development: IV. Fatty acid activation, acyl transfer and fatty acid oxidation during development of the chick and rat. *Developmental Biology*. 1972;28:537-544.
63. Dávila-Román VG, Vedala G, Herrero P, de las Fuentes L, Rogers JG, Kelly DP and Gropler RJ. Altered myocardial fatty acid and glucose metabolism in idiopathic dilated cardiomyopathy. *Journal of the American College of Cardiology*. 2002;40:271-7.
64. Nascimben L, Ingwall JS, Lorell BH, Pinz I, Schultz V, Tornheim K and Tian R. Mechanisms for increased glycolysis in the hypertrophied rat heart. *Hypertension (Dallas, Tex : 1979)*. 2004;44:662-7.
65. Sack MN, Rader TA, Park S, Bastin J, McCune SA and Kelly DPJC. Fatty acid oxidation enzyme gene expression is downregulated in the failing heart. 1996;94:2837-2842.
66. Osorio JC, Stanley WC, Linke A, Castellari M, Diep QN, Panchal AR, Hintze TH, Lopaschuk GD and Recchia FAJC. Impaired myocardial fatty acid oxidation and reduced protein expression of retinoid X receptor-α in pacing-induced heart failure. 2002;106:606-612.
67. Siddiqi N, Singh S, Beadle R, Dawson D and Frenneaux M. Cardiac metabolism in hypertrophy and heart failure: implications for therapy. *Heart Failure Reviews*. 2013;18:595-606.
68. Doenst T, Nguyen TD and Abel ED. Cardiac Metabolism in Heart Failure. 2013;113:709-724.
69. van Bilsen M, van der Vusse GJ and Reneman RS. Transcriptional regulation of metabolic processes: implications for cardiac metabolism. *Pflügers Archiv*. 1998;437:2-14.
70. Lopaschuk GD, Ussher JR, Folmes CDL, Jaswal JS and Stanley WC. Myocardial Fatty Acid Metabolism in Health and Disease. 2010;90:207-258.
71. Brandt JM, Djouadi F and Kelly DPJJoBC. Fatty acids activate transcription of the muscle carnitine palmitoyltransferase I gene in cardiac myocytes via the peroxisome proliferator-activated receptor α. 1998;273:23786-23792.
72. Gabriella C, Simona S and Paola P. n-3 Polyunsaturated Fatty Acids as Signal Transduction Modulators and Therapeutical Agents in Cancer. *Current Signal Transduction Therapy*. 2006;1:255-271.
73. Eyster KM. The membrane and lipids as integral participants in signal transduction: lipid signal transduction for the non-lipid biochemist. 2007;31:5-16.
74. Rennison JH and Van Wagoner DR. Impact of dietary fatty acids on cardiac arrhythmogenesis. *Circ Arrhythm Electrophysiol*. 2009;2:460-469.
75. Van der Vusse G, Glatz J, Stam H and Reneman RSJPr. Fatty acid homeostasis in the normoxic and ischemic heart. 1992;72:881-940.

76. Chaube R, Hess DT, Wang Y-J, Plummer B, Sun Q-A, Laurita K and Stamler JS. Regulation of the skeletal muscle ryanodine receptor/Ca2+-release channel RyR1 by S-palmitoylation. *The Journal of biological chemistry*. 2014;289:8612-8619.
77. Reilly L, Howie J, Wypijewski K, Ashford ML, Hilgemann DW and Fuller W. Palmitoylation of the Na/Ca exchanger cytoplasmic loop controls its inactivation and internalization during stress signaling. *FASEB journal : official publication of the Federation of American Societies for Experimental Biology*. 2015;29:4532-43.
78. Pei Z, Xiao Y, Meng J, Hudmon A and Cummins TRJNc. Cardiac sodium channel palmitoylation regulates channel availability and myocyte excitability with implications for arrhythmia generation. 2016;7:1-13.
79. Duncan PJ, Bi D, McClafferty H, Chen L, Tian L and Shipston MJJJoBC. S-Acylation controls functional coupling of BK channel pore-forming α-subunits and β1-subunits. 2019;294:12066-12076.
80. Runkle KB, Kharbanda A, Stypulkowski E, Cao XJ, Wang W, Garcia BA and Witze ES. Inhibition of DHHC20-Mediated EGFR Palmitoylation Creates a Dependence on EGFR Signaling. *Molecular cell*. 2016;62:385-396.
81. Barylko B, Mao YS, Wlodarski P, Jung G, Binns DD, Sun H-Q, Yin HL and Albanesi JP. Palmitoylation controls the catalytic activity and subcellular distribution of phosphatidylinositol 4-kinase II{alpha}. *The Journal of biological chemistry*. 2009;284:9994-10003.
82. Zhou Q, Li J, Yu H, Zhai Y, Gao Z, Liu Y, Pang X, Zhang L, Schulten K, Sun F and Chen C. Molecular insights into the membrane-associated phosphatidylinositol 4-kinase IIα. *Nature communications*. 2014;5:3552.
83. Berecki G, Den Ruijter HM, Verkerk AO, Schumacher CA, Baartscheer A, Bakker D, Boukens BJ, van Ginneken AC, Fiolet JW, Opthof T and Coronel R. Dietary fish oil reduces the incidence of triggered arrhythmias in pig ventricular myocytes. *Heart rhythm*. 2007;4:1452-60.
84. Huang JM, Xian H and Bacaner M. Long-chain fatty acids activate calcium channels in ventricular myocytes. *Proceedings of the National Academy of Sciences of the United States of America*. 1992;89:6452-6.
85. Moreno C, Macias A, Prieto A, de la Cruz A, Gonzalez T and Valenzuela C. Effects of n−3 Polyunsaturated Fatty Acids on Cardiac Ion Channels. 2012;3.
86. Roth GA, Abate D, Abate KH, Abay SM, Abbafati C, Abbasi N, Abbastabar H, Abd-Allah F, Abdela J and Abdelalim AJTL. Global, regional, and national age-sex-specific mortality for 282 causes of death in 195 countries and territories, 1980–2017: a systematic analysis for the Global Burden of Disease Study 2017. 2018;392:1736-1788.
87. Monnet E and Chachques JC. Animal Models of Heart Failure: What Is New? *The Annals of Thoracic Surgery*. 2005;79:1445-1453.

88. Fuster V, Kelly B and Health NRCJPCHitDWACCtAGHIoMBoG. Committee on preventing the global epidemic of cardiovascular disease: meeting the challenges in developing countries. 2010.
89. Kelly BB and Fuster V. *Promoting cardiovascular health in the developing world: a critical challenge to achieve global health*: National Academies Press; 2010.
90. Perbellini F, Watson SA, Bardi I and Terracciano CM. Heterocellularity and Cellular Cross-Talk in the Cardiovascular System. 2018;5.
91. Anderson JL and Morrow DA. Acute Myocardial Infarction. 2017;376:2053-2064.
92. Anversa P and Nadal-Ginard B. Myocyte renewal and ventricular remodelling. *Nature*. 2002;415:240-243.
93. Bergmann O, Bhardwaj RD, Bernard S, Zdunek S, Barnabé-Heider F, Walsh S, Zupicich J, Alkass K, Buchholz BA, Druid H, Jovinge S and Frisén J. Evidence for Cardiomyocyte Renewal in Humans. 2009;324:98-102.
94. Libby P, Ridker PM and Hansson GK. Progress and challenges in translating the biology of atherosclerosis. *Nature*. 2011;473:317-325.
95. Furie B and Furie BC. Mechanisms of Thrombus Formation. 2008;359:938-949.
96. Glass CK and Witztum JL. Atherosclerosis: The Road Ahead. *Cell*. 2001;104:503-516.
97. Reimer KA, Lowe JE, Rasmussen MM and Jennings RBJC. The wavefront phenomenon of ischemic cell death. 1. Myocardial infarct size vs duration of coronary occlusion in dogs. 1977;56:786-794.
98. Jennings RBJCr. Historical perspective on the pathology of myocardial ischemia/reperfusion injury. 2013;113:428-438.
99. Yellon DM and Hausenloy DJ. Myocardial reperfusion injury. *The New England journal of medicine*. 2007;357:1121-35.
100. Liehn EA, Postea O, Curaj A and Marx N. Repair After Myocardial Infarction, Between Fantasy and Reality: The Role of Chemokines. *Journal of the American College of Cardiology*. 2011;58:2357-2362.
101. Frangogiannis NG, Smith CW and Entman MLJCr. The inflammatory response in myocardial infarction. 2002;53:31-47.
102. Arslan F, De Kleijn DP and Pasterkamp GJNRC. Innate immune signaling in cardiac ischemia. 2011;8:292.
103. Jaeschke H and Smith CWJJolb. Mechanisms of neutrophil-induced parenchymal cell injury. 1997;61:647-653.
104. Swirski FK, Nahrendorf M, Etzrodt M, Wildgruber M, Cortez-Retamozo V, Panizzi P, Figueiredo J-L, Kohler RH, Chudnovskiy A and Waterman PJS. Identification of splenic reservoir monocytes and their deployment to inflammatory sites. 2009;325:612-616.

105. Soehnlein O, Zernecke A, Weber CJT and haemostasis. Neutrophils launch monocyte extravasation by release of granule proteins. 2009;102:198-205.
106. Nahrendorf M, Pittet MJ and Swirski FKJC. Monocytes: protagonists of infarct inflammation and repair after myocardial infarction. 2010;121:2437-2445.
107. Weil BR and Neelamegham S. Selectins and Immune Cells in Acute Myocardial Infarction and Post-infarction Ventricular Remodeling: Pathophysiology and Novel Treatments. 2019;10.
108. Prabhu SD and Frangogiannis NGJCr. The biological basis for cardiac repair after myocardial infarction: from inflammation to fibrosis. 2016;119:91-112.
109. Hofmann U, Beyersdorf N, Weirather J, Podolskaya A, Bauersachs J, Ertl G, Kerkau T and Frantz SJC. Activation of CD4+ T lymphocytes improves wound healing and survival after experimental myocardial infarction in mice. 2012;125:1652-1663.
110. Shinde AV, Humeres C and Frangogiannis NGJBeBA-MBoD. The role of α-smooth muscle actin in fibroblast-mediated matrix contraction and remodeling. 2017;1863:298-309.
111. Frangogiannis NGJTJoci. The extracellular matrix in myocardial injury, repair, and remodeling. 2017;127:1600-1612.
112. Roberts CS, Schoen FJ and Kloner RA. Effect of coronary reperfusion on myocardial hemorrhage and infarct healing. *The American Journal of Cardiology*. 1983;52:610-614.
113. Ibáñez B, Heusch G, Ovize M and Van de Werf F. Evolving Therapies for Myocardial Ischemia/Reperfusion Injury. 2015;65:1454-1471.
114. Chiong M, Wang Z, Pedrozo Z, Cao D, Troncoso R, Ibacache M, Criollo A, Nemchenko A, Hill J, Lavandero SJCd and disease. Cardiomyocyte death: mechanisms and translational implications. 2011;2:e244-e244.
115. Orogo AM and Gustafsson ÅBJIl. Cell death in the myocardium: my heart won't go on. 2013;65:651-656.
116. Tani M and Neely JR. Role of intracellular Na+ in Ca2+ overload and depressed recovery of ventricular function of reperfused ischemic rat hearts: Possible involvement of H+-Na+ and Na+-Ca2+ exchange. *Circulation research*. 1989;65:1045-1056.
117. Ladilov YV, Siegmund B and Piper HM. Protection of reoxygenated cardiomyocytes against hypercontracture by inhibition of Na+/H+ exchange. 1995;268:H1531-H1539.
118. Baines CP. The mitochondrial permeability transition pore and ischemia-reperfusion injury. *Basic Research in Cardiology*. 2009;104:181-188.
119. Heusch G, Boengler K and Schulz R. Inhibition of mitochondrial permeability transition pore opening: the holy grail of cardioprotection. *Basic Research in Cardiology*. 2010;105:151-154.
120. Orogo AM and Gustafsson ÅB. Cell death in the myocardium: My heart won't go on. 2013;65:651-656.

121. Zhou W and Yuan J. SnapShot: Necroptosis. *Cell*. 2014;158:464-464.e1.
122. Li X, Liu M, Sun R, Zeng Y, Chen S, Zhang PJE and medicine t. Protective approaches against myocardial ischemia reperfusion injury. 2016;12:3823-3829.
123. Balch WE, Morimoto RI, Dillin A and Kelly JWJs. Adapting proteostasis for disease intervention. 2008;319:916-919.
124. Levine B and Klionsky DJ. Development by self-digestion: molecular mechanisms and biological functions of autophagy. *Developmental cell*. 2004;6:463-77.
125. Jin J-K, Blackwood EA, Azizi K, Thuerauf DJ, Fahem AG, Hofmann C, Kaufman RJ, Doroudgar S and Glembotski CC. ATF6 Decreases Myocardial Ischemia/Reperfusion Damage and Links ER Stress and Oxidative Stress Signaling Pathways in the Heart. 2017;120:862-875.
126. Galluzzi L, Morselli E, Vicencio JM, Kepp O, Joza N, Tajeddine N and Kroemer G. Life, death and burial: multifaceted impact of autophagy. 2008.
127. Yang Z and Klionsky DJJCoicb. Mammalian autophagy: core molecular machinery and signaling regulation. 2010;22:124-131.
128. Matsui Y, Takagi H, Qu X, Abdellatif M, Sakoda H, Asano T, Levine B and Sadoshima JJCr. Distinct roles of autophagy in the heart during ischemia and reperfusion: roles of AMP-activated protein kinase and Beclin 1 in mediating autophagy. 2007;100:914-922.
129. Zhu H, Tannous P, Johnstone JL, Kong Y, Shelton JM, Richardson JA, Le V, Levine B, Rothermel BA and Hill JAJTJoci. Cardiac autophagy is a maladaptive response to hemodynamic stress. 2007;117:1782-1793.
130. Ma X, Liu H, Foyil SR, Godar RJ, Weinheimer CJ, Hill JA and Diwan A. Impaired Autophagosome Clearance Contributes to Cardiomyocyte Death in Ischemia/Reperfusion Injury. 2012;125:3170-3181.
131. Maejima Y, Isobe M and Sadoshima J. Regulation of autophagy by Beclin 1 in the heart. *Journal of molecular and cellular cardiology*. 2016;95:19-25.
132. Humeres C and Frangogiannis NG. Fibroblasts in the Infarcted, Remodeling, and Failing Heart. *JACC Basic Transl Sci*. 2019;4:449-467.
133. Jacobs M, Staufenberger S, Gergs U, Meuter K, Brandstätter K, Hafner M, Ertl G and Schorb W. Tumor necrosis factor-alpha at acute myocardial infarction in rats and effects on cardiac fibroblasts. *J Mol Cell Cardiol*. 1999;31:1949-59.
134. Shen H, Wang J, Min J, Xi W, Gao Y, Yin L, Yu Y, Liu K, Xiao J, Zhang YF and Wang ZN. Activation of TGF-β1/α-SMA/Col I Profibrotic Pathway in Fibroblasts by Galectin-3 Contributes to Atrial Fibrosis in Experimental Models and Patients. *Cell Physiol Biochem*. 2018;47:851-863.
135. Derynck R and Zhang YE. Smad-dependent and Smad-independent pathways in TGF-beta family signalling. *Nature*. 2003;425:577-84.
136. Duncan MR, Frazier KS, Abramson S, Williams S, Klapper H, Huang X and Grotendorst GR. Connective tissue growth factor mediates transforming growth

factor beta-induced collagen synthesis: down-regulation by cAMP. *FASEB journal : official publication of the Federation of American Societies for Experimental Biology*. 1999;13:1774-86.

137. Squires CE, Escobar GP, Payne JF, Leonardi RA, Goshorn DK, Sheats NJ, Mains IM, Mingoia JT, Flack EC and Lindsey ML. Altered fibroblast function following myocardial infarction. *Journal of Molecular and Cellular Cardiology*. 2005;39:699-707.

138. Thygesen K, Mair J, Katus H, Plebani M, Venge P, Collinson P, Lindahl B, Giannitsis E, Hasin Y and Galvani MJEhj. Recommendations for the use of cardiac troponin measurement in acute cardiac care. 2010;31:2197-2204.

139. Thygesen K, Alpert JS, Jaffe AS, Chaitman BR, Bax JJ, Morrow DA and White HD. Fourth Universal Definition of Myocardial Infarction (2018). 2018;138:e618-e651.

140. Effect of Enalapril on Survival in Patients with Reduced Left Ventricular Ejection Fractions and Congestive Heart Failure. 1991;325:293-302.

141. Pitt B, Zannad F, Remme WJ, Cody R, Castaigne A, Perez A, Palensky J and Wittes J. The Effect of Spironolactone on Morbidity and Mortality in Patients with Severe Heart Failure. 1999;341:709-717.

142. Packer M, Coats AJS, Fowler MB, Katus HA, Krum H, Mohacsi P, Rouleau JL, Tendera M, Castaigne A, Roecker EB, Schultz MK, Staiger C, Curtin EL and DeMets DL. Effect of Carvedilol on Survival in Severe Chronic Heart Failure. 2001;344:1651-1658.

143. Spath NB, Mills NL and Cruden NL. Novel cardioprotective and regenerative therapies in acute myocardial infarction: a review of recent and ongoing clinical trials. 2016;12:655-672.

144. Bristow MR, Saxon LA, Boehmer J, Krueger S, Kass DA, De Marco T, Carson P, DiCarlo L, DeMets D and White BGJNEJoM. Cardiac-resynchronization therapy with or without an implantable defibrillator in advanced chronic heart failure. 2004;350:2140-2150.

145. Rose EA, Gelijns AC, Moskowitz AJ, Heitjan DF, Stevenson LW, Dembitsky W, Long JW, Ascheim DD, Tierney AR and Levitan RGJNEJoM. Long-term use of a left ventricular assist device for end-stage heart failure. 2001;345:1435-1443.

146. Yacoub MJTL. Cardiac donation after circulatory death: a time to reflect. 2015;385:2554-2556.

147. Laflamme MA and Murry CEJN. Heart regeneration. 2011;473:326-335.

148. Xin M, Kim Y, Sutherland LB, Murakami M, Qi X, McAnally J, Porrello ER, Mahmoud AI, Tan W, Shelton JM, Richardson JA, Sadek HA, Bassel-Duby R and Olson EN. Hippo pathway effector Yap promotes cardiac regeneration. *Proceedings of the National Academy of Sciences of the United States of America*. 2013;110:13839-44.

149. Gourdie RG, Dimmeler S and Kohl PJNrDd. Novel therapeutic strategies targeting fibroblasts and fibrosis in heart disease. 2016;15:620.
150. Ieda M, Fu J-D, Delgado-Olguin P, Vedantham V, Hayashi Y, Bruneau BG and Srivastava DJC. Direct reprogramming of fibroblasts into functional cardiomyocytes by defined factors. 2010;142:375-386.
151. Song K, Nam Y-J, Luo X, Qi X, Tan W, Huang GN, Acharya A, Smith CL, Tallquist MD and Neilson EGJN. Heart repair by reprogramming non-myocytes with cardiac transcription factors. 2012;485:599-604.
152. Menasche PJC. Alfieri 0, Janssens S, et al.: The myoblast autologous grafting in ischémie cardiomyopathy (magic) triai: First randomized placebo-controlled study of myoblast transplantation. 2008;117:1189-1200.
153. Meyer GP, Wollert KC, Lotz J, Steffens J, Lippolt P, Fichtner S, Hecker H, Schaefer A, Arseniev L and Hertenstein BJC. Intracoronary bone marrow cell transfer after myocardial infarction. 2006;113:1287-94.
154. Hare JM, Fishman JE, Gerstenblith G, Velazquez DLD, Zambrano JP, Suncion VY, Tracy M, Ghersin E, Johnston PV and Brinker JAJJ. Comparison of allogeneic vs autologous bone marrow–derived mesenchymal stem cells delivered by transendocardial injection in patients with ischemic cardiomyopathy: the POSEIDON randomized trial. 2012;308:2369-2379.
155. Beltrami AP, Barlucchi L, Torella D, Baker M, Limana F, Chimenti S, Kasahara H, Rota M, Musso E and Urbanek KJC. Adult cardiac stem cells are multipotent and support myocardial regeneration. 2003;114:763-776.
156. Mummery CL, Zhang J, Ng ES, Elliott DA, Elefanty AG and Kamp TJJCr. Differentiation of human embryonic stem cells and induced pluripotent stem cells to cardiomyocytes: a methods overview. 2012;111:344-358.
157. Qiao H, Zhang H, Yamanaka S, Patel VV, Petrenko NB, Huang B, Muenz LR, Ferrari VA, Boheler KR and Zhou RJCCI. Long-term improvement in postinfarct left ventricular global and regional contractile function is mediated by embryonic stem cell–derived cardiomyocytes. 2011;4:33-41.
158. Kawamura M, Miyagawa S, Miki K, Saito A, Fukushima S, Higuchi T, Kawamura T, Kuratani T, Daimon T and Shimizu TJC. Feasibility, safety, and therapeutic efficacy of human induced pluripotent stem cell-derived cardiomyocyte sheets in a porcine ischemic cardiomyopathy model. 2012;126:S29-S37.
159. Hashimoto H, Olson EN and Bassel-Duby R. Therapeutic approaches for cardiac regeneration and repair. *Nature reviews Cardiology*. 2018;15:585-600.
160. Mukherjee B, Dey NS, Maji R, Bhowmik P, Das PJ and Paul P. Current status and future scope for nanomaterials in drug delivery *Application of Nanotechnology in Drug Delivery*: IntechOpen; 2014.
161. Bejarano J, Navarro-Marquez M, Morales-Zavala F, Morales JO, Garcia-Carvajal I, Araya-Fuentes E, Flores Y, Verdejo HE, Castro PF, Lavandero S and Kogan

MJ. Nanoparticles for diagnosis and therapy of atherosclerosis and myocardial infarction: evolution toward prospective theranostic approaches. *Theranostics*. 2018;8:4710-4732.

162. Ekladious I, Colson YL and Grinstaff MW. Polymer–drug conjugate therapeutics: advances, insights and prospects. *Nature Reviews Drug Discovery*. 2019;18:273-294.

163. Jatzkewitz HJZN. Peptamin (glycyl-L-leucyl-mescaline) bound to blood plasma expander (polyvinylpyrrolidone) as a new depot form of a biologically active primary amine (mescaline). 1955;10:27-31.

164. Ringsdorf H. Structure and properties of pharmacologically active polymers. *Journal of Polymer Science: Polymer Symposia*. 1975;51:135-153.

165. Duncan R. The dawning era of polymer therapeutics. *Nature Reviews Drug Discovery*. 2003;2:347-360.

166. Kopecek J and Kopecková PJDD. HPMA copolymers: Origins, early developments, present, and future. Ad V.122-149.

167. Tsuchiya K, Uchida T, Kobayashi M, Maeda H, Konno T and Yamanaka HJU. Tumor-targeted chemotherapy with SMANCS in lipiodol for renal cell carcinoma: longer survival with larger size tumors. 2000;55:495-500.

168. Graham MLJAddr. Pegaspargase: a review of clinical studies. 2003;55:1293-1302.

169. Autrata R, Krejčířová I, Šenková K, Holoušová M, Doležel Z and Borek IJEjoo. Intravitreal pegaptanib combined with diode laser therapy for stage 3+ retinopathy of prematurity in zone I and posterior zone II. 2012;22:687-694.

170. Macdougall IC, Robson R, Opatrna S, Liogier X, Pannier A, Jordan P, Dougherty FC and Reigner BJCJotASoN. Pharmacokinetics and pharmacodynamics of intravenous and subcutaneous continuous erythropoietin receptor activator (CERA) in patients with chronic kidney disease. 2006;1:1211-1215.

171. Pang X, Jiang Y, Xiao Q, Leung AW, Hua H and Xu C. pH-responsive polymer-drug conjugates: Design and progress. *Journal of controlled release : official journal of the Controlled Release Society*. 2016;222:116-29.

172. Liu S, Maheshwari R and Kiick KL. Polymer-Based Therapeutics. *Macromolecules*. 2009;42:3-13.

173. Apfelthaler C, Anzengruber M, Gabor F and Wirth M. Poly – (l) – glutamic acid drug delivery system for the intravesical therapy of bladder cancer using WGA as targeting moiety. *European Journal of Pharmaceutics and Biopharmaceutics*. 2017;115:131-139.

174. Arroyo-Crespo JJ, Deladriere C, Nebot VJ, Charbonnier D, Masiá E, Paul A, James C, Armiñán A and Vicent MJ. Anticancer Activity Driven by Drug Linker Modification in a Polyglutamic Acid-Based Combination-Drug Conjugate. 2018;28:1800931.

175. Bernabeu E, Cagel M, Lagomarsino E, Moretton M and Chiappetta DA. Paclitaxel: What has been done and the challenges remain ahead. *International Journal of Pharmaceutics*. 2017;526:474-495.
176. Vicent MJ and Pérez-Payá E. Poly-l-glutamic acid (PGA) Aided Inhibitors of Apoptotic Protease Activating Factor 1 (Apaf-1): An Antiapoptotic Polymeric Nanomedicine. *Journal of Medicinal Chemistry*. 2006;49:3763-3765.
177. Gortat A, Sancho M, Mondragón L, Messeguer À, Pérez-Payá E and Orzáez M. Apaf1 inhibition promotes cell recovery from apoptosis. *Protein & cell*. 2015;6:833-43.
178. Weinstock-Guttman B, Nair KV, Glajch JL, Ganguly TC and Kantor D. Two decades of glatiramer acetate: From initial discovery to the current development of generics. *Journal of the Neurological Sciences*. 2017;376:255-259.
179. Baabur-Cohen H, Vossen LI, Krüger HR, Eldar-boock A, Yeini E, Landa-Rouben N, Tiram G, Wedepohl S, Markovsky E, Leor J, Calderón M and Satchi-Fainaro R. In vivo comparative study of distinct polymeric architectures bearing a combination of paclitaxel and doxorubicin at a synergistic ratio. *Journal of Controlled Release*. 2017;257:118-131.
180. Larson N and Ghandehari H. Polymeric Conjugates for Drug Delivery. *Chemistry of Materials*. 2012;24:840-853.
181. Sergiel JP, Martine L, Raederstorff D, Grynberg A and Demaison L. Individual effects of dietary EPA and DHA on the functioning of the isolated working rat heart. *Canadian journal of physiology and pharmacology*. 1998;76:728-36.
182. Ponsard B, Durot I, Delerive P, Oudot F, Cordelet C, Grynberg A and Athias P. Cross-influence of membrane polyunsaturated fatty acids and hypoxia-reoxygenation on α- and β-adrenergic function of rat cardiomyocytes. 1999;34:457.
183. Ander BP, Weber AR, Rampersad PP, Gilchrist JS, Pierce GN and Lukas A. Dietary flaxseed protects against ventricular fibrillation induced by ischemia-reperfusion in normal and hypercholesterolemic Rabbits. *The Journal of nutrition*. 2004;134:3250-6.
184. Abdukeyum GG, Owen AJ and McLennan PL. Dietary (n-3) long-chain polyunsaturated fatty acids inhibit ischemia and reperfusion arrhythmias and infarction in rat heart not enhanced by ischemic preconditioning. *The Journal of nutrition*. 2008;138:1902-9.
185. Abdukeyum GG, Owen AJ, Larkin TA and McLennan PL. Up-Regulation of Mitochondrial Antioxidant Superoxide Dismutase Underpins Persistent Cardiac Nutritional-Preconditioning by Long Chain n-3 Polyunsaturated Fatty Acids in the Rat. *Journal of clinical medicine*. 2016;5.
186. Farías JG, Carrasco-Pozo C, Carrasco Loza R, Sepúlveda N, Álvarez P, Quezada M, Quiñones J, Molina V and Castillo RL. Polyunsaturated fatty acid induces cardioprotection against ischemia-reperfusion through the inhibition of

NF-kappaB and induction of Nrf2. *Experimental biology and medicine (Maywood, NJ)*. 2017;242:1104-1114.

187. Shysh AM, Nagibin VS, Kaplinskii SP and Dosenko VE. N-3 long chain polyunsaturated fatty acids increase the expression of PPARγ-target genes and resistance of isolated heart and cultured cardiomyocytes to ischemic injury. *Pharmacological reports : PR*. 2016;68:1133-1139.

188. Maehre HK, Jensen IJ, Elvevoll EO and Eilertsen KE. ω-3 Fatty Acids and Cardiovascular Diseases: Effects, Mechanisms and Dietary Relevance. *International journal of molecular sciences*. 2015;16:22636-61.

189. Schjøtt J, Brekke OL, Jynge P, Bjerve KS and Hamazaki T. Infusion of EPA and DHA lipid emulsions: effects on heart lipids and tolerance to ischaemia-reperfusion in the isolated rat heart. *Scandinavian journal of clinical and laboratory investigation*. 1993;53:873-82.

190. Goel DP, Maddaford TG and Pierce GN. Effects of ω-3 polyunsaturated fatty acids on cardiac sarcolemmal Na+/H+ exchange. 2002;283:H1688-H1694.

191. Xiao YF, Sigg DC, Ujhelyi MR, Wilhelm JJ, Richardson ES and Iaizzo PA. Pericardial delivery of omega-3 fatty acid: a novel approach to reducing myocardial infarct sizes and arrhythmias. *American journal of physiology Heart and circulatory physiology*. 2008;294:H2212-8.

192. Richard D, Oszust F, Guillaume C, Millart H, Laurent-Maquin D, Brou C, Bausero P and Visioli F. Infusion of docosahexaenoic acid protects against myocardial infarction. *Prostaglandins, leukotrienes, and essential fatty acids*. 2014;90:139-43.

193. Burban M, Meyer G, Olland A, Séverac F, Yver B, Toti F, Schini-Kerth V, Meziani F and Boisramé-Helms J. An Intravenous Bolus of Epa: Dha 6: 1 Protects Against Myocardial Ischemia-Reperfusion-Induced Shock. *Shock (Augusta, Ga)*. 2016;46:549-556.

194. Darwesh AM, Jamieson KL, Wang C, Samokhvalov V and Seubert JM. Cardioprotective effects of CYP-derived epoxy metabolites of docosahexaenoic acid involve limiting NLRP3 inflammasome activation (1). *Canadian journal of physiology and pharmacology*. 2019;97:544-556.

195. Zirpoli H, Abdillahi M, Quadri N, Ananthakrishnan R, Wang L, Rosario R, Zhu Z, Deckelbaum RJ and Ramasamy R. Acute administration of n-3 rich triglyceride emulsions provides cardioprotection in murine models after ischemia-reperfusion. *PloS one*. 2015;10:e0116274.

196. Halliwell B. Lipid peroxidation, antioxidants and cardiovascular disease: how should we move forward? *Cardiovascular research*. 2000;47:410-418.

197. Arab-Tehrany E, Jacquot M, Gaiani C, Imran M, Desobry S and Linder M. Beneficial effects and oxidative stability of omega-3 long-chain polyunsaturated fatty acids. *Trends in Food Science & Technology*. 2012;25:24-33.

198. Richard D, Oszust F, Guillaume C, Millart H, Laurent-Maquin D, Brou C, Bausero P and Visioli F. Infusion of docosahexaenoic acid protects against myocardial infarction. *Prostaglandins, Leukotrienes and Essential Fatty Acids*. 2014;90:139-143.
199. Friedenstein A, Piatetzky-Shapiro I and Petrakova KJD. Osteogenesis in transplants of bone marrow cells. 1966;16:381-390.
200. Dominici M, Le Blanc K, Mueller I, Slaper-Cortenbach I, Marini F, Krause D, Deans R, Keating A, Prockop D and Horwitz E. Minimal criteria for defining multipotent mesenchymal stromal cells. The International Society for Cellular Therapy position statement. *Cytotherapy*. 2006;8:315-7.
201. Pittenger MF, Mackay AM, Beck SC, Jaiswal RK, Douglas R, Mosca JD, Moorman MA, Simonetti DW, Craig S and Marshak DRJs. Multilineage potential of adult human mesenchymal stem cells. 1999;284:143-147.
202. Planat-Benard V, Menard C, André M, Puceat M, Perez A, Garcia-Verdugo J-M, Pénicaud L and Casteilla LJCr. Spontaneous cardiomyocyte differentiation from adipose tissue stroma cells. 2004;94:223-229.
203. Antonitsis P, Ioannidou-Papagiannaki E, Kaidoglou A, Papakonstantinou CJIc and surgery t. In vitro cardiomyogenic differentiation of adult human bone marrow mesenchymal stem cells. The role of 5-azacytidine. 2007;6:593-597.
204. Li X, Yu X, Lin Q, Deng C, Shan Z, Yang M, Lin SJJom and cardiology c. Bone marrow mesenchymal stem cells differentiate into functional cardiac phenotypes by cardiac microenvironment. 2007;42:295-303.
205. Amado LC, Saliaris AP, Schuleri KH, John MS, Xie J-S, Cattaneo S, Durand DJ, Fitton T, Kuang JQ and Stewart GJPotNAoS. Cardiac repair with intramyocardial injection of allogeneic mesenchymal stem cells after myocardial infarction. 2005;102:11474-11479.
206. Quevedo HC, Hatzistergos KE, Oskouei BN, Feigenbaum GS, Rodriguez JE, Valdes D, Pattany PM, Zambrano JP, Hu Q and McNiece IJPotNAoS. Allogeneic mesenchymal stem cells restore cardiac function in chronic ischemic cardiomyopathy via trilineage differentiating capacity. 2009;106:14022-14027.
207. Nygren JM, Jovinge S, Breitbach M, Säwén P, Röll W, Hescheler J, Taneera J, Fleischmann BK and Jacobsen SE. Bone marrow-derived hematopoietic cells generate cardiomyocytes at a low frequency through cell fusion, but not transdifferentiation. *Nature medicine*. 2004;10:494-501.
208. Fraidenraich D, Stillwell E, Romero E, Wilkes D, Manova K, Basson CT and Benezra R. Rescue of cardiac defects in id knockout embryos by injection of embryonic stem cells. *Science (New York, NY)*. 2004;306:247-52.
209. Ibraheim H, Giacomini C, Kassam Z, Dazzi F and Powell N. Advances in mesenchymal stromal cell therapy in the management of Crohn's disease. *Expert Review of Gastroenterology & Hepatology*. 2017;12:1-13.

210. Rodríguez-Pardo V, Aristizabal J, Jaimes D, Quijano S, Reyes I, Herrera M, Solano J and Vernot J. Mesenchymal stem cells promote leukaemic cells aberrant phenotype from B-cell acute lymphoblastic leukaemia. *Hematology/oncology and stem cell therapy*. 2013;6.
211. Ortiz LA, Dutreil M, Fattman C, Pandey AC, Torres G, Go K and Phinney DG. Interleukin 1 receptor antagonist mediates the antiinflammatory and antifibrotic effect of mesenchymal stem cells during lung injury. *Proceedings of the National Academy of Sciences of the United States of America*. 2007;104:11002-7.
212. Le Blanc K, Frassoni F, Ball L, Locatelli F, Roelofs H, Lewis I, Lanino E, Sundberg B, Bernardo ME, Remberger M, Dini G, Egeler RM, Bacigalupo A, Fibbe W and Ringdén O. Mesenchymal stem cells for treatment of steroid-resistant, severe, acute graft-versus-host disease: a phase II study. *Lancet (London, England)*. 2008;371:1579-86.
213. Shabbir A, Zisa D, Suzuki G and Lee T. Heart failure therapy mediated by the trophic activities of bone marrow mesenchymal stem cells: a noninvasive therapeutic regimen. *American journal of physiology Heart and circulatory physiology*. 2009;296:H1888-97.
214. Togel F, Hu Z, Weiss K, Isaac J, Lange C and Westenfelder CJAJoP-RP. Administered mesenchymal stem cells protect against ischemic acute renal failure through differentiation-independent mechanisms. 2005;289:F31-F42.
215. Aslam M, Baveja R, Liang OD, Fernandez-Gonzalez A, Lee C, Mitsialis SA, Kourembanas SJAjor and medicine cc. Bone marrow stromal cells attenuate lung injury in a murine model of neonatal chronic lung disease. 2009;180:1122-1130.
216. Pierro M, Ionescu L, Montemurro T, Vadivel A, Weissmann G, Oudit G, Emery D, Bodiga S, Eaton F and Péault BJT. Short-term, long-term and paracrine effect of human umbilical cord-derived stem cells in lung injury prevention and repair in experimental bronchopulmonary dysplasia. 2013;68:475-484.
217. Gnecchi M, He H, Noiseux N, Liang OD, Zhang L, Morello F, Mu H, Melo LG, Pratt RE and Ingwall JSJTFJ. Evidence supporting paracrine hypothesis for Akt-modified mesenchymal stem cell-mediated cardiac protection and functional improvement. 2006;20:661-669.
218. Uemura R, Xu M, Ahmad N and Ashraf MJCr. Bone marrow stem cells prevent left ventricular remodeling of ischemic heart through paracrine signaling. 2006;98:1414-1421.
219. Caplan AI and Correa D. The MSC: an injury drugstore. *Cell stem cell*. 2011;9:11-5.
220. Arslan F, Lai RC, Smeets MB, Akeroyd L, Choo A, Aguor EN, Timmers L, van Rijen HV, Doevendans PA and Pasterkamp GJScr. Mesenchymal stem cell-derived exosomes increase ATP levels, decrease oxidative stress and activate PI3K/Akt pathway to enhance myocardial viability and prevent adverse remodeling after myocardial ischemia/reperfusion injury. 2013;10:301-312.

221. Maacha S, Sidahmed H, Jacob S, Gentilcore G, Calzone R, Grivel J-C and Cugno C. Paracrine Mechanisms of Mesenchymal Stromal Cells in Angiogenesis. *Stem Cells International*. 2020;2020:4356359.
222. Kordelas L, Rebmann V, Ludwig AK, Radtke S, Ruesing J, Doeppner TR, Epple M, Horn PA, Beelen DW and Giebel B. MSC-derived exosomes: a novel tool to treat therapy-refractory graft-versus-host disease. *Leukemia*. 2014;28:970-3.
223. Amable PR, Teixeira MV, Carias RB, Granjeiro JM and Borojevic R. Protein synthesis and secretion in human mesenchymal cells derived from bone marrow, adipose tissue and Wharton's jelly. *Stem cell research & therapy*. 2014;5:53.
224. Eirin A, Riester SM, Zhu XY, Tang H, Evans JM, O'Brien D, van Wijnen AJ and Lerman LO. MicroRNA and mRNA cargo of extracellular vesicles from porcine adipose tissue-derived mesenchymal stem cells. *Gene*. 2014;551:55-64.
225. Mirotsou M, Jayawardena TM, Schmeckpeper J, Gnecchi M and Dzau VJ. Paracrine mechanisms of stem cell reparative and regenerative actions in the heart. *J Mol Cell Cardiol*. 2011;50:280-9.
226. Yáñez-Mó M, Siljander PR-M, Andreu Z, Bedina Zavec A, Borràs FE, Buzas EI, Buzas K, Casal E, Cappello F and Carvalho JJJoev. Biological properties of extracellular vesicles and their physiological functions. 2015;4:27066.
227. Samsonraj RM, Raghunath M, Nurcombe V, Hui JH, van Wijnen AJ and Cool SM. Concise Review: Multifaceted Characterization of Human Mesenchymal Stem Cells for Use in Regenerative Medicine. *Stem cells translational medicine*. 2017;6:2173-2185.
228. Feng Y, Huang W, Wani M, Yu X and Ashraf MJPo. Ischemic preconditioning potentiates the protective effect of stem cells through secretion of exosomes by targeting Mecp2 via miR-22. 2014;9.
229. Rosová I, Dao M, Capoccia B, Link D and Nolta JA. Hypoxic preconditioning results in increased motility and improved therapeutic potential of human mesenchymal stem cells. *Stem cells (Dayton, Ohio)*. 2008;26:2173-82.
230. Cerrada I, Ruiz-Saurí A, Carrero R, Trigueros C, Dorronsoro A, Sanchez-Puelles JM, Diez-Juan A, Montero JA and Sepúlveda P. Hypoxia-inducible factor 1 alpha contributes to cardiac healing in mesenchymal stem cells-mediated cardiac repair. *Stem cells and development*. 2013;22:501-11.
231. Gonzalez-King H, García NA, Ontoria-Oviedo I, Ciria M, Montero JA and Sepúlveda P. Hypoxia Inducible Factor-1α Potentiates Jagged 1-Mediated Angiogenesis by Mesenchymal Stem Cell-Derived Exosomes. 2017;35:1747-1759.
232. Mangi AA, Noiseux N, Kong D, He H, Rezvani M, Ingwall JS and Dzau VJ. Mesenchymal stem cells modified with Akt prevent remodeling and restore performance of infarcted hearts. *Nature medicine*. 2003;9:1195-1201.
233. Gnecchi M, He H, Noiseux N, Liang OD, Zhang L, Morello F, Mu H, Melo LG, Pratt RE, Ingwall JS and Dzau VJ. Evidence supporting paracrine hypothesis for Akt-

modified mesenchymal stem cell-mediated cardiac protection and functional improvement. 2006;20:661-669.
234. Kang K, Ma R, Cai W, Huang W, Paul C, Liang J, Wang Y, Zhao T, Kim HW and Xu MJSCI. Exosomes secreted from CXCR4 overexpressing mesenchymal stem cells promote cardioprotection via Akt signaling pathway following myocardial infarction. 2015;2015.
235. Yu B, Kim HW, Gong M, Wang J, Millard RW, Wang Y, Ashraf M and Xu MJIjoc. Exosomes secreted from GATA-4 overexpressing mesenchymal stem cells serve as a reservoir of anti-apoptotic microRNAs for cardioprotection. 2015;182:349-360.
236. Hood JL, Wickline SAJWIRN and Nanobiotechnology. A systematic approach to exosome-based translational nanomedicine. 2012;4:458-467.
237. Malhotra H, Sheokand N, Kumar S, Chauhan AS, Kumar M, Jakhar P, Boradia VM, Raje CI and Raje MJJobn. Exosomes: tunable nano vehicles for macromolecular delivery of transferrin and lactoferrin to specific intracellular compartment. 2016;12:1101-1114.
238. Rupert DL, Claudio V, Lässer C and Bally MJBeBA-GS. Methods for the physical characterization and quantification of extracellular vesicles in biological samples. 2017;1861:3164-3179.
239. Yang Y, Hong Y, Cho E, Kim GB and Kim I-S. Extracellular vesicles as a platform for membrane-associated therapeutic protein delivery. *Journal of extracellular vesicles*. 2018;7:1440131.
240. Vader P, Mol EA, Pasterkamp G and Schiffelers RMJAddr. Extracellular vesicles for drug delivery. 2016;106:148-156.
241. Kim MS, Haney MJ, Zhao Y, Mahajan V, Deygen I, Klyachko NL, Inskoe E, Piroyan A, Sokolsky M, Okolie OJNN, Biology and Medicine. Development of exosome-encapsulated paclitaxel to overcome MDR in cancer cells. 2016;12:655-664.
242. Fuhrmann G, Serio A, Mazo M, Nair R and Stevens MMJJoCR. Active loading into extracellular vesicles significantly improves the cellular uptake and photodynamic effect of porphyrins. 2015;205:35-44.
243. Sato YT, Umezaki K, Sawada S, Mukai S-a, Sasaki Y, Harada N, Shiku H and Akiyoshi KJSr. Engineering hybrid exosomes by membrane fusion with liposomes. 2016;6:21933.
244. Alvarez-Erviti L, Seow Y, Yin H, Betts C, Lakhal S and Wood MJJNb. Delivery of siRNA to the mouse brain by systemic injection of targeted exosomes. 2011;29:341-345.
245. Haney MJ, Klyachko NL, Zhao Y, Gupta R, Plotnikova EG, He Z, Patel T, Piroyan A, Sokolsky M and Kabanov AVJJoCR. Exosomes as drug delivery vehicles for Parkinson's disease therapy. 2015;207:18-30.

246. Smyth T, Petrova K, Payton NM, Persaud I, Redzic JS, Graner MW, Smith-Jones P and Anchordoquy TJJBc. Surface functionalization of exosomes using click chemistry. 2014;25:1777-1784.
247. Hood JLJN. Post isolation modification of exosomes for nanomedicine applications. 2016;11:1745-1756.
248. Higginbotham JN, Zhang Q, Jeppesen DK, Scott AM, Manning HC, Ochieng J, Franklin JL and Coffey RJJJoev. Identification and characterization of EGF receptor in individual exosomes by fluorescence-activated vesicle sorting. 2016;5:29254.
249. Luan X, Sansanaphongpricha K, Myers I, Chen H, Yuan H and Sun D. Engineering exosomes as refined biological nanoplatforms for drug delivery. *Acta Pharmacologica Sinica*. 2017;38:754-763.
250. Sun D, Zhuang X, Xiang X, Liu Y, Zhang S, Liu C, Barnes S, Grizzle W, Miller D and Zhang H-GJMT. A novel nanoparticle drug delivery system: the anti-inflammatory activity of curcumin is enhanced when encapsulated in exosomes. 2010;18:1606-1614.
251. Pascucci L, Coccè V, Bonomi A, Ami D, Ceccarelli P, Ciusani E, Viganò L, Locatelli A, Sisto F and Doglia SMJJoCR. Paclitaxel is incorporated by mesenchymal stromal cells and released in exosomes that inhibit in vitro tumor growth: a new approach for drug delivery. 2014;192:262-270.
252. Morishita M, Takahashi Y, Matsumoto A, Nishikawa M and Takakura YJB. Exosome-based tumor antigens–adjuvant co-delivery utilizing genetically engineered tumor cell-derived exosomes with immunostimulatory CpG DNA. 2016;111:55-65.
253. Stickney Z, Losacco J, McDevitt S, Zhang Z, Lu BJB and communications br. Development of exosome surface display technology in living human cells. 2016;472:53-59.
254. Sciences NAo. *In the Light of Evolution: Volume I: Adaptation and Complex Design*. Washington, DC: The National Academies Press; 2007.
255. Maehle AH. "Receptive substances": John Newport Langley (1852-1925) and his path to a receptor theory of drug action. *Medical history*. 2004;48:153-74.
256. Uzman A. Molecular biology of the cell (4th ed.): Alberts, B., Johnson, A., Lewis, J., Raff, M., Roberts, K., and Walter, P. 2003;31:212-214.
257. Valadi H, Ekström K, Bossios A, Sjöstrand M, Lee JJ and Lötvall JOJNcb. Exosome-mediated transfer of mRNAs and microRNAs is a novel mechanism of genetic exchange between cells. 2007;9:654-659.
258. Hegmans JP, Bard MP, Hemmes A, Luider TM, Kleijmeer MJ, Prins J-B, Zitvogel L, Burgers SA, Hoogsteden HC and Lambrecht BNJTAjop. Proteomic analysis of exosomes secreted by human mesothelioma cells. 2004;164:1807-1815.
259. Balaj L, Lessard R, Dai L, Cho Y-J, Pomeroy SL, Breakefield XO and Skog JJNc. Tumour microvesicles contain retrotransposon elements and amplified oncogene sequences. 2011;2:1-9.

260. Llorente A, Skotland T, Sylvänne T, Kauhanen D, Róg T, Orłowski A, Vattulainen I, Ekroos K, Sandvig KJBeBA-M and Lipids CBo. Molecular lipidomics of exosomes released by PC-3 prostate cancer cells. 2013;1831:1302-1309.
261. Thakur BK, Zhang H, Becker A, Matei I, Huang Y, Costa-Silva B, Zheng Y, Hoshino A, Brazier H and Xiang JJCr. Double-stranded DNA in exosomes: a novel biomarker in cancer detection. 2014;24:766-769.
262. Skotland T, Sandvig K and Llorente AJPilr. Lipids in exosomes: current knowledge and the way forward. 2017;66:30-41.
263. Böing AN, Van Der Pol E, Grootemaat AE, Coumans FA, Sturk A and Nieuwland RJJoev. Single-step isolation of extracellular vesicles by size-exclusion chromatography. 2014;3:23430.
264. Muller L, Hong C-S, Stolz DB, Watkins SC and Whiteside TLJJoim. Isolation of biologically-active exosomes from human plasma. 2014;411:55-65.
265. Crawford NJBjoh. The presence of contractile proteins in platelet microparticles isolated from human and animal platelet-free plasma. 1971;21:53-69.
266. Pisitkun T, Shen R-F and Knepper MAJPotNAoS. Identification and proteomic profiling of exosomes in human urine. 2004;101:13368-13373.
267. Michael A, Bajracharya SD, Yuen PS, Zhou H, Star RA, Illei GG and Alevizos IJOd. Exosomes from human saliva as a source of microRNA biomarkers. 2010;16:34-38.
268. Admyre C, Johansson SM, Qazi KR, Filén J-J, Lahesmaa R, Norman M, Neve EP, Scheynius A and Gabrielsson SJTJoi. Exosomes with immune modulatory features are present in human breast milk. 2007;179:1969-1978.
269. Marchant R, Peat A and Banbury GJNP. The ultrastructural basis of hyphal growth. 1967;66:623-629.
270. Marchant R and Robards AJAoB. Membrane systems associated with the plasmalemma of plant cells. 1968;32:457-471.
271. Dorward DW and Garon CFJAEM. DNA is packaged within membrane-derived vesicles of Gram-negative but not Gram-positive bacteria. 1990;56:1960-1962.
272. Lee EY, Choi DY, Kim DK, Kim JW, Park JO, Kim S, Kim SH, Desiderio DM, Kim YK and Kim KPJP. Gram-positive bacteria produce membrane vesicles: proteomics-based characterization of Staphylococcus aureus-derived membrane vesicles. 2009;9:5425-5436.
273. Albuquerque PC, Nakayasu ES, Rodrigues ML, Frases S, Casadevall A, Zancope-Oliveira RM, Almeida IC and Nosanchuk JDJCm. Vesicular transport in Histoplasma capsulatum: an effective mechanism for trans-cell wall transfer of proteins and lipids in ascomycetes. 2008;10:1695-1710.

274. Nosanchuk JD, Nimrichter L, Casadevall A, Rodrigues MLJC and biology i. A role for vesicular transport of macromolecules across cell walls in fungal pathogenesis. 2008;1:37-39.
275. Silverman JM, Chan SK, Robinson DP, Dwyer DM, Nandan D, Foster LJ and Reiner NEJGb. Proteomic analysis of the secretome of Leishmania donovani. 2008;9:R35.
276. Zaborowski MP, Balaj L, Breakefield XO and Lai CP. Extracellular Vesicles: Composition, Biological Relevance, and Methods of Study. *Bioscience*. 2015;65:783-797.
277. Théry C, Zitvogel L and Amigorena S. Exosomes: composition, biogenesis and function. *Nature Reviews Immunology*. 2002;2:569-579.
278. Caruso S and Poon IKH. Apoptotic Cell-Derived Extracellular Vesicles: More Than Just Debris. 2018;9.
279. Zhou X, Xie F, Wang L, Zhang L, Zhang S, Fang M and Zhou F. The function and clinical application of extracellular vesicles in innate immune regulation. *Cellular & Molecular Immunology*. 2020;17:323-334.
280. Cocucci E and Meldolesi J. Ectosomes and exosomes: shedding the confusion between extracellular vesicles. *Trends in cell biology*. 2015;25:364-72.
281. Raposo G and Stoorvogel W. Extracellular vesicles: Exosomes, microvesicles, and friends. *Journal of Cell Biology*. 2013;200:373-383.
282. Harding C and Stahl P. Transferrin recycling in reticulocytes: pH and iron are important determinants of ligand binding and processing. *Biochemical and biophysical research communications*. 1983;113:650-8.
283. Pan BT and Johnstone RM. Fate of the transferrin receptor during maturation of sheep reticulocytes in vitro: selective externalization of the receptor. *Cell*. 1983;33:967-78.
284. Zhang H, Freitas D, Kim HS, Fabijanic K, Li Z, Chen H, Mark MT, Molina H, Martin AB, Bojmar L, Fang J, Rampersaud S, Hoshino A, Matei I, Kenific CM, Nakajima M, Mutvei AP, Sansone P, Buehring W, Wang H, Jimenez JP, Cohen-Gould L, Paknejad N, Brendel M, Manova-Todorova K, Magalhães A, Ferreira JA, Osório H, Silva AM, Massey A, Cubillos-Ruiz JR, Galletti G, Giannakakou P, Cuervo AM, Blenis J, Schwartz R, Brady MS, Peinado H, Bromberg J, Matsui H, Reis CA and Lyden D. Identification of distinct nanoparticles and subsets of extracellular vesicles by asymmetric flow field-flow fractionation. *Nature Cell Biology*. 2018;20:332-343.
285. Zhang Q, Higginbotham JN, Jeppesen DK, Yang Y-P, Li W, McKinley ET, Graves-Deal R, Ping J, Britain CM, Dorsett KA, Hartman CL, Ford DA, Allen RM, Vickers KC, Liu Q, Franklin JL, Bellis SL and Coffey RJ. Transfer of Functional Cargo in Exomeres. *Cell Reports*. 2019;27:940-954.e6.
286. Zhang M, Jin K, Gao L, Zhang Z, Li F, Zhou F and Zhang LJSM. Methods and technologies for exosome isolation and characterization. 2018;2:1800021.

287. Jeppesen DK, Fenix AM, Franklin JL, Higginbotham JN, Zhang Q, Zimmerman LJ, Liebler DC, Ping J, Liu Q and Evans RJC. Reassessment of exosome composition. 2019;177:428-445. e18.
288. Smith ZJ, Lee C, Rojalin T, Carney RP, Hazari S, Knudson A, Lam K, Saari H, Ibañez EL, Viitala T, Laaksonen T, Yliperttula M and Wachsmann-Hogiu S. Single exosome study reveals subpopulations distributed among cell lines with variability related to membrane content. *Journal of extracellular vesicles*. 2015;4:28533.
289. Tkach M and Théry C. Communication by Extracellular Vesicles: Where We Are and Where We Need to Go. *Cell*. 2016;164:1226-1232.
290. Denzer K, Kleijmeer MJ, Heijnen H, Stoorvogel W and Geuze HJJJocs. Exosome: from internal vesicle of the multivesicular body to intercellular signaling device. 2000;113:3365-3374.
291. Colombo M, Raposo G, Théry CJAroc and biology d. Biogenesis, secretion, and intercellular interactions of exosomes and other extracellular vesicles. 2014;30:255-289.
292. Mathieu M, Martin-Jaular L, Lavieu G and Thery CJNcb. Specificities of secretion and uptake of exosomes and other extracellular vesicles for cell-to-cell communication. 2019;21:9-17.
293. Babst M, Katzmann DJ, Estepa-Sabal EJ, Meerloo T and Emr SDJDc. Escrt-III: an endosome-associated heterooligomeric protein complex required for mvb sorting. 2002;3:271-282.
294. Wollert T and Hurley JHJN. Molecular mechanism of multivesicular body biogenesis by ESCRT complexes. 2010;464:864-869.
295. Colombo M, Moita C, van Niel G, Kowal J, Vigneron J, Benaroch P, Manel N, Moita LF, Théry C and Raposo GJJCS. Analysis of ESCRT functions in exosome biogenesis, composition and secretion highlights the heterogeneity of extracellular vesicles. 2013;126:5553-5565.
296. Trajkovic K, Hsu C, Chiantia S, Rajendran L, Wenzel D, Wieland F, Schwille P, Brügger B and Simons MJs. Ceramide triggers budding of exosome vesicles into multivesicular endosomes. 2008;319:1244-1247.
297. Van Niel G, Charrin S, Simoes S, Romao M, Rochin L, Saftig P, Marks MS, Rubinstein E and Raposo GJDc. The tetraspanin CD63 regulates ESCRT-independent and-dependent endosomal sorting during melanogenesis. 2011;21:708-721.
298. Pelham HRJTicb. SNAREs and the specificity of membrane fusion. 2001;11:99-101.
299. Edgar JR. Q&A: What are exosomes, exactly? *BMC Biology*. 2016;14:46.
300. Cai H, Reinisch K and Ferro-Novick SJDc. Coats, tethers, Rabs, and SNAREs work together to mediate the intracellular destination of a transport vesicle. 2007;12:671-682.
301. Wollert T, Wunder C, Lippincott-Schwartz J and Hurley JH. Membrane scission by the ESCRT-III complex. *Nature*. 2009;458:172-7.

302. Hurley JH and Hanson PI. Membrane budding and scission by the ESCRT machinery: it's all in the neck. *Nature reviews Molecular cell biology*. 2010;11:556-66.
303. Johnstone RM, Adam M, Hammond J, Orr L and Turbide CJJoBC. Vesicle formation during reticulocyte maturation. Association of plasma membrane activities with released vesicles (exosomes). 1987;262:9412-9420.
304. Tkach M, Kowal J, Zucchetti AE, Enserink L, Jouve M, Lankar D, Saitakis M, Martin-Jaular L and Théry CJTEj. Qualitative differences in T-cell activation by dendritic cell-derived extracellular vesicle subtypes. 2017;36:3012-3028.
305. Parolini I, Federici C, Raggi C, Lugini L, Palleschi S, De Milito A, Coscia C, Iessi E, Logozzi M, Molinari A, Colone M, Tatti M, Sargiacomo M and Fais S. Microenvironmental pH is a key factor for exosome traffic in tumor cells. *The Journal of biological chemistry*. 2009;284:34211-22.
306. Doherty GJ and McMahon HTJArob. Mechanisms of endocytosis. 2009;78:857-902.
307. Ehrlich M, Boll W, Van Oijen A, Hariharan R, Chandran K, Nibert ML and Kirchhausen T. Endocytosis by random initiation and stabilization of clathrin-coated pits. *Cell*. 2004;118:591-605.
308. Escrevente C, Keller S, Altevogt P and Costa J. Interaction and uptake of exosomes by ovarian cancer cells. *BMC cancer*. 2011;11:108.
309. Nanbo A, Kawanishi E, Yoshida R and Yoshiyama H. Exosomes derived from Epstein-Barr virus-infected cells are internalized via caveola-dependent endocytosis and promote phenotypic modulation in target cells. *Journal of virology*. 2013;87:10334-47.
310. Izquierdo-Useros N, Naranjo-Gómez M, Archer J, Hatch SC, Erkizia I, Blanco J, Borràs FE, Puertas MC, Connor JH and Fernández-Figueras MTJB, The Journal of the American Society of Hematology. Capture and transfer of HIV-1 particles by mature dendritic cells converges with the exosome-dissemination pathway. 2009;113:2732-2741.
311. Fitzner D, Schnaars M, van Rossum D, Krishnamoorthy G, Dibaj P, Bakhti M, Regen T, Hanisch U-K and Simons MJJocs. Selective transfer of exosomes from oligodendrocytes to microglia by macropinocytosis. 2011;124:447-458.
312. Rudt S and Müller RJEjops. In vitro phagocytosis assay of nano-and microparticles by chemiluminescence. III. Uptake of differently sized surface-modified particles, and its correlation to particle properties and in vivo distribution. 1993;1:31-39.
313. Feng D, Zhao WL, Ye YY, Bai XC, Liu RQ, Chang LF, Zhou Q and Sui SF. Cellular internalization of exosomes occurs through phagocytosis. *Traffic (Copenhagen, Denmark)*. 2010;11:675-87.
314. Escola JM, Kleijmeer MJ, Stoorvogel W, Griffith JM, Yoshie O and Geuze HJ. Selective enrichment of tetraspan proteins on the internal vesicles of multivesicular

endosomes and on exosomes secreted by human B-lymphocytes. *The Journal of biological chemistry*. 1998;273:20121-7.
315. Rana S, Yue S, Stadel D and Zöller M. Toward tailored exosomes: the exosomal tetraspanin web contributes to target cell selection. *Int J Biochem Cell Biol*. 2012;44:1574-84.
316. Nazarenko I, Rana S, Baumann A, McAlear J, Hellwig A, Trendelenburg M, Lochnit G, Preissner KT and Zöller M. Cell surface tetraspanin Tspan8 contributes to molecular pathways of exosome-induced endothelial cell activation. *Cancer research*. 2010;70:1668-78.
317. Morelli AE, Larregina AT, Shufesky WJ, Sullivan ML, Stolz DB, Papworth GD, Zahorchak AF, Logar AJ, Wang Z, Watkins SC, Falo LD, Jr. and Thomson AW. Endocytosis, intracellular sorting, and processing of exosomes by dendritic cells. *Blood*. 2004;104:3257-66.
318. Aplin AE, Howe A, Alahari SK and Juliano RL. Signal transduction and signal modulation by cell adhesion receptors: the role of integrins, cadherins, immunoglobulin-cell adhesion molecules, and selectins. *Pharmacological reviews*. 1998;50:197-263.
319. Franzen CA, Simms PE, Van Huis AF, Foreman KE, Kuo PC and Gupta GN. Characterization of uptake and internalization of exosomes by bladder cancer cells. *Biomed Res Int*. 2014;2014:619829-619829.
320. Hao S, Bai O, Li F, Yuan J, Laferte S and Xiang JJI. Mature dendritic cells pulsed with exosomes stimulate efficient cytotoxic T-lymphocyte responses and antitumour immunity. 2007;120:90-102.
321. Van Niel G, Porto-Carreiro I, Simoes S and Raposo GJJob. Exosomes: a common pathway for a specialized function. 2006;140:13-21.
322. Morita E, Sandrin V, Chung HY, Morham SG, Gygi SP, Rodesch CK and Sundquist WIJTEj. Human ESCRT and ALIX proteins interact with proteins of the midbody and function in cytokinesis. 2007;26:4215-4227.
323. Crescitelli R, Lässer C, Szabó TG, Kittel A, Eldh M, Dianzani I, Buzás EI and Lötvall J. Distinct RNA profiles in subpopulations of extracellular vesicles: apoptotic bodies, microvesicles and exosomes. *Journal of extracellular vesicles*. 2013;2.
324. Doyle LM and Wang MZ. Overview of Extracellular Vesicles, Their Origin, Composition, Purpose, and Methods for Exosome Isolation and Analysis. *Cells*. 2019;8.
325. Mathivanan S, Fahner CJ, Reid GE and Simpson RJ. ExoCarta 2012: database of exosomal proteins, RNA and lipids. *Nucleic acids research*. 2012;40:D1241-4.
326. Raposo G, Nijman HW, Stoorvogel W, Liejendekker R, Harding CV, Melief C and Geuze HJJTJoem. B lymphocytes secrete antigen-presenting vesicles. 1996;183:1161-1172.
327. Willms E, Johansson HJ, Mäger I, Lee Y, Blomberg KEM, Sadik M, Alaarg A, Smith CIE, Lehtiö J, El Andaloussi S, Wood MJA and Vader P. Cells release

subpopulations of exosomes with distinct molecular and biological properties. *Scientific Reports*. 2016;6:22519.
328. Bergtrom G and Library OT. *Basic Cell and Molecular Biology 3e: What We Know & How We Found Out*: Independent; 2018.
329. Cohen S, Bigazzi PE and Yoshida T. Commentary. Similarities of T cell function in cell-mediated immunity and antibody production. *Cellular immunology*. 1974;12:150-9.
330. . In: J. M. Anaya, Y. Shoenfeld, A. Rojas-Villarraga, R. A. Levy and R. Cervera, eds. *Autoimmunity: From Bench to Bedside* Bogota (Colombia): El Rosario University Press© 2013 Universidad del Rosario.; 2013.

331. Altan-Bonnet G and Mukherjee R. Cytokine-mediated communication: a quantitative appraisal of immune complexity. *Nature Reviews Immunology*. 2019;19:205-217.
332. Lins Ferreira V, Borba H, Bonetti A, Leonart L and Pontarolo R. Cytokines and Interferons: Types and Functions; 2018.
333. Yi F, Frazzette N, Cruz AC, Klebanoff CA and Siegel RM. Beyond Cell Death: New Functions for TNF Family Cytokines in Autoimmunity and Tumor Immunotherapy. *Trends in Molecular Medicine*. 2018;24:642-653.
334. Murakami M, Kamimura D and Hirano T. Pleiotropy and Specificity: Insights from the Interleukin 6 Family of Cytokines. *Immunity*. 2019;50:812-831.
335. Kubin T, Pöling J, Kostin S, Gajawada P, Hein S, Rees W, Wietelmann A, Tanaka M, Lörchner H, Schimanski S, Szibor M, Warnecke H and Braun T. Oncostatin M is a major mediator of cardiomyocyte dedifferentiation and remodeling. *Cell stem cell*. 2011;9:420-32.
336. Hu J, Zhang L, Zhao Z, Zhang M, Lin J, Wang J, Yu W, Man W, Li C, Zhang R, Gao E, Wang H and Sun D. OSM mitigates post-infarction cardiac remodeling and dysfunction by up-regulating autophagy through Mst1 suppression. *Biochimica et Biophysica Acta (BBA) - Molecular Basis of Disease*. 2017;1863:1951-1961.
337. Huguier V, Giot J-P, Simonneau M, Levillain P, Charreau S, Garcia M, Jégou J-F, Bodet C, Morel F, Lecron J-C and Favot L. Oncostatin M exerts a protective effect against excessive scarring by counteracting the inductive effect of TGFβ1 on fibrosis markers. *Scientific Reports*. 2019;9:2113.
338. Abe H, Takeda N, Isagawa T, Semba H, Nishimura S, Morioka MS, Nakagama Y, Sato T, Soma K, Koyama K, Wake M, Katoh M, Asagiri M, Neugent ML, Kim JW, Stockmann C, Yonezawa T, Inuzuka R, Hirota Y, Maemura K, Yamashita T, Otsu K, Manabe I, Nagai R and Komuro I. Macrophage hypoxia signaling regulates cardiac fibrosis via Oncostatin M. *Nature communications*. 2019;10:2824.
339. Zarling JM, Shoyab M, Marquardt H, Hanson MB, Lioubin MN and Todaro GJ. Oncostatin M: a growth regulator produced by differentiated histiocytic lymphoma cells. *Proceedings of the National Academy of Sciences of the United States of America*. 1986;83:9739-43.

340. Nair BC, DeVico AL, Nakamura S, Copeland TD, Chen Y, Patel A, O'Neil T, Oroszlan S, Gallo RC and Sarngadharan MG. Identification of a major growth factor for AIDS-Kaposi's sarcoma cells as oncostatin M. *Science (New York, NY)*. 1992;255:1430-2.
341. Tian S-S, Tapley P, Sincich C, Stein RB, Rosen J and Lamb P. Multiple signaling pathways induced by granulocyte colony-stimulating factor involving activation of JAKs, STAT5, and/or STAT3 are required for regulation of three distinct classes of immediate early genes. 1996.
342. Yoshimura A, Ichihara M, Kinjyo I, Moriyama M, Copeland NG, Gilbert DJ, Jenkins NA, Hara T and Miyajima AJTEj. Mouse oncostatin M: an immediate early gene induced by multiple cytokines through the JAK-STAT5 pathway. 1996;15:1055-1063.
343. Elbjeirami WM, Donnachie EM, Burns AR and Smith CWJAJoP-CP. Endothelium-derived GM-CSF influences expression of oncostatin M. 2011;301:C947-C953.
344. Ramsborg CG and Papoutsakis ETJEh. Global transcriptional analysis delineates the differential inflammatory response interleukin-15 elicits from cultured human T cells. 2007;35:454-464. e4.
345. Grenier A, Dehoux M, Boutten A, Arce-Vicioso M, Durand Gv, Gougerot-Pocidalo M-A and Chollet-Martin SJB, The Journal of the American Society of Hematology. Oncostatin M production and regulation by human polymorphonuclear neutrophils. 1999;93:1413-1421.
346. Rogge L, Bianchi E, Biffi M, Bono E, Chang S-YP, Alexander H, Santini C, Ferrari G, Sinigaglia L and Seiler MJNg. Transcript imaging of the development of human T helper cells using oligonucleotide arrays. 2000;25:96-101.
347. Kastl SP, Speidl WS, Kaun C, Katsaros KM, Rega G, Afonyushkin T, Bochkov VN, Valent P, Assadian A, Hagmueller GWJA, thrombosis, and biology v. In human macrophages the complement component C5a induces the expression of oncostatin M via AP-1 activation. 2008;28:498-503.
348. Kastl SP, Speidl WS, Katsaros KM, Kaun C, Rega G, Assadian A, Hagmueller GW, Hoeth M, de Martin R and Ma YJB, The Journal of the American Society of Hematology. Thrombin induces the expression of oncostatin M via AP-1 activation in human macrophages: a link between coagulation and inflammation. 2009;114:2812-2818.
349. Mosley B, De Imus C, Friend D, Boiani N, Thoma B, Park LS and Cosman D. Dual oncostatin M (OSM) receptors. Cloning and characterization of an alternative signaling subunit conferring OSM-specific receptor activation. *The Journal of biological chemistry*. 1996;271:32635-43.
350. Heinrich PC, Behrmann I, Müller-Newen G, Schaper F and Graeve L. Interleukin-6-type cytokine signalling through the gp130/Jak/STAT pathway. *The Biochemical journal*. 1998;334 (Pt 2):297-314.

351. Adrian-Segarra JM, Schindler N, Gajawada P, Lörchner H, Braun T and Pöling J. The AB loop and D-helix in binding site III of human Oncostatin M (OSM) are required for OSM receptor activation. *The Journal of biological chemistry*. 2018;293:7017-7029.
352. Deller MC, Hudson KR, Ikemizu S, Bravo J, Jones EY and Heath JK. Crystal structure and functional dissection of the cytostatic cytokine oncostatin M. *Structure (London, England : 1993)*. 2000;8:863-74.
353. Stahl N, Farruggella TJ, Boulton TG, Zhong Z, Darnell JE, Jr. and Yancopoulos GD. Choice of STATs and other substrates specified by modular tyrosine-based motifs in cytokine receptors. *Science (New York, NY)*. 1995;267:1349-53.
354. Hemmann U, Gerhartz C, Heesel B, Sasse J, Kurapkat G, Grötzinger J, Wollmer A, Zhong Z, Darnell JE, Jr., Graeve L, Heinrich PC and Horn F. Differential activation of acute phase response factor/Stat3 and Stat1 via the cytoplasmic domain of the interleukin 6 signal transducer gp130. II. Src homology SH2 domains define the specificity of stat factor activation. *The Journal of biological chemistry*. 1996;271:12999-3007.
355. Dey G, Radhakrishnan A, Syed N, Thomas JK, Nadig A, Srikumar K, Mathur PP, Pandey A, Lin SK, Raju R and Prasad TS. Signaling network of Oncostatin M pathway. *Journal of cell communication and signaling*. 2013;7:103-8.
356. Hermanns HM. Oncostatin M and interleukin-31: Cytokines, receptors, signal transduction and physiology. *Cytokine & growth factor reviews*. 2015;26:545-58.
357. Richards C. The Enigmatic Cytokine Oncostatin M and Roles in Disease. *ISRN inflammation*. 2013;2013:512103.
358. West NR, Owens BMJ and Hegazy AN. The oncostatin M-stromal cell axis in health and disease. 2018;88:e12694.
359. Richards CD. The enigmatic cytokine oncostatin m and roles in disease. *ISRN Inflamm*. 2013;2013:512103.
360. Stawski L and Trojanowska M. Oncostatin M and its role in fibrosis. *Connective tissue research*. 2019;60:40-49.
361. Vasse M, Pourtau J, Trochon V, Muraine M, Vannier J-P, Lu H, Soria J, Soria CJA, thrombosis, and biology v. Oncostatin M induces angiogenesis in vitro and in vivo. 1999;19:1835-1842.
362. Wijelath ES, Carlsen B, Cole T, Chen J, Kothari S and Hammond WPJJocs. Oncostatin M induces basic fibroblast growth factor expression in endothelial cells and promotes endothelial cell proliferation, migration and spindle morphology. 1997;110:871-879.
363. Pourtau J, Mirshahi F, Li H, Muraine M, Vincent L, Tedgui A, Vannier J-P, Soria J, Vasse M and Soria CJFl. Cyclooxygenase-2 activity is necessary for the angiogenic properties of oncostatin M. 1999;459:453-457.

364. Demyanets S, Kaun C, Rychli K, Pfaffenberger S, Kastl SP, Hohensinner PJ, Rega G, Katsaros KM, Afonyushkin T and Bochkov VNJBric. Oncostatin M-enhanced vascular endothelial growth factor expression in human vascular smooth muscle cells involves PI3K-, p38 MAPK-, Erk1/2-and STAT1/STAT3-dependent pathways and is attenuated by interferon-γ. 2011;106:217-231.
365. Schnittker D, Kwofie K, Ashkar A, Trigatti B and Richards CDJMoi. Oncostatin M and TLR-4 ligand synergize to induce MCP-1, IL-6, and VEGF in human aortic adventitial fibroblasts and smooth muscle cells. 2013;2013.
366. Rychli K, Kaun C, Hohensinner P, Rega G, Pfaffenberger S, Vyskocil E, Breuss J, Furnkranz A, Uhrin P, Zaujec JJJoT and Haemostasis. The inflammatory mediator oncostatin M induces angiopoietin 2 expression in endothelial cells in vitro and in vivo. 2010;8:596-604.
367. Strand K, Murray J, Aziz S, Ishida A, Rahman S, Patel Y, Cardona C, Hammond WP, Savidge G and Wijelath ESJJoCB. Induction of the urokinase plasminogen activator system by oncostatin M promotes endothelial migration. 2000;79:239-248.
368. Latroche C, Weiss-Gayet M, Muller L, Gitiaux C, Leblanc P, Liot S, Ben-Larbi S, Abou-Khalil R, Verger N and Bardot PJSCR. Coupling between myogenesis and angiogenesis during skeletal muscle regeneration is stimulated by restorative macrophages. 2017;9:2018-2033.
369. Modur V, Feldhaus MJ, Weyrich AS, Jicha DL, Prescott SM, Zimmerman GA and McIntyre TMJTJoci. Oncostatin M is a proinflammatory mediator. In vivo effects correlate with endothelial cell expression of inflammatory cytokines and adhesion molecules. 1997;100:158-168.
370. Kerfoot SM, Raharjo E, Ho M, Kaur J, Serirom S, McCafferty D-M, Burns AR, Patel KD and Kubes PJTAjop. Exclusive neutrophil recruitment with oncostatin M in a human system. 2001;159:1531-1539.
371. Lafontant PJ, Burns AR, Donnachie E, Haudek SB, Smith CW and Entman MLJAJoP-CP. Oncostatin M differentially regulates CXC chemokines in mouse cardiac fibroblasts. 2006;291:C18-C26.
372. Hohensinner P, Kaun C, Rychli K, Niessner A, Pfaffenberger S, Rega G, Furnkranz A, Uhrin P, Zaujec J and Afonyushkin TJTFJ. The inflammatory mediator oncostatin M induces stromal derived factor-1 in human adult cardiac cells. 2009;23:774-782.
373. Pöling J, Gajawada P, Lörchner H, Polyakowa V, Szibor M, Böttger T, Warnecke H, Kubin T and Braun T. The Janus face of OSM-mediated cardiomyocyte dedifferentiation during cardiac repair and disease. *Cell Cycle*. 2012;11:439-445.
374. Maass AH and Buvoli M. Cardiomyocyte Preparation, Culture, and Gene Transfer. In: J. Zhang and G. Rokosh, eds. *Cardiac Gene Expression: Methods and Protocols* Totowa, NJ: Humana Press; 2007: 321-330.

375. Théry C, Amigorena S, Raposo G and Clayton A. Isolation and Characterization of Exosomes from Cell Culture Supernatants and Biological Fluids. *Current Protocols in Cell Biology*. 2006;30:3.22.1-3.22.29.
376. Er F, Dahlem KM, Nia AM, Erdmann E, Waltenberger J, Hellmich M, Kuhr K, Le MT, Herrfurth T, Taghiyev Z, Biesenbach E, Yüksel D, Eran-Ergöknil A, Vanezi M, Caglayan E and Gassanov N. Randomized Control of Sympathetic Drive With Continuous Intravenous Esmolol in Patients With Acute ST-Segment Elevation Myocardial Infarction: The BEtA-Blocker Therapy in Acute Myocardial Infarction (BEAT-AMI) Trial. *JACC Cardiovasc Interv*. 2016;9:231-240.
377. Barone FC, White RF, Spera PA, Ellison J, Currie RW, Wang X and Feuerstein GZ. Ischemic preconditioning and brain tolerance: temporal histological and functional outcomes, protein synthesis requirement, and interleukin-1 receptor antagonist and early gene expression. *Stroke*. 1998;29:1937-50; discussion 1950-1.
378. Chen-Scarabelli C, Agrawal PR, Saravolatz L, Abuniat C, Scarabelli G, Stephanou A, Loomba L, Narula J, Scarabelli TM and Knight R. The role and modulation of autophagy in experimental models of myocardial ischemia-reperfusion injury. *J Geriatr Cardiol*. 2014;11:338-48.
379. Ni M, Zhang Y and Lee AS. Beyond the endoplasmic reticulum: atypical GRP78 in cell viability, signalling and therapeutic targeting. *The Biochemical journal*. 2011;434:181-8.
380. Palano G, Jansson M, Backmark A, Martinsson S, Sabirsh A, Hultenby K, Åkerblad P, Granberg KL, Jennbacken K, Müllers E and Hansson EM. A high-content, in vitro cardiac fibrosis assay for high-throughput, phenotypic identification of compounds with anti-fibrotic activity. *J Mol Cell Cardiol*. 2020;142:105-117.
381. Lu Y, Lou J, Liu X and Wang S. Oxysophocarpine reduces oxygen-glucose deprivation-induced microglial activation and injury. *Am J Transl Res*. 2017;9:2266-2275.
382. Gustafsson Åsa B and Gottlieb Roberta A. Autophagy in Ischemic Heart Disease. *Circulation Research*. 2009;104:150-158.
383. Thorburn A. Apoptosis and autophagy: regulatory connections between two supposedly different processes. *Apoptosis*. 2008;13:1-9.
384. Semenza GL and Prabhakar NR. The role of hypoxia-inducible factors in oxygen sensing by the carotid body. *Adv Exp Med Biol*. 2012;758:1-5.
385. Dallabrida SM, Ismail N, Oberle JR, Himes BE and Rupnick MA. Angiopoietin-1 Promotes Cardiac and Skeletal Myocyte Survival Through Integrins. *Circulation research*. 2005;96:e8-e24.
386. Huang B, Qian J, Ma J, Huang Z, Shen Y, Chen X, Sun A, Ge J and Chen H. Myocardial transfection of hypoxia-inducible factor-1α and co-transplantation of mesenchymal stem cells enhance cardiac repair in rats with experimental myocardial infarction. *Stem cell research & therapy*. 2014;5:22.

387. Zhang SJ, Song XY, He M and Yu SB. Effect of TGF-β1/SDF-1/CXCR4 signal on BM-MSCs homing in rat heart of ischemia/perfusion injury. *Eur Rev Med Pharmacol Sci*. 2016;20:899-905.
388. Fu X, Liu G, Halim A, Ju Y, Luo Q and Song AG. Mesenchymal Stem Cell Migration and Tissue Repair. *Cells*. 2019;8.
389. Deng J-H, Li Z-J, Wang Z-X, Feng J, Huang X-J and Zeng Z-M. Electron Microscopy-Based Comparison and Investigation of the Morphology of Exosomes Derived from Hepatocellular Carcinoma Cells Isolated at Different Centrifugal Speeds. *Microscopy and Microanalysis*. 2020;26:310-318.
390. Braunwald E and Kloner RA. Myocardial reperfusion: a double-edged sword? *J Clin Invest*. 1985;76:1713-9.
391. Olsson A-K, Dimberg A, Kreuger J and Claesson-Welsh L. VEGF receptor signalling ? in control of vascular function. *Nature Reviews Molecular Cell Biology*. 2006;7:359-371.
392. Gustafsson ÅB and Gottlieb RA. Autophagy in Ischemic Heart Disease. *Circulation research*. 2009;104:150-158.
393. Huang MH, Wu Y, Nguyen V, Rastogi S, McConnell BK, Wijaya C, Uretsky BF, Poh KK, Tan HC and Fujise K. Heart protection by combination therapy with Esmolol and milrinone at late-ischemia and early reperfusion. *Cardiovasc Drugs Ther*. 2011;25:223-32.
394. Zhang Q and Li C. Combination of epinephrine with Esmolol attenuates post-resuscitation myocardial dysfunction in a porcine model of cardiac arrest. *PloS one*. 2013;8:e82677.
395. García-Ruiz JM, Fernández-Jiménez R, García-Alvarez A, Pizarro G, Galán-Arriola C, Fernández-Friera L, Mateos A, Nuno-Ayala M, Aguero J, Sánchez-González J, García-Prieto J, López-Melgar B, Martínez-Tenorio P, López-Martín GJ, Macías A, Pérez-Asenjo B, Cabrera JA, Fernández-Ortiz A, Fuster V and Ibáñez B. Impact of the Timing of Metoprolol Administration During STEMI on Infarct Size and Ventricular Function. *Journal of the American College of Cardiology*. 2016;67:2093-2104.
396. Webber M, Jackson SP, Moon JC and Captur G. Myocardial Fibrosis in Heart Failure: Anti-Fibrotic Therapies and the Role of Cardiovascular Magnetic Resonance in Drug Trials. *Cardiology and Therapy*. 2020;9:363-376.
397. Gandia C, Armiñan A, García-Verdugo JM, Lledó E, Ruiz A, Miñana MD, Sanchez-Torrijos J, Payá R, Mirabet V, Carbonell-Uberos F, Llop M, Montero JA and Sepúlveda P. Human Dental Pulp Stem Cells Improve Left Ventricular Function, Induce Angiogenesis, and Reduce Infarct Size in Rats with Acute Myocardial Infarction. *STEM CELLS*. 2008;26:638-645.
398. Li Q, Wang H, Peng H, Huyan T and Cacalano NA. Exosomes: Versatile Nano Mediators of Immune Regulation. *Cancers (Basel)*. 2019;11.
399. Robbins PD and Morelli AE. Regulation of immune responses by extracellular vesicles. *Nat Rev Immunol*. 2014;14:195-208.

400. Khan M, Nickoloff E, Abramova T, Johnson J, Verma SK, Krishnamurthy P, Mackie AR, Vaughan E, Garikipati VN, Benedict C, Ramirez V, Lambers E, Ito A, Gao E, Misener S, Luongo T, Elrod J, Qin G, Houser SR, Koch WJ and Kishore R. Embryonic stem cell-derived exosomes promote endogenous repair mechanisms and enhance cardiac function following myocardial infarction. *Circulation research*. 2015;117:52-64.
401. Gallet R, Dawkins J, Valle J, Simsolo E, de Couto G, Middleton R, Tseliou E, Luthringer D, Kreke M, Smith RR, Marbán L, Ghaleb B and Marbán E. Exosomes secreted by cardiosphere-derived cells reduce scarring, attenuate adverse remodelling, and improve function in acute and chronic porcine myocardial infarction. *Eur Heart J*. 2017;38:201-211.
402. Deng S, Zhou X, Ge Z, Song Y, Wang H, Liu X and Zhang D. Exosomes from adipose-derived mesenchymal stem cells ameliorate cardiac damage after myocardial infarction by activating S1P/SK1/S1PR1 signaling and promoting macrophage M2 polarization. *Int J Biochem Cell Biol*. 2019;114:105564.
403. Wu Q, Wang J, Tan WLW, Jiang Y, Wang S, Li Q, Yu X, Tan J, Liu S, Zhang P, Tiang Z, Chen Z, Foo RS and Yang HT. Extracellular vesicles from human embryonic stem cell-derived cardiovascular progenitor cells promote cardiac infarct healing through reducing cardiomyocyte death and promoting angiogenesis. *Cell Death Dis*. 2020;11:354.
404. Stanko P, Altanerova U, Jakubechova J, Repiska V and Altaner C. Dental Mesenchymal Stem/Stromal Cells and Their Exosomes. *Stem Cells Int*. 2018;2018:8973613.
405. Merckx G, Hosseinkhani B, Kuypers S, Deville S, Irobi J, Nelissen I, Michiels L, Lambrichts I and Bronckaers A. Angiogenic Effects of Human Dental Pulp and Bone Marrow-Derived Mesenchymal Stromal Cells and their Extracellular Vesicles. *Cells*. 2020;9.
406. Turinetto V, Vitale E and Giachino C. Senescence in Human Mesenchymal Stem Cells: Functional Changes and Implications in Stem Cell-Based Therapy. *International journal of molecular sciences*. 2016;17.
407. Lörchner H, Pöling J, Gajawada P, Hou Y, Polyakova V, Kostin S, Adrian-Segarra JM, Boettger T, Wietelmann A, Warnecke H, Richter M, Kubin T and Braun T. Myocardial healing requires Reg3β-dependent accumulation of macrophages in the ischemic heart. *Nature medicine*. 2015;21:353-62.
408. Hasegawa M, Sato S, Ihn H and Takehara K. Enhanced production of interleukin-6 (IL-6), oncostatin M and soluble IL-6 receptor by cultured peripheral blood mononuclear cells from patients with systemic sclerosis. *Rheumatology (Oxford)*. 1999;38:612-7.
409. Hamada T, Sato A, Hirano T, Yamamoto T, Son G, Onodera M, Torii I, Nishigami T, Tanaka M, Miyajima A, Nishiguchi S, Fujimoto J and Tsujimura T.

Oncostatin M gene therapy attenuates liver damage induced by dimethylnitrosamine in rats. *Am J Pathol*. 2007;171:872-881.